Rethinking Black Hole Accretion Discs

by

Greg Salvesen

B.S., University of Michigan Ann Arbor, 2009

B.S.E., University of Michigan Ann Arbor, 2009

M.S., University of Colorado Boulder, 2011

A thesis submitted to the

Faculty of the Graduate School of the

University of Colorado in partial fulfillment

of the requirements for the degree of

Doctor of Philosophy

Department of Astrophysical and Planetary Sciences

2016

This thesis entitled:
Rethinking Black Hole Accretion Discs
written by Greg Salvesen
has been approved for the Department of Astrophysical and Planetary Sciences

_____
Prof. Mitchell C. Begelman

_____
Prof. Philip J. Armitage

_____
Dr. Jacob B. Simon

_____
Prof. Jeremy Darling

_____
Prof. J. Michael Shull

Date _____

The final copy of this thesis has been examined by the signatories, and we find that both the content and
the form meet acceptable presentation standards of scholarly work in the above mentioned discipline.

Salvesen, Greg (Ph.D., Astrophysical and Planetary Sciences)

Rethinking Black Hole Accretion Discs

Thesis directed by Prof. Mitchell C. Begelman

Accretion discs are staples of astrophysics. Tapping into the gravitational potential energy of the accreting material, these discs are highly efficient machines that produce copious radiation and extreme outflows. While interesting in their own right, accretion discs also act as tools to study black holes and directly influence the properties of the Universe. Black hole X-ray binaries are fantastic natural laboratories for studying accretion disc physics and black hole phenomena. Among many of the curious behaviors exhibited by these systems are black hole state transitions — complicated cycles of dramatic brightening and dimming. Using X-ray observations with high temporal cadence, we show that the evolution of the accretion disc spectrum during black hole state transitions can be described by a variable disc atmospheric structure without invoking a radially truncated disc geometry. The accretion disc spectrum can be a powerful diagnostic for measuring black hole spin if the effects of the disc atmosphere on the emergent spectrum are well-understood; however, properties of the disc atmosphere are largely unconstrained. Using statistical methods, we decompose this black hole spin measurement technique and show that modest uncertainties regarding the disc atmosphere can lead to erroneous spin measurements. The vertical structure of the disc is difficult to constrain due to our ignorance of the contribution to hydrostatic balance by magnetic fields, which are fundamental to the accretion process. Observations of black hole X-ray binaries and the accretion environments near supermassive black holes provide mounting evidence for strong magnetization. Performing numerical simulations of accretion discs in the shearing box approximation, we impose a net vertical magnetic flux that allows us to effectively control the level of disc magnetization. We study how dynamo activity and the properties of turbulence driven by the magnetorotational instability depend on the magnetized state of the gas, spanning weak-to-strong disc magnetization regimes. We also demonstrate that a background poloidal magnetic flux is required to form and sustain a strongly magnetized accretion disc. This thesis motivates the need for understanding how magnetic fields affect the observed spectrum from black hole accretion discs.

Dedication

To mom and dad

who inspired it,

but will never read it.

Acknowledgements

For better or worse — I think better — I never would have entered astronomy graduate school had it not been for my undergraduate advisor, Jon Miller. Jon made a big school feel small and made me realize that I could avoid real life for awhile by worrying about black holes. With the encouragement of another stellar mentor, Mateusz Ruszkowski, I chose Boulder, Colorado for graduate school. Jon's parting advice was, "Graduate school is a marathon, not a sprint."

In my case, graduate school was an ultra marathon. I owe a big thanks to my advisors, Mitch Begelman and Phil Armitage, who allowed me the freedom to pursue my interests during my seven year sabbatical while looking out for me along the way. I was surrounded by top-notch postdocs who hugely influenced my interests — Rubens Reis, Jake Simon, Chris Nixon, Becca Martin, and Kaitlin Kratter, you've all been inspiring colleagues and great friends. To my officemates, Susanna Kohler and Eric Coughlin, you made me feel like we were in this thing together, even though I finished last with a burro in tow. Jordan Mirocha was always game for a coffee or beer to talk science, while Grant Buckingham insisted on nixing the astronomy talk and commencing the party.

I met some very bad influences through the Boulder Banditos and Rocky Mountain Runners, without whom this thesis would have been completed two years earlier. Thank you guys for enabling my running obsession, through which I met Cassie. Cassie, you really get me and I can't wait for all of the adventures we will have together. Summit is excited, too!

Of course, my family members are largely to blame for how I wound up. My dad used to give me the change in his pocket if I could deduce the denominations from the total value and coin count. My mom never got me that basketball hoop I wanted, forcing me to put all of my eggs in the astronomy basket with no backup plan as an NBA star. I enjoyed sharing Boulder with my brothers, Jeff and Brian, but I was here first for the record. I love you all a lot.

Contents

Chapter

7 Conclusions   185

Appendix

Tables

Table

Figures

Figure

Chapter 1

Introduction

An accretion disc is an astrophysical machine that can be incredibly efficient at converting gravitational potential energy into electromagnetic radiation (and sometimes kinetic energy in the form of outflows). This property of accretion discs allows Galactic X-ray binaries to be discovered, which sometimes turn out to harbor a black hole accretor. The high radiative efficiency of accretion discs also led astronomers to realize their role as the central engines of active galactic nuclei and quasars, which are among the most powerful objects in the Universe.

But, why would one expect an accretion disc to form around a black hole in the first place? In the case of radial inflow of gas at low mass accretion rates onto a black hole (e.g., Bondi, 1952), gravity is the only important force in dictating the dynamics of the flow. However, in realistic situations the accreting gas will have non-negligible specific angular momentum, which the gas must somehow lose if it is to be accreted. This need for accreting material to lose angular momentum, along with the small spatial scale of black holes compared to their fuel reservoir, gives rise to accretion discs. Consider a binary system consisting of a black hole primary and a donor star secondary that has filled its Roche lobe. As the gas from the secondary streams toward the black hole, centrifugal forces on the material of a given angular momentum increase faster ($F_{\mathrm{cent}} \propto R^{-3}$) than the force of gravity from the black hole ($F_{\mathrm{grav}} \propto R^{-2}$) (e.g., Blaes, 2014). Consequently, the flow will be rotationally supported and a disc of gas will naturally form around the black hole. Inward accretion of disc material toward the black hole and the liberation of gravitational binding energy can then proceed if angular momentum is transported outward.

It would seem that identifying the angular momentum transport process that is ultimately responsible

for mediating energy conversion (i.e., gravitational binding energy $\rightarrow$ radiation) is of central importance in accretion disc theory. While this is true and we will touch on this soon, it is important to highlight perhaps the most salient feature of accretion disc theory. Namely, that the predicted spectrum emitted by the disc requires no knowledge of the details of the angular momentum transport mechanism (Shakura & Sunyaev, 1973).

1.1   Accretion Disc Spectrum

The spectrum of an accretion disc that is geometrically thin and optically thick in the direction perpendicular to the disc mid-plane can be derived from considering mass and angular momentum conservation within a given disc annulus (e.g., Shakura & Sunyaev, 1973; Pringle, 1981). The subsequent derivations closely follow Frank et al. (2002). We adopt cylindrical coordinates (R, ϕ, z) with the disc mid-plane at $z = 0$ and a black hole of mass M residing at the origin. The motion of the disc material is circular orbits around the black hole with angular velocity profile $\Omega(R)$. The surface area of one face of a disc annulus with inner edge at radius R and outer edge at $R + \Delta R$ is,

$$A = \pi \left[(R + \Delta R)^2 - R^2 \right] \simeq 2\pi R \Delta R, \tag{1.1}$$

where we've assumed the limit of small ΔR (i.e., neglecting second order terms). We assume the disc material has a small radial drift velocity $v_R = dR/dt$, where inward (outward) flow corresponds to negative (positive) v_R by convention. The mass per unit surface area of the disc is the surface density $\Sigma(R, t)$, which is obtained locally by integrating the gas density ρ in the z-direction,

$$\Sigma = \frac{1}{2} \int_{-\infty}^{+\infty} \rho \, dz, \tag{1.2}$$

A subtle but important point to mention is that both A and Σ as we define them above consider one face of the disc. The rate of change of mass and angular momentum in the disc comes from considering the net flow of each of these conserved quantities into/out of a given annulus.

The mass contained in an annulus is $2\pi R \Delta R \Sigma$ and the mass conservation equation in the limit $\Delta R \rightarrow 0$ is (Frank et al., 2002),

$$R \frac{\partial \Sigma}{\partial t} + \frac{\partial}{\partial R} (R \Sigma v_R) = 0. \tag{1.3}$$

In a steady state (i.e., $\partial/\partial t = 0$) this becomes,

$$\dot{M} = 2\pi R \Sigma \left(-v_R\right), \tag{1.4}$$

where $\dot{M}$ is the mass accretion rate and we recall that $v_R < 0$.

The angular momentum contained in an annulus is $2\pi R \Delta R \Sigma R^2 \Omega$. In addition to the net flow of angular momentum through the disc annulus, the net angular momentum transport from viscous torques $G\left(R, t\right)$ from neighboring annuli must also be included. The torque exerted by an outer ring on an inner ring at radius R is given by,

$$G\left(R\right) = 2\pi R \nu \Sigma R^2 \frac{d\Omega}{dR}, \tag{1.5}$$

where ν is the fluid viscosity. Note that if $d\Omega/dR < 0$ then $G\left(R\right)$ is negative, which means that inner annuli lose angular momentum to the outer annuli and gas will spiral inwards. The net torque on an annulus of gas between R and $R + \Delta R$ is then,

$$G\left(R + \Delta R\right) - G\left(R\right) = \frac{\partial G}{\partial R} \Delta R. \tag{1.6}$$

We suppose that the disc has a Keplerian orbital velocity profile (i.e., balance between gravity and the centripetal force for a circular orbit), $v_\phi = R\Omega_{\mathrm{K}}\left(R\right)$ where we've adopted $\Omega\left(R\right) = \Omega_{\mathrm{K}}\left(R\right) = \sqrt{GM/R^3}$. Taking all of this into consideration, the angular momentum conservation in the limit $\Delta R \to 0$ brings us to an equation describing the temporal evolution of the surface density in a Keplerian accretion disc (Frank et al., 2002),

$$\frac{\partial \Sigma}{\partial t} = \frac{3}{R} \frac{\partial}{\partial R} \left\{ R^{1/2} \frac{\partial}{\partial R} \left[\nu \Sigma R^{1/2} \right] \right\}. \tag{1.7}$$

In a steady state with $\partial/\partial t = 0$ and applying the boundary condition $d\Omega/dR = 0$ (i.e., zero torque) at the inner disc edge R_{in}, the angular momentum conservation equation 1.7 becomes,

$$\nu \Sigma = \frac{\dot{M}}{3\pi} \left[1 - \left(\frac{R_{\mathrm{in}}}{R} \right)^{1/2} \right]. \tag{1.8}$$

We will have cause to use Equation 1.8 shortly, but we must first derive the energy loss rate from the disc (i.e., the viscous dissipation rate). The rate of work done on the gas by the viscous torque is (Frank et al., 2002),

$$\Omega \frac{\partial G}{\partial R} \Delta R = \left[\frac{\partial}{\partial R} \left(G\Omega \right) - G \frac{d\Omega}{dR} \right] dR. \tag{1.9}$$

The first term on the right hand side is the rate at which rotational energy is convected through the disc annulus. The second term $-G d\Omega/dR$ is the local rate that mechanical energy goes into heating the gas. Therefore, viscous torques cause viscous dissipation of energy within the gas — which must ultimately be radiated away from the disc faces — at the rate $G d\Omega/dR$. The rate of viscous dissipation per unit surface area is then,

$$
\begin{aligned}
D\left(R\right) &= \frac{\text{Total dissipation rate (due to viscous torques) per annulus width } \Delta\text{R}}{\text{Disc emitting area (both faces)}} \\
&= \frac{G\left(d\Omega/dR\right)\Delta R}{2 \times 2\pi R \Delta R} \\
&= \frac{9}{8}\frac{GM}{R^3}\nu\Sigma,
\end{aligned}
\tag{1.10}
$$

where we used Equation 1.5 and a Keplerian angular velocity $\Omega = \Omega_{\text{K}}$ to arrive at the expression on the bottom line. Inserting Equation 1.8 into Equation 1.10 gives,

$$
D\left(R\right) = \frac{3GM\dot{M}}{8\pi R^3}\left[1 - \left(\frac{R_{\text{in}}}{R}\right)^{1/2}\right].
\tag{1.11}
$$

Arriving at this dissipation rate per unit disc face area took some effort, but the implication is profound: the energy flux escaping the disc is independent of viscosity!

We are now in a position to derive the spectrum emitted by a face of an accretion disc. Assuming that the accretion disc is geometrically thin and optically thick disc in the z-direction, each element of a disc face will radiate a local blackbody spectrum with radial temperature profile $T\left(R\right)$. Therefore, $\sigma\left[T\left(R\right)\right]^4 = D\left(R\right)$ with σ being the Stefan-Boltzmann constant and plugging in $D\left(R\right)$ from Equation 1.11 gives,

$$
T\left(R\right) = \left\{\frac{3GM\dot{M}}{8\pi R^3\sigma}\left[1 - \left(\frac{R_{\text{in}}}{R}\right)^{1/2}\right]\right\}^{1/4}.
\tag{1.12}
$$

From Equation 1.12 one can show that the maximum disc temperature occurs at $R = \left(49/36\right)R_{\text{in}}$ and is given by,

$$
T_{\text{max}} = \frac{6^{3/2}}{7^{7/4}}\left(\frac{3GM\dot{M}}{8\pi R_{\text{in}}\sigma}\right)^{1/4}.
\tag{1.13}
$$

Defining the dimensionless radius $\tilde{r} \equiv R/R_{\text{in}}$ and re-parametrizing in terms of T_{max}, Equation 1.12 becomes,

$$
T\left(\tilde{r}\right) = \frac{7^{7/4}}{6^{3/2}}T_{\text{max}}\tilde{r}^{-3/4}\left(1 - \tilde{r}^{-1/2}\right)^{1/4}.
\tag{1.14}
$$

The disc spectrum emitted over the area of a disc face then comes from integrating the Planck function over the disc area (e.g., Zimmerman et al., 2005),

$$F_E = K_{\text{flux}} \frac{4\pi E^3}{h^3 c^2} \int_1^\infty \frac{\tilde{r}}{\exp\left[E/kT\left(\tilde{r}\right)\right] - 1} d\tilde{r} \; \left[\text{erg s}^{-1} \text{ cm}^{-2} \text{ keV}^{-1}\right], \tag{1.15}$$

where,

$$K_{\text{flux}} = \left(\frac{R_{\text{in}}}{D}\right)^2 \cos\left(i\right), \tag{1.16}$$

is the flux normalization parameter for a source distance D and disc inclination i. In some circumstances it is useful to replace R_{in} with $r_{\text{in}} \equiv R_{\text{in}}/R_{\text{g}}$, where $R_{\text{g}} = GM/c^2$ is the gravitational radius.

Amazingly, not only is the disc spectrum independent of viscosity, but it is also fully described by two parameters: T_{max} is a shape parameter (Equation 1.13) and K_{flux} is a normalization constant (Equation 4.3), which itself depends on intrinsic properties of the source. Equation 1.15 is a composite of the local blackbody spectrum emitted by each disc annulus according to a radial temperature profile. Therefore, this accretion disc spectral model is known as the multi-colour disc blackbody (Mitsuda et al., 1984; Makishima et al., 1986).

The accretion disc spectrum from a supermassive black holes peaks in the ultraviolet and therefore will be heavily attenuated by Galactic absorption. However, the spectrum from an accretion disc around a stellar mass black hole peaks in the soft X-ray band (~ 1 keV), which makes black hole X-ray binaries ideal sources for studying accretion discs. High quality CCDs on-board X-ray observatories (e.g., *XMM-Newton*, *Chandra*) are at best sensitive down to ~ 0.1 keV; therefore, observers are often faced with the challenge of relying on the Wien tail to fit the X-ray disc spectrum. In practice, X-ray data can only constrain two free parameters, which makes the multi-colour disc blackbody solution immensely powerful.

If the black hole mass, distance to the source, and disc inclination are known independently, then measuring K_{flux} becomes equivalent to constraining the dimensionless inner disc radius r_{in} (e.g., Zhang et al., 1997; McClintock et al., 2006). One might then reasonably assume that the inner edge of the accretion disc, r_{in}, coincides with the innermost stable circular orbit (ISCO), r_{ISCO}, inside of which the gas must dynamically plunge into the black hole. This $r_{\text{in}} = r_{\text{ISCO}}$ assumption is physically motivated because the gas viscous timescale is long relative to the free-fall timescale for gas at the ISCO; therefore, the gas interior to r_{ISCO}
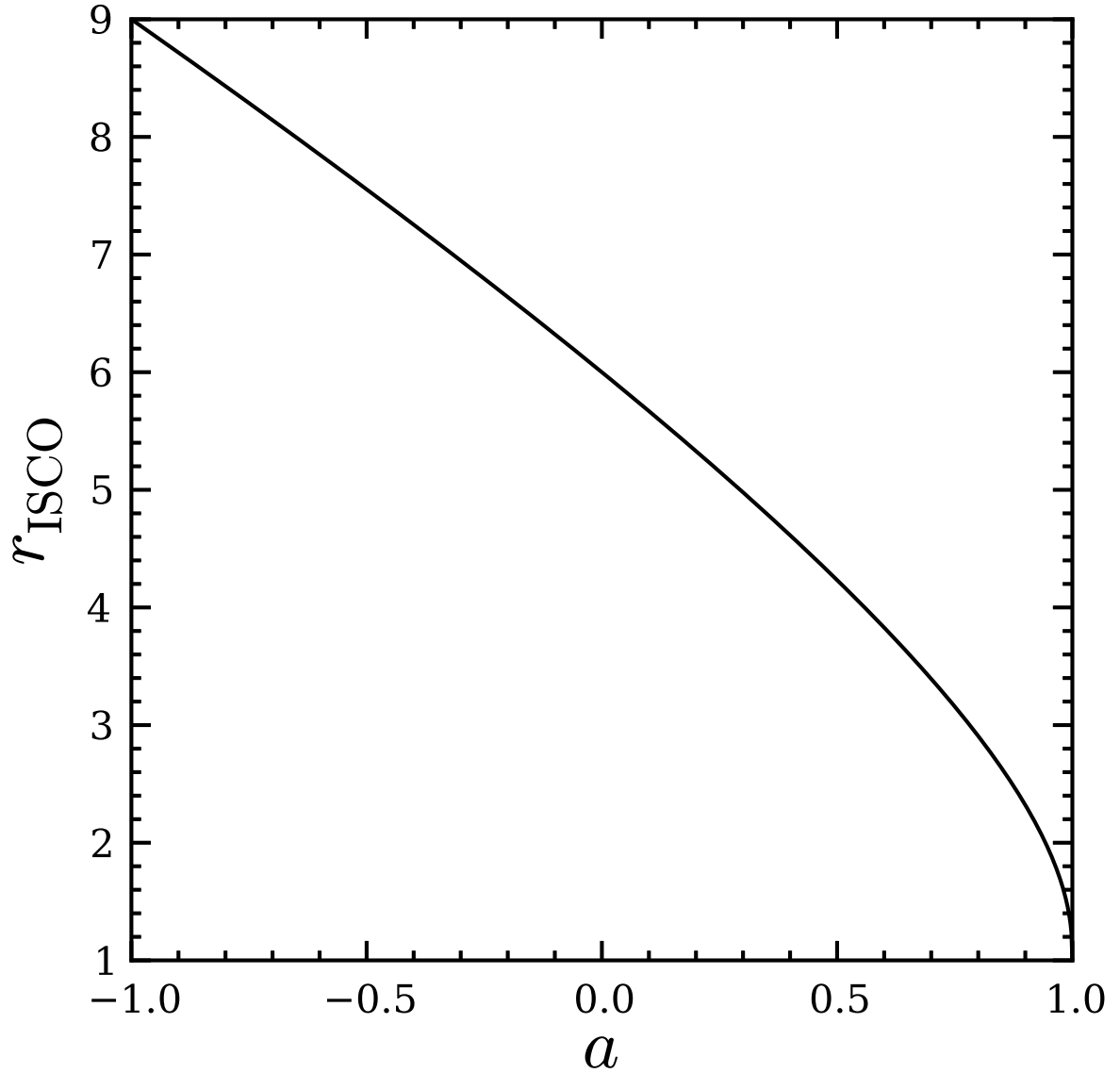
Figure 1.1: Location of the innermost stable circular orbit, r_{ISCO}, as a function of the dimensionless black hole spin parameter, a (Bardeen et al., 1972). A prograde (retrograde) system consists of the black hole and disc angular momenta being aligned (anti-aligned). A maximally-spinning retrograde system ($a = -1$) has $r_{\mathrm{ISCO}} = 9$, a non-spinning black hole ($a = 0$) has $r_{\mathrm{ISCO}} = 6$, and a maximally-spinning prograde system ($a = 1$) has $r_{\mathrm{ISCO}} = 1$, where r_{ISCO} is given in units of gravitational radii $R_{\mathrm{g}} = GM/c^2$ and M is the black hole mass.

does not have time to radiate appreciably before being accreted. Additionally, numerical simulations of magnetized accretion discs demonstrate that a magnetic field is unable to couple the disc material to the gas interior to the ISCO (Armitage et al., 2001).

A robust measurement of the location of the ISCO is important because it turns out that r_{ISCO} is a monotonic function of the non-dimensional black hole spin parameter, $a = cJ/\left(GM^2\right)$, where J is the black hole angular momentum (see Figure 1.1; Bardeen et al., 1972). Therefore, measuring r_{ISCO} is equivalent to measuring black hole spin, a. This demonstrates that accretion discs, while interesting in their own right, also provide powerful diagnostics from which fundamental properties of black holes can be probed. How the black hole spin measurements are affected by uncertainties in the disc vertical structure is the topic of Chapter 4.

Another well-known interesting result of accretion disc theory comes from integrating Equation 1.11 from $R = R_{\mathrm{in}}$ to $R_{\mathrm{out}} \to \infty$ over both faces of the disc to obtain the bolometric disc luminosity,

$$L_{\mathrm{disc}} = \frac{GM\dot{M}}{2R_{\mathrm{in}}}. \tag{1.17}$$

The accretion luminosity corresponding to converting *all* of the gravitational binding energy of the accretion gas into radiation is $L_{\mathrm{acc}} = GM\dot{M}/R_{\mathrm{in}}$ (e.g., Frank et al., 2002). Therefore, *half* of the available accretion power is radiated away by the disc during the accretion process and *half* goes into kinetic energy of the gas at the inner disc edge. This means that for an accretion disc around a black hole with an inner edge extending down to the ISCO, half of the available accretion energy is presumably swallowed by the hole!

1.2   Vertical Disc Structure and Spectral Hardening

The thorn in the side of the multi-colour disc blackbody model (Equation 1.15) from the previous section is that the effects of the disc atmosphere are neglected. In other words, the details of the disc vertical structure — temperature, density, ionization state — where the optical depth $\tau \lesssim 1$ will modify the spectrum emitted at the disc photosphere. Modeling the disc atmosphere quickly becomes quite complicated, with the relevant physics including free-free/bound-free opacities and electron scattering (i.e., incoherent Compton scattering). Adopting the methodology of Ross et al. (1978, 1992) to self-consistently solve the radiative

transfer along with the vertical disc structure, Shimura & Takahara (1995) demonstrated that the complicated effects of the disc atmosphere on the emitted spectrum can be approximated by a phenomenological constant factor. This is the spectral hardening factor f_{col} (also called the colour correction factor). A pure blackbody spectrum has $f_{col} = 1$. The concept of exploiting the simplistic and practical f_{col} parametrization to incorporate the effects of the disc vertical structure is central to this thesis.

It is important to distinguish between the effective temperature and the colour temperature, which are related by $T_{col} = f_{col}T_{eff}$. The *effective temperature* depends on the source intensity and is described by the familiar blackbody relation for the emergent flux (e.g., Rybicki & Lightman, 1979),

$$F = \sigma T_{eff}^4. \tag{1.18}$$

When a spectrum has a blackbody shape but the incorrect normalization, the *color temperature* corresponds to the blackbody that best describes the spectrum without regard to the vertical scale; therefore, T_{col} depends only on the shape of the observed spectrum (Rybicki & Lightman, 1979). The spectral hardening factor can be incorporated into a *modified* multi-colour disc blackbody model, which is derived as before by replacing each occurrence of $T(R)$ with $T_{col}(R) = f_{col}T(R)$. Then, Equation 1.15 becomes,

$$F_E = K_{flux}\frac{4\pi E^3}{h^3 c^2}\int_1^\infty \frac{\tilde{r}}{\exp\left[E/kT_{col}\left(\tilde{r}\right)\right]-1}d\tilde{r}\ \left[\mathrm{erg\ s^{-1}\ cm^{-2}\ keV^{-1}}\right], \tag{1.19}$$

where now,

$$K_{flux} = \frac{1}{f_{col}^4}\left(\frac{R_{in}}{D}\right)^2\cos\left(i\right), \tag{1.20}$$

The colour temperature describes the observed accretion disc spectrum, while f_{col} tells us by how much to translate the spectrum in energy space in order to recover the underlying photospheric spectrum. Sophisticated disc atmospheric models tend to converge on the range $1.4 \lesssim f_{col} \lesssim 2.0$ (e.g., Shimura & Takahara, 1995; Davis et al., 2005). However, f_{col} can potentially be significantly enhanced if vertical magnetic pressure support is considered.

Introducing a magnetic pressure contribution in the disc to stave off the vertical gravity due to the black hole means that less gas pressure support is now required in order to achieve vertical equilibrium. This diminished gas pressure support means the vertical density gradients are less steep than they would be

without magnetic pressure support. Therefore, when magnetic support is included, the density scale height increases and the disc atmosphere becomes vertically extended. The location of the effective photosphere, z_{eff}, is the important location to consider for determining the observed disc spectrum and is set by a constant value of the effective optical depth, $\tau_{\mathrm{eff}} \simeq 1$. Therefore, as shown schematically in Figure 1.2, an astronomer observing a magnetically supported disc will encounter the effective photosphere at a larger disc height and lower density compared to a disc without magnetic support. The gas density determines the relative contributions to the total opacity from absorption ($\kappa_{\mathrm{abs}} \propto \rho$) and electron scattering ($\kappa_{\mathrm{es}} \propto \rho^0$), with a lower density reducing the ratio $\kappa_{\mathrm{abs}}/\kappa_{\mathrm{es}}$. Taking all of this together, a disc with magnetic pressure support has a lower density at the effective photosphere, ρ_{eff} and, therefore, enhanced electron scattering, which acts to harden the disc spectrum, as shown in Figure 1.3. Blaes et al. (2006) used numerical simulations to show that this hardening is modest for very weakly magnetized discs (*dashed line*), while the analytic arguments of Begelman & Pringle (2007) predict substantial hardening for strongly magnetized discs (*dotted line*).

Although magnetic fields are undeniably fundamental to disc accretion, their potentially important effects on the observed disc spectrum have gone largely unappreciated. Chapter 2 addresses the possibility that the evolution of the inner disc regions during black hole state transitions is attributed to a variable vertical disc structure (as parametrized by f_{col}).

1.3   Magnetorotational Instability

In a landmark paper, Balbus & Hawley (1991) identified the magnetorotational instability (MRI; Velikhov, 1959; Chandrasekhar, 1961) as the physical mechanism that mediates angular momentum transport in accretion discs. Accretion discs around black holes are expected to be highly ionized due to the high temperature of the gas, especially in the inner disc regions. Therefore, if a magnetic field is present and the fluid is a perfect conductor (i.e., resistivity $\eta = 0$), then the magnetic flux is "frozen-in" to the plasma. In other words, the plasma and the magnetic field move together. Because magnetic fields have tension, any displacement of a fluid element perpendicular to a magnetic field line results in an attractive force that is proportional to the displacement. Usually, such a force is restorative and acts to stabilize the plasma; however, it turns out that this attractive force can be destabilizing if the fluid is rotating. The MRI is a
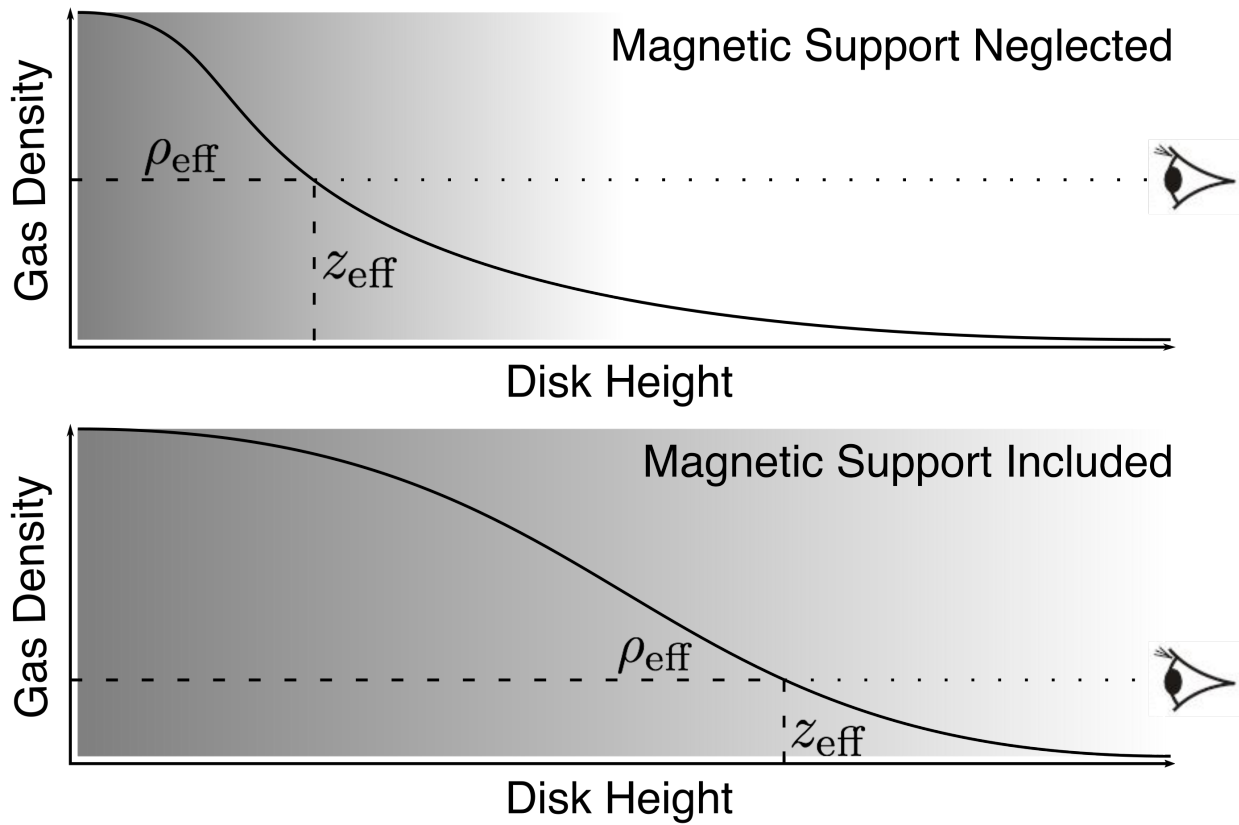
Figure 1.2: Vertical magnetic pressure support causes the disc atmosphere to become vertically extended. Consequently, the effective photosphere is encountered at a larger disc height (z_{eff}) and lower density (ρ_{eff}) compared to a disc without magnetic support. This lower density leads to enhanced electron scattering by reducing the ratio of absorption-to-scattering opacities ($\kappa_{\mathrm{abs}}/\kappa_{\mathrm{es}} \propto \rho/\rho^0$). Therefore, an accretion disc with magnetic pressure support (*bottom panel*) will have a harder spectrum than one without magnetic pressure support (*top panel*).
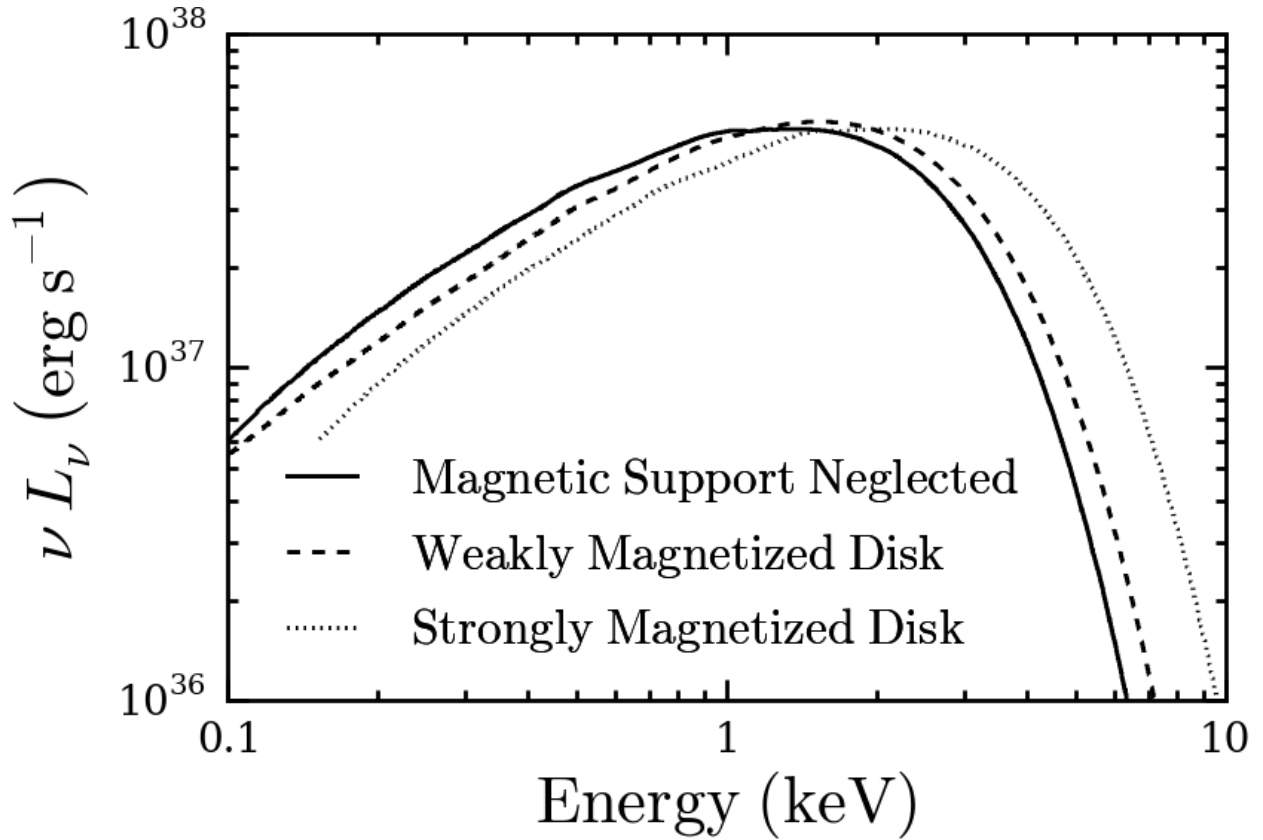
Figure 1.3: The enhanced electron scattering resulting from vertical magnetic pressure support in the disc leads to a hardened disc spectrum. Numerical simulations of very weakly magnetized discs show that the spectral hardening is modest (*dashed line*) (Blaes et al., 2006). Simplified analytic models of strongly magnetized discs predict drastic spectral hardening (*dotted line*) (Begelman & Pringle, 2007), but the details remain unknown. Adapted from Blaes et al. (2006).

consequence of this unintuitive behavior.

An intuition for how the MRI operates can be gleaned by the almost exact analogy to the mechanical system shown in Figure 1.4 of a spring under tension in a differentially rotating disc. Imagine two masses connected by a spring in a Keplerian orbit about a central object. Allowing the inner mass to orbit slightly closer to the center than the outer mass results in the inner mass having a greater angular velocity (*left panel*), but smaller angular momentum, than the outer mass. In response to this displacement, the spring pulls backward on the inner mass while pulling forward on the outer mass (*right panel*). The inner mass therefore experiences a negative torque, causing it to lose angular momentum and move further inward where the angular momentum of an orbit is smaller. Conversely, the outer mass experiences a positive torque, causing it to gain angular momentum and move further outward where the angular momentum of an orbit is larger. Now, the inner (outer) mass has even higher (lower) angular momentum than it had before, the spring stretches even more, the torques exerted on the masses by the attractive force of the spring are even greater, the masses must be displaced even further apart, and we have a runaway process! Figure 1.5 shows a schematic of the MRI operating in an accretion disc, where a vertical magnetic field threading the disc replaces the instructive spring analogy and fluid parcels replace the masses.

The MRI is a weak field instability, meaning that so long as a vertical magnetic field is present — however weak — an accretion disc with the appropriate differential rotation profile (e.g., Keplerian) will be unstable to the MRI. The stability requirement for MRI assuming a Keplerian orbital velocity profile in the disc is (Balbus & Hawley, 1998),

$$v_{\mathrm{A},z}^2 \gtrsim \frac{6}{\pi^2} c_{\mathrm{s}}, \tag{1.21}$$

where c_{s} is the gas sound speed and $v_{\mathrm{A},z} = \sqrt{B_z^2/(4\pi\rho)}$ is the Alfvén speed associated with the vertical magnetic field B_z and gas density ρ. A useful parametrization for the magnetization of a plasma is the β parameter, defined as the ratio of gas pressure-to-magnetic pressure,

$$\beta \equiv \frac{p_{\mathrm{gas}}}{p_B} = \frac{\rho c_{\mathrm{s}}^2/\gamma}{B^2/(8\pi)}. \tag{1.22}$$

Combining Equations 1.21 and 1.22 and arbitrarily choosing the adiabatic index $\gamma = 5/3$, we find that the MRI stability requirement becomes $\beta_z \lesssim 2.0$. Therefore, the MRI is a weak field instability in the sense that
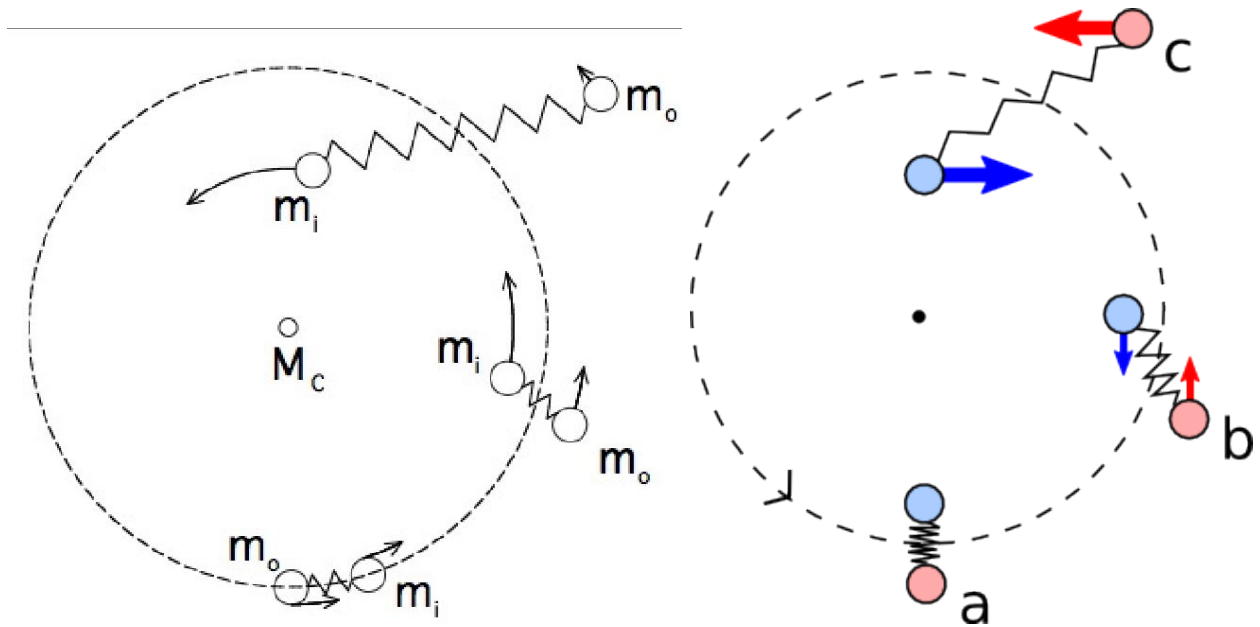
Figure 1.4: Magnetorotational instability analog of two masses connected by a spring in Keplerian-like orbits about a central object. The arrows on the masses in the *left panel* represent the angular velocity, which increases for orbits closer to the central object unlike the angular momentum, which decreases for orbits closer to the central object. The arrows on the masses in the *right panel* represent the attractive force of the spring pulling backward on the inner mass and forward on the outer mass. A description of the runaway process represented by this schematic is given in the text.
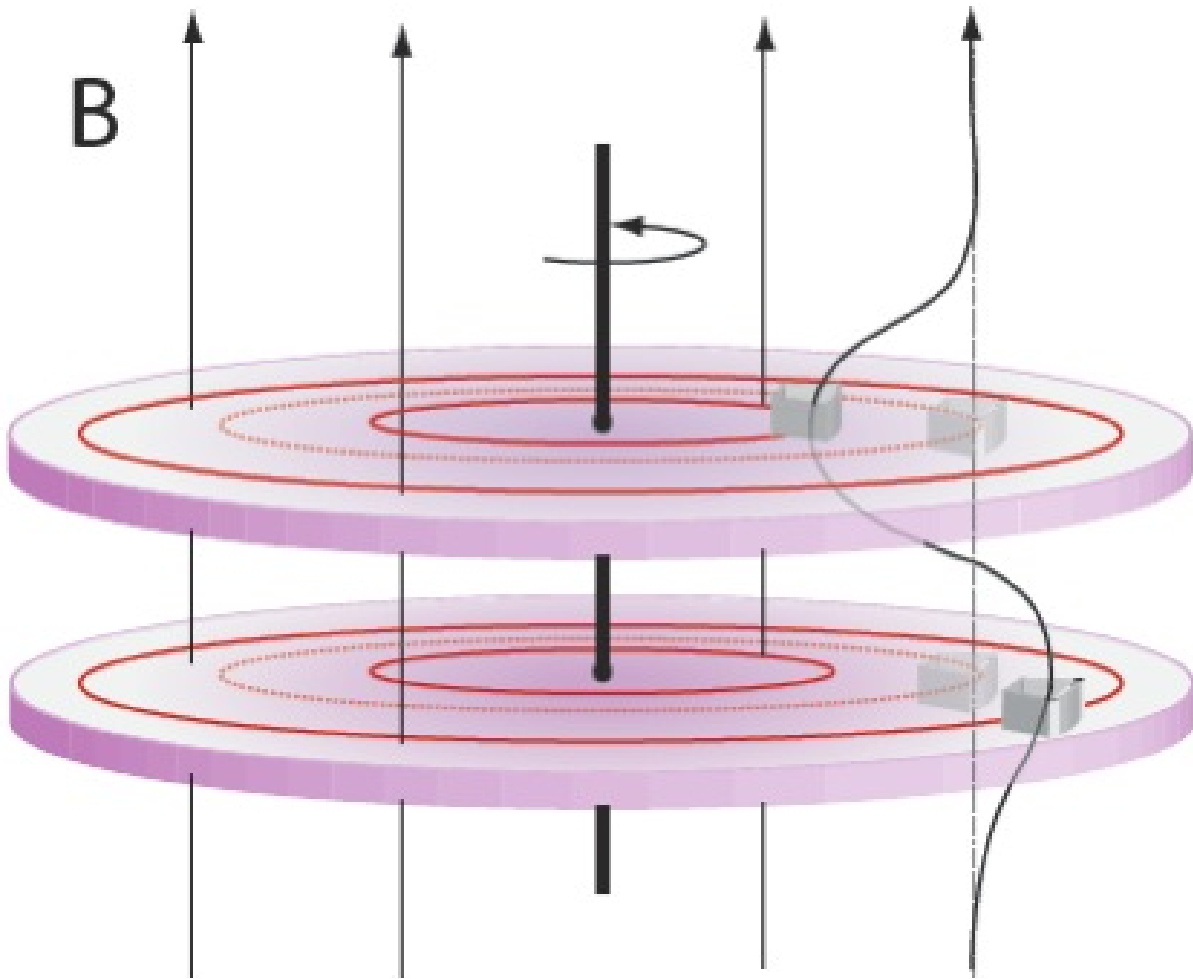
Figure 1.5: Schematic diagram of the magnetorotational instability in a Keplerian-like accretion disc. The *red dotted line* marks the initial orbit of the two parcels of gas, shown by the translucent grey boxes. Initially, these two fluid elements are connected by a vertical magnetic field line, shown by the *dashed vertical line*. When one parcel is perturbed inward, the magnetic field is also displaced due to the frozen-in condition. The attractive force from magnetic tension acts to negatively torque this inner parcel. This causes angular momentum loss and the parcel moves further inward, while the outer parcel is instead positively torqued and moves further outward due to angular momentum gain. The process repeats starting from this new configuration where the torques exerted on the parcels by the increased magnetic tension will be more extreme than before; therefore, the disc is dynamically unstable.

the vertical magnetic field must be subthermal if the disc is to be MRI-active. The tension associated with

a sufficiently strong vertical magnetic field would suppress the MRI.

As we will discuss below, a dynamo process generates a dominant toroidal magnetic field in the

accretion disc. Therefore, the disc can still achieve a state of strong magnetization (i.e., $\beta \lesssim 1$) thanks to

this dominant toroidal field, while the vertical field can remain unstable to the MRI. Pessah & Psaltis (2005)

showed that magnetic tension due to the toroidal magnetic field will quench the MRI when the Alfvén speed

exceeds the geometric mean of the Keplerian speed and the gas speed: $v_{\mathrm{A}} \gtrsim \sqrt{v_{\mathrm{K}} c_{\mathrm{s}}}$ for stability. From this

relation, we can obtain a limit on the maximal magnetic field strength that an MRI-active accretion disc can

achieve. Assuming that the toroidal field is dominant (i.e., $B \simeq B_\phi$), we can rewrite the Pessah & Psaltis

(2005) stability criterion as,

$$B_\phi^2 \gtrsim 4\pi \rho v_{\mathrm{K}} c_{\mathrm{s}}. \tag{1.23}$$

Combining this with the relations,

$$\rho = \frac{\Sigma}{H} \tag{1.24}$$

$$\Sigma = \frac{\dot{M}}{3\pi \alpha c_{\mathrm{s}} R}, \tag{1.25}$$

we obtain the maximal magnetic field strength,

$$B_{\phi,\mathrm{max}} \simeq 2.9 \times 10^9 \alpha^{-8/17} \left(\frac{\dot{M}}{\dot{M}_{\mathrm{Edd}}} \right)^{31/68} \left(\frac{M}{M_\odot} \right)^{-1/2} \left(\frac{R}{R_{\mathrm{g}}} \right)^{-179/136} \quad \text{Gauss.} \tag{1.26}$$

Recently, Miller et al. (2016) placed a lower limit of 10^{3-5} Gauss on the magnitude of the magnetic field

that drives the accretion disc wind in the black hole X-ray binary GRS 1915+105. Adopting a typical wind

launching radius $R \sim 10^{2-4} R_{\mathrm{g}}$, mass accretion rate in a disc wind-producing state $\dot{M} \sim 0.1 \dot{M}_{\mathrm{Edd}}$, black

hole mass $M \sim 10 M_\odot$, and $\alpha \sim 0.1$, Equation 1.26 implies a maximal magnetic field strength in the disc

of $\sim 10^{4-6}$ Gauss. Therefore, the lower limit measured by Miller et al. (2016) is suggestive of strongly

magnetized accretion discs in black hole X-ray binaries. How strongly magnetized discs can form and persist

is the topic of Chapter 6.

We established that a black hole accretion disc is expected to be MRI-unstable, but how does this

instability develop and produce an effective viscosity? After the initial linear growth described above, the

MRI will enter a non-linear growth phase that causes the accretion disc to enter a self-sustaining turbulent steady state, wherein an effective viscosity is generated that drives accretion. Therefore, in order to understand angular momentum transport in accretion discs, one must understand MRI-driven turbulence. This requires numerical simulations of accretion discs with high temporal and spatial resolution.

1.4 Local Simulations of Accretion Discs

Before the MRI was identified as the generator of turbulent stresses that redistribute angular momentum within an accretion disc, Shakura & Sunyaev (1973) introduced the α-prescription,

$$w_{R\phi} = \alpha P, \tag{1.27}$$

which relates the *local* (vertically-averaged) stress $w_{R\phi}$ to the *local* (vertically-averaged) pressure P — usually taken to be the total pressure. With turbulence in mind as the source of the effective viscosity, Shakura & Sunyaev (1973) suggest the relation,

$$\nu = \alpha H c_{\mathrm{s}}, \tag{1.28}$$

where the disc scale-height H roughly corresponds to the maximum turbulent eddy size and the sound speed c_{s} corresponds to the maximum expected velocity of turbulent motions, as shocks would likely thermalize supersonic turbulence. Therefore, we expect α to lie somewhere between 0 (no accretion) and ~ 1. The practical importance of Equation 1.28 is that it allows one to solve for the radial structure of vertically-integrated, geometrically thin accretion discs (see e.g., Frank et al., 2002). However, the validity of the α-prescription could not be tested until the advent of sophisticated numerical simulations of accretion discs in the local limit.

The ultimate goal of numerical simulations of MRI turbulence is to replace the phenomenological α-prescription with observationally testable models rooted in real physics. While this ambitious goal remains far off, tremendous progress has been made since the first studies of MRI turbulence by Hawley et al. (1995). Ideally, simulations of MRI turbulence in accretion discs would capture all relevant spatial scales from the large-scale energy injection associated with the differential rotation to the microscopic dissipation scales associated with the plasma viscosity and resistivity. These simulations would also resolve the short

timescales associated with wave propagation to the very long timescales associated with viscous evolution. Of course, this is an absurdly tall order even given modern-day supercomputing resources. Instead, the approach to numerical studies of MRI turbulence has been to devise local "shearing box" simulations and hope that the relevant physics is properly captured and converged, provided that one uses enough grid zones.

The shearing box (see Figure 1.6; Hawley et al., 1995) adopts the geometry of a Cartesian rectangular patch inserted into the differentially rotating fluid disc. The box co-rotates locally with the background shear flow and includes the effects of Coriolis forces, centrifugal forces, and gravity, while neglecting curvature and radial gradients. Therefore, any non-local behavior of the turbulence cannot be captured by the shearing box (e.g., Simon et al., 2012). Boundary conditions are perfectly periodic in the azimuthal direction and shearing periodic in the radial direction, as dictated by the differential rotation profile of the disc. There is more freedom in the choice of vertical boundary conditions, with outflowing boundary conditions now being generally preferred over periodic boundary conditions. Next, we highlight some of the major findings from shearing box simulations of MRI turbulence relevant to this thesis.

Shearing box simulations conserve any initial *net vertical magnetic flux*. A net vertical flux provides a reservoir from which an MRI dynamo process can more efficiently generate toroidal field. This increases the MRI turbulent stress $w_{R\phi}^{\mathrm{MRI}}$ arising from correlated radial and azimuthal fluctuations in the magnetic field and fluid velocity, given by,

$$w_{R\phi}^{\mathrm{MRI}} = \left\langle \rho v_R \delta v_\phi - \frac{B_R B_\phi}{4\pi} \right\rangle, \tag{1.29}$$

where δv_ϕ is the local turbulent azimuthal velocity (i.e., the background shear velocity is subtracted off). The expected increased stress due to increased net vertical magnetic flux is seen in shearing box simulations (e.g., Hawley et al., 1995; Pessah et al., 2007) and in local regions of global simulations (Sorathia et al., 2010). Encouragingly, shearing box simulations show that the stress from the combined Reynolds and Maxwell components of Equation 1.29 is well-described by the α-prescription of Equation 1.27, with a tight correlation emerging between α and the imposed net vertical magnetic flux (e.g., Blackman et al., 2008).

Including vertical stratification in shearing box simulations due to the vertical gravity of the black hole allows for magnetic buoyancy, which is essential to the accretion disc dynamo. This dynamo mechanism channels the accretion power liberated by the MRI into a self-sustaining, ordered toroidal magnetic field.

Local Disk
Simulation
(Shearing Box)

Radial (x)

Vertical (z)

Toroidal (y)

Black
Hole

Global Disk Simulation
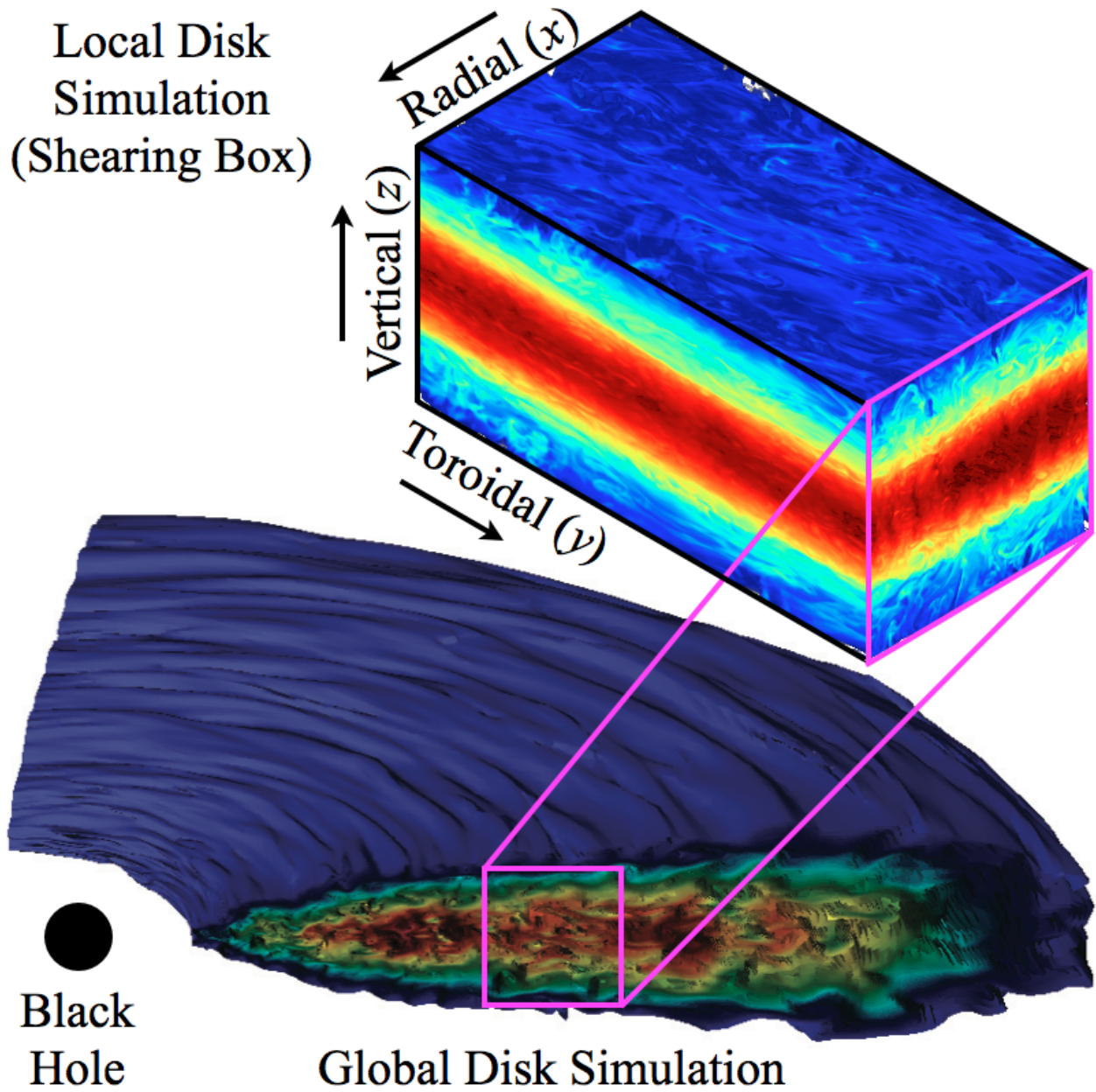
Figure 1.6: Gas density renderings showing the concept of the shearing box as a local approximation of a global accretion disc.

The dynamo quasi-periodically creates toroidal field of alternating sign that buoyantly rises through the disc atmosphere and escapes, which has been seen in both local (e.g., Brandenburg et al., 1995) and global (e.g., O'Neill et al., 2011) simulations. We emphasize that when thinking about disc magnetization, it is important not to conflate the imposed net vertical magnetic flux and the dynamo-generated toroidal magnetic field. How the properties of MRI turbulence and dynamo activity depend on net vertical magnetic flux is the topic of Chapter 5.

Ultimately, global simulations of accretion discs are required to test the results of the shearing box simulations. Indeed, much progress has already been made toward understanding accretion discs and MRI turbulence from global simulations (e.g., Fragile, 2014). However, computational limitations require that this thesis adopts the shearing box approximation in order to perform long-duration (i.e., hundreds of orbits) accretion disc simulations that spatially resolve MRI turbulence.

1.5   Black Hole X-ray Binary Phenomenology

Accretion onto compact objects, particularly black holes, is an inherently variable process. For supermassive black holes that are intricately linked to galaxy growth and evolution, the long timescales for accretion variability are observationally inaccessible. Conversely, accretion variability in black hole X-ray binaries operates on comparatively short timescales, showcasing dramatic transitions between quiescent and luminous states. Supposing that variability in accreting supermassive black holes can be treated in a self-similar fashion to variability in black hole X-ray binaries (e.g., Cui, 2004) allows astronomers to circumvent the problem of observational inaccessibility and proceed to study black hole accretion physics.

The most dramatic variability observed in black hole X-ray binaries involves transitions between a state of low luminosity, where the X-ray spectrum is dominated by a non-thermal high-energy component, and a state of high luminosity, where the X-ray spectrum is dominated by a soft thermal component. The observational approach toward black hole X-ray binary state transitions has been to devise a powerful model-independent phenomenology based on spectral and timing properties (e.g., Remillard & McClintock, 2006; Belloni, 2010). General trends emerge from this phenomenology, with the most notable and robust being the mysterious hysteresis cycle in the X-ray intensity *vs.* spectral hardness diagram (Homan et al., 2001). Shown

in Figure 1.7, an outburst begins with the system climbing out of a low luminosity, spectrally hard state into a spectrally soft state of high luminosity, sometimes nearing the Eddington limit. Instead of retracing this path on the hardness-intensity diagram back down to the pre-outburst state, the system curiously decays to its original state along a horizontal track of lower luminosity than it did during the outburst rise. The 'q'-shaped hysteresis path traversed in intensity *vs.* hardness for a full black hole state transition cycle is sometimes affectionately referred to as the "turtle head" diagram (Fender et al., 2004). The timescale to complete the turtle head is typically between many months and a year. The phenomenological spectral/timing states involved in a black hole state transition cycle are marked on the hardness-intensity diagram of Figure 1.7, which will be a useful reference while reading this thesis.

Complicating matters, no two black hole X-ray binaries display identical state transition behavior and even multiple state transitions within the same source are far from being periodic replications of each other. Furthermore, state transitions observed in some systems fall into a category all their own (e.g., GRS 1915+105). The hysteresis cycle is characteristic of, but not exclusive to, black hole X-ray binary transients. State transition behavior is also observed in neutron star X-ray binaries (e.g., Muñoz-Darias et al., 2014) and ultraluminous X-ray sources (e.g., Feng & Kaaret, 2006), yet whether the state transitions observed in these different systems all share a common physical origin remains unknown. A candidate physical mechanism for black hole state transitions is proposed in Chapter 3.

My original interest in astronomy research was inspired by the enigmatic behavior displayed by black hole X-ray binaries. In this thesis, I hope to convey to the reader the value of a research approach that appreciates the junction of theory, numerics, observations, and phenomenology.
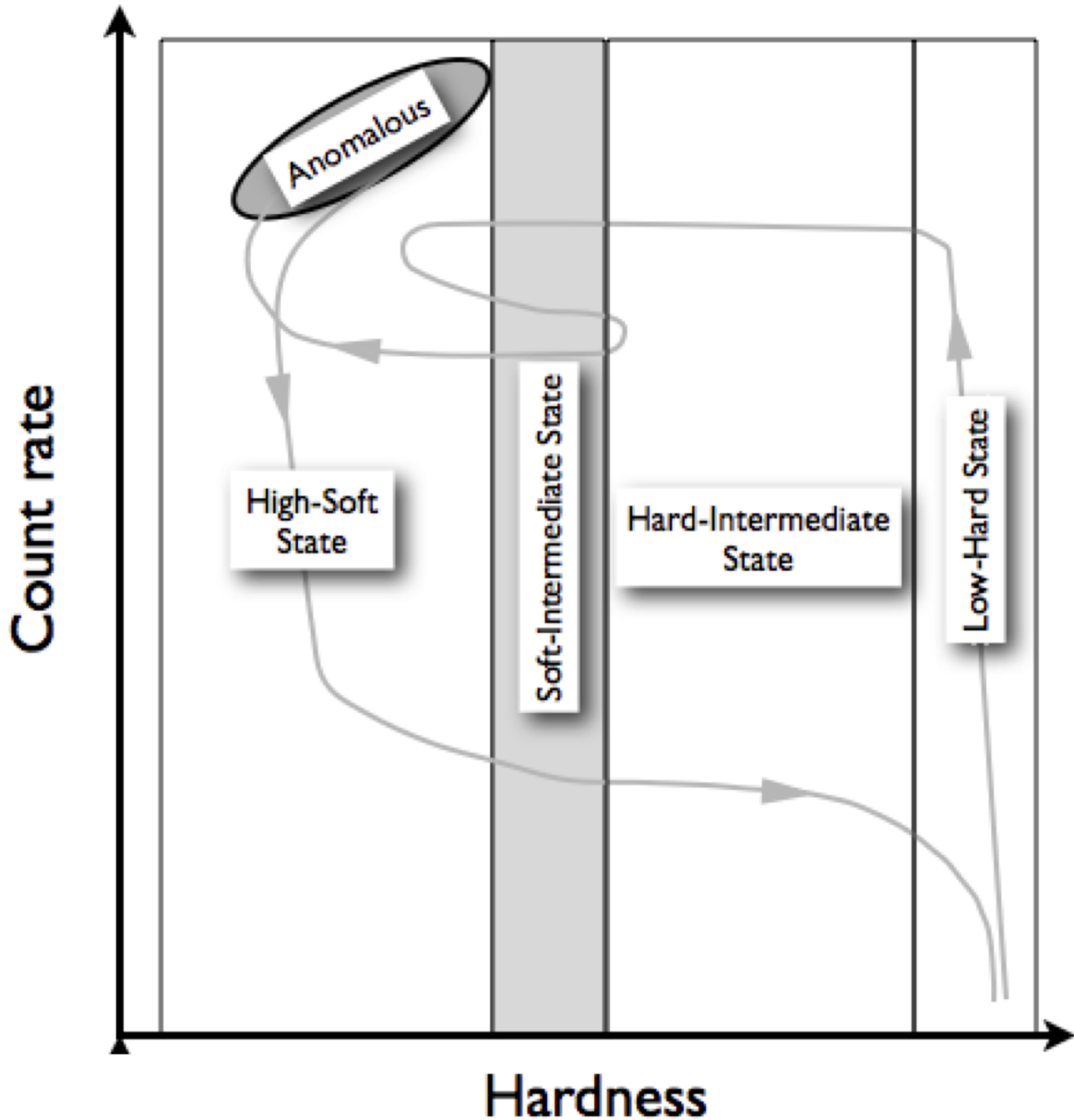
Figure 1.7: General behavior of black hole X-ray binary transients in the hardness-intensity diagram (*top*) and the hardness-rms diagram (*bottom*). Hardness is defined as the ratio of photon counts in a hard X-ray band to those in a soft X-ray band. Labels show the locations of the phenomenological spectral/timing states on these diagrams. The low/hard state is accompanied by a steady jet. Transitions from the hard-intermediate to soft-intermediate states are often contemporaneous with a transient jet with Lorentz factor $\Gamma \gtrsim 2$. The high/soft state is accompanied by accretion disc winds, which are thought to have an equatorial geometry (**?**) and to sometimes require a magnetic driving mechanism (e.g., Miller et al., 2006b). Jets and disc winds appear to be mutually exclusive (Miller et al., 2006c). Taken from Belloni (2010).

Chapter 2

Spectral Hardening as a Viable Alternative to Disc Truncation in Black Hole State Transitions

2.1 Preface

This paper was published in Monthly Notices of the Royal Astronomical Society, Volume 431, Issue 4, pp. 3510-3532 on June 01, 2013. The author list is: Salvesen, G., Miller, J. M., Reis, R. C., & Begelman, M. C. The spectral evolution of the accretion disc during black hole state transitions is commonly attributed to the radial migration of the inner edge of the disc. However, there is no clear reason to expect a geometrically thin, optically thick accretion disc around a black hole to be severely truncated. Instead, this paper demonstrates that changes in the accretion disc atmosphere can conceivably explain the observed evolution of the disc spectral component during black hole state transitions.

Abstract

Constraining the accretion flow geometry of black hole binaries in outburst is complicated by the inability of simplified multi-colour disc models to distinguish between changes in the inner disc radius and alterations to the emergent spectrum, parameterised by the phenomenological colour correction factor, $f_{\rm col}$. We analyse *Rossi X-ray Timing Explorer* observations of the low mass Galactic black hole X-ray binary, GX 339–4, taken over seven epochs when the source was experiencing a state transition. The accretion disc component is isolated using a pipeline resulting in robust detections for disc luminosities, $10^{-3} \lesssim L_{\rm disc}/L_{\rm Edd} \lesssim 0.5$. Assuming that the inner disc remains situated at the innermost stable circular orbit over

the course of a state transition, we measure the *relative* degree of change in f_{col} required to explain the spectral evolution of the disc component. A variable f_{col} that increases by a factor of $\sim 2.0 - 3.5$ as the source transitions from the high/soft state to the low/hard state can adequately explain the observed disc spectral evolution. For the observations dominated by a disc component, the familiar scaling between the disc luminosity and effective temperature, $L_{\mathrm{disc}} \propto T_{\mathrm{eff}}^4$, is observed; however, significant deviations from this relation appear when GX 339–4 is in the hard intermediate and low/hard states. Allowing for an evolving f_{col} between spectral states, the $L_{\mathrm{disc}} - T_{\mathrm{eff}}^4$ law is recovered over the full range of disc luminosities, although this depends heavily on the physically conceivable range of f_{col}. We demonstrate that physically reasonable changes in f_{col} provide a viable description for multiple state transitions of a black hole binary without invoking radial motion of the inner accretion disc.

2.2 Introduction

The nature of the accretion flow for black hole binaries (BHBs) undergoing state transitions remains unclear and is an active topic of observational and theoretical pursuit. The phenomenology describing the predominant spectral states experienced by BHBs include the high/soft state (HSS), characterised by high luminosity and a standard thin accretion disc as the dominant spectral component; the low/hard state (LHS), characterised by low luminosity with a dominant hard power-law spectral component that is likely produced by inverse Compton scattering of soft photons by a relativistic electron corona (Shapiro et al., 1976); and the intermediate state (IS), which is itself further divided into the hard intermediate state (HIS) and soft intermediate state (SIS) (see, e.g., Belloni 2010 for an extensive description of these phenomenological states).

Currently, the picture of a black hole accreting at a significant fraction of the Eddington mass accretion rate, $\dot{M}_{\mathrm{Edd}}$, from a geometrically thin, optically thick disc extending to the innermost stable circular orbit (ISCO) is the accepted description of the HSS. However, there is a lack of consensus regarding a universal geometry of the disc and innermost accretion flow in the LHS when the black hole feeds at a low fraction of $\dot{M}_{\mathrm{Edd}}$ and/or the flow has a low radiative efficiency. According to the paradigm put forth by Esin et al. (1997), the accretion disc in the LHS is radially recessed (i.e., truncated) with the interior region being composed of a radiatively inefficient accretion flow (RIAF) (Narayan & Yi, 1994). Alternatively, models where the inner

disc remains at the ISCO in the LHS have been proposed by invoking magnetically reconnecting flares driving a coronal outflow (e.g., Beloborodov, 1999). Another model advocating against disc truncation is a standard thin disc that generates a magnetically dominated corona where the amount of accretion energy liberated in the corona increases with decreasing mass accretion rate (Merloni & Fabian, 2002). Recently, Reis et al. (2013) proposed that the intermediate states may differ from one another only in the geometrical extent of the X-ray corona, with the SIS being the result of a collapse of the previously extended corona as the system moves into the disc-dominated HSS. The notion of an accretion disc, where the magnetorotational instability governs dissipation and angular momentum transport (Balbus & Hawley, 1991), producing a magnetically dominated corona is supported by sophisticated numerical simulations of local shearing boxes (e.g., Hirose et al., 2006, 2009) and global discs (e.g., Beckwith et al., 2009). By varying only the mass accretion rate, the spectral signatures of the HSS and LHS were reproduced in the global disc simulations of Schnittman et al. (2013), without the need for radial variation of the inner accretion disc. The physical mechanism responsible for triggering a state transition is poorly understood, making it difficult to conceive what would drive a sudden disc recession or a drastic change in coronal activity required to explain the observed spectral evolution; thus, lending credence to the need for a focused study of disc evolution during state transitions.

Observational studies of BHB spectra have successfully applied a multi-colour disc (MCD) blackbody model (Mitsuda et al., 1984; Makishima et al., 1986) to the observed quasi-thermal soft X-ray spectral component in the HSS and even in the LHS in some cases (e.g., Miller et al., 2006a; Reis et al., 2010). Provided the observational parameters are well-constrained, the radial location of the inner disc boundary can be measured from the best-fit MCD model parameters. However, this technique makes the critical assumption that the deviations to the emergent disc spectrum caused by the disc vertical structure can be parametrized by a frequency-independent constant, known as the colour-correction, or spectral hardening, factor, f_{col} (Shimura & Takahara, 1995).

Recently, investigations into the possibility of a variable f_{col} experienced a strong revival in the observational community. Studies of black hole X-ray binary accretion discs across various luminosity states using data from the *Rossi X-ray Timing Explorer* (*RXTE*) (e.g., Nowak et al., 2002; Ibragimov et al., 2005; Wilms et al., 2006; Dunn et al., 2011) and the *Swift* observatory (Reynolds & Miller, 2013) provide

extensive systematic analyses of the properties of disc evolution in BHBs. The global studies of Dunn et al. (2011) and Reynolds & Miller (2013) examined all of the available archived data for all of the well-known, confirmed BHBs. For nearly all BHBs where an outburst was observed, Dunn et al. (2011) found that f_{col} remained relatively constant in the most disc-dominated states (i.e., the HSS), closely following the theoretical $L_{\mathrm{disc}} \propto T_{\mathrm{eff}}^4$ relation between the disc luminosity and disc effective temperature. For observations with a relatively weaker disc component, characteristic of the IS, deviations from the luminosity-temperature relationship arose. Supposing that the inner disc radius does not change and allowing for a variable colour correction factor, $1.6 \lesssim f_{\mathrm{col}} \lesssim 2.6$, where f_{col} increased as the disc fraction decreased, the $L_{\mathrm{disc}} \propto T_{\mathrm{eff}}^4$ scaling was recovered. This finding sets the stage for a thorough consideration of an increasing f_{col} when a BHB transitions from the HSS to the LHS as a possible alternative to a truncated disc geometry in the LHS. Performing a similar analysis, Reynolds & Miller (2013) speculate that f_{col} may attain values as high as 5 as the BHB spectrum becomes less disc dominated. The main differences between our work and these recent observational studies are: (1) We focus exclusively on a single source, the well-known BHB transient, GX 339–4, over multiple state transitions. (2) We systematically explore different Comptonisation models.[1] (3) We introduce a novel approach for making relative measurements in order to reduce uncertainties.

The methodology of this paper is to systematically investigate to what extent variations in the disc structure and/or disc truncation can explain the observed spectral evolution for multiple state transitions of a BHB. Most importantly, we will demonstrate that a colour correction factor that dynamically evolves within a physically reasonable range provides an adequate alternative to a truncated disc for explaining the changing disc spectrum.

2.3   Observations and Data Reduction

Motivated by the lack of consensus on accretion disc evolution over the course of a BHB state transition, we aim to address the question: Can physically reasonable changes in the vertical disc structure alone explain the observed evolution of disc properties during a state transition without invoking a truncated disc geometry? In light of this question, we sought a source that met the following criteria: (1) The source was

---

[1] Reynolds & Miller (2013) also consider both phenomenological and physical Comptonisation models.

observed over multiple state transitions, permitting comparison of disc variations between different transitions. (2) Given that our methodology hinges on the presence of a disc, a disc component must have been robustly detected in the LHS. (3) Conflicting claims for both a severely recessed disc and a disc extending to the ISCO in the LHS are published for the source. (4) Variable low-frequency quasi-periodic oscillations (LFQPOs), which may be linked to the disc evolution, have been observed coincident with state transitions. (5) Reasonable constraints are known on mass, distance, and inclination; however, this is of ancillary importance. Based on these criteria, we selected GX 339–4 as the focus of our analysis.

Trans. ID	Start dd/mm/yy (MJD)	End dd/mm/yy (MJD)	Type	N_{obs}	$N_{\mathrm{disc}}^{\mathrm{pow/bknpow}}$	$N_{\mathrm{disc}}^{\mathrm{simpl}}$	$N_{\mathrm{disc}}^{\mathrm{comptt}}$	$\nu_{\mathrm{QPO}}^{\mathrm{min}}$ (Hz)	$\nu_{\mathrm{QPO}}^{\mathrm{max}}$ (Hz)	$R_{\mathrm{Kep}}^{\mathrm{max}}/R_{\mathrm{Kep}}^{\mathrm{min}}$
R02	18/04/02 (52382)	23/05/02 (52417)	Rise	33	32	22	31	0.159(1)[a]	7.9(1)[a]	14
D03	15/02/03 (52685)	11/05/03 (52770)	Decay	53	33	30	23	0.29(1)[a]	8.8(3)[a]	9.7
R04	05/07/04 (53191)	25/08/04 (53242)	Rise	30	21	21	21	0.306(7)[a]	8.0(2)[a]	8.8
R07	17/01/07 (54117)	23/02/07 (54154)	Rise	34	28	17	29	0.142(3)[a]	6.67(2)[a]	13
D07	02/05/07 (54222)	06/06/07 (54257)	Decay	46	40	39	40	0.070(3)[a]	4.05(9)[a]	15
R10	26/03/10 (55281)	20/05/10 (55336)	Rise	59	11	9	10	0.22(1)[b]	6.7(2)[b]	9.8
D11	07/01/11 (55568)	15/02/11 (55607)	Decay	28	12	12	12	0.9(1)[c]	4.5(3)[b]	2.9

Table 2.1: Table summarising the key features of each GX 339−4 state transition. From *left* to *right*, the columns are the state transition ID, start time of the transition, end time of the transition, type of the transition, number of archived *RXTE* observations, number of observations requiring a disc component for Comptonisation models pow/bknpow, simpl, and comptt, minimum/maximum LFQPO frequency observed, and fractional change in inner disc radius implied if $\nu_{\mathrm{QPO}}^{\mathrm{min}}$ and $\nu_{\mathrm{QPO}}^{\mathrm{max}}$ are associated with the Keplerian frequency and assumed to trace the inner disc location. [a]Shaposhnikov & Titarchuk (2009); [b]Motta et al. (2011); [c]Stiele et al. (2011)

2.3.1   GX 339–4

GX 339–4, discovered by Markert et al. (1973), is a low-mass X-ray binary and recurring transient hosting a dynamically confirmed black hole with a mass $M \geq 5.8 M_\odot$ (Hynes et al. 2003; see also Muñoz-Darias et al. 2008) and distance $D = 8 \pm 2$ kpc (Zdziarski et al. 2004; see also Hynes et al. 2004). Supposing that the inner disc inclination, i (0° for face on, 90° for edge on), can be assumed to align with the binary inclination, then the lack of observed eclipses constrain $i \leq 60°$ (Cowley et al., 2002), while radio observations imply $i \leq 30°$ (Gallo et al., 2004). Results from modelling the X-ray reflection features of GX 339–4 in the SIS also suggest a lower disc inclination of $i \sim 10° - 30°$ (Miller et al., 2004, 2009b) and in the LHS (Reis et al., 2008). Owing to the uncertainties on the intrinsic parameters (namely, M, D, i) of GX 339–4 and the limitations of existing X-ray data, seeking absolute measurements that depend on these parameters presents a serious challenge.

GX 339–4 experienced multiple outbursts since its discovery, making it an appealing source for temporal evolution studies. The seven state transitions we select to study are listed in Table 2.1. The notation convention we adopt for referring to a transition is the letter R or D, signifying a rise or decay type, respectively, followed by the year associated with the transition. A rise (decay) type indicates a transition from the LHS (HSS) to the HSS (LHS). The intervals of each transition were selected based on previously published dates and the emergence/disappearance of LFQPOs (Shaposhnikov & Titarchuk, 2009; Motta et al., 2011; Stiele et al., 2011).[2] We chose to extend the transition start/end times by ~ 5 days beyond the intervals quoted in the literature to ensure that we capture the full transition behavior in our subsequent analysis.

Alarming discrepancies in the location of the inner accretion disc edge, particularly in the LHS, appear in the literature based on spectral fits to X-ray observations of GX 339–4. The strongest case for disc truncation is presented in Tomsick et al. (2009), which used fluorescent iron emission lines to find $R_{\mathrm{in}} > 175 \ R_{\mathrm{g}}$ (90% confidence, assuming $i = 30°$) when GX 339–4 was in the LHS with luminosity $L_{\mathrm{X}} \simeq 1.4 \times 10^{-3} \ L_{\mathrm{Edd}}$ (assuming $D = 8$ kpc). Claims of a truncated disc in the LHS also appear based on modelling of direct disc emission accounting for irradiation of the inner disc (Cabanac et al., 2009). Even

---

[2] The end date listed for transition ID GX339-D03 in Table 1 of Shaposhnikov & Titarchuk (2009) is mistyped and should read 06/05/03 (June 05 2003).

in the SIS, Yamada et al. (2009) suggest a recessed disc with $R_{\rm in} = 5 - 32\ R_{\rm g}$ (68% confidence, assuming $i = 30°$). These measurements suggest that the inner portion of the disc is absent in low luminosity states, perhaps replaced by a RIAF. In stark contrast, there are numerous claims of the inner disc radius in GX 339–4 remaining consistent with the ISCO in the LHS. Using physically motivated, sophisticated spectral fitting techniques, the disc inner radius was determined to lie within $R_{\rm in} = 2.0 - 3.0\ R_{\rm g}$ in the SIS (Miller et al., 2004) and $R_{\rm in} = 3.0 - 5.0\ R_{\rm g}$ in the LHS with luminosity $L_{\rm X} \simeq 0.05\ L_{\rm Edd}$ (assuming $D = 8$ kpc) (Miller et al., 2006a). Both of these results were confirmed by a systematic reanalysis that employed detailed disc reflection modelling (Reis et al., 2008). Using the same data set as in Miller et al. (2006a), Wilkinson & Uttley (2009) also measured a disc extending down to $4\ R_{\rm g}$ from their best-fit iron line model. Tomsick et al. (2008) observed GX 339–4 in the LHS at luminosities $L_{\rm X} \simeq 0.023\ L_{\rm Edd}$ and $L_{\rm X} \simeq 8 \times 10^{-3}\ L_{\rm Edd}$, finding the disc to extend within $10\ R_{\rm g}$ and being consistent with the disc remaining fixed at $\sim 4\ R_{\rm g}$. Reis et al. (2010) performed a systematic study of eight BHBs (including GX 339–4) in the LHS, robustly detecting a thermal component in all sources and placing a stringent upper limit of $10\ R_{\rm g}$ on the truncation radius for six sources confirmed by both broad iron line and thermal disc modelling independently.

In order to measure black hole spin, one must associate $R_{\rm in}$ with the ISCO, located at $R_{\rm ISCO}$. A measurement of the inner disc radius is the crucial diagnostic for measuring black hole spin, as $R_{\rm ISCO}$ is a monotonically decreasing function of the dimensionless spin parameter, $a_* \equiv Jc/GM^2$, where J is the black hole angular momentum (Bardeen et al., 1972). Perhaps unsurprisingly, conflicting claims regarding the behaviour of $R_{\rm in}$ have led to discrepancies in spin measurements of GX 339–4. Spin measurements employing the relativistically broadened iron line method (Fabian et al., 1989; Laor, 1991) suggest that GX339–4 harbours a near-maximally spinning black hole with $a_* = 0.94 \pm 0.02$ (Miller et al., 2009b; Reis et al., 2008), while the thermal disc continuum fitting technique (Zhang et al., 1997) supports a low-to-moderately spinning black hole with $a_* < 0.4$ (Yamada et al. 2009; see also Kolehmainen & Done 2010; Kolehmainen et al. 2011).

LFQPOs exhibit variability simultaneous with transitions between the LHS and HSS (Rutledge et al., 1999b). Variable LFQPOs were observed in each GX 339–4 transition studied here, with the measured frequency ranges listed in Table 2.1 and typically spanning $0.2 - 8$ Hz (Belloni et al., 2005; Shaposhnikov

& Titarchuk, 2009; Motta et al., 2011; Stiele et al., 2011; Nandi et al., 2012). The idea that LFQPOs may originate from oscillating modes of a quasi-spherical RIAF that is interior to, or partially overlapping with, a truncated thin disc was proposed by Giannios & Spruit (2004). Long time-scale variability of the disc blackbody component of GX 339–4 was associated with disc instabilities and interpreted as arising from intrinsic variability of the disc (Wilkinson & Uttley, 2009). This suggests that the variable LFQPOs may be intricately linked to disc truncation; however, the truncation radius cannot exceed $\sim 20~R_{\mathrm{g}}$ if the observed variations are limited by the viscous timescale.

2.3.2 *Rossi X-ray Timing Explorer*

The monitoring campaign of the *Rossi X-ray Timing Explorer* (*RXTE*) (Bradt et al., 1993; Swank, 1999) observed GX 339–4 transitioning between states in 2002, 2003, 2004, 2007, 2010, and 2011, obtaining well-sampled (in time) observations spanning each transition before being decommissioned in early 2012. We examined 283 *RXTE* observations of GX 339–4 covering seven time intervals, during which the source experienced state transitions (see Table 2.1). The *RXTE* standard products, comprised of the source and background spectra along with instrument response matrices, were obtained from the High Energy Astrophysics Science Archive Research Center data archive.[3]   The Proportional Counter Array (PCA) (Jahoda et al., 1996) and High Energy X-ray Timing Experiment (HEXTE) (Rothschild et al., 1998) standard source spectra were analysed jointly. The PCA energy spectrum (Standard 2 mode) is built from summing all layers from various Proportional Counter Units (PCUs). The PCU-1, PCU-2, and PCU-3 are used in all observations prior to 25 December 2006 (i.e., R02, D03, R04), while only the PCU-2 and PCU-3 are used in observations thereafter (i.e., R07, D07, R10, D11) due to a propane loss in the top layer of PCU-1.[4] For observations corresponding to transitions R02, D03, R04, R07, and D07, we used the HEXTE Cluster B spectrum, but could not use these data for R10 and D11 because the HEXTE Cluster B was permanently left in an off-source pointing position from 29 March 2010 onward.[5]   The HEXTE Cluster A data for transitions R10 and D11 are affected by strong residuals, resulting from difficultly in determining the appropriate con-

---

[3] http://heasarc.gsfc.nasa.gov/cgi-bin/W3Browse/w3browse.pl
[4] http://heasarc.nasa.gov/docs/xte/recipes/stdprod_guide.html
[5] http://heasarc.nasa.gov/docs/xte/xhp_new.html

tribution of the background spectra. Consequently, we excluded all HEXTE data while analysing transitions R10 and D11, using PCA data only for these observations. This resulted in many observations with a strong soft component, which is indicative of a disc, being excised from our sample due to poor spectral modelling of the high-energy continuum (see §2.5.1).

While the time sampling capability of the *RXTE* satellite makes it well-suited for a study of BHB state transitions, which are a highly time-dependent phenomenon, *RXTE* has important limitations. Determining the spectral properties of the disc component for a given observation is made difficult by the limited low-energy coverage of *RXTE*, which only extends down to ~ 3 keV, while the disc spectrum peaks at ~ 1 keV. Especially in the HIS and LHS, the diminished disc component, if present, is difficult to characterise due to a combination of its weakness and the dominance of a Comptonised component. Figure 2.1 presents a hardness-intensity diagram (HID) of all 283 *RXTE* observations of GX 339–4 considered in this work. Observations that do not statistically require a disc component (see §2.5.1) are indicated by *grey crosses*, while the various glyphs indicate the transition associated with the observation. The plethora of IS and HSS observations (i.e., low-to-moderate hardnesses) deemed to not require a disc comes from the R10 and D11 data sets, where the absence of HEXTE data prevented acceptable fits to disc-dominated spectra. Notably, Figure 2.1 shows that the set of observations considered in the subsequent analysis span all spectral states, which indicates that we are studying the complete evolution of state transitions in GX 339–4.

For a given observation, hardness and intensity are calculated from the PCA data as follows. The distribution of counts across all channels is obtained from both the standard PCA source spectral file and background spectral file. The background counts are then subtracted from the source counts channel-by-channel, yielding the counts in each channel associated with GX 339–4. The hardness is then defined as the ratio of GX 339–4 counts in channels 15 - 24 (6.3 - 10.5 keV) to those in channels 8 - 14 (3.8 - 6.3 keV) (Belloni et al., 2005). A count rate is obtained by summing the counts across all channels and dividing by the exposure time. Good time intervals (GTIs) are identified from the GTI file included in the standard products. The average number of PCUs that are turned on during the GTIs is determined from the filter file included in the standard products. The intensity is then defined as the count rate divided by the average number of active PCUs during the observation GTIs.
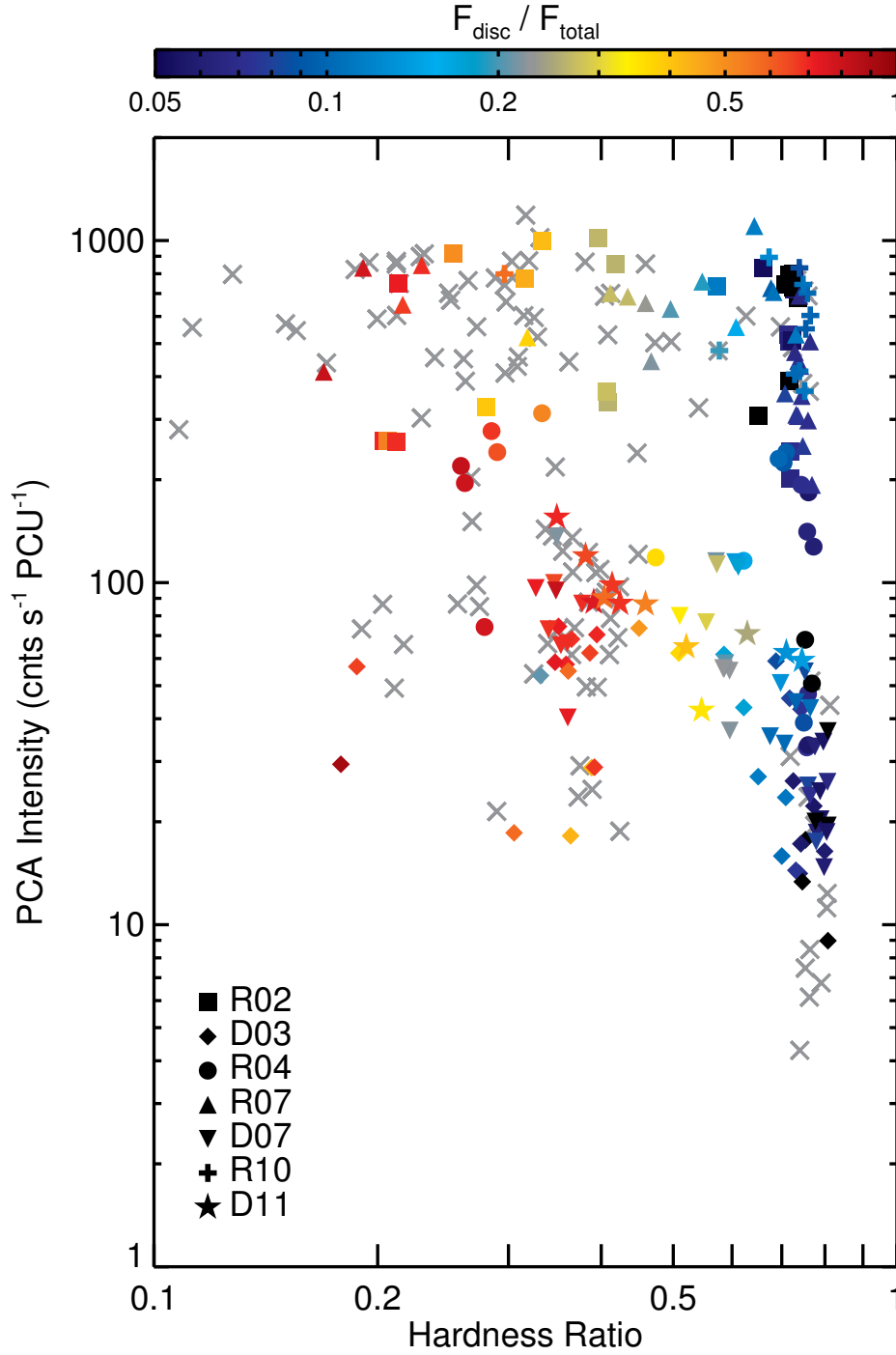
Figure 2.1: Hardness-intensity diagram for all observations of GX 339–4 considered in this work generated from the results of the `pow/bkn` model (see §2.5.2). The disc fraction for each observation is given by the glyph colour and is an indicator of the spectral state. Data points marked by a *grey cross* correspond to observations that were not deemed to statistically require a disc component. The key in the *bottom left* identifies the glyph associated with each transition ID. See §2.3.2 for a description of how the HID was generated. A wide range of hardness is considered in this work.

To justify using the χ^2 fitting statistic for deriving parameter constraints, both the PCA and HEXTE spectra were binned to require a minimum of 20 counts per energy bin using the `FTOOL grppha`. A systematic error of 0.6% was added to the PCA spectrum using `grppha`; however, the PCA spectra without systematic errors added are used when deriving relative measurements (see §2.5.3.1). All spectral fits are performed with `XSPEC` version 12.7.1 (Arnaud, 1996). The PCA and HEXTE spectra are fitted over the $2.8 - 25$ keV and $20-100$ keV energy ranges, respectively. The response energy range over which spectral models are calculated is extended to 0.1 keV and 100 keV using the `energies extend` command in `XSPEC` with 50 logarithmic steps in each direction. All observation times correspond to the midpoint of the PCA observation. Quoted errors from spectral fits are 1σ uncertainties, unless specified otherwise.

2.4   Multi-colour Disc Blackbody Models

The accretion disc in BHBs manifests itself as a soft, quasi-blackbody component with a typical peak inner disc temperature of ~ 1 keV (e.g., Fender & Belloni, 2004). While the accepted description for the origin of the soft thermal component in the HSS is a geometrically thin, optically thick accretion disc (Shakura & Sunyaev, 1973) extending down to the ISCO, no such consensus has been reached for the nature of the innermost flow in the HIS or LHS. Appealing to spectral fits of the thermal continuum with multi-colour disc (MCD) blackbody models to isolate the disc component, one can measure the temporal evolution of the accretion disc over the course of a state transition.

2.4.1   The Standard MCD Model

The most commonly adopted disc model is the MCD blackbody model (`diskbb` in `XSPEC`) (Mitsuda et al., 1984; Makishima et al., 1986). The attractiveness of the MCD model is owed to its legacy, applicability, and simplicity. However, the familiarity and broad acceptance of `diskbb` often mask subtle features of the model, possibly leading to unintended misuse. Here, we dissect the `diskbb` model in order to elucidate its underlying assumptions and expose its limitations. Assuming a geometrically thin, optically thick accretion disc that locally emits a blackbody spectrum in concentric annuli, the colour temperature for a MCD model

at a given radius is described as,

$$T_{\rm col}(r) = T_* \left(\frac{r}{R_{\rm in}} \right)^{-3/4} \left[1 - \beta \left(\frac{r}{R_{\rm in}}, \right)^{-1/2} \right]^{1/4}, \tag{2.1}$$

where $R_{\rm in}$ is the radius of the inner disc edge and β describes the boundary condition at this location. For discs in the HSS, $R_{\rm in}$ is commonly associated with $R_{\rm ISCO}$. A zero-torque boundary condition at $R_{\rm in}$ corresponds to $\beta = 1$, while $\beta = 0$ allows for non-zero stresses at the inner disc and is the choice adopted in `diskbb` (Zhang et al., 1997; Gierliński et al., 1999; Zimmerman et al., 2005). The leading factor, which roughly describes the colour temperature at the inner disc, is given by,

$$T_* = f_{\rm col} \left(\frac{3GM\dot{M}}{8\pi\sigma R_{\rm in}^3} \right)^{1/4}, \tag{2.2}$$

where G is the gravitational constant, σ is the Stefan-Boltzmann constant, M is the compact object mass, $\dot{M}$ is the mass accretion rate, and $f_{\rm col}$ is the colour correction factor (Shimura & Takahara, 1995), also referred to as the spectral hardening factor. For a zero-torque condition at $R_{\rm in}$ (i.e., $\beta = 1$ in Equation 2.1), T_* is related to the maximum temperature attained in the disc by $T_{\rm col,max} = 0.488T_*$, which occurs at $r = (49/36)R_{\rm in}$. Since the disc temperature does not reach T_* at any radius, $T_{\rm col,max}$ is a more physically meaningful characterisation of the blackbody temperature associated with the spectrum. For a thin disc that is torqued at the inner boundary, as is the case for `diskbb`, $T_{\rm col,max}$ coincides with T_* because the temperature profile grows asymptotically with decreasing r (see Figure 1 of Zimmerman et al. 2005). One of the two free parameters of the `diskbb` model is T_*, implicitly assuming $f_{\rm col} = 1$. The 'normalisation' is the other free parameter of `diskbb` and is given by,

$$K_{\rm bb} = 100 \frac{1}{f_{\rm col}^4} \left(\frac{R_{\rm in,km}}{D_{\rm kpc}} \right)^2 \cos i, \tag{2.3}$$

where, again, $f_{\rm col} = 1$, $D_{\rm kpc}$ is the distance to the source in kiloparsecs, $R_{\rm in,km}$ is the inner disc radius in kilometers, and i is the inner disc inclination. Inner disc radii are commonly derived from $K_{\rm bb}$ by measuring intrinsic system properties and imposing a *constant* $f_{\rm col}$ (not necessarily unity as assumed by `diskbb`), regardless of the source luminosity state (e.g., Zdziarski et al., 2004). Remarkably, the simple two-parameter `diskbb` model fully describes the accretion disc spectrum under the appropriate assumptions of a non-zero torque inner disc boundary condition and a fixed colour correction factor for characterising the

overall deviation from a blackbody spectrum.

2.4.2 Zero-Torque Boundary Condition and Disc Vertical Structure

If the inner disc radius can be identified with the ISCO, a zero-torque boundary condition becomes attractive from the physical consideration that the gas viscous inspiral timescale is long relative to the free-fall timescale for gas at the ISCO; therefore, the gas interior to R_{in} does not have time to radiate appreciably before being accreted (Shakura & Sunyaev, 1973; Novikov & Thorne, 1973; Page & Thorne, 1974; Abramowicz & Kato, 1989; Frank et al., 1992; Afshordi & Paczyński, 2003). In principle, for a geometrically thin disc in the presence of a magnetic field, non-negligible torque resulting from magnetic stresses may be present at the ISCO (Krolik, 1999; Gammie, 1999; Agol & Krolik, 2000; Afshordi & Paczyński, 2003). However, magnetohydrodynamic three-dimensional simulations of global thin accretion discs around black holes demonstrate that a weak magnetic field is unable to couple the gas within the plunging region to the disc, despite large fluctuating magnetic stresses inside the ISCO, in accordance with the zero-torque boundary condition (Armitage et al., 2001; Reynolds & Armitage, 2001). Similar simulations exploring initially purely poloidal and toroidal field topologies instead observe significant stress at the ISCO and continuing deep within the plunging region, refuting the zero-torque assumption (Hawley & Krolik, 2001, 2002). A difficulty with allowing for a non-zero torque in disc models is that there is no obvious choice for the magnitude of the torque, necessitating the introduction of a free parameter. The zero-torque choice is both physically motivated and is not arbitrary; however, the presence of significant torque on the inner disc may be important in real systems depending on highly unknown factors such as the disc thickness, dissipation properties, and magnetisation.

The underlying physics responsible for altering the locally emitted spectrum of an optically thick disc from a pure blackbody are parameterised into the colour correction factor. The result of this approximation is the colour-corrected, or 'diluted', blackbody,

$$I_\nu = \frac{1}{f_{\mathrm{col}}^4} B_\nu \left(f_{\mathrm{col}} T_{\mathrm{eff}} \right), \tag{2.4}$$

where I_ν is the specific intensity, B_ν is the Planck function, $T_{\mathrm{eff}} = T_{\mathrm{col}}/f_{\mathrm{col}}$ is the effective temperature,

and $f_{\mathrm{col}} = 1$ refers to a pure blackbody spectrum. In reality, deviations in the emergent disc spectrum from a canonical blackbody arise from frequency-dependent opacities determined from the disc vertical structure, which is neglected in the standard thin disc treatment. The degree of spectral modification will be governed by the combined effects of electron scattering (i.e., Comptonisation in the disc), free-free emission/absorption, and bound-free absorption, resulting in a departure from local thermodynamic equilibrium and a hardening of the spectrum (Felten & Rees, 1972; Shimura & Takahara, 1995; Zavlin et al., 1996; Rutledge et al., 1999a; McClintock et al., 2004). A surrounding corona acting as a depository for some fraction of the disc accretion power provides yet another means for altering the emergent disc spectrum (Svensson & Zdziarski, 1994; Merloni et al., 2000). Furthermore, magnetic pressure support likely contributes significantly to hydrostatic balance in the disc photosphere and may act to vertically extend the disc atmosphere, producing a harder spectrum (Blaes et al., 2006; Begelman & Pringle, 2007). The phenomenological colour-correction prescription avoids all of these complications by neglecting any frequency dependence, only permitting translational (i.e., frequency-independent) hardening and attenuation of the Planck function. Provided that this model yields a satisfactory fit to the observed disc spectrum, one presumes that f_{col}, which is assumed to be constant for all radial locations in the disc, provides an adequate description of the disc vertical structure in an average sense.

The two disc models we appeal to in this work differ from `diskbb` in that they both adopt a zero-torque inner boundary condition and allow for the possibility of a variable colour correction factor. The `ezdiskbb` model (Zimmerman et al., 2005) is the analog of `diskbb`, but with the zero-torque boundary condition enforced. The free parameters are the maximum disc colour temperature, $T_{\mathrm{col,max}}$ defined above, and the normalisation, given by

$$K_{\mathrm{ez}} = 100 \frac{1}{f_{\mathrm{col}}^{4}} \left(\frac{R_{\mathrm{in,km}}}{D_{\mathrm{kpc}}} \right)^{2} \cos i, \tag{2.5}$$

where f_{col} is not specified. We emphasize that changes in K_{ez} do not necessarily imply changes in the disc inner radius, due to the parameter degeneracy between R_{in} and f_{col}. The `diskpn` model (Gierliński et al., 1999), along with the zero-torque boundary condition, incorporates a pseudo-Newtonian potential (Paczyńsky & Wiita, 1980) to more accurately calculate the radial temperature distribution in the disc at the expense of introducing the inner disc radius as a free parameter. The two remaining free parameters are

$T_{\rm col,max}$ and the normalisation,

$$K_{\rm pn} = \frac{1}{f_{\rm col}^4} \left(\frac{M_{\rm M_\odot}}{D_{\rm kpc}} \right)^2 \cos i, \qquad (2.6)$$

where $M_{\rm M_\odot}$ is the compact object mass in solar mass units. In all of the MCD model normalisations, $f_{\rm col}$ enters to the fourth power. Therefore, asking how much $f_{\rm col}$ could conceivably change during a state transition is not unreasonable, as only small changes in $f_{\rm col}$ are required to explain the observed spectral evolution, which may not necessitate disc truncation.

The disc models described up to this point neglect many important physical considerations. We wish to emphasize that sophisticated, physically motivated models are available in `XSPEC` that account for irradiation of the disc (`diskir`; Gierliński et al., 2008), general relativistic effects around a Schwarzschild (`grad`; Ebisawa et al., 1991) and Kerr black hole (`kerrbb`; Li et al., 2005), and detailed modelling of the disc vertical structure around a Kerr black hole (`bhspec`; Davis et al., 2005). Realistic disc models come with the expense of introducing additional parameters. The limited quality of X-ray observations and the desire to limit the number of model parameters forces the use of over-simplified disc models, with the hope that they can adequately capture the most important aspects of the accretion physics. The purpose of the subsequent analysis is to demonstrate that simplistic disc models produce good spectral fits but they cannot be used to make reliable claims regarding the behaviour of the inner disc radius.

2.5   Analysis and Results

In what follows, we exploit the timing and monitoring capabilities of *RXTE*, which provide multiple sequential spectra of moderate resolution tracking the transition between spectral states, to study the evolution of the accretion disc in GX 339–4. The ultimate goal of our spectral analysis is to isolate the disc component in order to measure relative changes in disc properties during transitions over the rise (LHS → HSS) and decay (HSS → LHS) stages of an outburst. We show that allowing for physically reasonable changes in $f_{\rm col}$ provides an alternative explanation to disc truncation for the observed disc spectral evolution during state transitions. Table 2.3 provides a sample of best-fit parameters for the fits used in this work.

2.5.1   Requirement of a Disc Component

We wish to verify the presence of a thermal disc component with adequate confidence using phenomenological models that have proven successful in characterising the general features of BHB X-ray spectra. To determine whether or not a disc component is required in a given *RXTE* spectrum, we adopt a methodology based on χ^2 statistics that uses phenomenological models to fit numerous observations in various spectral states, as motivated by previous works (Dunn et al., 2008, 2010, 2011; Reynolds & Miller, 2013). The PCA and HEXTE data are fit jointly, allowing an energy-independent constant factor to vary for the HEXTE data to account for any normalisation offset relative to the PCA and linking all parameters between the PCA and HEXTE spectra. The spectral models are modified by photoelectric absorption using the `phabs` model with a fixed equivalent neutral hydrogen column density of $N_{\mathrm{H}} = 5.7 \times 10^{21}$ cm^{-2} (Miller et al., 2009b). Both Galactic and intrinsic absorption are folded into the `phabs` model, leading to a potential ambiguity as to whether low-energy spectral evolution is due to changes in the intrinsic absorption or to evolution of the source. Miller et al. (2009a) fitted high-resolution BHB spectra (including GX 339–4) over a wide range in luminosity and spectral states, demonstrating that the low-energy spectral evolution is a consequence of the evolution of the source itself, rather than a variable neutral photoelectric absorption. Notably, Cabanac et al. (2009) present the case for possible variations in N_{H} during outbursts of GX 339–4; however, the restricted low-energy coverage of *RXTE* does not permit N_{H} to be a free parameter in our spectral fits.

As a first attempt, the spectra are fitted with a simple model consisting of an absorbed power-law and MCD blackbody (i.e., `phabs×(powerlaw+diskbb)` in XSPEC) to model the continuum and accretion disc, respectively. In many observations, this simple prescription does not yield an adequate fit due to the presence of a broad Fe Kα emission line. To check for the requirement of an iron line component, a Gaussian line profile (`gauss` in XSPEC) is added to the model at fixed centroid energy of 6.4 keV with the width, σ, and normalisation, K_{line}, as free parameters. An *F*-test is inappropriate for determining whether the inclusion of a spectral line is a statistically significant improvement (Protassov et al., 2002). The alternative diagnostics outlined by Protassov et al. (2002) for testing for the presence of a line are not easily incorporated into

the spectral fitting framework used here. We are concerned with obtaining an acceptable fit in order to determine the presence of a disc component and do not wish to make any strong statements regarding Fe Kα emission; therefore, we adopt the line detection procedure of Dunn et al. (2008). In order for a line to be considered significant, two criteria must be met: (1) An F-test must determine that the line is significant at $\geq 3\sigma$ (F-statistic probability $\mathcal{P} \leq 0.0027$). (2) Given the 1σ uncertainty in the line normalisation, $\sigma_{K_{\mathrm{line}}}$, obtained with the XSPEC error command, we require $K_{\mathrm{line}} \geq 3\sigma_{K_{\mathrm{line}}}$. This procedure for line determination is more conservative than appealing to an F-test alone, though we note that some detected line features may be erroneous.

We next test for the presence of a high energy break in the spectrum by replacing the power-law component with the broken power-law model, bknpower, and repeating the aforementioned fitting procedure. If an F-test determines that the broken power-law model is a significant improvement over the power-law model at $\geq 3\sigma$ confidence, then we proceed with the broken power-law model imposing the parameter ranges for the spectral indices and break energy of $1 \leq \Gamma \leq 4$ and $E_{\mathrm{b}} \geq 10$ keV, respectively. In instances where a line component was deemed necessary in the power-law model but not the broken power-law model, or *vice versa*, we select the best fitting model determined by the lowest reduced χ^2-statistic, $\chi^2_\nu \equiv \chi^2/\nu$, where ν is the number of degrees of freedom in the model. For cases when the best-fit converges to the parameter limits of the bknpower model, the pipeline reverts to the powerlaw model for that observation. If the best-fit powerlaw model also runs into a parameter bound, the observation is discarded.

At this point in the phenomenological fitting pipeline, for a fit to be considered acceptable for use in subsequent analysis, we require $\chi^2_\nu \leq 2$. Often, a poor fit to the high-energy spectrum is the culprit for failure to meet this criterion. For instance, a poor fit may result from the inability of simplistic, unphysical models to properly fit a reflection component or a complicated spectrum arising from a dynamic corona. Since we are using phenomenological models to characterize the soft disc component and are not interested in a detailed characterization of the high-energy spectrum, if the best-fit model to the combined PCA/HEXTE data gives $\chi^2_\nu > 2$, then we repeat the above fitting procedure on the PCA data alone in search of an acceptable fit. In these cases where only the PCA data are being fitted, we use the powerlaw model only because any spectral energy break is expected to lie beyond the high-energy cutoff of the PCA, rendering the use of the bknpower

model inappropriate.

The disc component (`diskbb`) is then removed from the best-fit model and the spectrum is re-fitted. An F-test is performed to determine whether or not the inclusion of the disc improved the fit by $\geq 3\sigma$. Observations that meet these criteria are kept for further analysis, while those that do not statistically require a disc are discarded. Running this model fitting procedure on 283 total observations of GX 339–4 in different stages of transition between the low/hard and high/soft states resulted in 177 observations where a disc component was deemed statistically required from spectral fitting techniques (see Table 2.1).

We caution that the absence of a quasi-blackbody component in a given $RXTE$ spectrum does not imply the absence or truncation of the physical accretion disc. The low energy cutoff of the $RXTE$ PCA is restricted to ~ 3 keV; thus, only the Wien tail of the MCD blackbody spectrum will be in the observable band. Although we may not detect a disc, especially in the HIS and LHS, this is not enough to claim the absence of a disc component, which may be dominant at energies below the sensitivity of $RXTE$ (e.g., Dunn et al., 2008) and has been observed with XMM-$Newton$ in the LHS of GX 339–4 (e.g., Miller et al., 2006a; Reis et al., 2008).

Figure 2.2 shows the data-to-model ratios with the disc component removed from the best-fit model for representative observations of each state transition. Disc fractions are defined by,

$$DF \equiv \frac{F_{\mathrm{disc}}^{0.1-10 \ \mathrm{keV}}}{F_{\mathrm{total}}^{0.1-100 \ \mathrm{keV}}}, \tag{2.7}$$

where F_{disc} and F_{total} are the unabsorbed fluxes of the disc component and overall model, respectively, taken over the energy ranges indicated by the superscripts. Fluxes were obtained with the `cflux` command in `XSPEC`. Disc components are robustly detected by the pipeline described above, even for moderately low disc fractions, which is essential for tracking the evolution of the disc throughout each transition in the subsequent analysis.

2.5.2   Sensitivity of Spectral Fits to the Continuum Model

The motivation for employing a simple power-law model with limited free parameters is to fit the portion of the spectrum that is thought to arise from Comptonisation of thermal disc photons by a low
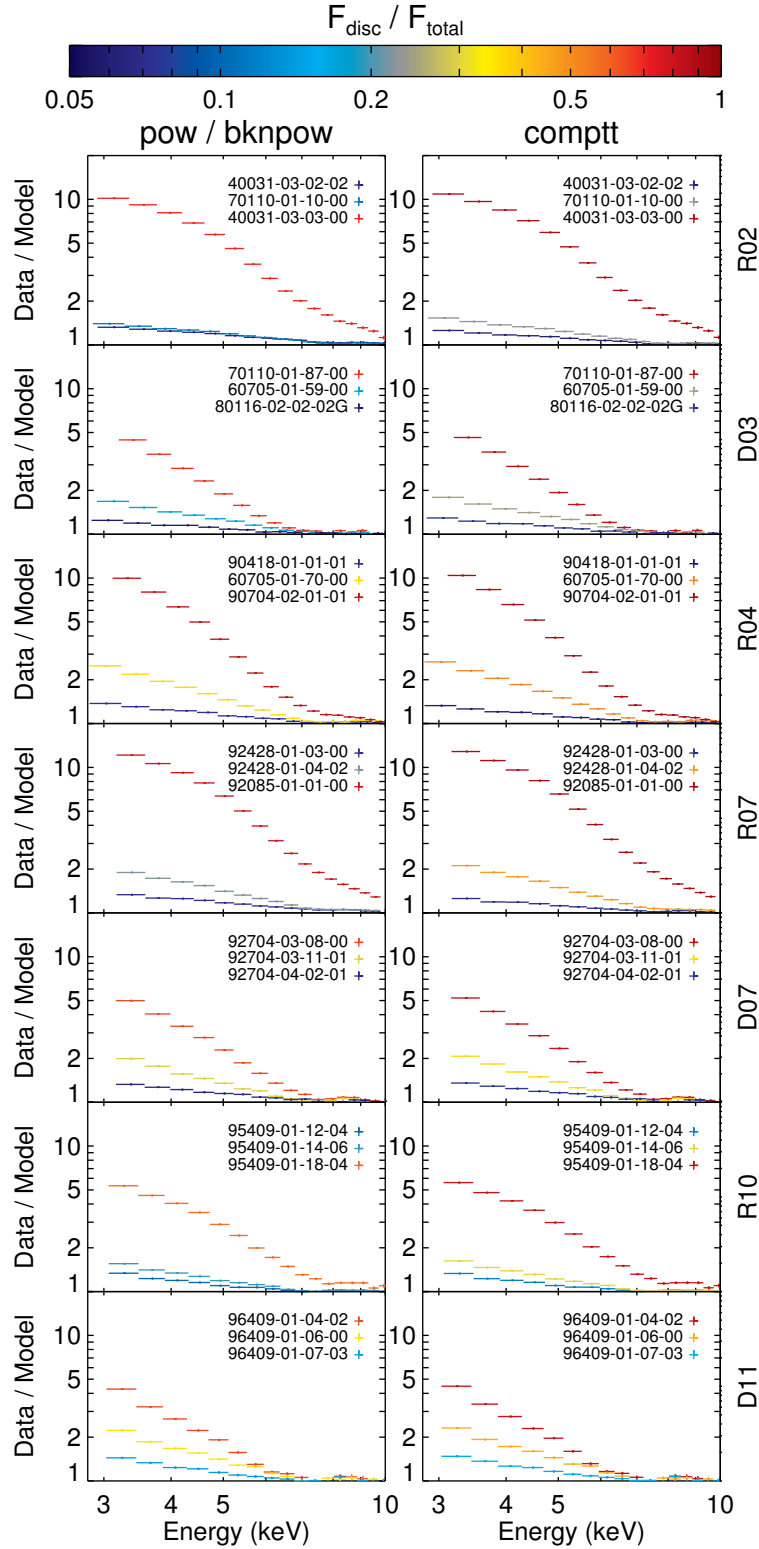
Figure 2.2: Ratios of the *RXTE* data to the best-fit models with the `diskbb` component removed to highlight the need for a quasi-blackbody feature to model the soft excess. For each transition, three data/model ratios are shown that representatively span the range in measured disc fractions. Glyph colours denote the disc fraction for each fit. For comparison, the best-fit models where Comptonisation is modelled by the `powerlaw` or `bknpower` (*left column*) and `comptt` (*right column*) XSPEC models are shown. For each row, the observation IDs are given in the *upper right* corner of the plots and the transition ID on the *rightmost* ordinate.

density, energetic electron corona of unknown geometry, which produces a power-law spectrum to first order. The phenomenological power-law model extends to arbitrarily low energies, which does not mimic a physical Comptonisation process where a sharp cutoff is expected at an energy comparable to the characteristic energy of the input seed photon distribution, namely, the quasi-blackbody disc spectrum. Therefore, the extension of the power-law component toward arbitrarily low energies results in 'flux stealing' from the disc component, making a disc more difficult to detect than had we adopted a more physical Comptonisation model.

To investigate the sensitivity of fitting the disc component on the choice of Comptonisation model, we explore two different models to characterise the continuum. The Comptonisation model `comptt` (Titarchuk, 1994; Hua & Titarchuk, 1995) provides an analytic description of the spectrum produced from a soft photon distribution propagating through a hot plasma cloud. We re-ran the disc detection pipeline with `comptt` in place of the power-law component, allowing only the plasma temperature, T_{p}, plasma optical depth, τ_{p}, and normalisation, K_{comptt}, to be free parameters. The remaining `comptt` parameters that we chose were a redshift $z = 0$, a seed photon temperature, $T_0 = T_{\mathrm{col,max}}$ (i.e., 0.488 times the `diskbb` temperature), and a spherical plasma cloud geometry. The additional free parameter introduced by `comptt` is justified by the physical, as opposed to phenomenological, nature of the model. For cases where the best-fit converges to the enforced plasma temperature limit, $T_{\mathrm{p}} = 100$ keV, the data are re-fitted with T_{p} fixed at 100 keV. When the disc component is removed to check for the requirement of a disc, T_0 becomes a free parameter, as there is no longer an obvious, physically motivated choice for the seed photon distribution injected into the corona in the absence of a disc. A total of 166/283 observations required a disc component when `comptt` was used, compared to the 177/283 using the standard phenomenological `powerlaw` and `bknpower` models.

An alternative empirical substitute for a power-law model is `simpl` (Steiner et al., 2009), which truncates the power-law spectrum at an energy comparable to the characteristic input seed photon energy; thus, avoiding the unphysical low-energy extension of the `powerlaw` and `bknpower` models. Since `simpl` is a convolution model, we cannot apply the disc detection pipeline of §2.5.1 to determine whether or not a disc component is required. Instead, the previously determined 177 best-fit models are re-fitted with `simpl` as the component responsible for modelling Comptonisation, allowing for both up- and down-scattering of
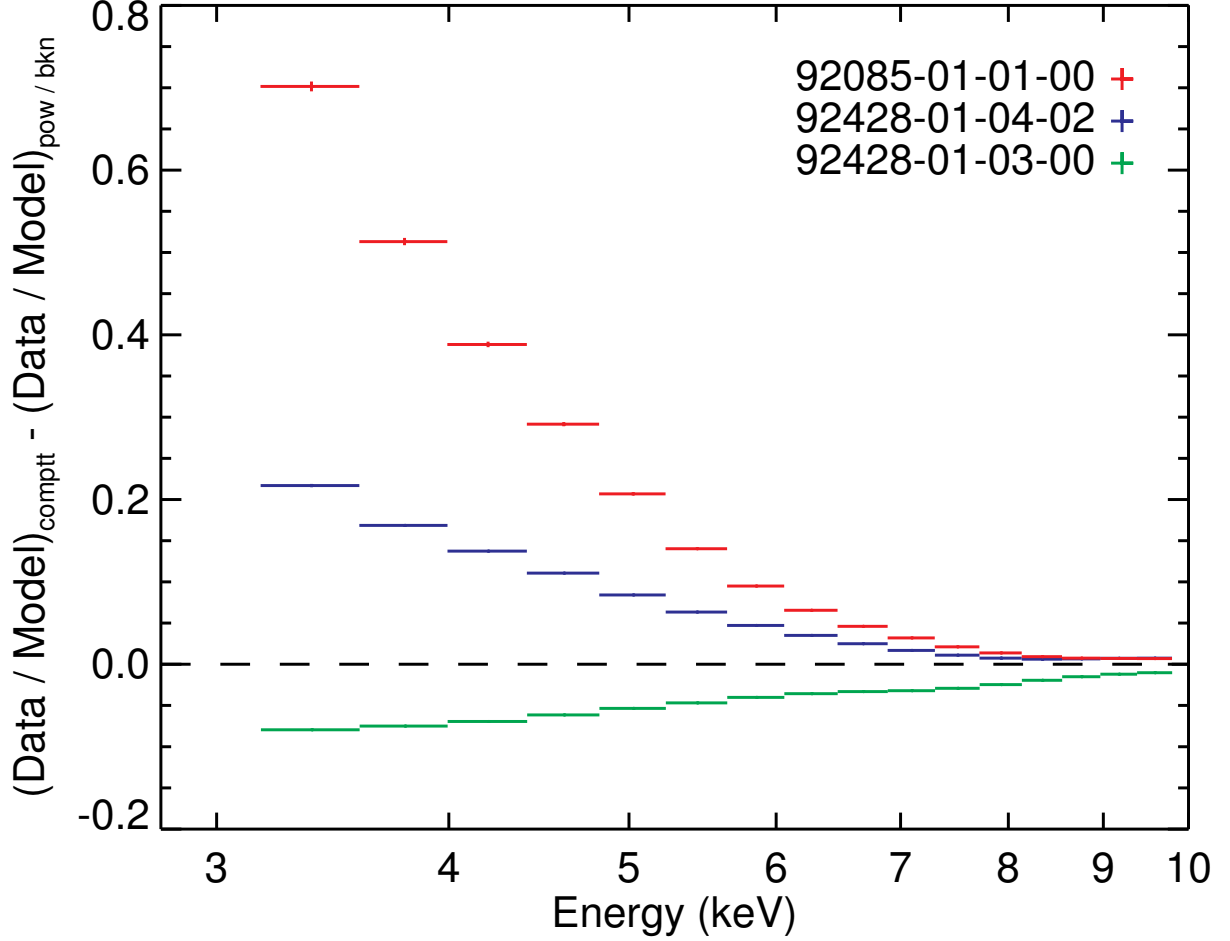
Figure 2.3: Dependence of the strength and spectral shape of the disc component on the choice of Comptonisation model for transition R07. The residuals plotted are computed by subtracting the data-to-model ratio for the `pow/bknpow` best-fit model from the best-fit `comptt` data-to-model ratio. The data-to-model ratios used are those where the disc component was removed, as done in Figure 2.2. Residuals falling on the *dashed* line indicate no difference in the measured disc component between the two Comptonisation models, while a positive excess implies flux stealing from the disc component by the `pow/bkn` model relative to the `comptt` model. From *top* to *bottom*, the residuals were computed from observation IDs 92428-01-03-00 (*red glyphs*), 92428-01-04-02 (*blue glyphs*), and 92085-01-01-00 (*green glyphs*), which represent the HSS, IS, and LHS, respectively. The flux stealing effect is most pronounced in the HSS and IS.
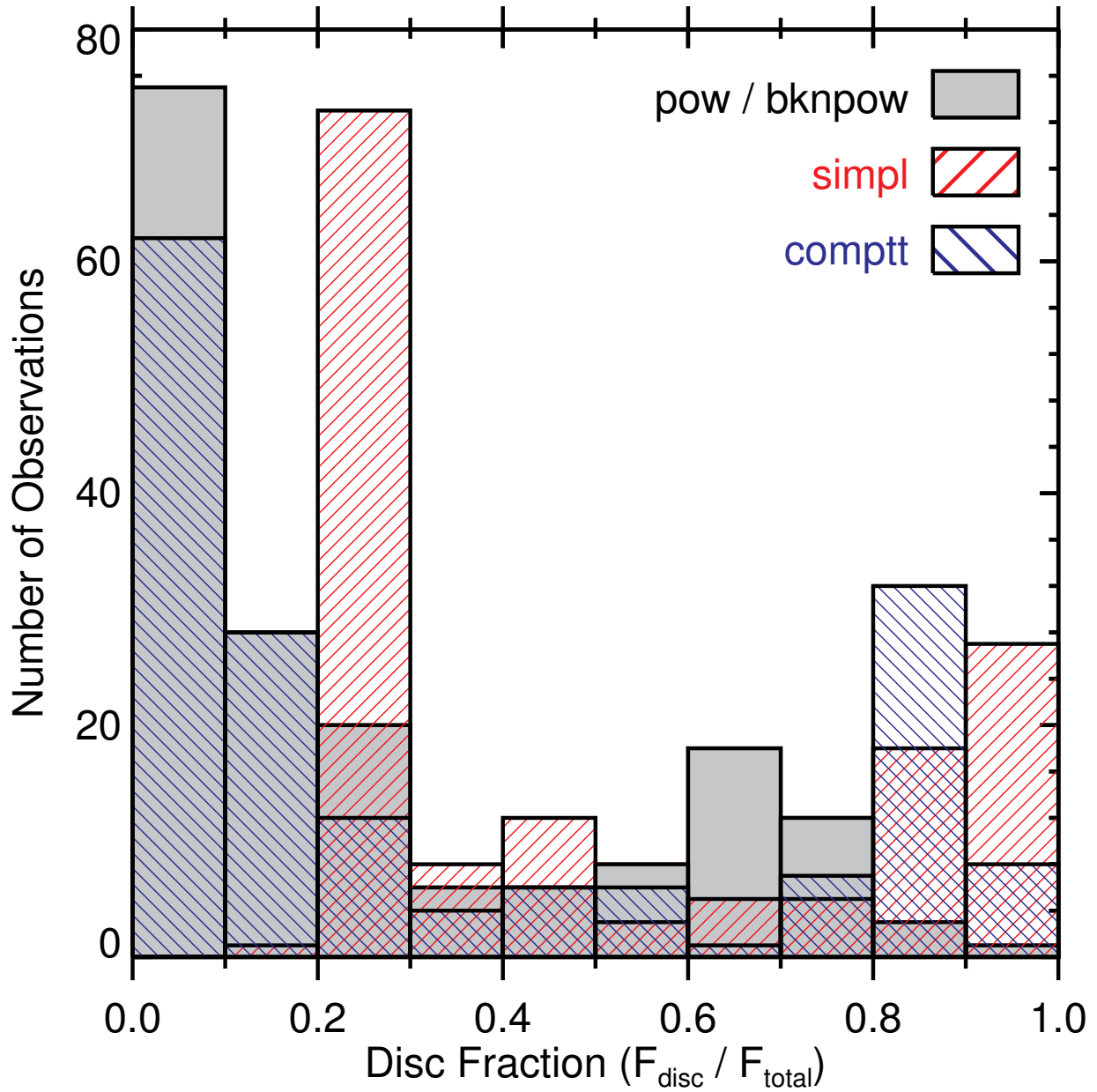
Figure 2.4: Histogram of disc fractions for fits performed with Comptonisation models `pow/bknpow` (*grey filled*), `simpl` (*red forward slashes*), and `comptt` (*blue backward slashes*). The excess of low disc fractions for the `pow/bknpow` model is a consequence of the power-law extending to arbitrarily low energies, effectively stealing flux from the disc component.

the input seed spectrum. Again, as was done for the disc detection pipelines using `powerlaw`/`bknpower` and `comptt` as the continuum models, the observation is discarded if the best-fit converges on a parameter limit. This returned 150/177 observations where the best-fit does not encounter a parameter limit. While `simpl` cannot capture the high energy break commonly observed in BHB spectra, often resulting in the dismissal of the HEXTE data in order to obtain acceptable fits, this excision of data is justified because a detailed model of the high-energy spectrum is ancillary to a reliable model of the disc spectrum.

The choice of Comptonisation model influences the measured disc properties. As discussed above, the three Comptonisation models we explore in this work are: (1) standard power-law or broken power-law (hereafter, `pow/bknpow`), (2) power-law with a low-energy cut-off (hereafter, `simpl`), and (3) physical Comptonisation model (hereafter, `comptt`). For representative observations over all transitions fit with the `pow/bknpow` and `comptt` models, Figure 2.2 shows data-to-model ratios with the disc component removed from the best-fit model, which is a probe of the spectral shape and strength of the disc component. The disc is strong in the HSS and gradually weakens, but remains detectable, in the LHS down to $DF \simeq 0.05$.

Figure 2.3 shows the residuals for the data-to-model ratios of the `comptt` fits compared to those for the best-fit `pow/bknpow` models for a representative transition. The flux stealing phenomenon inherent to the low-energy extension of the `pow/bknpow` model is apparent from the positive excess in the residuals and affects the measured disc spectrum, particularly for high disc fractions that are characteristic of the HSS. A histogram of measured disc fractions for all observations deemed to require a disc and for each choice of Comptonisation model is shown in Figure 2.4. Generally, replacing the power-law model with more physically motivated Comptonisation models produces higher disc fractions and yields disc model spectra that are unplagued by flux stealing. The measured disc fraction for a given observation generally follows $DF_{\texttt{simpl}} > DF_{\texttt{comptt}} > DF_{\texttt{pow/bknpow}}$.

Given this study on the sensitivity of the spectral fits to the choice of continuum model, we must decide how to proceed with the subsequent analysis in order to best represent the true character of the disc evolution during a state transition. In the interest of comparison and because discrepancies in the measured disc properties arise between the three different, but seemingly adequate, Comptonisation models, we do not favour one model over another. Instead, we elect to perform the subsequent analysis in three branches,

identical in all respects except for the Comptonisation model (i.e., `pow/bknpow`, `simpl`, `comptt`) being used in the spectral fits.

2.5.3   Disc Evolution Results from Spectral Fitting

A parameter degeneracy exists between the inner disc radius and the colour correction factor within the normalisation of the standard `diskbb` model. Therefore, decomposing the contributions to the disc evolution due to changes in the vertical disc structure, parametrized into f_{col}, and a migrating inner disc region is nontrivial. Combining the models `diskpn` and `ezdiskbb`, while appealing to relative measurements of the disc model normalisation evolution, we examine the degree of change in f_{col} and R_{in} required to explain the disc spectral evolution in state transitions of GX 339–4.

2.5.3.1   Relative Measurements

Obtaining reliable *absolute* measurements of quantities locked up in the disc normalisation is limited by constraints on the observables, namely, the mass, distance, and disc inclination, which all appear in the normalisation. However, *relative* changes in f_{col} and/or R_{in} are accessible from the evolution of the disc normalisation because the intrinsic parameters do not change between successive observations.

Imposing a small systematic error on *RXTE* PCA data is common practice, resulting in a substantial improvement in the quality of spectral fits. Applying model fits to data where no systematic error is added will result in poor fits but with best-fit parameter errors dramatically reduced. While the best-fit parameter values may be unreliable, they should be affected in a systematic sense and systematic errors associated with instrument calibration will be removed from the parameter errors. Provided that relative, rather than absolute, measurements are of interest, the evolution of a parameter may be tracked from fits to spectra without systematic error incorporated into the PCA data.

To test the validity of this proposition, we re-fitted all spectra deemed to require a disc component with the best-fit models determined from the aforementioned fitting pipeline, but with no systematic error added to the PCA data. Figure 2.5 compares the distribution of the `diskbb` normalisation relative error, defined as $\sigma_{K_{bb}}/K_{bb}$, for fits to all GX 339–4 spectra when no systematic error and the standard 0.6%
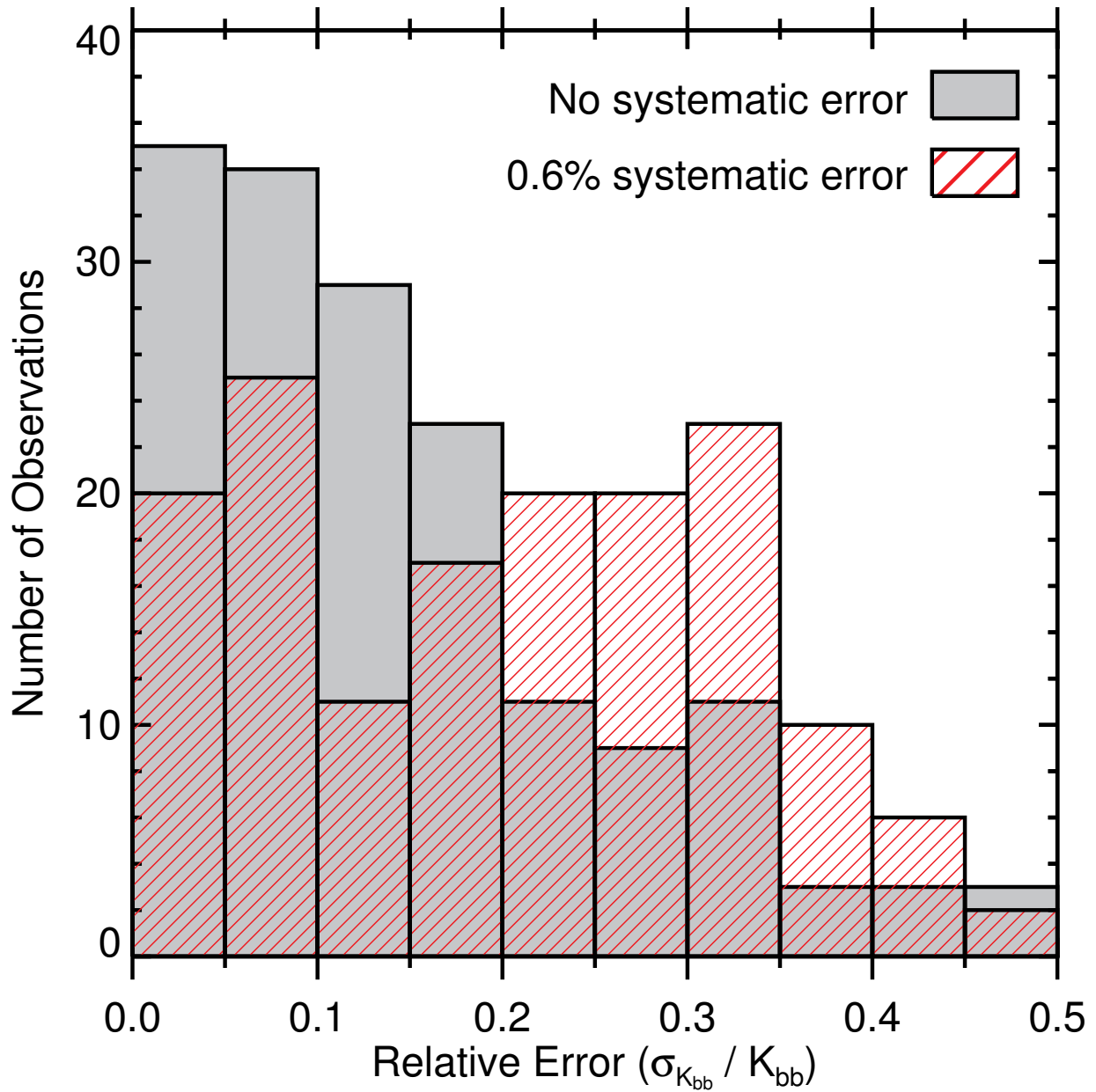
Figure 2.5: Histogram of relative errors on the best-fit `diskbb` normalisation, $\sigma_{K_{\rm bb}}/K_{\rm bb}$, for all *RXTE* observations requiring a disc component. Models fit with a systematic error of 0.6% added to all PCA energy channels and no systematic error added to the PCA data are shown as *red forward slashes* and *grey bars*, respectively. The relative error on the disc normalisation is reduced when systematic error is not added to the data.
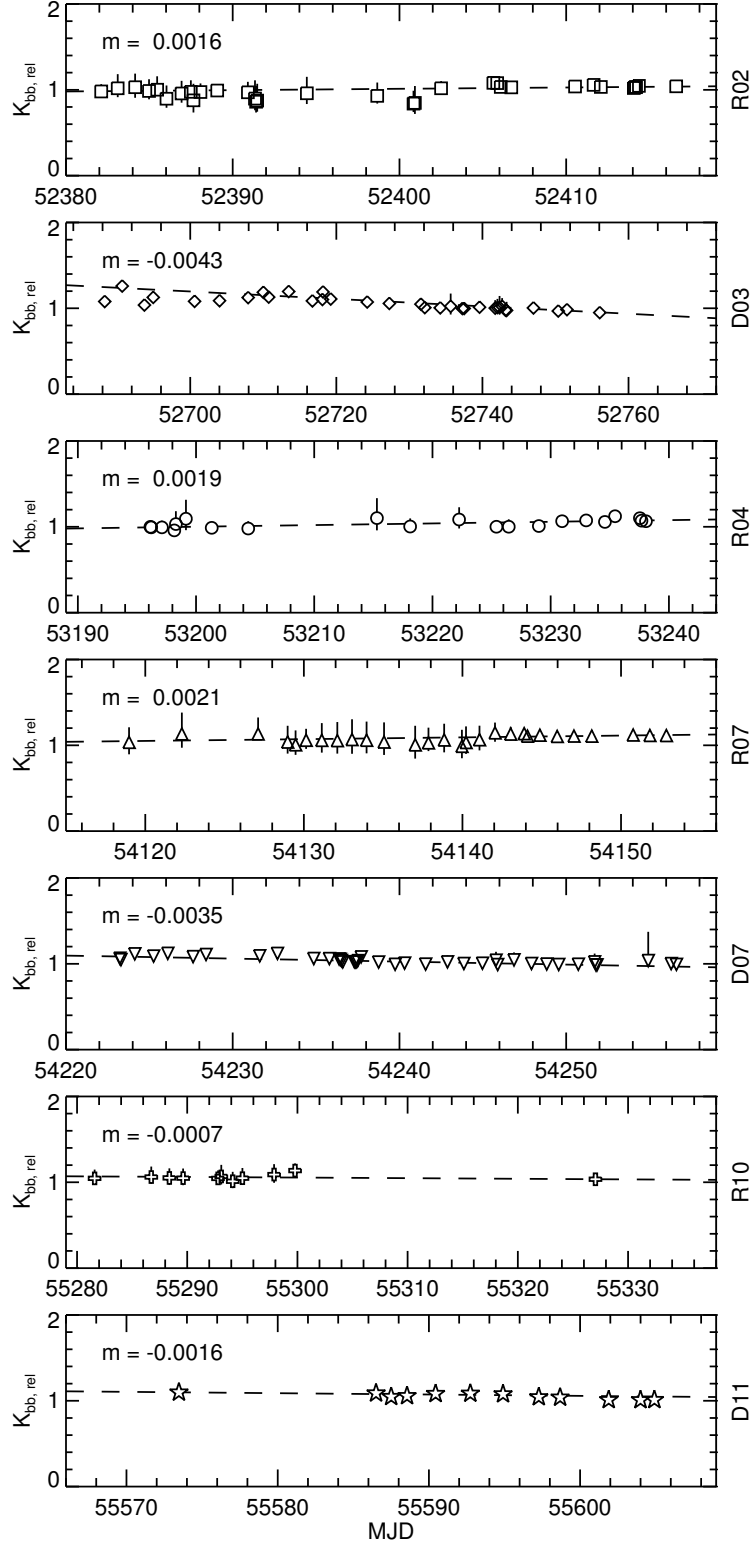
Figure 2.6: Relative comparison of `diskbb` normalisations, $K_{\mathrm{bb,rel}}$ (see text for definition), for each transition. The slope, m, from a linear fit to the data is displayed in the *upper left* corner for each plot. A zero-slope means that relative changes in K_{bb} with time are unaffected by neglecting to add systematic errors to the PCA data, indicating that the systematics remain constant from observation to observation for the time intervals considered. The flatness of $K_{\mathrm{bb,rel}}$ justifies the use of relative measurements for studying the disc evolution throughout a state transition. From *top* to *bottom*, the panels show the time evolution of $K_{\mathrm{bb,rel}}$ for transitions R02, D03, R04, R07, D07, R10, and D11.

systematic error were added to the PCA data (Jahoda et al., 2006). As expected, not including systematic errors results in improved relative errors on the `diskbb` normalisation. Adopting an analysis technique based on omitting systematic errors from the PCA data requires that the disc normalisation values are only affected in a systematic way as a result. For each transition, Figure 2.6 shows $K_{\mathrm{bb,rel}} = K_{\mathrm{bb,nosys}}/K_{\mathrm{bb}}$, which is defined as the best-fit `diskbb` normalisation for fits with no systematic error added, $K_{\mathrm{bb,nosys}}$, relative to the normalisation for fits with 0.6% systematic error added, K_{bb}. The constancy of this ratio throughout the spectral evolution of all transitions suggests that excluding systematic error for the PCA data to study the evolution of the disc normalisation in a relative sense is justified in practice.

Occasionally, an observation that was adequately fitted when a 0.6% systematic error was added to the PCA data will converge on parameter limits or grossly unphysical values when the data without systematic error are fitted. In these situations, the data without systematic error added are fitted by hand in order to achieve a fit with more realistic best-fit parameters. All errors presented in this work are 1σ and are appropriately propagated when making relative measurements.[6]

2.5.3.2   Disc Spectral Evolution: Variable f_{col}

A variable colour correction factor has been considered from both a numerical (e.g., Shimura & Takahara, 1995; Merloni et al., 2000; Davis et al., 2005) and observational (e.g., Dunn et al., 2011; Reynolds & Miller, 2013) approach, with $1.4 < f_{\mathrm{col}} < 3$ generally believed to be a conservatively broad allowable range, implying at most a factor of ~ 2 change in f_{col}. However, this range in f_{col} does not consider regimes extending to the low disc luminosities associated with the HIS and LHS nor the effects of disc inhomogeneities and strong magnetisation. Spectra that are less disc-dominated are harder; thus, requiring an increased f_{col}. The possibility of extending the upper f_{col} bound for discs in the HIS and LHS (i.e., non-disc-dominated regimes where $L_{\mathrm{disc}} \lesssim 0.01\ L_{\mathrm{Edd}}$) and whether a colour-corrected blackbody is an appropriate description of the disc spectrum in this regime remain open questions.

Using the `diskpn` model with the inner disc radius fixed ensures that the evolution of the disc normal-

---

[6] Two identical data sets, one with a small systematic error added (X) and one without (Y), are nearly perfectly correlated (i.e., the correlation coefficient, $\rho_{X,Y} = \mathrm{cov}(X,Y)/(\sigma_X \sigma_Y) \simeq 1$). Since both X and Y only differ in the uncertainties associated with the data, their covariance is given by, $\mathrm{cov}(X,Y) = \mathrm{cov}(X,X) = \sigma_X^2$. The resulting correlation coefficient becomes, $\rho_{X,Y} = \sigma_X/\sigma_Y \simeq 1$, assuming that the systematic errors added to Y are small, which is true for our purposes.
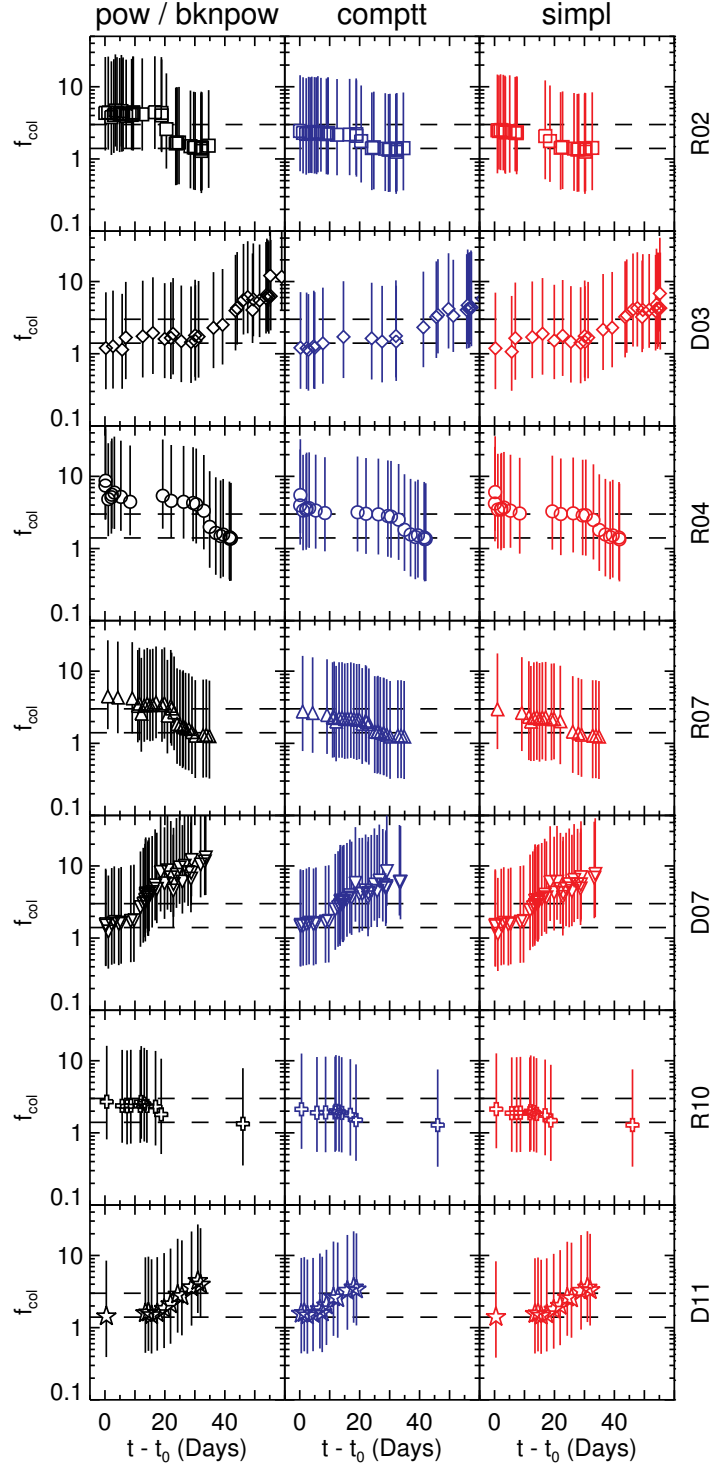
Figure 2.7: Evolution of the colour correction factor over all state transitions derived from best-fit `diskpn` normalisations where the inner disc radius was held at 6 R_{g}. The *left*, *middle*, and *right* panels correspond to fits using the `pow/bknpow`, `comptt`, and `simpl` continuum models, respectively. The abscissa shows time elapsed since the start time, t_0, of the transition (see Table 2.1). Error bars account for the maximum conceivable ranges of the mass, distance, and inclination of GX 339–4 (see text). The *dashed lines* enclose $1.4 < f_{\mathrm{col}} < 3$, which is the adopted allowable range in f_{col}. The transition ID corresponding to each row is indicated on the *rightmost* ordinate. Within the large uncertainties, a non-truncated disc with a variable f_{col} can adequately explain the observed disc spectral evolution.

isation is due entirely to a variable colour correction factor, which can be computed directly from Equation 2.6, as demonstrated by Reynolds & Miller (2013). We elect to explore the degree of change in $f_{\rm col}$ alone that is required to explain the disc spectral evolution for a fixed inner disc radius of 6 $R_{\rm g}$. This choice for $R_{\rm in}$ is motivated by considering a disc extending down to the ISCO for a Schwarzschild black hole and is the minimum value allowed by `diskpn`.

To measure the evolution of *absolute* $f_{\rm col}$ values required to explain the disc evolution in each transition for a fixed inner disc radius, we re-fit all of the spectra with 0.6% systematic error added to the PCA data using the best-fit models, but replacing the `diskbb` component with `diskpn` and freezing $R_{\rm in}$ at 6 $R_{\rm g}$. Figure 2.7 shows the evolution in $f_{\rm col}$ that is necessary to account for each transition, with the error bars incorporating the best-fit $K_{\rm pn}$ error and the range in intrinsic parameters of GX 339–4. The values adopted for the GX 339–4 observables, along with their (lower, upper) limits, are $M = 7\ (5.8, 12)\ \rm M_{\odot}$, $D = 8\ (6, 10)$ kpc, and $i = 29° \ (10°, 60°)$ (see §2.3.1 and references therein). Figure 2.7 shows that, within the uncertainties, the disc spectral evolution can potentially be explained by a variable $1.4 \lesssim f_{\rm col} \lesssim 3$ for an inner disc radius that remains at 6 $R_{\rm g}$ throughout each state transition.

Studying the evolution of absolute $f_{\rm col}$ values for a fixed $R_{\rm in}$ is limited by the large uncertainties in the mass, distance, and inclination of GX 339–4. Given that an inner disc that remains at 6 $R_{\rm g}$ combined with a modestly variable $f_{\rm col}$ may be a viable model for accretion disc evolution in the state transitions studied here, we use the relative measurement technique introduced in §2.5.3.1 to better understand the degree of change in $f_{\rm col}$ that is required to explain the observations without appealing to disc truncation.

The PCA data are replaced with a duplicate copy where no systematic errors have been added. Next, the `diskpn` fits where $R_{\rm in} = 6\ R_{\rm g}$ are re-fitted and a best-fit is found for each observation. This is done for each of the three Comptonisation models `pow/bknpow`, `simpl`, and `comptt`. For each observation in a given transition, $f_{\rm col}$ is computed from $K_{\rm pn}$ using Equation 2.6, without specifying the intrinsic parameters (i.e., M, D, i). The resulting $f_{\rm col}$ values are normalised to the $f_{\rm col}$ from a representative HSS observation, $f_{\rm col,HSS}$, and further normalised to the adopted $f_{\rm col} = 1.4$ value for the HSS (Davis et al., 2005), yielding

the relative colour correction factor,

$$f_{\mathrm{col,rel}} \equiv 1.4 \left(\frac{f_{\mathrm{col}}}{f_{\mathrm{col,HSS}}} \right). \tag{2.8}$$

Supposing that the inner disc remains fixed at 6 R_{g} throughout each state transition, Figures 2.8-2.10 show the relative change in f_{col} alone required to explain the observed disc spectral evolution. Notably, the `pow/bknpow` model requires more drastic change in f_{col} compared to `comptt` and `simpl`. Under the presumption that $f_{\mathrm{col,rel}} = 3$ is a conservative upper bound, the notion of a variable f_{col} alone is perhaps possible for transitions R02, R07, R10, and D11; however, an evolving f_{col} is an inadequate description of the evolving disc spectrum for transitions D03, R04, and D07, regardless of the Comptonisation model employed. For the later set of transitions, one must invoke disc truncation or an alternative disc model to satisfactorily explain the observed disc evolution. Reynolds & Miller (2013) speculate that if the colour-corrected blackbody is a viable model of the LHS, then f_{col} may be as large as ~ 5 based on spectral fits to a comprehensive set of BHB spectra. Inspecting Figures 2.9-2.10, where the `comptt` and `simpl` models were adopted, all seven transitions essentially conform to this extended f_{col} range; although, making definitive claims regarding the physically plausible f_{col} range and applicability of the MCD model in the LHS is beyond our scope.

2.5.4 A Hot Inner Disc Can Masquerade as an Increased f_{col}

Observational evidence suggests that GX 339–4 harbors a near-maximally spinning black hole (see §2.3.1). Consequently, the inner disc extends deep into the black hole potential and relativistic effects become non-negligible, rendering Newtonian disc models inappropriate. The disc models used in this work to derive f_{col} measurements impose an effective lower limit on the inner disc radius of 6 R_{g}, whereas the ISCO of a Kerr black hole with $a_* = 0.998$ lies at 1.24 R_{g}, corresponding to a substantially hotter inner disc. Consider attempting to use a Newtonian prescription to model an accretion disc around a Kerr black hole, where $R_{\mathrm{in}} = R_{\mathrm{ISCO}}$. The Newtonian disc model is restricted by $R_{\mathrm{in}} \geq 6 \ R_{\mathrm{g}}$ and will attempt to fit the true hotter disc, located at $R_{\mathrm{ISCO}} < 6 \ R_{\mathrm{g}}$, by increasing the colour correction factor as follows. The colour temperature determined by the model depends on both f_{col} and T_{eff} according to $T_{\mathrm{col}} = f_{\mathrm{col}} T_{\mathrm{eff}}$. The maximum effective temperature of the Kerr disc exceeds that of the Newtonian model with $R_{\mathrm{in}} = 6 R_{\mathrm{g}}$; therefore, the only way
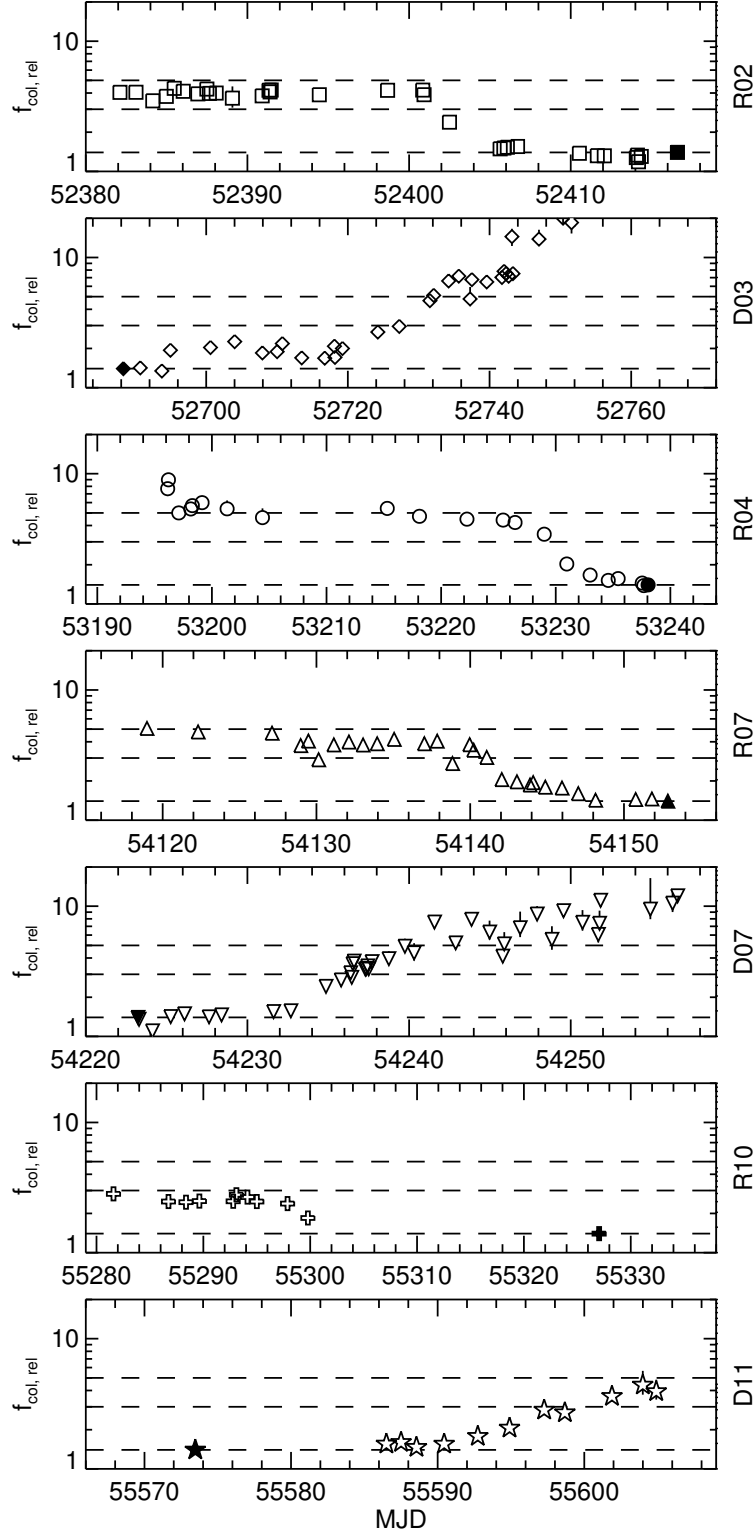
Figure 2.8: Relative measurements of the evolution of f_{col} for each transition derived from fits using `pow/bknpow` to model Comptonisation. The two *lower dashed lines* enclose $1.4 < f_{col} < 3$, while the *upper dashed line* marks $f_{col} = 5$. The $f_{col,rel}$ measurements for each transition were made relative to the filled glyphs and normalised to $f_{col} = 1.4$, which is appropriate for the HSS. The disc evolution can be explained for transitions R02, R07, R10, and D11 by a non-truncated disc with $1.4 \leq f_{col,rel} \leq 5$.
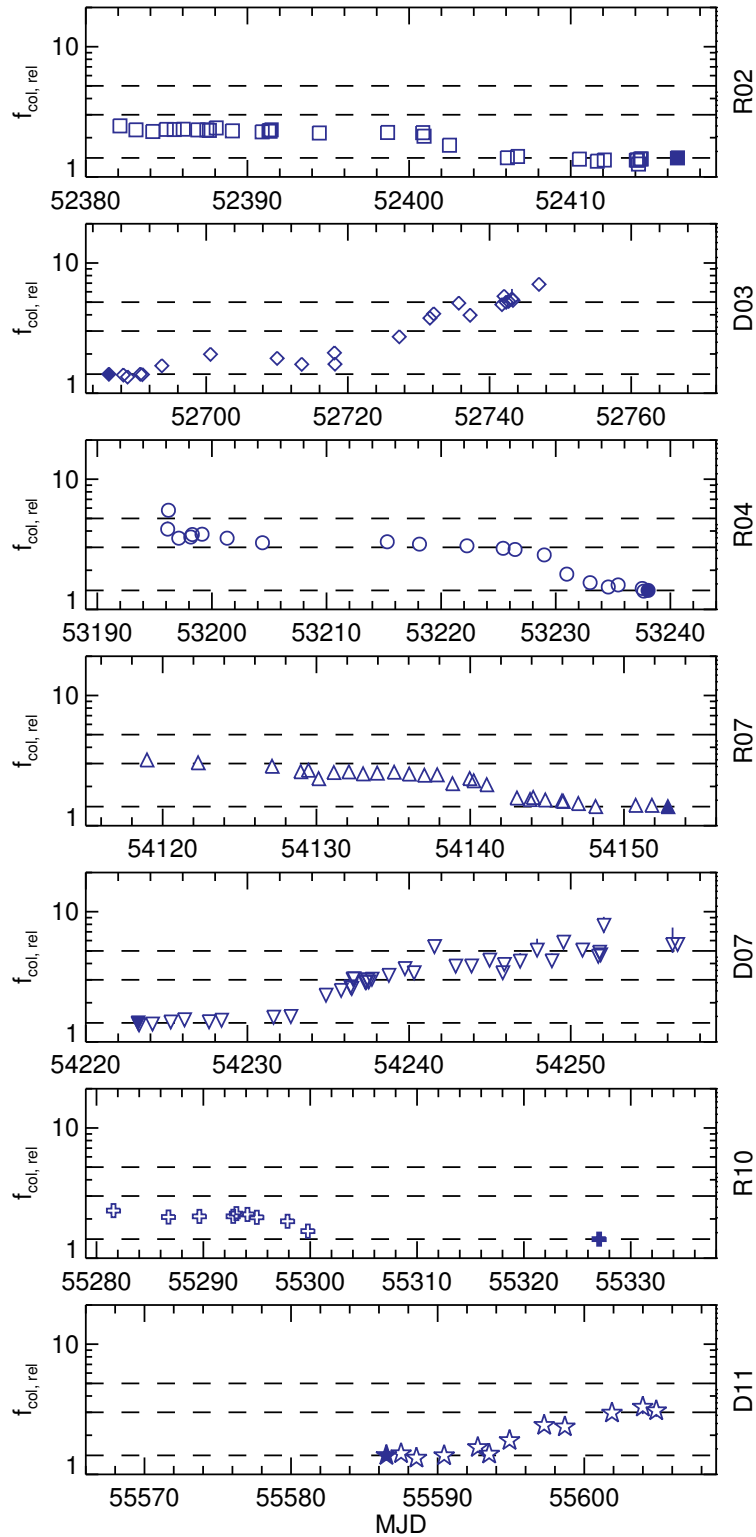
Figure 2.9: Same as Figure 2.8, but with the Comptonisation model `comptt` replacing `pow/bknpow`. The required evolution in $f_{\rm col,rel}$ is systematically reduced compared to results from the `pow/bknpow` continuum model.
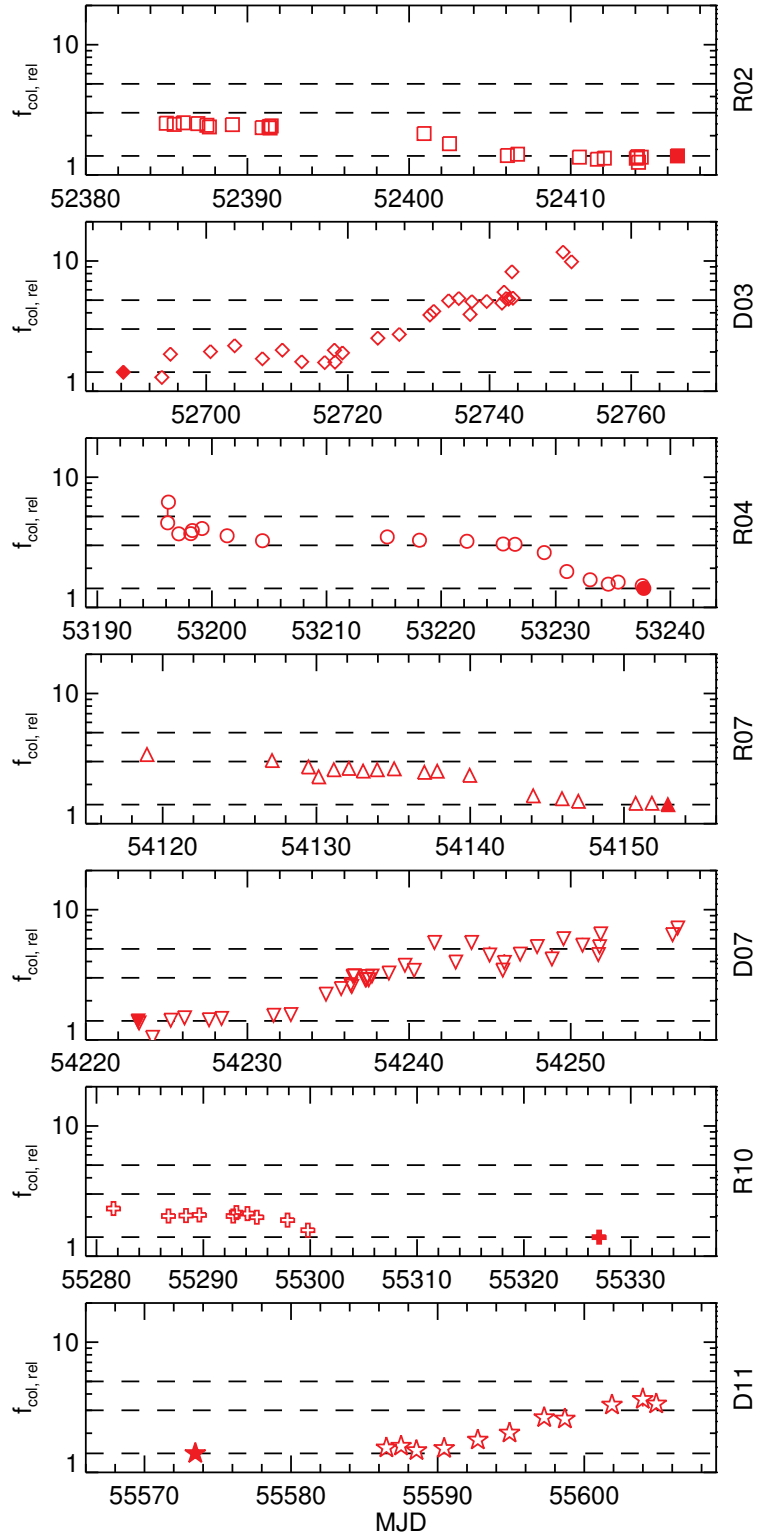
Figure 2.10: Same as Figure 2.8, but with the Comptonisation model `simpl` replacing `pow/bknpow`. The required evolution in $f_{col,rel}$ is systematically reduced compared to results from the `pow/bknpow` continuum model.

for the model to achieve the colour temperature demanded by the data is to increase $f_{\rm col}$ to an erroneously high value.

Using the XSPEC command `fakeit none`, we generate a suite of simulated disc spectra with the `kerrbb` model of a spinning black hole with an *RXTE* response matrix and integration time of 2000 seconds. The cases considered are a Schwarzschild black hole ($a_* = 0$, $\eta = 0.057$) and maximal Kerr black hole ($a_* = 0.998$, $\eta = 0.30$) (Thorne, 1974), each having mass 7 $M_\odot$ located at a distance of 8 kpc with a disc inclination of 30°. The inner disc torque is set to zero and the effects of both self-irradiation and limb-darkening on the disc spectrum are switched on. We pair mass accretion rates with colour correction factors that are reasonably representative of the spectral state corresponding to each $\dot{M}$ that we select. For the $a_* = 0$ black hole, we simulate disc spectra for $\dot{M} = 0.05\ \dot{M}_{\rm Edd}$ with $f_{\rm col} = 1.4$, attempting to mimic a HSS/SIS accretion disc; and $\dot{M} = 0.005\ \dot{M}_{\rm Edd}$ with $f_{\rm col} = 3$, which is more representative of a HIS/LHS observation. Similarly, for the $a_* = 0.998$ black hole, we choose $\dot{M} = 0.01\ \dot{M}_{\rm Edd}$ with $f_{\rm col} = 1.4$ and $\dot{M} = 0.001\ \dot{M}_{\rm Edd}$ with $f_{\rm col} = 3$. Extending $\dot{M}$ beyond these ranges for a fixed $f_{\rm col}$ resulted in either simulated data with unconstrained uncertainties or unacceptable fits (i.e., $\chi^2_\nu \gg 1$) using the procedure described below.

Each spectrum is fit over the energy range 2.8-10 keV using the `diskpn` model with $R_{\rm in}$ fixed at 6 $R_{\rm g}$. The best-fit colour correction factor is computed from the normalisation using Equation 2.6. Table 2.2 presents the results of this exercise. In general, the psuedo-Newtonian model, `diskpn`, reliably recovers the true $f_{\rm col}$ value for a non-spinning black hole, but requires a factor of ~ 1.9 increase in $f_{\rm col}$ for a maximally spinning black hole. This demonstrates that the inability of Newtonian disc models to properly model $R_{\rm in}$ and $T_{\rm eff}$ for Kerr black holes can result in unphysically large $f_{\rm col}$ measurements to account for the hotter inner disc.

One may wonder if relative measurements of $f_{\rm col}$ derived from Newtonian disc models, as done in this work, are affected by the inability of these models to properly represent the hotter discs around spinning black holes. A colour correction factor evolving in a HSS $\rightarrow$ LHS transition from $f_{\rm col} = 1.4 \rightarrow 3$ corresponds to a factor of 2.1 increase in $f_{\rm col}$. Inspection of Table 2.2 indicates that the `diskpn` model requires a factor of ~ 2.1 increase in $f_{\rm col}$ for an order of magnitude decrease in $\dot{M}$ for both the Schwarzschild and maximal Kerr black holes. This result is fully consistent with the 'true' $f_{\rm col}$ evolution and shows that relative measurements of $f_{\rm col}$

a_*	$\dot{M}$ $(\dot{M}_{\mathrm{Edd}})$	$T_{\mathrm{col,max}}$ (keV)	K_{pn}	$f_{\mathrm{col,true}}$	f_{col}	χ^2_ν
0	0.05	0.416(2)	0.177(8)	1.4	1.39(2)	1.35
0	0.005	0.493(5)	0.0098(8)	3.0	2.87(6)	1.26
0.998	0.01	0.455(5)	0.015(2)	1.4	2.58(9)	0.87
0.998	0.001	0.56(1)	0.0006(1)	3.0	5.8(2)	0.71

Table 2.2: Results from fitting simulated spectra generated from the `kerrbb` model of a Kerr black hole with the pseudo-Newtonian model, `diskpn`, where the inner disc radius was set to 6 R_{g}. The first two columns are the black hole spin and mass accretion rate in Eddington units used to generate the simulated disc spectra. Proceeding from *left* to *right*, the columns are the best-fit maximum disc colour temperature, best-fit disc normalisation, colour correction factor used to generate the disc spectrum, colour correction factor recovered from the best-fit normalisation, and reduced χ^2. All models had 15 degrees of freedom. Uncertainties on the last significant digit are given in parentheses and correspond to the 90% level.

made with Newtonian disc models are reliable, even when the black hole under consideration is maximally spinning.

2.5.5 Disc Temperature and Luminosity

The luminosity of a geometrically thin, optically thick disc is theoretically expected to obey a relation of the form $L_{\mathrm{disc}} = \sigma A T_{\mathrm{eff}}^4$, where A is the radiating surface area. The disc luminosity depends on both A, which scales as R_{in}^2, and effective temperature, which depends on f_{col}. The purpose of this section is to explore the $L_{\mathrm{disc}} - R_{\mathrm{in}}^2 T_{\mathrm{eff}}^4$ relation, particularly extended to low luminosities (i.e., the HIS and LHS), and the effect of introducing the possibility of a variable colour correction factor.

For the `ezdiskbb` disc model of a Newtonian disc with a zero-torque inner boundary condition, Zimmerman et al. (2005) finds the disc luminosity is given by,

$$L_{\mathrm{disc}} = 73.9\sigma \left(\frac{T_{\mathrm{col,max}}}{f_{\mathrm{col}}} \right)^4 R_{\mathrm{in}}^2. \tag{2.9}$$

Observationally, we measure an unabsorbed disc flux,

$$F_{\mathrm{disc}} = \frac{L_{\mathrm{disc}}}{4\pi D^2}. \tag{2.10}$$

In practice, F_{disc} is obtained by operating the `XSPEC` `cflux` command on the disc component with the normalisation frozen to its best-fit value. Unabsorbed disc fluxes and unabsorbed total model fluxes, F_{total}, are calculated over 0.1-10 keV and 0.1-100 keV, respectively. Figure 2.11 shows the relation between unabsorbed
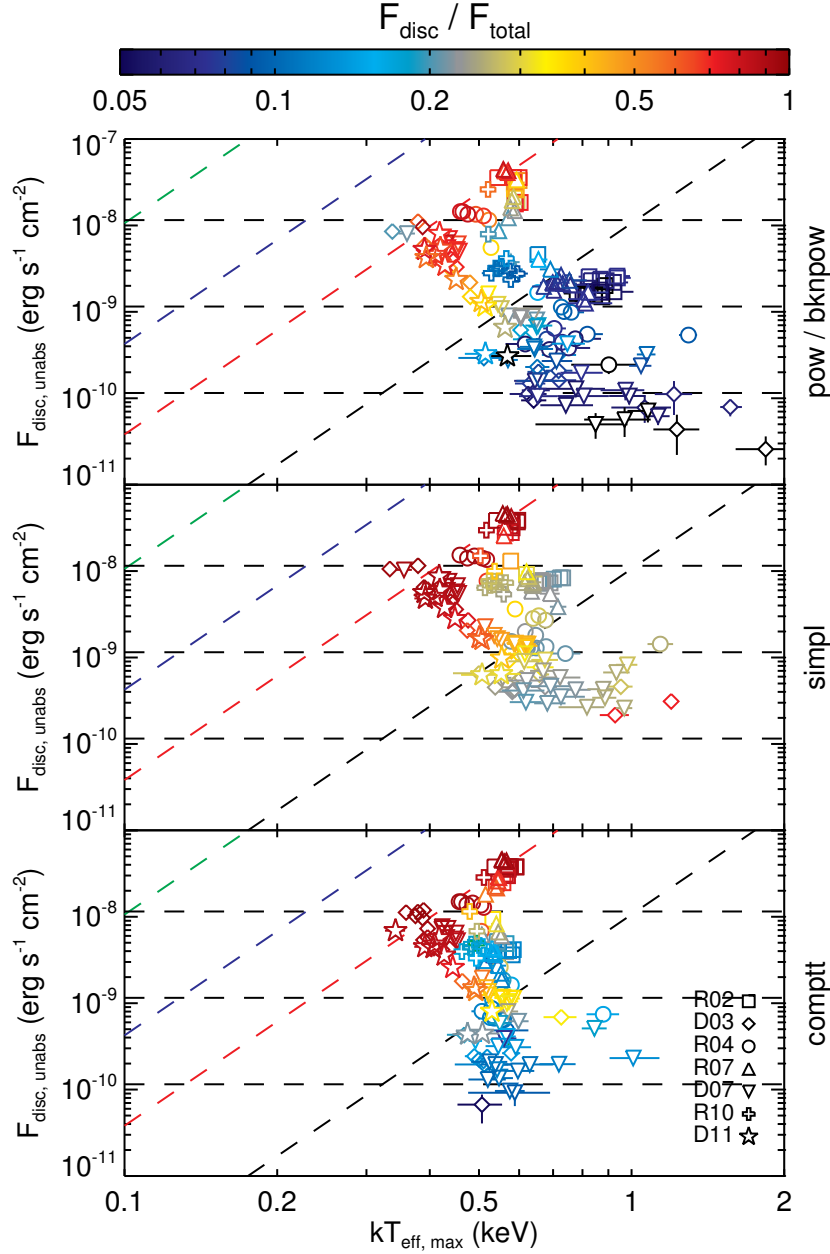
Figure 2.11: Unabsorbed disc flux (0.1-10 keV) vs. maximum disc effective temperature ($T_{\mathrm{eff,max}} = T_{\mathrm{col,max}}/f_{\mathrm{col}}$) for all transitions, where $T_{\mathrm{col,max}}$ is measured using `ezdiskbb` to model the disc component and a constant $f_{\mathrm{col}} = 1.4$ is assumed. Comptonisation is modelled using the `XSPEC` models `pow/bknpow` (*top panel*), `simpl` (*center panel*), and `comptt` (*bottom panel*). From *top* to *bottom*, the *horizontal dashed lines* indicate $L_{\mathrm{disc}}/L_{\mathrm{Edd}} = 10^{-1}, 10^{-2}, 10^{-3}$, where L_{disc} was converted to F_{disc} using Equation 2.10 with $D = 8$ kpc. The Eddington luminosity is given by, $L_{\mathrm{Edd}} = 4\pi GMm_{\mathrm{p}}c/\sigma_{\mathrm{T}}$, where m_{p} is the proton mass, σ_T is the Thomson cross section, and we adopt $M = 7\,\mathrm{M}_\odot$. Uncertainties in M and D are not incorporated because the shape of the $F_{\mathrm{disc}} - T_{\mathrm{eff,max}}$ relation is insensitive to these intrinsic parameters. The *diagonal dashed lines* represent the expected $F_{\mathrm{disc}} \propto T_{\mathrm{eff,max}}^4$ relation for an optically thick, geometrically thin, zero-torque disc (Equation 2.9) assuming the aforementioned intrinsic parameters and constant $R_{\mathrm{in}} = 1\,R_{\mathrm{g}}$ (*black line*), 6 R_{g} (*red line*), 20 R_{g} (*blue line*), and 100 R_{g} (*green line*). Glyph colours denote the disc fraction of each observation. The key in the *bottom right* identifies the glyph associated with each transition ID. When a constant f_{col} is assumed, departure from the $L_{\mathrm{disc}} - T_{\mathrm{eff}}^4$ is evident for low-luminosity discs characteristic of the HIS and LHS.

disc flux and maximum effective temperature for each of the three Comptonisation models `pow/bknpow`, `comptt`, and `simpl`. $T_{\mathrm{col,max}}$ is measured from fits to all observations with the disc component modelled by `ezdiskbb` and $T_{\mathrm{eff,max}} = T_{\mathrm{col,max}}/f_{\mathrm{col}}$, assuming a constant $f_{\mathrm{col}} = 1.4$. The disc fractions, defined by Equation 2.7, are given by the glyph colours. We note that this work includes observations with very low disc fractions compared to previous investigations of the luminosity-temperature relation for BHBs, which tend to be restricted to the HSS where $DF \gtrsim 0.8$ (e.g., Gierliński & Done, 2004).

If one assumes a constant disc geometry, the disc emitting area is unchanging and we expect to recover the scaling, $F_{\mathrm{disc}} \propto T_{\mathrm{eff}}^4$, denoted by the diagonal lines in Figure 2.11 for various choices of R_{in} and f_{col}. While the theoretical relation is achieved for disc luminosities, $L_{\mathrm{disc}} \gtrsim 0.05 L_{\mathrm{Edd}}$, clear departure is evident below this threshold where the BHB is categorized in the HIS or LHS.

The `diskbb` and `ezdiskbb` models are purely Newtonian and correction factors accounting for various general relativistic and viewing angle effects (Cunningham, 1975; Zhang et al., 1997) have been applied in previous observational studies of the luminosity-temperature relation for BHBs (e.g., Gierliński & Done, 2004; Dunn et al., 2011). Selecting the proper correction factors requires knowledge of the disc inclination and spin, for which there is considerable debate for GX 339–4 (see §2.3.1). Fortunately, the correction factors are independent of flux and temperature; therefore, we can safely neglect incorporating these modifications without altering the shape of the $F_{\mathrm{disc}} - T_{\mathrm{eff}}$ diagram, irrespective of the accuracy of the F_{disc} and T_{eff} values.

The effective temperature plotted in Figure 2.11 is calculated under the assumption of a constant colour correction factor, which will subsequently be relaxed. Deriving relative measurements for the colour correction factor according to Equation 2.8 and as described in §2.5.3.2, Figure 2.12 shows the relationship between f_{col} and the maximum colour temperature, which is a parameter in the disc models. Supposing that the inner disc remains fixed at $R_{\mathrm{in}} = 6\ R_{\mathrm{g}}$, which is the implicit assumption behind all of our $f_{\mathrm{col,rel}}$ measurements, the colour correction factor increases with colour temperature approximately linearly. The majority of observations yield colour corrections that fall within the range $1.4 \lesssim f_{\mathrm{col,rel}} \lesssim 5$, in agreement with Reynolds & Miller (2013). Notably, the models `simpl` and `comptt`, which are rooted in physical considerations of Comptonisation, constrict the range of $f_{\mathrm{col,rel}}$ as compared to the phenomenological and widely used `powerlaw` and `bknpower` models. Particularly for best-fit colour temperatures, $T_{\mathrm{col,max}} \gtrsim 1$ keV,
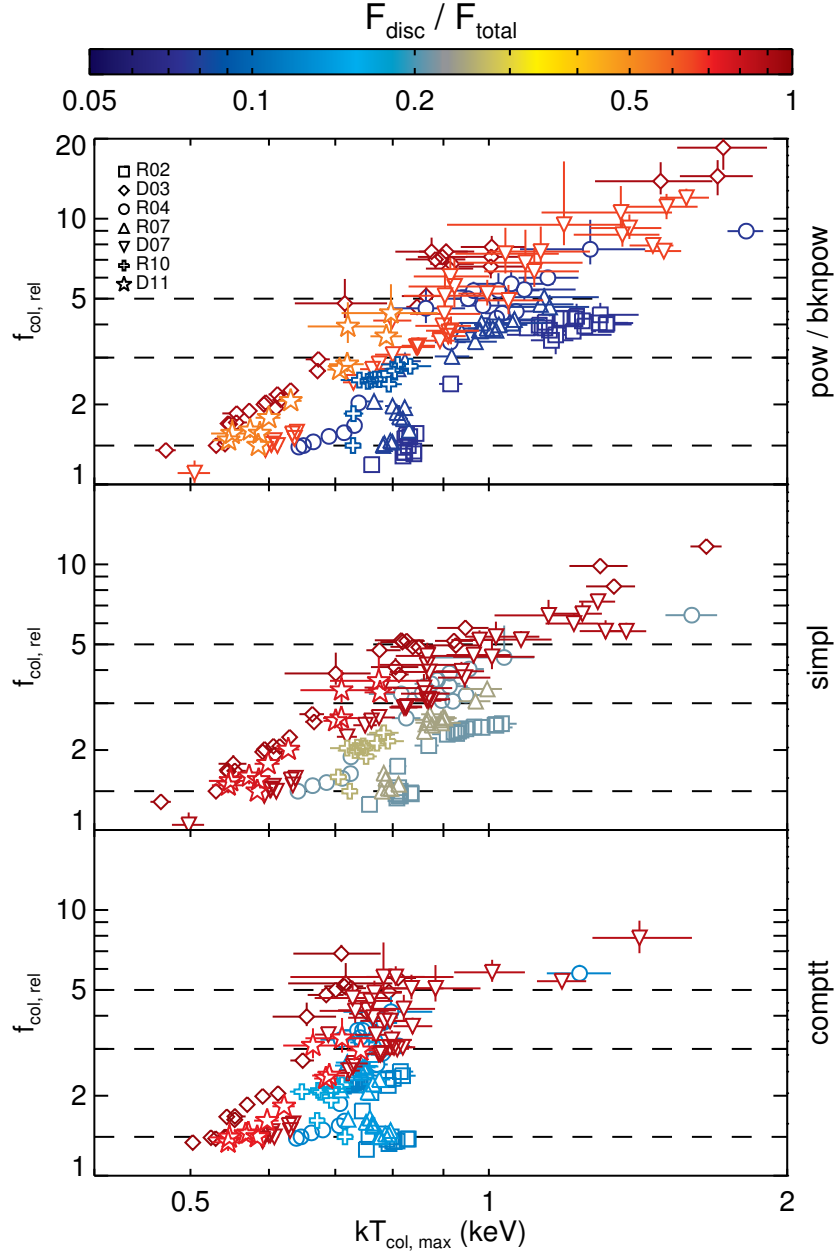
Figure 2.12: Relative measurements of the colour correction factor shown against the maximum colour temperature of the disc from best-fits using the `XSPEC` Comptonisation models `pow/bknpow` (*top panel*), `simpl` (*center panel*), and `comptt` (*bottom panel*). Results from all transitions are shown together, with the disc fraction given by the glyph colour. The key in the *upper left* portion of the *top panel* identifies the glyph associated with each transition ID. $T_{col,max}$ is obtained from the best-fit `ezdiskbb` parameter and $f_{col,rel}$ is computed using the same procedure as in Figure 2.8 (see text). Horizontal *dashed lines* mark $f_{col,rel} = 1.4, 3, 5$. For a disc inner radius fixed at $6R_g$, the majority of observations yield $1.4 \lesssim f_{col,rel} \lesssim 5$ and show a roughly linear relation between f_{col} and T_{col}.
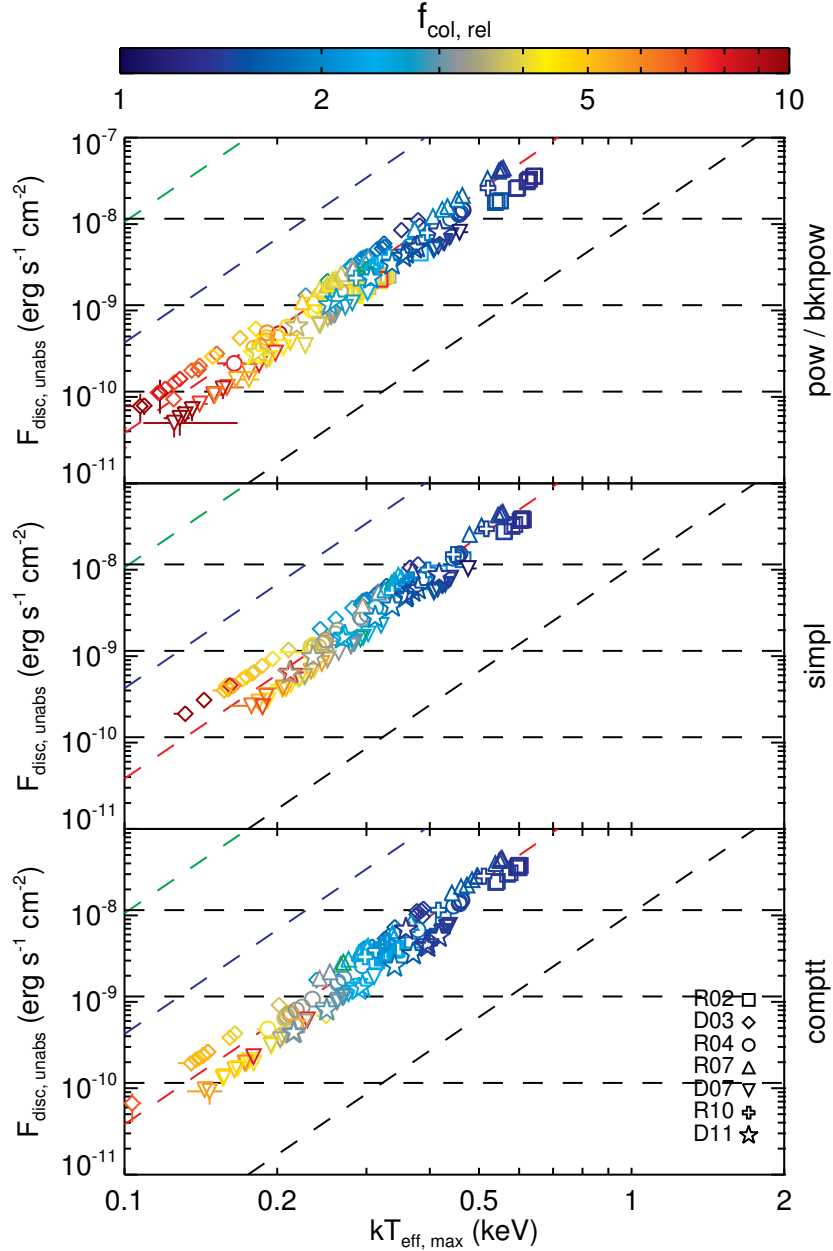
Figure 2.13: Unabsorbed disc flux (0.1-10 keV) vs. maximum disc effective temperature for all transitions, where $T_{\mathrm{col,max}}$ is measured using `ezdiskbb`. Relaxing the assumption of a constant f_{col}, all observations were re-fitted with `ezdiskbb` replaced by `diskpn` with $R_{\mathrm{in}} = 6\ R_{\mathrm{g}}$. Relative values of f_{col} were computed from the best-fit `diskpn` normalisation, using the same procedure as in Figure 2.8. The abscissa shows $T_{\mathrm{eff,max}} = T_{\mathrm{col,max}}/f_{\mathrm{col,rel}}$. Glyph colours correspond to the $f_{\mathrm{col,rel}}$ of each observation. The various lines are the same as those in Figure 2.11. The $L_{\mathrm{disc}} \propto T_{\mathrm{eff}}^4$ relation is recovered for disc luminosities, $L_{\mathrm{disc}} \gtrsim 10^{-3}\ L_{\mathrm{Edd}}$, when f_{col} is considered to be variable.
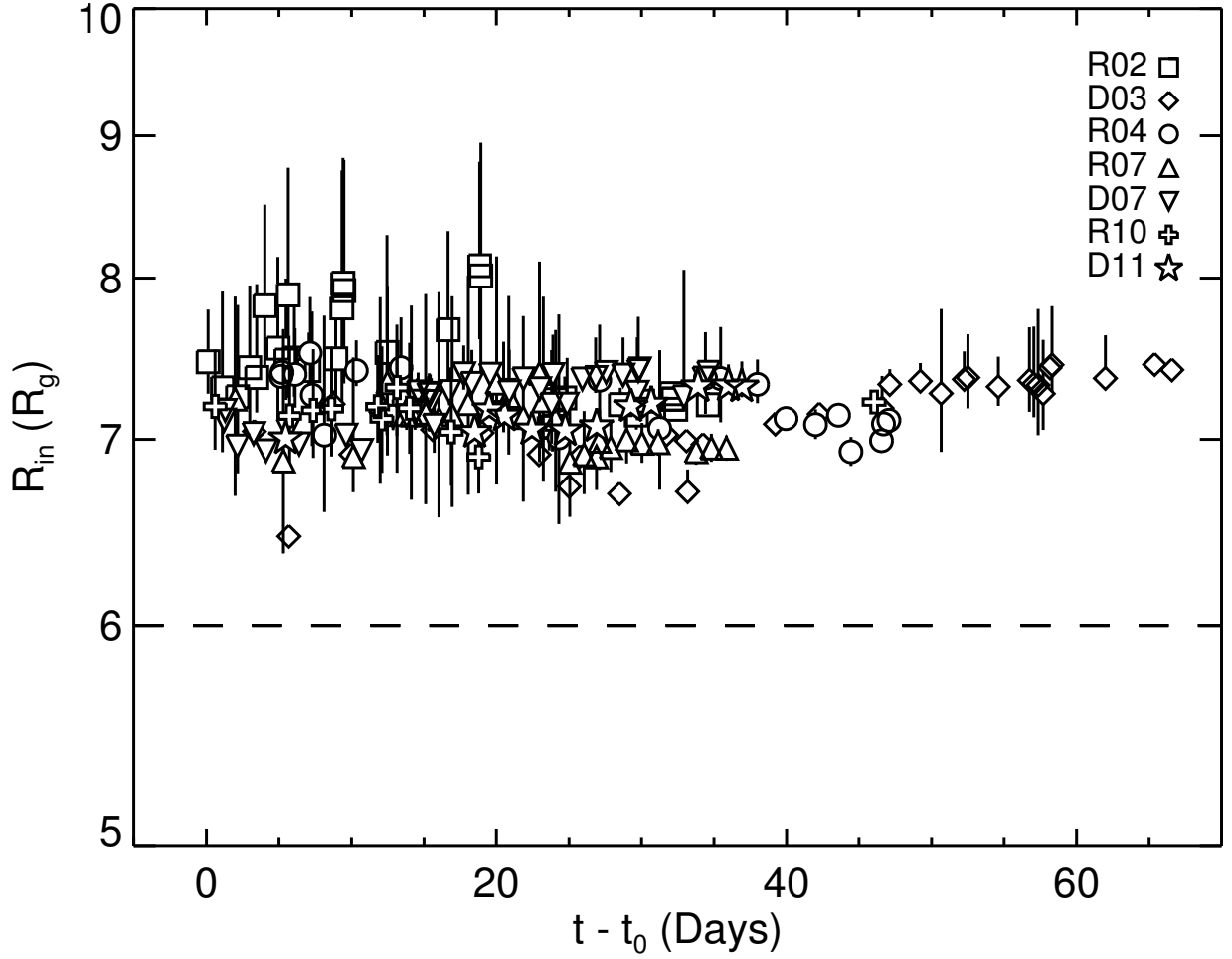
Figure 2.14: Time evolution, as measured from the start of the transition listed in Table 2.1, of the inner disc radius computed from the `ezdiskbb` and `diskpn` normalisations (Equation 2.11) when R_{in} was fixed in the `diskpn` model at 6 R_g. The *dashed line* marks $R_{in} = 6$ R_g. The key in the *upper right* corner denotes the glyphs corresponding to each transition. The constancy of R_{in} implies that relative measurements made from combining results from fits made with `ezdiskbb` and `diskpn` are unaffected by the minor differences between those disc models.

the `powerlaw` and `bknpower` continuum models may return erroneously low values for the disc normalisation.

We attempt to explore whether the luminosity-temperature relation can be extended to lower luminosities characteristic of the HIS and LHS by allowing for a variable f_{col}. Figure 2.13 shows the $F_{disc} - T_{eff}$ diagram with the only difference to Figure 2.11 being that the effective temperature is now calculated by, $T_{eff,max} = T_{col,max}/f_{col,rel}$. In other words, Figure 2.11 is recomputed using the $f_{col,rel}$ values of Figure 2.12 in place of the constant $f_{col} = 1.4$. Accepting the dynamic range in f_{col} suggested by Figure 2.12, $F_{disc} \propto T_{eff}^4$ is recovered for disc luminosities, $L_{disc} \gtrsim 10^{-3} L_{Edd}$. Furthermore, the relation falls neatly on the expected track corresponding to the emitting surface area remaining constant with the inner disc located at $R_{in} = 6 R_g$.

Caution must be exercised when combining different disc models. The relative measurements $f_{col,rel}$ used to recompute $T_{eff,max}$ in Figure 2.13 called upon `diskpn` and `ezdiskbb` separately to model the disc component in order to take advantage of the strengths of each model for our purposes. One may reasonably ask if these two disc models, which both adopt the zero-torque inner boundary condition, are consistent. The significant difference between the models is that `diskpn` approximates the general relativistic effects on the accretion disc with a pseudo-Newtonian potential, while `ezdiskbb` is strictly Newtonian; therefore, discrepancies between the two may materialize in the spectral fits. Combining the normalisations from each disc model, given by Equations 2.5 and 2.6, the inner disc radius is obtained,

$$\frac{R_{in}}{R_g} = 0.0677 \left(\frac{K_{ez}}{K_{pn}}\right)^{1/2}. \tag{2.11}$$

Since R_{in} is a separate parameter in `diskpn` instead of being incorporated into the normalisation, we expect to exactly recover this value for R_{in} from Equation 2.11 if `diskpn` and `ezdiskbb` are identical. Figure 2.14 shows R_{in} computed from Equation 2.11 for fits to all observations where $R_{in} = 6 R_g$ in the `diskpn` fits. Values of R_{in} falling on 6 R_g would indicate that the inner radius enforced in the `diskpn` fits was exactly recovered in the independent `ezdiskbb` fits, while deviations from 6 R_g arise from differences in the `ezdiskbb` and `diskpn` models. Although the inner disc radius value of 6 R_g set in `diskpn` is not exactly recovered, R_{in} remains constant throughout each transition at $\sim 7.5 R_g$, merely a systematic offset that does not affect the interpretation of Figure 2.13.

2.5.6   Low Frequency Quasi-Periodic Oscillations

LFQPOs are observed in the temporal power spectra of BHBs and remain a long-standing puzzle of active observational and theoretical interest. Explanations for the origin of LFQPOs appeal to an exhaustive array of production models including trapped waves (Kato, 1990), discoseismic modes (Nowak & Wagoner, 1991, 1992, 1993; Reynolds & Miller, 2009), Lense-Thirring precession (Ipser, 1996; Stella et al., 1999; Ingram et al., 2009), accretion-ejection instability (Tagger & Pellat, 1999; Varnière et al., 2002; Varnière & Tagger, 2002), and a truncated disc LHS geometry (Giannios & Spruit, 2004). Recent simulations of global, magnetised accretion discs suggest that LFQPOs have an origin in the corona rather than the disc directly (O'Neill et al., 2011). While the origin of LFQPOs is not firmly established, the details of the disc geometry may provide clues to their nature.

X-ray spectra alone cannot distinguish between a truncated disc and changing disc structure/coronal activity as the underlying accretion geometry. Given a plausible production mechanism, LFQPOs have the potential to be diagnostics of the inner accretion flow. In the LFQPO excitation model envisioned by Giannios & Spruit (2004), quasi-spherical oscillations of the RIAF interior to a truncated disc in the LHS produce modes with frequencies near the Keplerian frequency of the inner disc,

$$\frac{R_{\mathrm{Kep}}}{R_{\mathrm{g}}} = \left(\frac{GM}{c^3} 2\pi \nu_{\mathrm{QPO}} \right)^{-2/3} , \tag{2.12}$$

where ν_{QPO} is the frequency of the LFQPO. In this framework, Giannios & Spruit (2004) require that the RIAF, and hence the recessed inner disc, extend out to $R_{\mathrm{in}} \sim 100\ R_{\mathrm{g}}$.

LFQPOs observed in GX 339–4 and their frequency migration over the course of the state transitions studied here has received considerable attention in the literature. The frequency of LFQPOs is observed to decrease (increase) over a decay (rise) transition with a typical range $0.1\ \mathrm{Hz} \lesssim \nu_{\mathrm{QPO}} \lesssim 10\ \mathrm{Hz}$, implying that accretion rate and QPO frequency are intricately linked. In an attempt to test the truncated disc LFQPO production model, which predicts that $R_{\mathrm{Kep}} \simeq R_{\mathrm{in}} \gtrsim 100\ R_{\mathrm{g}}$ in the LHS, we collect measured ν_{QPO} values for all of the GX 339–4 state transitions considered (Belloni et al., 2005; Shaposhnikov & Titarchuk, 2009; Stiele et al., 2011; Motta et al., 2011; Nandi et al., 2012). Given the uncertainty in black hole mass for GX 339–4, we seek relative measurements of R_{Kep} normalized to the ISCO for a non-spinning black hole in the
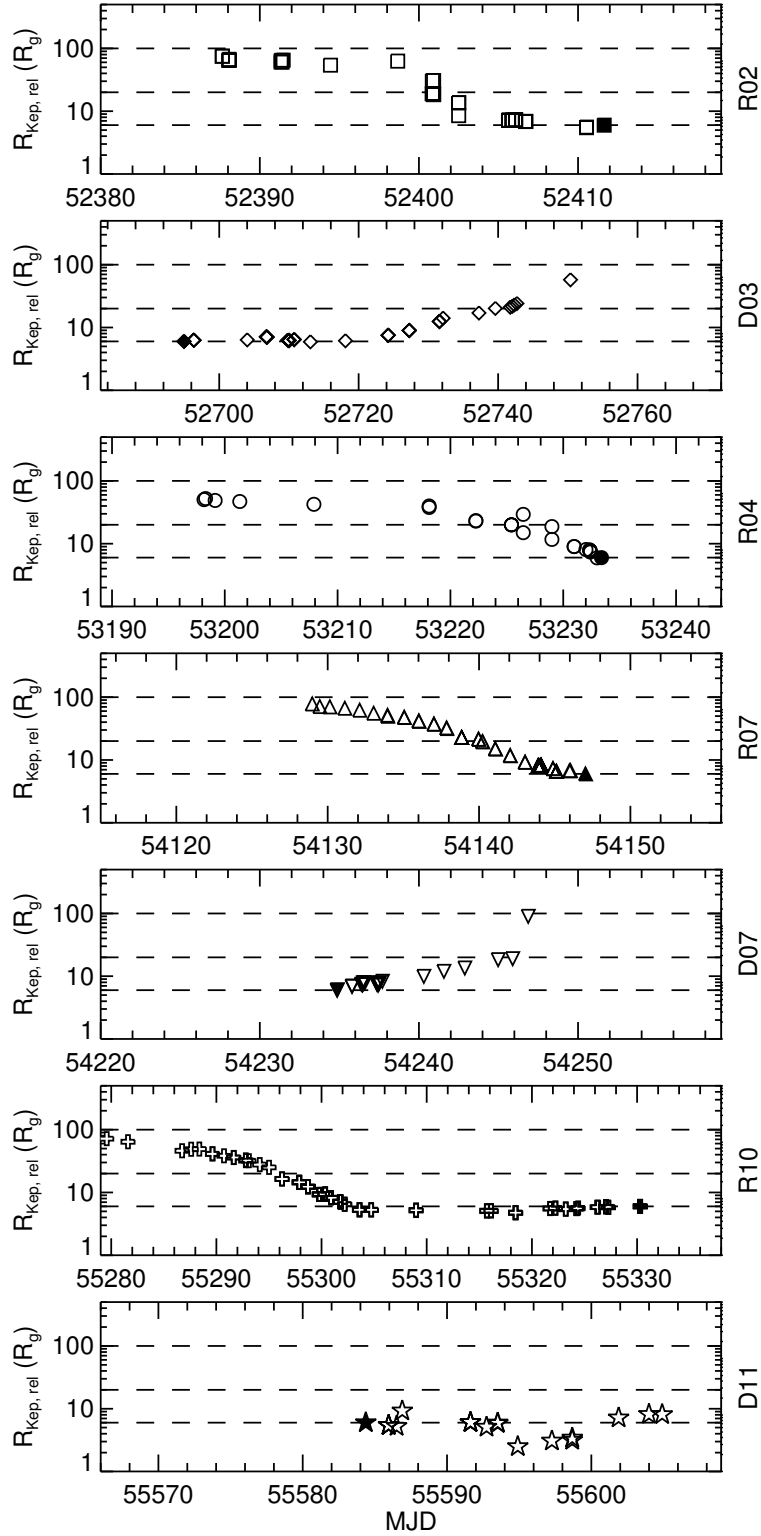
Figure 2.15: Relative measurements of the evolution of $R_{\mathrm{Kep,rel}}$ for each transition (see text for definition) derived from LFQPO frequency evolution. The *dashed lines* mark $R_{\mathrm{in}} = 6, 20, 100\ R_{\mathrm{g}}$. The $R_{\mathrm{Kep,rel}}$ measurements for each transition were made relative to the filled glyphs and normalized to $R_{\mathrm{in}} = 6\ R_{\mathrm{g}}$, which is appropriate for a Schwarzschild black hole in the HSS.

HSS,

$$R_{\mathrm{Kep,rel}} \equiv 6R_{\mathrm{g}} \left(\frac{R_{\mathrm{Kep}}}{R_{\mathrm{Kep,HSS}}} \right), \tag{2.13}$$

where $R_{\mathrm{Kep,HSS}}$ is the Keplerian radius computed for a given transition from the ν_{QPO} of the observation nearest to the HSS in time using Equation 2.12, without specifying M. Supposing that R_{Kep} is associated with R_{in}, Figure 2.15 shows the evolution in disc inner radius implied by the observed migrating LFQPOs for each transition. With the exception of transition D11, the Keplerian frequencies implied by the LFQPOs reach out to $\sim 50 - 100$ R_{g} in the LHS, which is broadly consistent with the degree of recession required by the RIAF/truncated disc LFQPO excitation model. If LFQPOs are associated with the inner disc in a similar manner to that described by Giannios & Spruit (2004), then a truncated disc geometry may be a plausible description for state transitions. However, the spectral fits in this work suggest that R_{in} does not truncate to such extreme disc locations, which would demand reconciling.

2.6   Discussion

We have shown that a moderately increasing f_{col} as the disc fraction decreases can adequately and consistently describe the spectral evolution of the accretion disc in GX 339–4 over multiple state transitions. The purpose of this work is *not* to debunk a truncated disc geometry as a viable model for the LHS of BHBs. We recognize that the observations in this work interpreted with simplistic disc models are unable to distinguish between changes in R_{in} and/or f_{col}. Rather, we demonstrate that reasonable variations in f_{col} provide an alternative explanation to disc truncation for accretion disc evolution. Motivated by this result and supposing that f_{col} is variable, we consider the impacts that this would have on the interpretation of BHB observations, ultraluminous X-ray sources, and models of the accretion flow across spectral states. We then discuss the physically expected range of attainable values for f_{col} and conclude the discussion with a cautionary commentary on the widely used disc models.

2.6.1   Implications of a Variable Colour Correction

Imposing an unchanging inner accretion disc radius located at the ISCO of a Schwarzschild black hole, we measured the relative changes in f_{col} necessary to adequately fit *RXTE* spectra of GX 339–4 over seven

state transitions. Arbitrarily selecting a normalisation of $f_{\mathrm{col}} = 1.4$ for the HSS and denoting measurements of f_{col} relative to this value by $f_{\mathrm{col,rel}}$ (see Equation 2.8), we tracked the evolution of $f_{\mathrm{col,rel}}$ for each transition (see Figures 2.8-2.10). Transitions R02, R07, R10, and D11 require colour corrections conforming to the range $1.4 \lesssim f_{\mathrm{col,rel}} \lesssim 3$, while transition R04 demands the range be extended to $1.4 \lesssim f_{\mathrm{col,rel}} \lesssim 5$. These ranges in f_{col} evolution, which can account for the majority of the transitions, correspond to a factor of $\sim 2.0 - 3.5$ increase in f_{col} for a HSS $\rightarrow$ LHS transition. Transitions D03 and D07 require more extreme evolution in $f_{\mathrm{col,rel}}$, with values as high as $f_{\mathrm{col,rel}} \sim 10$. Our main finding is to demonstrate that an evolving f_{col} provides an alternative and adequate description of the changing disc spectrum during a state transition, which is perhaps a more attractive scenario to imagine than the sudden evacuation or replenishment of the inner accretion flow.

2.6.1.1 Recovering $L - T_{\mathrm{eff}}^4$ at Low Luminosities

A blackbody source of constant emitting area is expected to obey the $L - T_{\mathrm{eff}}^4$ scaling, which relates the source luminosity to its effective temperature. Accretion flows corresponding to the HSS of BHBs, where the thermal accretion disc dominates the total flux and the inner disc location does not deviate from the ISCO, nicely follow this expected relation (e.g., Gierliński & Done, 2004); however, deviations arise in the HIS and LHS (e.g., Dunn et al., 2011). This work encompasses the disc luminosity range, $10^{-3} \lesssim L_{\mathrm{disc}}/L_{\mathrm{Edd}} \lesssim 0.5$, finding that a f_{col} that evolves with spectral state can reproduce the theoretical $L_{\mathrm{disc}} - T_{\mathrm{eff}}^4$ across all spectral states. Studying the disc-dominated states (i.e., $DF \gtrsim 0.8$) of many BHBs over a typical luminosity range, $0.01 \lesssim L_{\mathrm{disc}}/L_{\mathrm{Edd}} \lesssim 0.5$, Gierliński & Done (2004) found that the $L_{\mathrm{disc}} - T_{\mathrm{eff}}^4$ relation holds for a *constant* f_{col}. We observe similar and consistent behaviour for GX 339–4 in the HSS. As the disc fraction drops and the source enters the HIS or LHS, significant departures from $L_{\mathrm{disc}} - T_{\mathrm{eff}}^4$ are apparent in Figure 2.11, in agreement with Dunn et al. (2011). These 'spurs' on the luminosity-temperature diagram can be interpreted as either a decrease in the inner disc radius, and hence the emitting area, or the result of neglecting to account for a decrease in $T_{\mathrm{eff}} = T_{\mathrm{col}}/f_{\mathrm{col}}$ caused by an increased f_{col} in the LHS. Of course, some combination of these two effects is possible as well. Dunn et al. (2011) measured the incremental degree of change in f_{col} from a canonical HSS value that was required to return the spurs to the expected $L_{\mathrm{disc}} \propto T_{\mathrm{eff}}^4$ law for a constant

emitting area (see their Figure A.1). For GX 339–4, they found that fairly modest changes in $f_{\rm col}$, consistent with the relative changes we determined, could restore the theoretical relation; however, they argue that the most severe departures from $L_{\rm disc} - T_{\rm eff}^4$, which occur for the lowest disc fractions, are not likely the result of a variable $f_{\rm col}$. Here, we suggest that the physically realizable range of $f_{\rm col}$ is perhaps not as narrow as commonly assumed (see §2.6.2) and that a thin disc geometry with a fixed inner radius and evolving $f_{\rm col}$ is a viable phenomenological model for BHB state transitions.

We expand on the work of Dunn et al. (2011) by breaking the observations of a BHB into individual transitions, exploiting relative measurements, and exploring empirical and physical Comptonisation models. Comparing Figures 2.8-2.10, we find that employing physically motivated Comptonisation models that avoid the 'flux stealing' phenomenon from the disc component require less severe $f_{\rm col}$ evolution for any given transition. Inspection of the panels of Figure 2.13 shows that the $L_{\rm disc} - T_{\rm eff}^4$ relation is recovered when a changing $f_{\rm col}$ is incorporated, regardless of the choice of Comptonisation model. Relative measurements of $f_{\rm col}$ broken down by transition in Figures 2.8-2.10 hint at an underlying difference in the details of the accretion flow depending on whether the source is in the rise or decay stage of outburst. Qualitatively, the decay transitions demand more extreme and perhaps physically unattainable $f_{\rm col}$ evolution, while the rise transitions fit more comfortably into the idea of a moderately variable $f_{\rm col}$. Given that decoupling the true behaviour of the inner disc from that of the colour correction factor is impossible with simplistic disc models and *RXTE* data, we leave the possibility of different accretion scenarios between rise and decay transitions as pure speculation.

2.6.1.2   The Ultraluminous State

Adopting a variable colour correction factor parameterises the various physical processes in BHB accretion into a single factor. This work suggests that moderate changes in $f_{\rm col}$ may conceivably account for the wide range of spectral states observed when a BHB undergoes a state transition. Recently, a new spectral class, dubbed the ultraluminous state (ULS), has been postulated for the class of ultraluminous X-ray sources (ULXs) (Gladstone et al., 2009). Here, we explore whether the ULS, which has never been observed in a confirmed BHB, is consistent with the interpretation of spectral states arising from physical

processes that are observationally manifested as an evolving colour correction factor.

ULXs are X-ray sources that exceed the Eddington luminosity of stellar mass black holes ($L_{\rm X} \gtrsim 10^{39}$ erg s^{-1}), but are not spatially coincident with galactic nuclei; therefore, ULXs are distinct from AGNs. Two possible explanations for ULXs are: (1) intermediate mass black holes (IMBHs; $M \sim 10^2 - 10^4$ $M_\odot$) accreting at sub-Eddington rates, but the production rate of binaries composed of an IMBH and donor star is likely too low to account for the number of observed ULXs (Madhusudhan et al., 2006); and/or (2) stellar mass black holes accreting at super-Eddington rates, which requires a mechanism for achieving super-Eddington accretion, such as beaming/viewing effects of outflows (e.g., King et al., 2001; Begelman et al., 2006) or disc inhomogeneities (Begelman, 2001, 2002, 2006).

The spectral characteristics of ULXs were studied by Gladstone et al. (2009), leading them to propose that ULXs are super-Eddington accreting stellar mass black holes with ubiquitous spectral features. These commonalities suggest that ULXs are indeed a spectral class of BHBs, dubbed the ultraluminous state (ULS); however, this accretion state does not appear to arise in the well-studied Galactic BHBs. The ULS is characterised by both a broadened, hardened thermal disc component and a break in the power-law component at lower energies ($\gtrsim 3$ keV) than typically observed in less luminous BHB states. The Gladstone et al. (2009) ULX sample was adequately fitted with a physically motivated disc plus Comptonising corona model, where the best-fit models called for optically thick coronae ($\tau_{\rm p} \sim 5 - 30$) and cool disc colour temperatures ($T_{\rm col,max} \sim 0.2$ keV). Physically, the broadened/hardened disc and low-energy spectral break may be attributed to a complicated inner geometry where an optically thick corona obscures and alters the energetics of the inner disc. Normally, disc temperatures this low would imply a black hole of mass $\sim 10^3$ $M_\odot$ (e.g., Kaaret et al., 2003); however, the measured disc temperature may be lowered if a significant fraction of the accretion energy is dissipated in the corona (e.g., Svensson & Zdziarski, 1994). Based on the requirement of an optically thick corona, as opposed to the $\tau_{\rm p} \sim 1$ coronae typically observed in BHBs, sub-Eddingtion accretion onto an IMBH was ruled out.

Figure 2.16 shows the coronal optical depth versus the maximum disc colour temperature for GX 339–4 determined from the best-fits to the disc plus Comptonising corona XSPEC model, `phabs`$\times$`(comptt+diskpn)`, with $R_{\rm in} = 6$ $R_{\rm g}$. Replacing the disc component with either `diskbb` or `ezdiskbb` produces essentially
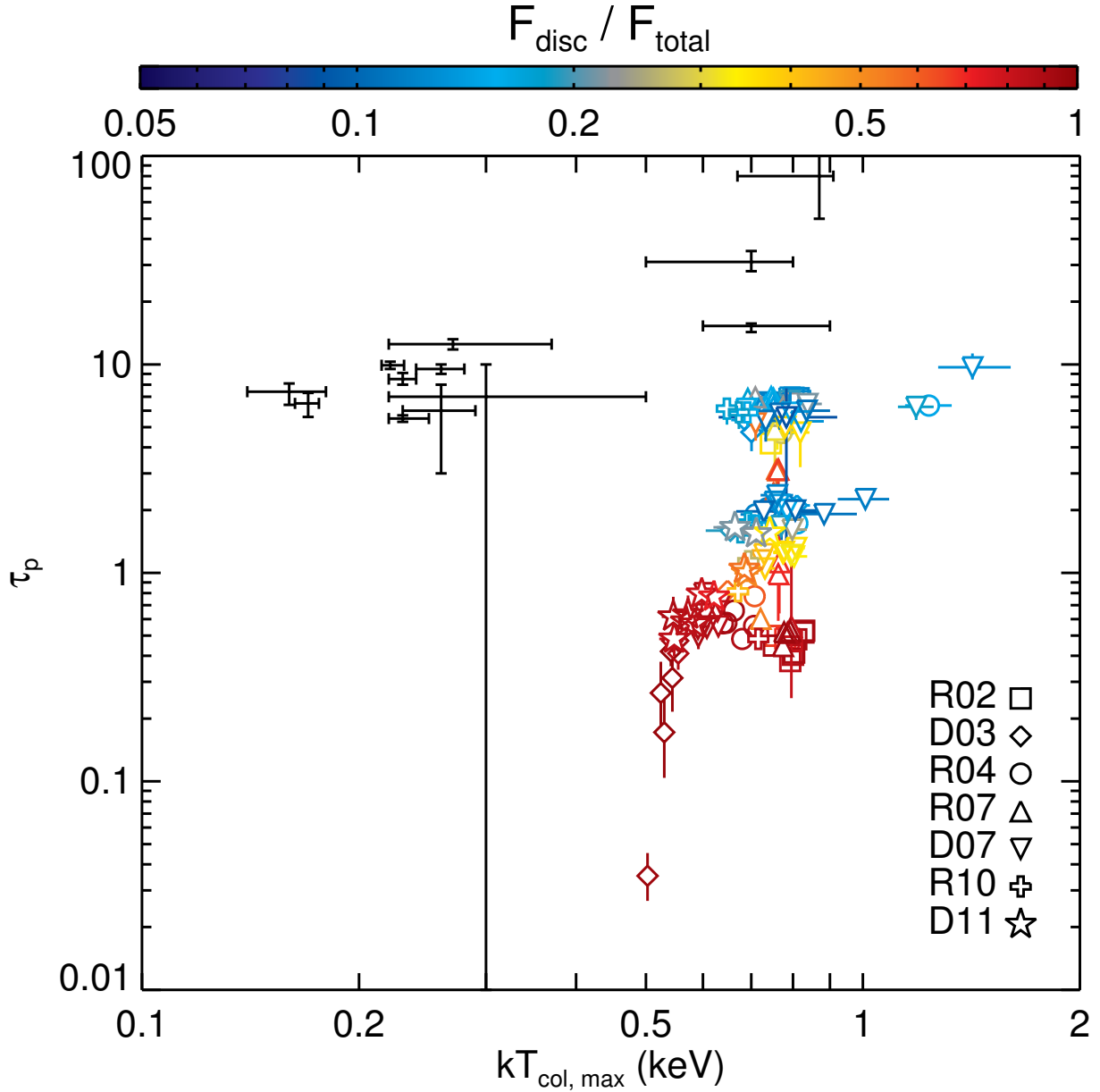
Figure 2.16: Coronal optical depth vs. maximum disc colour temperature for all transitions, where τ_p and $T_\mathrm{col,max}$ are measured using `comptt` and `diskpn` with $R_\mathrm{in} = 6\ R_\mathrm{g}$, respectively. The disc fraction is given by the glyph colour. The results from a sample of 12 ULXs (Table 8 of Gladstone et al. (2009)) are overlaid in *black crosshairs*. The HIS/LHS GX 339–4 *RXTE* data analysed in this work permit moderately optically thick coronae in the same range as found for ULXs.

indistinguishable results. For comparison, the results from Table 8 of Gladstone et al. (2009) are shown for a sample of 12 ULXs determined from fits to high-quality *XMM-Newton* data, where `diskpn` and `comptt` were also adopted as the disc and Comptonising models, respectively.[7]   When GX 339–4 is in the HIS/LHS (i.e., low disc fractions), the typical best-fit coronal optical depth falls in the range, $\tau_{\mathrm{p}} \sim 2 - 10$. The coronal optical depth of the ULX sample is described by $\tau_{\mathrm{p}} \sim 5 - 15$ ($\tau_{\mathrm{p}} \sim 10 - 100$) for discs with temperatures $T_{\mathrm{col,max}} \lesssim 0.5$ keV ($T_{\mathrm{col,max}} \gtrsim 0.5$ keV). Figure 2.16 challenges the claim that spectral fits to sub-Eddington BHBs do not permit moderately optically thick coronae.

Although the data are consistent with an optically thick corona model, here we point out a strong parameter degeneracy between the colour correction factor and the coronal optical depth. Of the three models we considered to represent Comptonisation, all of which provided equally good fits to the data, only `comptt` incorporates the coronal temperature and optical depth as physical parameters. Inspection of Figure 2.12 reveals that the `pow/bkn` and `simpl` models require higher colour correction factors than `comptt`. Particularly for the HIS/LHS observations of GX 339–4, introducing a physical corona drives f_{col} to lower values with preference for an optically thick corona (see Figure 2.12). Therefore, the data cannot distinguish between an increased colour correction factor and an optically thick corona.

In the IMBH model, ULXs are massive scaled up versions of BHBs in the LHS (i.e., IMBHs accreting at sub-Eddington rates). The IMBH model for ULXs was discarded by Gladstone et al. (2009) because the measured coronal optical depths were larger than commonly observed in BHBs. In the case of GX 339–4 in the HIS/LHS, using the same disc plus Comptonisation model, we see that the best-fit coronal optical depths lie precisely in the same moderately optically thick range as the ULX sample of Gladstone et al. (2009). Therefore, the data *do* permit optically thick coronae in the HIS/LHS of GX 339–4, but we stress that the measurement of coronal optical depth from basic disc + corona modelling cannot be made definitive due to the degeneracy between τ_{p} and f_{col}. This possibility alleviates the hesitation for supposing that ULXs are analogous to scaled up BHBs on the grounds of coronal optical depth. Allowing for a variable colour correction factor, the broadened/hardened ULX disc spectra and low measured ULX disc temperatures naturally fit into the IMBH description; therefore, introducing arguments for reducing the disc temperature

---

[7] Gladstone et al. (2009) do not specify the R_{in} value used in the `diskpn` model. Our results suggest that the coronal properties and disc temperature are largely unchanged in the spectral fits, regardless of what one chooses for R_{in}.

by dissipating accretion energy into the corona become unnecessary. An important discrepancy in coronal properties between the HIS/LHS GX 339–4 data and the ULX sample is the temperature of the corona. While the data permit $\tau_\mathrm{p} \sim 5-10$ for both the HIS/LHS and ULXs (see Figure 2.16), the associated coronal temperature for ULXs ($T_\mathrm{p} \sim 1-3$ keV) is an order of magnitude below that of GX 339–4 in the HIS/LHS ($T_\mathrm{p} \sim 10-30$ keV) (see Figure 2.17). We stress that the purpose of this section is to highlight an interesting possibility that the ULS may not be an intrinsic feature of BHBs; however, this is highly speculative and further investigations are required to shed more light on the nature of ULXs.

2.6.1.3 The Role of f_col in State Transitions

A triggering mechanism for state transitions is not yet well understood. Schnittman et al. (2013) demonstrated that all of the spectral states of BHBs could be recovered by varying only the mass accretion rate, $\dot{M}$, (i.e., effectively changing the location of the disc photosphere, or the disc/corona boundary) in the magnetohydrodynamic general relativistic global disc simulation of Noble et al. (2010). The disc was assumed to produce a diluted blackbody spectrum at the photosphere with a constant $f_\mathrm{col} = 1.8$, which could be further altered (e.g., broadened/hardened) by bremsstrahlung, synchrotron, and inverse Compton processes in the corona. The emergent spectrum was computed with a post-processing radiative transfer technique for choices of $\dot{M}$ representative of the observed BHB states. In this simulation, the inner accretion disc remained extended down toward the ISCO. Only details of the coronal physics for a given location of the disc photosphere (i.e., for a given value of $\dot{M}$) provided alterations to a diluted blackbody spectrum and all BHB spectral states were reproduced within this framework. This result emphasises the importance of coronal physics in modifying the underlying disc spectrum, suggesting that perhaps f_col is a variable function of $\dot{M}$ and can be dependent on processes external to the disc.

A changing mass accretion rate plays a key role in state transitions, but is likely not the whole picture, nor is it clear what mechanism drives changes in $\dot{M}$. For an inner disc remaining at the ISCO during a state transition, a large change in $\dot{M}$ is implied. In the HSS, the inner portions of the disc are expected to be radiation pressure-dominated, where instabilities may lead to an inhomogeneous disc structure and a low $f_\mathrm{col} \sim 1$ (Begelman, 2006). As $\dot{M}$ decreases, the ratio of radiation-to-gas pressures drops and below
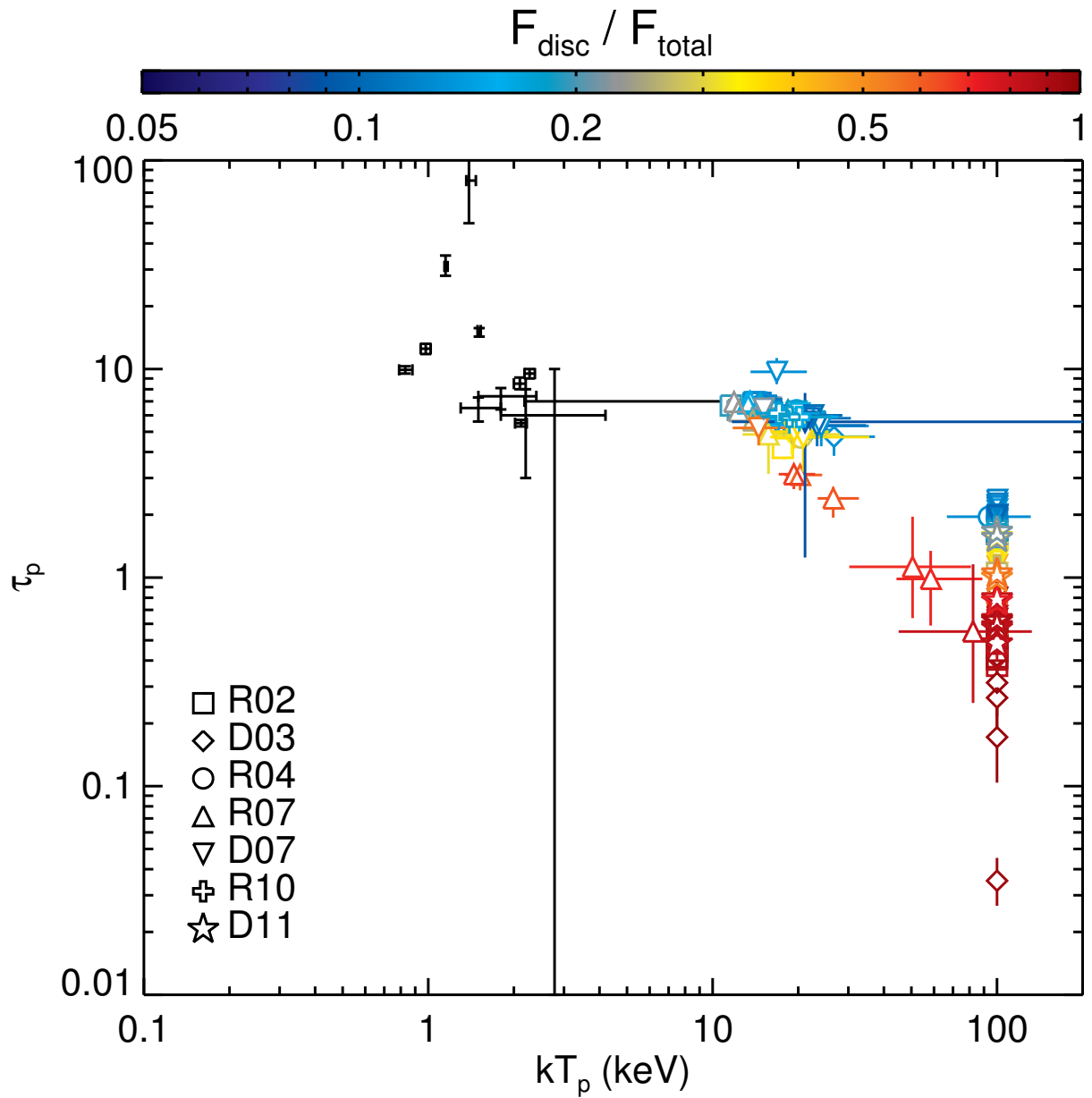
Figure 2.17: Coronal optical depth vs. coronal temperature, both measured using `comptt`. The disc model was `diskpn` with $R_{in} = 6 R_g$. The disc fraction is given by the glyph colour. The results from a sample of 12 ULXs (Table 8 of Gladstone et al. (2009)) are overlaid in *black crosshairs*.

some $L_{\mathrm{disc}}/L_{\mathrm{Edd}}$ the density inhomogeneities would disappear and f_{col} would increase. If the disc is strongly magnetised, values of $f_{\mathrm{col}} \gtrsim 5$ are conceivable (Begelman & Pringle, 2007). For a disc that instead transitions from a standard thin disc to a truncated disc with an interior RIAF, a relatively constant $\dot{M}$ is implied at this stage with a decreased radiative efficiency. Both scenarios of an inner disc remaining extended to the ISCO and a truncated disc + RIAF predict different $\dot{M}$ behaviour, which is difficult to distinguish observationally.

The phenomenological picture of a variable colour correction factor being capable of describing the disc spectral evolution observed in BHB outbursts advocates for the development and consideration of models that appeal to an evolving vertical disc structure and/or intricate disc-corona-jet connection. Recent observational work supports the idea of a coupled disc + corona playing a critical role in the LHS. Adopting sophisticated, self-consistent modelling techniques, Reis et al. (2013) studied the BHB XTE J1650-500 during its 2001/2002 outburst and found definite correlations between the reflected X-ray flux and power-law flux associated with the corona. These results fit into the interpretation of a light bending + collapsing corona model for state transitions (e.g., Miniutti & Fabian, 2004) and do not lend support to the truncated disc picture. An organized campaign of contemporaneous and frequent X-ray/radio monitoring of Cygnus X-1 in the LHS reveal that the reflected X-ray flux and the radio flux are positively correlated (Miller et al., 2012), which is consistent with the coronal ejection model of Beloborodov (1999). As the promising prospect of disc + corona coupling in BHB outbursts receives more attention, we hope that the relative measurements of f_{col} presented here serve as a useful reference for physical models that seek to generate predictive diagnostics of spectral hardening in accretion systems.

2.6.2   Physical Range of the Colour Correction Factor

The colour correction factor phenomenologically parameterises our ignorance of spectral alterations arising from the highly unknown and complicated combinations of disc vertical structure, accretion power dissipation properties, magnetisation, and inhomogeneities. Lumping the effects of these physical processes into the frequency-independent f_{col} parameter is attractive from the standpoint of limiting the parameters in MCD blackbody models; however, whether this treatment is an appropriate description of BHB discs in all spectral stages remains disputed. Here, we discuss the results from theoretical endeavors to constrain the

physically realisable range of the colour correction factor.

2.6.2.1 Radiative Transfer in One-Dimensional Disc Atmospheres

Investigations into the physically reasonable f_{col} range and the regimes for which the colour-corrected blackbody model is justified have focused on one-dimensional atmospheric disc models. These atmospheres are assumed to have no azimuthal structure and are constructed at many disc radii from self-similar standard thin disc equations. In brief, frequency-dependent opacities are computed at each radial position, allowing the modification of the locally emitted blackbody spectrum to be determined for multiple concentric annuli. The emergent spectrum, which is modified by the vertical structure, is computed for each annulus. The integrated disc spectrum is obtained by summing over all annuli and is fitted with the colour-corrected blackbody model, yielding a best-fit f_{col}.

Following the technique of self-consistently computing the radiative transfer and vertical disc structure (Ross et al., 1992), Shimura & Takahara (1995) considered the effects of electron scattering and free-free emission/absorption on the emergent disc spectrum. Regardless of the black hole mass and radial position in the disc, the local spectra (i.e., the emergent spectrum from an annulus) were adequately fit with $f_{\mathrm{col}} \simeq 1.8 - 2.0$ and $f_{\mathrm{col}} \simeq 1.7$ for $\dot{M} \simeq \dot{M}_{\mathrm{Edd}}$ and $\dot{M} \simeq 0.1\,\dot{M}_{\mathrm{Edd}}$, respectively, suggesting a relatively constant f_{col} over a large range of mass accretion rates expected in the HSS. For $\dot{M} \lesssim 0.01\,\dot{M}_{\mathrm{Edd}}$, which is characteristic of the LHS, the local spectrum was not well-described by the colour-corrected blackbody model due to ineffective (i.e., unsaturated) Comptonisation within the disc.

Merloni et al. (2000) extended the study of Shimura & Takahara (1995) by considering the effects of Doppler blurring, gravitational redshift, and allowing the dissipated accretion energy to be partitioned between the corona and disc (Svensson & Zdziarski, 1994). Assuming all of the accretion energy is dissipated within the disc, Merloni et al. (2000) found $f_{\mathrm{col}} \simeq 1.8$ for $\dot{M} = 0.1 - 0.3\,\dot{M}_{\mathrm{Edd}}$, fully consistent with Shimura & Takahara (1995). Exploring the lower accretion rate, $\dot{M} = 0.05\,\dot{M}_{\mathrm{Edd}}$ and allowing a significant fraction of the energy to be dissipated in the corona, Merloni et al. (2000) instead found a variable f_{col} ranging from $\sim 1.9 - 2.7$. Therefore, if coronal activity is important, f_{col} cannot be considered constant, with the suggested physical range being $1.7 \lesssim f_{\mathrm{col}} \lesssim 3$.

Davis et al. (2005) presents the most sophisticated study to date of the effects of disc vertical structure on the emergent spectrum, incorporating bound-free opacities and a fully relativistic radiative transfer treatment. For disc luminosities, $L_{\mathrm{disc}} = 0.01 - 0.3\ L_{\mathrm{Edd}}$, which spans the luminosity regimes of the LHS and HSS, Davis et al. (2005) found a weakly evolving $f_{\mathrm{col}} \simeq 1.4 - 1.6$, concluding that f_{col} remains fairly constant over broad ranges in mass accretion rate. The results of Davis et al. (2005) are at odds with those of Merloni et al. (2000); however, a direct comparison is complicated by the different methodologies used in each work.

2.6.2.2 Magnetisation

Although the details of magnetic fields (e.g., topology, strength, variability) in accreting black hole systems are poorly understood, magnetisation is central to many aspects of accretion physics. Perhaps most notable is the role of the magnetorotational instability (MRI) (Balbus & Hawley, 1991), which is widely accepted as the mechanism for angular momentum transport; hence, allowing accretion to persist. The turbulence generated within the disc by the MRI amplifies the toroidal component of magnetic field, perhaps reaching a state where magnetic pressure dominates over the combined gas and radiation pressures. Begelman & Pringle (2007) present analytic arguments for the maximal toroidal magnetic field strength achievable by the MRI and compute the corresponding disc structure, finding that magnetically dominated discs are thicker and have harder spectra compared to the standard Shakura-Sunyaev thin disc. Under the conjecture that the toroidal field attains the limiting value set by the MRI, Begelman & Pringle (2007) derive a lower limit for the colour correction factor,

$$ f_{\mathrm{col}} \geq 6.9 \left(\frac{\rho_*}{\rho} \right)^{-2/9} \alpha^{5/27} \left(\frac{M}{M_\odot} \right)^{-1/108} \left(\frac{\dot{M}}{\dot{M}_{\mathrm{Edd}}} \right)^{5/108} \left(\frac{r}{R_{\mathrm{g}}} \right)^{25/108}, $$

where ρ is the mid-plane density, ρ_* is the density corresponding to the thermalization layer (i.e., effective photosphere) of the disc, and $\rho_*/\rho < 1$. Shearing box simulations place the disc photosphere a few scale heights above the mid-plane, corresponding to density contrasts, $\rho_*/\rho \simeq 10^{-2} - 10^{-4}$ (Hirose et al., 2006, 2009). Therefore, if the disc around a stellar mass black hole is magnetically dominated, the colour correction factor can far surpass the values predicted by thin disc treatments that neglect the effects of a magnetic field

on the disc structure.

Conceivably, the details of vertical dissipation and coronal properties could alter the emergent disc spectrum considerably. Beloborodov (1999) envisaged a picture where buoyant magnetic loops subject to Parker instability rise into the corona and the magnetic energy available within the loops is subsequently dissipated by reconnection. Recently, Uzdensky (2013) analytically computed the vertical structure of a gas pressure-dominated disc threaded by a poloidal magnetic field where turbulent (i.e., dissipative) heating arising from the MRI is balanced by radiative cooling. Based on this disc model, Uzdensky (2013) argue that the *minimum* fraction of available accretion energy that ends up being released in the corona is, $f_{\min} \sim \beta_{0,\max}^{-1/5} \sim 0.4$, where $\beta_{0,\max} \sim 100$ is a reasonable estimate of the gas-to-magnetic pressure ratio at the disc mid-plane. Under conditions where a substantial fraction of accretion power is dissipated in the corona, Merloni et al. (2000) demonstrate that substantial spectral hardening is expected.

Numerical simulations show that magnetically supported, gas pressure-dominated discs have harder emergent spectra than their unmagnetised counterparts (Blaes et al., 2006). Blaes et al. (2006) calculated local accretion disc spectra from stratified shearing box simulations and found the disc spectrum hardened due to magnetic pressure support dominating in the upper atmosphere. This magnetic pressure acts to vertically extend the disc atmosphere and decrease the density at the effective photosphere, leading to saturated Comptonisation and spectral hardening. In deriving the local disc spectrum, Blaes et al. (2006) considered two vertical dissipation profiles: (1) a constant dissipation per unit mass and (2) a broken power-law fit to the numerical dissipation profile. Both treatments produced identical emergent spectra, implying that the local emergent disc spectrum is insensitive to the vertical dissipation profile and that magnetic pressure support is solely responsible for the observed spectral hardening. Motivated by the result that magnetic pressure support drives the spectral hardening and assuming the dissipation profile has no radial dependence, Blaes et al. (2006) constructed global disc spectra and found only modest hardening, with f_{col} increasing from 1.48 to 1.74 upon introducing magnetic pressure support. Blaes et al. (2006) caution that the numerical dissipation occurs at the grid scale and may be sensitive to grid resolution. Recent work indicates that numerical dissipation in ideal magnetohydrodynamic grid-based simulations does behave like physical dissipation, but acts to effectively diminish the resolution (Salvesen et al., 2014). Adopting dissipation

profiles motivated by numerical simulations is an important step toward merging accretion disc theory with simulations.

2.6.2.3   Inhomogeneous Discs

Strong disc inhomogeneities are expected to arise in moderate-to-strongly magnetised, radiation pressure-dominated regions of accretion discs (Begelman, 2002, 2006) due to photon bubble instability (Arons, 1992; Gammie, 1998; Begelman, 2001). In this picture, strong density contrasts arise on scales smaller than the disc scale height, resulting in a porous disc where radiation preferentially 'leaks' through the underdense regions. Due to the typical densities in photon bubble-dominated discs being higher than in standard thin discs of the same luminosity, thermalization of radiation is more effective in inhomogeneous discs. Consequently, radiation that is thermalized near the disc mid-plane and escapes through optically thin chutes can result in a colour correction factor near unity for inhomogeneous discs (Begelman, 2006). Dexter & Quataert (2012) computed inhomogeneous disc spectra based on a toy model (Dexter & Agol, 2011) and found that the disc spectrum broadens and hardens as the amplitude of the local temperature fluctuations increases. Inhomogeneous discs can substantially alter the standard disc spectrum and further investigation is required to characterise their properties.

2.6.3   Limitations of Simplistic Accretion Disc Models

While significant strides have been made in exploring the imprints of the disc structure on the emergent spectrum in the HSS, the applicability of the colour-corrected blackbody model to discs in the LHS remains elusive. From a theoretical perspective, thin discs with low mass accretion rates will be fully gas pressure-dominated with absorption overtaking electron scattering as the dominant opacity source, nullifying the approximation of the emergent spectrum as a colour-corrected blackbody (e.g., Ebisuzaki et al., 1984). Nevertheless, standard MCD models consistently produce exceptional fits to LHS accretion disc spectra, giving credence to the notion that the MCD model successfully describes real astrophysical discs in the LHS. Analogously, standard thin discs are expected to suffer from thermal (Shakura & Sunyaev, 1976) and viscous (Lightman & Eardley, 1974) instabilities, yet the MCD model provides an acceptable description of

the observed disc spectrum, which should not be the case if the disc were plagued by catastrophic insta-bilities. While it may turn out that f_{col} has a very narrow allowable range and/or it is an inappropriate parameterisation to use for low disc luminosities, there is currently no compelling evidence that this should be so based on fits to observed disc spectra alone.

Direct measurements of f_{col} should not be made with Newtonian disc models when the black hole is known to possess a nonzero spin and an inner disc extending to the ISCO. Newtonian disc models have the strength of being able to describe a standard black hole accretion disc spectrum with very few parameters; however, the important physical effects of light bending, Doppler blurring, and gravitational redshift inherent to Kerr black holes are neglected. The pseudo-Newtonian disc model, `diskpn`, provides accurate fits to fully relativistic disc spectra from a non-spinning black hole, but requires uncomfortably large values of f_{col} when fitting a disc spectrum from an extreme Kerr black hole (see §2.5.4). When attempting to fit the hotter disc spectra intrinsic to spinning black holes, Newtonian disc models are forced to artificially increase the colour correction factor to achieve the colour temperature demanded by the data. Fortunately, relative measurements of f_{col} do not appear to be appreciably affected in the way that absolute measurements are, at least for the low disc inclination considered in this work. This implies that the relative measurements of f_{col} evolution during state transitions of GX 339–4 are sound, regardless of the intrinsic spin possessed by GX 339–4. The possibility that the inner disc recedes radially outward or progresses inward between successive observations cannot be ruled out and would manifest itself in the relative measurements of f_{col}, rendering them moot.

The main outcome of this work is that an evolving colour correction factor in a standard thin disc with inner radius fixed at the ISCO is a viable, albeit not the only, explanation for the changing disc spectrum of the BHB GX 339–4 over many state transitions. Given the uncertainty in accretion flow geometry as BHBs transition between spectral states, we emphasise that inner disc radii cannot be reliably computed from spectral fits made with simplified disc models. Instead, self-consistent, physically motivated spectral modelling applied to high-quality CCD X-ray spectra is necessary to distinguish between opposing accretion scenarios. Future insights into the complicated disc-corona-jet connections in BHBs will likely progress by concentrated observing campaigns and the development of physical models that can provide testable

diagnostics.

2.7   Summary & Conclusions

The purpose of this work is to show that physically reasonable changes in the colour correction factor provide a valid, alternative explanation to disc truncation for explaining the accretion disc spectral evolution observed in black hole binary state transitions. To this end, we systematically performed spectral fits to *RXTE* observations of the low-mass X-ray binary GX 339–4 over seven state transitions and collected the observations that statistically required a disc component. The disc detection pipeline measured discs with luminosities as low as $L_{\mathrm{disc}} \simeq 10^{-3}\ L_{\mathrm{Edd}}$ and disc fractions down to $DF \simeq 0.05$. In a suite of spectral fits to the observations deemed to require a disc, we imposed an unchanging inner disc radius located at the ISCO for a Schwarzschild black hole in order to ensure that a changing colour correction factor, rather than a radially receding/advancing inner disc, was responsible for any spectral evolution of the disc component. We give our conclusions as a bulleted list below.

- For nearly all state transitions of GX 339–4 investigated here, relative changes in f_{col} in the range $1.4 \lesssim f_{\mathrm{col,rel}} \lesssim 5$, which corresponds to a factor of ~ 3.5 change, can fully account for disc evolution in a state transition without invoking a truncated disc geometry.

- Accounting for an f_{col} evolution in the range quoted above over the course of state transitions in GX 339–4, the $F_{\mathrm{disc}} \propto T_{\mathrm{eff}}^4$ relation is recovered for a constant emitting area (i.e., non-truncated disc) down to the low luminosities characteristic of the HIS and LHS.

- The validity of the results mentioned above are insensitive to the Comptonisation model adopted for fitting the high-energy continuum. Adopting a continuum model that avoids the low-energy flux stealing character of a simple power-law reduces the degree of f_{col} variability required to explain the observed disc evolution in state transitions.

- The practice of measuring the inner disc radius from the best-fit disc normalisation is unreliable when both R_{in} and f_{col} are worked into the disc normalisation. Instead, we suggest that disc models where these two parameters are decoupled (e.g., `diskpn`) be used to break the degeneracy.

- We stress that this work *does not* demonstrate that the inner accretion disc remains at the radius of marginal stability during a state transition. Instead, we argue that variations of f_{col} within a theoretically reasonable range can account for most, if not all, of the disc spectral evolution observed over the course of a state transition.

- Relative measurements, unlike absolute measurements, of f_{col} are not appreciably affected by our ignorance of black hole spin.

- When a physically motivated Comptonisation model is used in conjunction with a disc component to fit the *RXTE* data of GX 339–4 in the HIS and LHS, we observe a parameter degeneracy between the coronal optical depth and the colour correction factor. This calls into question the association of ULXs with super-Eddington stellar mass black hole binaries based on measurements of coronal optical depth without allowing for a variable f_{col}.

Simple disc models of the MCD family are attractive and useful from the standpoint that they consistently achieve superb fits with limited free parameters to accretion disc spectra, where the intrinsic system parameters are often poorly constrained. This work illustrates that allowing for the possibility of reasonable variations in the colour correction factor provides an adequate description of disc spectra over a wide range in luminosity states. We advocate that f_{col} may be dynamic and should not be dismissed as a mere constant in studies of accretion disc spectra spanning a broad range in luminosity, as is often done in practice. Numerous factors may contribute to altering the emergent disc spectrum including the vertical disc structure, details of accretion energy dissipation, coronal dynamics, magnetisation, and disc inhomogeneities. Given that the available X-ray data cannot isolate these effects, common practice is to adopt a blanket term, the colour correction factor, which is supposed to account for the overall deviations from a multi-colour blackbody disc spectrum. We encourage an increased awareness for the implications of presuming a constant f_{col}. Important physics are wrapped up into f_{col} that should be considered before making definitive claims based on the assumption of an invariant f_{col}.

The standard theoretical emergent disc spectrum hinges on the assumptions that the accretion energy is dissipated within the disc (i.e., where the majority of the mass resides) and that the density structure

is smooth and homogeneous. The effects of magnetisation, which surely play a crucial role in accretion physics and disc structure, are also ignored in the disc models applied to observations. Radiation pressure-dominated, magnetised discs, as expected in the HSS, are subject to clumping instabilities, resulting in a porous disc structure and lowered colour correction factor (Begelman, 2006). Considerations of the corona as an energy dissipation reservoir (Svensson & Zdziarski, 1994; Merloni et al., 2000; Merloni & Fabian, 2002) and of strongly magnetised discs (Begelman & Pringle, 2007) indicate that f_{col} may extend well beyond the canonical value of ~ 1.7 and into a realm consistent with the values required here and in similar observational studies (Dunn et al., 2011; Reynolds & Miller, 2013). With the advent of sophisticated codes capable of treating magnetohydrodynamics with radiative transport and general relativity, state-of-the-art numerical simulations provide a promising avenue for studying accretion disc structure with the aforementioned assumptions relaxed. Striving toward the development of sophisticated models that capture the relevant physics of realistic accreting black hole systems, provide predictive diagnostics, and are accessible to observers is a crucial step toward disentangling the details of the accretion flow and distinguishing between different accretion scenarios.

Acknowledgments

Trans. ID	Observation ID	MJD	Best-fit Model	Γ_1	E_b (keV)	Γ_2	K_{pow}	σ (eV)	K_{line}	kT_{in} (keV)	K_{disc}	C	ν	χ^2_ν	$\log(F_{disc})$ erg/s/cm^2	DF (%)
R02	40031-03-01-00	52382.114	bkn×(bb+ga)	1.47(2)	33(1)	2.43(6)	1.13(5)	1.26(7)	0.040(4)	1.38(8)	31(8)	0.76(1)	70	0.91	-8.62(3)	7.2(4)
R02	40031-03-02-00	52383.103	bkn×(bb+ga)	1.52(1)	32(1)	2.34(6)	1.38(4)	1.32(6)	0.044(4)	1.35(9)	30(9)	0.719(8)	70	1.08	-8.67(2)	5.8(3)
R02	40031-03-02-01	52384.147	bkn×(bb+ga)	1.526(8)	34.0(9)	2.42(4)	1.36(3)	1.31(5)	0.046(3)	1.21(6)	54(12)	0.749(6)	70	0.96	-8.60(2)	6.9(2)
R02	40031-03-02-02	52384.979	bkn×(bb+ga)	1.517(9)	33.6(6)	2.44(3)	1.31(3)	1.29(5)	0.044(3)	1.28(7)	41(10)	0.765(5)	70	1.30	-8.63(2)	6.6(3)
R02	70110-01-05-00	52385.469	bkn×(bb+ga)	1.58(2)	33(1)	2.40(6)	1.34(6)	0.9(1)	0.024(4)	1.3(1)	24(10)	0.91(1)	70	0.84	-8.78(4)	5.4(4)
R02	40031-03-02-03	52386.026	pow×(bb+ga)	1.565(7)	-	-	1.51(3)	1.23(5)	0.042(3)	1.30(7)	32(8)	-	43	1.62	-8.71(2)	4.7(2)
R02	40031-03-02-04	52386.934	bkn×(bb+ga)	1.540(8)	32.0(7)	2.37(3)	1.43(3)	1.30(5)	0.045(3)	1.31(7)	36(8)	0.775(6)	70	1.26	-8.65(2)	6.2(2)
R02	70110-01-06-00	52387.490	bkn×(bb+ga)	1.60(1)	34(2)	2.43(8)	1.42(6)	1.04(9)	0.029(3)	1.3(1)	25(10)	0.91(2)	70	0.72	-8.84(5)	4.7(4)
R02	70109-01-04-00	52387.646	bkn×(bb+ga)	1.593(6)	33.1(13)	2.44(1)	1.44(2)	1.05(5)	0.033(2)	1.18(7)	38(10)	0.908(4)	70	1.90	-8.81(2)	4.9(2)
R02	40031-03-02-05	52388.065	bkn×(bb+ga)	1.51(1)	32.1(9)	2.39(4)	1.33(5)	1.26(6)	0.045(4)	1.37(8)	33(8)	0.739(8)	70	1.16	-8.60(2)	6.9(4)
R02	40031-03-02-06	52389.071	bkn×(bb+ga)	1.53(3)	35(3)	2.4(1)	1.4(1)	1.2(1)	0.043(8)	1.2(2)	46(29)	0.79(2)	70	0.79	-8.65(7)	6.3(8)
R02	70110-01-07-00	52390.910	bkn×(bb+ga)	1.59(1)	32(1)	2.51(8)	1.45(6)	1.11(8)	0.038(4)	1.2(1)	40(15)	0.88(2)	70	1.07	-8.74(4)	5.7(5)
R02	70109-01-05-01G	52391.336	bkn×(bb+ga)	1.608(8)	33.9(7)	2.46(3)	1.50(3)	1.05(6)	0.032(3)	1.24(9)	29(10)	0.914(6)	70	0.98	-8.83(2)	4.7(2)
R02	70109-01-05-00	52391.402	bkn×(bb+ga)	1.616(7)	32.5(8)	2.41(3)	1.55(3)	0.99(6)	0.031(2)	1.20(8)	35(10)	0.901(6)	71	1.31	-8.82(2)	4.7(2)
R02	70109-01-05-02	52391.469	bkn×(bb+ga)	1.610(7)	32.7(7)	2.44(3)	1.52(3)	1.04(6)	0.033(3)	1.25(8)	30(9)	0.901(6)	70	1.07	-8.82(2)	4.8(2)
R02	70110-01-08-00	52394.445	bkn×(bb+ga)	1.623(9)	30.6(9)	2.37(3)	1.60(4)	1.05(6)	0.036(3)	1.20(8)	38(12)	0.901(8)	70	1.19	-8.79(3)	5.0(3)
R02	70110-01-09-00	52398.668	bkn×(bb+ga)	1.68(1)	33(1)	2.61(6)	1.81(5)	1.10(6)	0.037(3)	1.28(9)	29(9)	0.93(1)	70	0.88	-8.79(3)	5.0(3)
R02	70110-01-06-00	52400.842	bkn×(bb+ga)	1.785(8)	30(1)	2.56(4)	2.23(5)	1.05(5)	0.036(3)	1.27(7)	31(8)	0.925(9)	70	1.05	-8.76(3)	5.3(3)
R02	70108-03-01-00	52400.924	pow×(bb+ga)	1.836(6)	-	-	2.50(4)	1.01(4)	0.036(2)	1.15(7)	42(13)	-	43	1.80	-8.80(3)	4.3(3)
R02	70110-01-10-00	52402.499	bkn×(bb+ga)	2.07(1)	28(3)	2.6(1)	3.5(1)	1.10(4)	0.043(2)	0.96(3)	243(36)	0.96(2)	70	1.16	-8.35(2)	11.5(5)
R02	70109-04-01-00	52405.632	bkn×(bb+ga)	2.41(1)	32(3)	2.85(8)	5.4(1)	1.11(3)	0.040(2)	0.867(8)	1507(81)	0.99(1)	70	1.76	-7.742(8)	26.3(2)
R02	70109-04-01-01	52405.865	bkn×(bb+ga)	2.386(7)	30(2)	2.79(5)	5.1(1)	1.12(3)	0.041(2)	0.877(8)	1431(73)	0.972(7)	70	1.78	-7.745(7)	27.8(1)
R02	70109-04-01-02	52406.077	bkn×(bb+ga)	2.38(1)	28(7)	2.8(3)	5.1(2)	1.05(4)	0.042(2)	0.871(8)	1411(76)	0.97(6)	70	1.11	-7.763(9)	26.4(3)
R02	70110-01-11-00	52406.707	pow×(bb+ga)	2.42(1)	-	-	5.2(2)	1.08(4)	0.036(2)	0.890(8)	1342(70)	0.99(2)	73	1.11	-7.747(8)	26.53(6)
R02	70110-01-12-00	52410.535	pow×(bb+ga)	2.43(1)	-	-	3.8(1)	1.12(4)	0.030(2)	0.867(6)	2147(80)	0.99(2)	73	1.03	-7.589(5)	41.5(1)
R02	70109-01-07-00	52411.645	pow×(bb+ga)	2.58(1)	-	-	4.3(1)	0.99(3)	0.027(1)	0.866(5)	2507(84)	1.02(2)	72	1.48	-7.523(5)	39.9(4)
R02	70110-01-13-00	52412.080	pow×(bb+ga)	2.53(2)	-	-	3.0(2)	0.98(4)	0.024(1)	0.867(5)	2591(78)	0.99(4)	73	0.83	-7.507(4)	50.4(5)
R02	40031-03-03-00	52414.057	pow×(bb+ga)	2.42(6)	-	-	1.5(2)	1.04(9)	0.017(2)	0.864(5)	2957(103)	0.95(8)	72	0.66	-7.457(6)	70.0(3)
R02	40031-03-03-01	52414.126	pow×bb	2.63(9)	-	-	2.6(6)	-	-	0.885(6)	2491(77)	1.3(2)	74	1.37	-7.488(6)	53.6(5)
R02	40031-03-03-02	52414.193	pow×(bb+ga)	2.46(7)	-	-	1.6(3)	0.89(9)	0.016(2)	0.803(5)	3967(154)	-	43	1.22	-7.457(7)	69.4(5)
R02	40031-03-03-04	52414.363	pow×(bb+ga)	2.36(2)	-	-	1.49(8)	1.10(5)	0.015(1)	0.885(4)	2669(72)	0.87(3)	72	1.13	-7.457(4)	71.1(2)
R02	70110-01-14-00	52416.601	pow×(bb+ga)	2.43(2)	-	-	3.3(2)	1.08(5)	0.028(2)	0.874(6)	2017(73)	-	43	1.67	-7.601(6)	44.4(3)
D03	70109-01-36-02	52688.301	pow×(bb+ga)	3.0(3)	-	-	0.3(3)	0.4(2)	0.0009(3)	0.557(8)	5467(443)	-	43	1.05	-7.96(1)	66(1)
D03	70111-01-01-000	52690.691	pow×(bb+ga)	2.5(1)	-	-	0.08(2)	0.76(5)	0.0014(1)	0.567(3)	4401(144)	1.2(3)	72	1.63	-8.019(6)	92.31(9)
D03	70110-01-86-00	52693.734	pow×bb	3.20(6)	-	-	1.5(2)	-	-	0.50(1)	6782(1224)	2.9(6)	74	1.72	-8.07(3)	21(3)
D03	70109-01-37-00	52694.944	pow×(bb+ga)	2.28(4)	-	-	0.21(2)	0.82(4)	0.0033(2)	0.640(6)	1429(87)	1.3(1)	72	1.55	-8.30(1)	71.7(8)

Trans. ID	Observation ID	MJD	Best–fit Model	Γ_1	E_b (keV)	Γ_2	K_{pow}	σ (eV)	K_{line}	kT_{in} (keV)	K_{disc}	C	ν	χ^2_ν	$\log(F_{disc})$ erg/s/cm^2	DF (%)
D03	70110-01-87-00	52700.602	pow×(bb+ga)	2.32(5)	-	-	0.19(3)	0.72(6)	0.0024(2)	0.624(8)	1230(100)	1.1(2)	72	1.12	-8.40(1)	68.3(9)
D03	70110-01-88-00	52704.021	pow×(bb+ga)	2.10(6)	-	-	0.14(2)	0.96(6)	0.0040(3)	0.662(9)	799(72)	0.7(2)	72	1.28	-8.49(1)	70(1)
D03	70110-01-89-00	52707.932	pow×(bb+ga)	2.7(1)	-	-	0.5(1)	0.4(1)	0.0020(4)	0.58(2)	1712(334)	-	43	1.30	-8.38(2)	43.1(4)
D03	70109-02-01-01	52710.012	pow×(bb+ga)	2.29(6)	-	-	0.21(3)	0.81(5)	0.0032(3)	0.601(8)	1492(126)	-	43	1.97	-8.39(1)	67.4(8)
D03	60705-01-56-00	52710.747	pow×(bb+ga)	2.48(6)	-	-	0.43(7)	0.91(5)	0.0038(4)	0.64(1)	878(97)	1.3(1)	71	1.73	-8.50(1)	42.7(2)
D03	70110-01-91-00	52713.486	pow×(bb+ga)	2.43(9)	-	-	0.20(5)	0.75(7)	0.0021(3)	0.572(9)	2295(217)	1.4(3)	72	1.36	-8.29(1)	73.1(5)
D03	60705-01-57-00	52716.732	pow×(bb+ga)	2.8(1)	-	-	0.4(1)	0.88(8)	0.0021(3)	0.57(1)	2581(260)	2.2(4)	71	1.02	-8.23(1)	57.6(6)
D03	50117-01-04-01	52718.102	pow×(bb+ga)	2.23(5)	-	-	0.17(2)	0.93(4)	0.0035(2)	0.647(7)	1096(75)	1.0(1)	71	1.72	-8.39(1)	71(1)
D03	50117-01-04-02	52718.180	pow×(bb+ga)	2.5(1)	-	-	0.4(1)	0.90(8)	0.0035(5)	0.58(2)	2212(377)	-	42	1.53	-8.27(2)	57.7(6)
D03	70110-01-93-00	52719.234	pow×(bb+ga)	2.27(7)	-	-	0.22(4)	0.78(7)	0.0035(4)	0.62(1)	1270(119)	1.1(2)	72	1.58	-8.40(1)	66.0(6)
D03	70110-01-94-00	52724.232	pow×(bb+ga)	2.14(5)	-	-	0.23(3)	0.99(5)	0.0053(4)	0.71(1)	408(49)	0.9(1)	72	1.19	-8.67(2)	48(1)
D03	70110-01-95-00	52727.257	pow×(bb+ga)	2.07(5)	-	-	0.24(3)	0.96(7)	0.0049(5)	0.71(2)	276(42)	1.2(1)	72	1.25	-8.83(2)	37(1)
D03	60705-01-59-00	52731.583	pow×(bb+ga)	1.82(2)	-	-	0.19(1)	1.22(5)	0.0058(3)	0.89(2)	44(6)	0.68(3)	71	1.43	-9.22(2)	17.4(8)
D03	70110-01-96-00	52732.119	bkn×(bb+ga)	1.72(5)	34(9)	2.6(7)	0.14(2)	1.0(1)	0.0034(6)	0.91(5)	32(10)	1.09(8)	70	0.72	-9.33(5)	18(1)
D03	70110-01-97-00	52734.228	pow×(bb+ga)	1.70(5)	-	-	0.13(2)	1.0(2)	0.0026(7)	1.06(9)	11(5)	0.93(7)	72	0.85	-9.51(7)	12(2)
D03	80116-02-01-00	52735.660	pow×(bb+ga)	1.65(1)	-	-	0.109(4)	0.86(9)	0.0019(2)	1.06(7)	8(3)	0.92(3)	72	1.18	-9.67(3)	8.6(6)
D03	70110-01-98-00	52737.253	pow×(bb+ga)	1.66(4)	-	-	0.11(1)	1.0(2)	0.0024(6)	0.75(8)	42(34)	0.86(6)	72	0.88	-9.54(8)	11(2)
D03	80116-02-01-01G	52737.502	pow×(bb+ga)	1.63(2)	-	-	0.100(5)	0.9(1)	0.0020(2)	0.97(5)	11(3)	0.91(3)	72	0.84	-9.71(4)	8.2(7)
D03	80116-02-01-02	52739.606	bkn×(bb+ga)	1.57(3)	35(9)	2.0(3)	0.079(6)	1.0(1)	0.0021(3)	0.96(5)	12(4)	0.97(4)	70	1.09	-9.65(4)	10.6(8)
D03	80116-02-02-00	52741.749	bkn×(bb+ga)	1.60(2)	34(4)	2.1(2)	0.082(5)	0.8(1)	0.0013(2)	0.93(7)	9(4)	0.96(3)	70	0.89	-9.84(5)	7.6(7)
D03	80116-02-02-01	52742.051	pow×(bb+ga)	1.51(2)	-	-	0.064(4)	1.0(1)	0.0014(2)	1.06(9)	6(2)	-	43	0.66	-9.80(4)	7.5(7)
D03	70128-02-03-00	52742.346	pow×(bb+ga)	1.60(2)	-	-	0.078(3)	0.7(1)	0.0010(1)	0.96(6)	7(2)	-	43	0.91	-9.92(4)	6.1(6)
D03	70128-02-03-01	52742.699	bkn×(bb+ga)	1.57(3)	52(17)	2.2(8)	0.069(6)	1.2(1)	0.0015(2)	0.95(6)	8(3)	0.92(2)	70	0.99	-10.04(6)	4.9(5)
D03	70110-01-02-10	52743.163	pow×bb	1.59(9)	-	-	0.07(2)	-	-	1.8(2)	0.5(3)	-	45	1.09	-8.0(2)	6(2)
D03	80116-02-02-02G	52743.305	pow×(bb+ga)	1.60(2)	-	-	0.075(4)	0.8(1)	0.0009(2)	0.92(8)	7(4)	0.94(3)	72	0.87	-9.96(6)	5.8(8)
D03	60705-01-61-00	52746.983	bkn×(bb+ga)	1.42(8)	17(2)	1.8(1)	0.041(8)	1.0(2)	0.0008(3)	1.6(2)	0.6(4)	0.94(7)	69	0.96	-10.1(2)	6(2)
D03	60705-01-62-00	52750.384	pow×bb	1.37(6)	-	-	0.026(4)	-	-	2.3(1)	0.14(4)	-	44	1.05	-10.1(1)	6(1)
D03	70110-01-04-10	52751.569	pow×bb	1.53(9)	-	-	0.029(7)	-	-	1.8(2)	0.2(1)	-	45	0.73	-10.4(3)	5(2)
D03	60705-01-63-00	52756.060	pow×bb	1.51(5)	-	-	0.022(3)	-	-	2.7(7)	0.02(3)	0.79(8)	73	1.19	-10.6(2)	3(1)
R04	90418-01-01-04	53196.146	pow×(bb+ga)	1.52(4)	-	-	0.19(2)	0.0(2)	0.0017(3)	1.3(2)	4(3)	0.91(5)	72	1.03	-9.62(3)	4.2(3)
R04	90418-01-01-00	53196.212	pow×bb	1.38(7)	-	-	0.12(3)	-	-	1.90(8)	1.9(3)	-	45	1.21	-9.29(8)	9(1)
R04	90418-01-01-01	53197.113	bkn×(bb+ga)	1.49(2)	44(7)	2.1(2)	0.182(9)	1.0(1)	0.0045(6)	1.00(5)	20(5)	0.90(2)	70	1.51	-9.36(3)	7.4(5)
R04	90418-01-01-02	53198.162	pow×(bb+ga)	1.54(1)	-	-	0.209(7)	0.8(1)	0.0033(4)	1.02(6)	16(5)	0.91(2)	72	1.53	-9.45(3)	5.7(4)
R04	60705-01-65-00	53198.295	bkn×(bb+ga)	1.48(2)	32(7)	1.8(1)	0.187(8)	0.9(1)	0.0039(7)	1.1(1)	11(5)	0.90(3)	70	0.71	-9.43(4)	6.1(5)
R04	90418-01-01-03	53199.146	bkn×(bb+ga)	1.48(1)	36(3)	1.92(9)	0.192(6)	0.8(1)	0.0034(5)	1.21(9)	9(3)	0.91(1)	70	0.55	-9.40(2)	6.5(2)
R04	60705-01-65-01	53201.330	bkn×(bb+ga)	1.52(3)	39(5)	2.2(2)	0.22(2)	1.0(2)	0.004(1)	1.1(1)	15(8)	0.94(3)	70	0.65	-9.36(6)	6.8(8)

Trans. ID	Observation ID	MJD	Best-fit Model	Γ_1	E_b (keV)	Γ_2	K_{pow}	σ (eV)	K_{line}	kT_{in} (keV)	K_{disc}	C	ν	χ^2_ν	$\log(F_{disc})$ erg/s/cm^2	DF (%)
R04	60705-01-66-00	53204.415	pow×(bb+ga)	1.57(2)	-	-	0.28(1)	0.9(1)	0.0047(8)	0.91(9)	28(16)	0.92(3)	72	1.05	-9.50(9)	4.2(7)
R04	60705-01-67-01	53215.299	bkn×(bb+ga)	1.55(1)	39(6)	1.9(1)	0.31(1)	0.8(1)	0.005(1)	1.1(1)	13(7)	0.93(2)	70	0.89	-9.32(4)	5.7(5)
R04	60705-01-68-00	53218.113	bkn×(bb+ga)	1.54(1)	32(5)	1.9(1)	0.32(1)	0.99(9)	0.0072(8)	1.04(6)	25(7)	0.98(2)	70	0.91	-9.20(3)	7.1(4)
R04	60705-01-68-01	53222.252	bkn×(bb+ga)	1.58(1)	38(2)	2.4(1)	0.41(1)	1.03(7)	0.010(1)	1.12(7)	28(8)	0.93(2)	70	1.07	-9.02(2)	9.6(4)
R04	60705-01-69-00	53225.412	bkn×(bb+ga)	1.63(1)	33(3)	2.07(9)	0.48(2)	1.05(6)	0.012(1)	1.09(5)	33(7)	0.91(2)	70	1.11	-9.01(2)	9.1(4)
R04	90704-01-01-00	53226.452	bkn×(bb+ga)	1.64(1)	34(2)	2.22(7)	0.50(1)	1.08(5)	0.0128(8)	1.07(4)	39(6)	0.90(1)	70	1.44	-8.96(2)	10.2(4)
R04	60705-01-69-01	53228.997	bkn×(bb+ga)	1.78(2)	28(3)	2.2(1)	0.62(4)	1.18(7)	0.016(1)	0.96(4)	89(17)	0.96(3)	70	1.18	-8.79(3)	15.0(8)
R04	60705-01-70-00	53230.964	pow×(bb+ga)	2.12(3)	-	-	0.93(8)	1.03(6)	0.018(1)	0.78(1)	694(62)	0.98(4)	72	1.70	-8.27(1)	36.6(8)
R04	90110-02-01-03	53233.000	pow×(bb+ga)	2.37(2)	-	-	1.10(6)	0.87(4)	0.0123(6)	0.770(6)	1509(73)	1.19(6)	72	1.27	-7.948(8)	52.0(2)
R04	60705-01-70-01	53234.587	pow×(bb+ga)	2.42(4)	-	-	0.81(9)	0.88(4)	0.0111(6)	0.726(4)	2243(81)	1.1(1)	72	1.76	-7.880(6)	62.66(8)
R04	90704-01-03-00	53235.445	pow×(bb+ga)	2.33(2)	-	-	0.63(4)	1.00(3)	0.0110(4)	0.752(4)	1863(71)	1.04(5)	72	1.81	-7.900(6)	67.7(3)
R04	90704-02-01-01	53237.547	pow×(bb+ga)	2.21(3)	-	-	0.30(2)	1.01(4)	0.0072(3)	0.699(4)	2629(93)	1.06(8)	72	1.67	-7.878(6)	82.0(4)
R04	90704-02-01-03	53237.682	pow×(bb+ga)	2.31(5)	-	-	0.43(6)	0.87(5)	0.0079(5)	0.676(4)	3229(126)	0.94(9)	72	1.49	-7.847(7)	77.82(5)
R04	60705-01-71-00	53238.058	pow×(bb+ga)	2.30(6)	-	-	0.39(6)	0.91(5)	0.0076(5)	0.683(4)	3078(108)	-	43	1.82	-7.848(6)	79.26(2)
R07	92052-07-06-01	54118.975	bkn×(bb+ga)	1.47(1)	37(2)	2.12(6)	0.52(2)	0.9(2)	0.011(3)	1.2(1)	28(12)	0.93(1)	70	1.32	-8.91(3)	7.3(4)
R07	92428-01-02-00	54122.304	bkn×(bb+ga)	1.49(1)	35.5(9)	2.21(3)	0.64(2)	0.8(1)	0.013(2)	1.18(9)	33(12)	0.918(7)	70	1.69	-8.87(2)	7.2(3)
R07	92428-01-03-00	54127.115	bkn×(bb+ga)	1.53(2)	37(2)	2.41(9)	0.84(4)	0.7(1)	0.015(3)	1.2(1)	36(18)	0.93(1)	70	0.82	-8.79(3)	7.3(4)
R07	92035-01-01-01	54128.976	bkn×(bb+ga)	1.556(8)	34.2(9)	2.27(4)	0.97(2)	0.95(6)	0.023(2)	0.99(6)	93(29)	0.936(7)	70	1.20	-8.72(3)	7.7(6)
R07	92035-01-01-00	54129.476	bkn×(bb+ga)	1.558(9)	37(2)	2.33(7)	0.99(2)	1.02(6)	0.024(2)	1.04(6)	70(21)	0.92(1)	70	1.00	-8.76(3)	6.9(4)
R07	92035-01-01-03	54130.140	bkn×(bb+ga)	1.531(8)	32(1)	2.26(4)	0.96(2)	0.97(5)	0.029(2)	0.87(3)	249(56)	0.921(9)	70	1.45	-8.52(3)	11.4(7)
R07	92035-01-01-02	54131.127	bkn×(bb+ga)	1.572(8)	33.3(9)	2.35(3)	1.14(2)	1.03(6)	0.027(2)	1.03(6)	87(27)	0.923(7)	70	1.89	-8.68(3)	7.6(5)
R07	92035-01-01-04	54132.109	bkn×(bb+ga)	1.577(8)	32.3(7)	2.35(3)	1.19(3)	0.94(7)	0.026(2)	1.08(7)	71(24)	0.937(7)	70	1.43	-8.69(3)	7.4(5)
R07	92035-01-02-00	54133.035	bkn×(bb+ga)	1.600(7)	33.7(7)	2.41(3)	1.30(3)	0.90(6)	0.027(2)	1.03(7)	87(30)	0.924(6)	70	1.55	-8.68(3)	7.2(5)
R07	92035-01-02-01	54133.953	bkn×(bb+ga)	1.594(8)	33.3(7)	2.42(3)	1.29(3)	0.98(6)	0.029(3)	1.06(7)	80(27)	0.916(7)	70	1.41	-8.66(3)	7.6(5)
R07	92035-01-02-02	54135.054	bkn×(bb+ga)	1.612(8)	32.9(8)	2.41(3)	1.36(3)	0.94(7)	0.027(3)	1.12(8)	60(21)	0.900(6)	70	1.41	-8.70(3)	6.8(4)
R07	92035-01-02-04	54137.018	bkn×(bb+ga)	1.640(7)	32.6(7)	2.46(3)	1.60(3)	1.03(5)	0.036(2)	1.05(6)	84(25)	0.905(6)	70	1.19	-8.66(3)	6.8(4)
R07	92035-01-02-08	54137.857	bkn×(bb+ga)	1.68(1)	34(1)	2.56(7)	1.76(6)	0.96(7)	0.033(3)	1.11(9)	69(29)	0.92(1)	70	1.48	-8.65(3)	8.2(6)
R07	92035-01-02-07	54138.846	bkn×(bb+ga)	1.702(6)	30.4(8)	2.49(4)	1.82(3)	0.96(4)	0.039(2)	0.85(3)	325(80)	0.935(7)	70	1.68	-8.44(3)	11.0(8)
R07	92035-01-02-06	54139.963	bkn×(bb+ga)	1.827(7)	30.8(7)	2.64(4)	2.39(5)	1.06(4)	0.040(2)	1.07(5)	92(24)	0.912(7)	70	1.28	-8.59(2)	9.7(5)
R07	92035-01-03-00	54140.225	bkn×(bb+ga)	1.871(8)	30.0(9)	2.59(4)	2.59(6)	0.99(4)	0.038(2)	1.02(5)	130(36)	0.935(8)	70	1.49	-8.52(3)	11.6(7)
R07	92035-01-03-01	54141.075	bkn×(bb+ga)	1.979(8)	31(1)	2.74(5)	3.14(7)	0.97(4)	0.039(2)	0.97(4)	211(49)	0.937(8)	70	1.38	-8.41(3)	15.4(8)
R07	92035-01-03-02	54142.056	bkn×(bb+ga)	2.088(7)	31(1)	2.82(6)	3.62(7)	0.98(3)	0.046(2)	0.81(2)	942(129)	0.944(9)	70	1.75	-8.07(2)	19.2(8)
R07	92035-01-03-03	54143.039	bkn×(bb+ga)	2.26(1)	26(5)	2.7(1)	5.1(1)	1.00(4)	0.046(2)	0.84(2)	1114(119)	0.98(3)	70	1.82	-7.92(2)	20.3(5)
R07	92428-01-04-00	54143.890	bkn×(bb+ga)	2.33(1)	34(2)	2.9(1)	5.4(1)	1.02(4)	0.044(2)	0.85(1)	1391(119)	0.97(1)	70	1.71	-7.81(1)	23.5(4)
R07	92428-01-04-02	54144.098	bkn×(bb+ga)	2.32(1)	33(3)	3.1(2)	5.5(2)	1.01(5)	0.044(3)	0.87(1)	1201(116)	0.99(2)	70	1.54	-7.84(1)	22.2(4)
R07	92428-01-04-03	54144.883	bkn×(bb+ga)	2.36(2)	22(8)	2.8(2)	5.5(3)	1.10(5)	0.047(3)	0.86(1)	1645(129)	1.04(5)	70	1.72	-7.73(1)	27.0(3)

Trans. ID	Observation ID	MJD	Best-fit Model	Γ_1	E_b (keV)	Γ_2	K_{pow}	σ (eV)	K_{line}	kT_{in} (keV)	K_{disc}	C	ν	χ^2_ν	$\log(F_{disc})$ erg/s/cm^2	DF (%)
R07	92428-01-04-04	54145.974	bkn×(bb+ga)	2.41(1)	41(6)	3.3(5)	5.8(2)	1.01(5)	0.039(2)	0.86(1)	1770(125)	0.94(2)	70	1.51	-7.68(1)	27.3(4)
R07	92035-01-04-00	54147.031	bkn×(bb+ga)	2.51(1)	29(3)	2.9(1)	5.4(2)	1.03(4)	0.036(2)	0.876(7)	2628(123)	1.00(2)	70	1.48	-7.484(7)	38.0(3)
R07	92035-01-04-01	54148.153	pow×(bb+ga)	2.47(3)	-	-	2.1(1)	0.84(5)	0.019(1)	0.826(5)	4196(154)	1.09(4)	72	1.90	-7.381(6)	66.5(5)
R07	92085-01-01-00	54150.761	pow×(bb+ga)	2.36(2)	-	-	1.29(6)	0.94(4)	0.018(1)	0.842(4)	3936(115)	0.99(3)	72	1.49	-7.377(4)	77.3(2)
R07	92085-01-01-04	54151.816	pow×(bb+ga)	2.38(2)	-	-	1.86(9)	1.03(4)	0.024(1)	0.838(4)	3806(123)	0.97(3)	72	1.74	-7.400(5)	69.2(3)
R07	92085-01-01-05	54152.855	pow×(bb+ga)	2.37(2)	-	-	1.04(7)	0.91(4)	0.016(1)	0.823(4)	4454(137)	1.01(4)	72	1.33	-7.362(5)	81.5(2)
D07	92704-03-06-02	54223.227	pow×(bb+ga)	2.34(7)	-	-	0.30(5)	0.71(6)	0.0048(4)	0.642(7)	1939(136)	1.3(2)	72	1.27	-8.16(1)	71.2(5)
D07	92704-03-06-03	54223.293	pow×(bb+ga)	2.40(9)	-	-	0.35(9)	0.73(8)	0.0044(6)	0.62(1)	2273(248)	1.4(3)	72	1.14	-8.14(2)	68.3(6)
D07	92704-03-07-00	54224.124	pow×bb	3.06(7)	-	-	1.6(3)	-	-	0.53(2)	4845(1518)	1.9(4)	74	1.74	-8.10(5)	22(2)
D07	92704-03-07-01	54225.253	pow×(bb+ga)	2.34(7)	-	-	0.28(5)	0.75(7)	0.0038(4)	0.633(9)	1802(157)	-	43	1.64	-8.22(1)	69.4(7)
D07	92704-03-08-00	54226.106	pow×(bb+ga)	2.33(4)	-	-	0.34(4)	0.82(4)	0.0054(3)	0.668(6)	1431(81)	1.0(1)	72	1.82	-8.220(9)	65.4(5)
D07	92704-03-08-01	54227.624	pow×(bb+ga)	2.08(7)	-	-	0.13(3)	0.86(6)	0.0042(4)	0.633(7)	1843(137)	1.1(2)	72	1.85	-8.21(1)	82(1)
D07	92704-03-09-00	54228.399	pow×(bb+ga)	2.24(6)	-	-	0.22(4)	0.76(6)	0.0038(3)	0.637(8)	1575(132)	1.0(1)	72	1.92	-8.26(1)	73(1)
D07	92704-03-10-00	54231.616	pow×(bb+ga)	2.22(6)	-	-	0.24(4)	0.83(5)	0.0052(4)	0.665(8)	1256(97)	1.0(1)	72	1.60	-8.29(1)	70(1)
D07	92704-03-10-11	54232.682	pow×(bb+ga)	2.16(4)	-	-	0.22(3)	0.93(4)	0.0060(3)	0.672(7)	1153(72)	1.1(1)	72	1.94	-8.30(1)	69.3(9)
D07	92704-03-11-00	54234.858	pow×(bb+ga)	1.98(3)	-	-	0.26(2)	0.82(6)	0.0056(4)	0.77(2)	214(32)	0.90(7)	72	1.41	-8.80(2)	35(2)
D07	92704-03-11-01	54235.797	pow×(bb+ga)	1.85(3)	-	-	0.20(2)	0.96(7)	0.0058(5)	0.80(2)	135(23)	0.91(6)	72	1.67	-8.92(3)	30(2)
D07	92704-04-01-00	54236.383	pow×(bb+ga)	1.90(3)	-	-	0.25(2)	0.76(7)	0.0049(5)	0.84(4)	81(21)	0.94(5)	72	1.12	-9.06(4)	22(2)
D07	92704-04-01-01	54236.455	pow×(bb+ga)	1.80(3)	-	-	0.19(1)	0.90(6)	0.0055(4)	0.82(2)	113(18)	0.94(5)	72	1.30	-8.97(2)	27(1)
D07	92704-04-01-02	54236.523	pow×(bb+ga)	1.80(3)	-	-	0.20(2)	0.86(8)	0.0046(5)	0.96(4)	43(10)	0.89(5)	72	1.12	-9.11(3)	21(1)
D07	92704-03-12-00	54236.597	pow×(bb+ga)	1.83(5)	-	-	0.21(3)	0.9(2)	0.0039(9)	0.97(7)	36(13)	0.92(7)	72	1.41	-9.28(4)	14(1)
D07	92704-04-01-03	54237.298	pow×(bb+ga)	1.78(4)	-	-	0.18(2)	1.0(1)	0.0052(7)	0.89(4)	64(15)	-	43	0.81	-9.06(3)	23(2)
D07	92704-04-01-04	54237.365	pow×(bb+ga)	1.78(3)	-	-	0.18(2)	0.96(7)	0.0054(5)	0.90(4)	62(14)	-	43	1.14	-9.07(3)	22(2)
D07	92704-04-01-05	54237.433	pow×(bb+ga)	1.74(3)	-	-	0.16(1)	1.00(7)	0.0053(5)	0.94(3)	51(10)	-	43	1.21	-9.07(3)	23(1)
D07	92704-03-12-01	54237.501	pow×(bb+ga)	1.78(3)	-	-	0.18(1)	0.93(7)	0.0050(5)	0.89(3)	62(13)	0.89(4)	72	1.67	-9.08(3)	22(1)
D07	92704-04-01-06	54237.704	pow×(bb+ga)	1.80(2)	-	-	0.20(1)	0.87(9)	0.0039(4)	0.96(4)	36(8)	-	43	1.65	-9.18(3)	18(1)
D07	92704-03-13-00	54238.750	pow×(bb+ga)	1.66(4)	-	-	0.15(2)	1.1(1)	0.0039(7)	0.95(6)	31(12)	0.95(5)	72	1.19	-9.42(5)	11(1)
D07	92704-03-13-01	54239.743	bkn×(bb+ga)	1.57(3)	39(5)	2.8(6)	0.12(1)	0.8(2)	0.0025(6)	1.10(9)	13(5)	0.93(4)	70	0.98	-9.38(4)	13.4(9)
D07	92704-03-13-02	54240.308	pow×(bb+ga)	1.63(3)	-	-	0.14(1)	0.6(1)	0.0024(4)	0.95(8)	21(11)	0.88(4)	72	0.79	-9.44(5)	10(1)
D07	92704-03-14-00	54241.570	pow×bb	1.49(5)	-	-	0.09(1)	-	-	1.58(7)	2.4(4)	0.91(5)	74	1.13	-9.51(6)	10(1)
D07	92704-03-14-01	54242.884	pow×(bb+ga)	1.52(2)	-	-	0.094(5)	0.7(1)	0.0018(3)	1.05(8)	10(4)	0.82(4)	72	0.83	-9.58(4)	8.5(7)
D07	92704-03-14-02	54243.864	pow×bb	1.48(5)	-	-	0.08(1)	-	-	1.53(8)	2.0(3)	-	45	1.07	-9.64(6)	8(1)
D07	92704-03-14-03	54244.979	pow×(bb+ga)	1.52(4)	-	-	0.083(4)	0.0(2)	0.0008(1)	1.2(1)	5(2)	-	43	0.89	-9.72(5)	7.2(8)
D07	92704-04-02-00	54245.794	pow×(bb+ga)	1.48(2)	-	-	0.070(3)	0.8(1)	0.0015(2)	0.84(4)	25(7)	-	43	1.09	-9.57(4)	10.6(9)
D07	92704-04-02-02	54245.892	pow×(bb+ga)	1.51(3)	-	-	0.078(6)	0.8(3)	0.00012(4)	1.0(1)	11(7)	0.89(4)	72	0.95	-9.80(5)	6.2(6)
D07	92704-03-15-00	54246.873	pow×(bb+ga)	1.52(4)	-	-	0.074(8)	0.0(4)	0.0005(1)	1.1(2)	3(3)	-	43	0.86	-9.90(7)	5.5(7)

Trans. ID	Observation ID	MJD	Best−fit Model	Γ_1	E_b (keV)	Γ_2	K_{pow}	σ (eV)	K_{line}	kT_{in} (keV)	K_{disc}	C	ν	χ^2_ν	$\log(F_{disc})$ erg/s/cm²	DF (%)
D07	92704-03-16-00	54247.923	bkn×bb	1.49(6)	29(11)	1.8(3)	0.06(1)	-	-	1.4(2)	1.4(5)	1.01(9)	72	1.18	-9.9(1)	6(1)
D07	92704-03-17-00	54248.836	bkn×(bb+ga)	1.46(4)	29(12)	1.8(3)	0.055(6)	0.9(2)	0.0011(3)	1.0(1)	8(6)	0.91(8)	70	0.71	-9.81(7)	8(1)
D07	92704-03-18-00	54249.556	pow×bb	1.48(5)	-	-	0.053(7)	-	-	1.5(1)	1.1(4)	0.91(6)	74	1.23	-8.0(1)	5(1)
D07	92704-03-19-00	54250.731	pow×(bb+ga)	1.45(4)	-	-	0.044(5)	0.2(2)	0.0004(1)	1.2(1)	2(2)	0.72(5)	72	0.83	-9.99(6)	6.0(7)
D07	92704-04-02-01	54251.708	pow×(bb+ga)	1.47(3)	-	-	0.042(3)	1.1(2)	0.0009(2)	0.96(9)	6(3)	0.87(4)	72	0.82	-9.99(7)	6.6(9)
D07	92704-04-02-03	54251.780	pow×(bb+ga)	1.50(3)	-	-	0.044(4)	0.8(2)	0.0006(2)	1.1(1)	3(2)	-	43	0.69	-10.09(7)	5.5(8)
D07	92704-04-02-04	54251.848	pow×bb	1.50(5)	-	-	0.044(6)	-	-	1.6(1)	0.5(2)	0.99(7)	74	1.18	-10.2(1)	5(1)
D07	92704-03-22-00	54254.925	pow×bb	1.57(6)	-	-	0.043(7)	-	-	1.2(3)	1(2)	-	45	1.19	-10.3(2)	4(1)
D07	92704-03-24-00	54256.302	pow×bb	1.51(8)	-	-	0.036(7)	-	-	1.4(2)	0.6(4)	-	45	1.05	-10.3(2)	5(2)
D07	92704-04-03-00	54256.612	pow×bb	1.48(5)	-	-	0.031(4)	-	-	1.7(1)	0.38(8)	0.89(6)	74	1.06	-10.2(1)	6(1)
R10	95409-01-12-00	55281.592	pow×(bb+ga)	1.53(1)	-	-	0.75(2)	0.87(7)	0.019(1)	0.85(4)	204(50)	-	43	1.57	-8.64(3)	9.8(7)
R10	95409-01-12-04	55286.738	pow×(bb+ga)	1.59(1)	-	-	1.00(3)	0.80(6)	0.021(2)	0.78(4)	349(104)	-	43	1.85	-8.56(4)	10.1(9)
R10	95409-01-13-03	55288.380	pow×(bb+ga)	1.575(9)	-	-	0.97(2)	0.96(5)	0.026(2)	0.80(3)	367(82)	-	43	1.98	-8.51(3)	11.2(8)
R10	95409-01-13-00	55289.628	pow×(bb+ga)	1.587(9)	-	-	1.02(2)	0.95(5)	0.026(2)	0.81(3)	340(78)	-	43	1.87	-8.51(3)	10.9(8)
R10	95409-01-13-05	55292.796	pow×(bb+ga)	1.61(1)	-	-	1.18(4)	0.93(7)	0.031(2)	0.82(4)	346(100)	-	43	1.49	-8.49(4)	10.6(9)
R10	95409-01-13-01	55293.095	pow×(bb+ga)	1.625(9)	-	-	1.25(3)	0.80(6)	0.025(2)	0.88(4)	212(63)	-	43	1.80	-8.57(4)	8.8(7)
R10	95409-01-13-06	55294.129	pow×(bb+ga)	1.624(9)	-	-	1.24(3)	0.97(5)	0.032(2)	0.85(3)	264(63)	-	43	1.33	-8.54(3)	9.4(7)
R10	95409-01-14-00	55295.008	pow×(bb+ga)	1.66(1)	-	-	1.32(4)	0.82(6)	0.026(2)	0.80(4)	352(106)	-	43	1.54	-8.51(4)	10.2(9)
R10	95409-01-14-02	55297.883	pow×(bb+ga)	1.852(8)	-	-	2.03(4)	0.96(4)	0.037(2)	0.84(3)	391(73)	-	43	1.89	-8.39(2)	12.5(7)
R10	95409-01-14-06	55299.787	pow×(bb+ga)	2.07(1)	-	-	3.01(8)	0.95(4)	0.039(2)	0.77(2)	1045(153)	-	43	1.85	-8.11(2)	19.7(9)
R10	95409-01-18-04	55327.044	pow×(bb+ga)	2.43(6)	-	-	2.0(3)	0.96(7)	0.028(2)	0.768(8)	3461(198)	-	43	1.61	-7.59(1)	57.3(2)
D11	96409-01-02-02	55573.469	pow×(bb+ga)	2.34(8)	-	-	0.35(8)	0.76(6)	0.0057(6)	0.61(1)	2662(271)	-	43	1.96	-8.10(2)	71(1)
D11	96409-01-04-02	55586.502	pow×(bb+ga)	2.3(1)	-	-	0.31(8)	0.8(1)	0.0044(6)	0.62(2)	1765(285)	-	43	1.86	-8.27(2)	65(1)
D11	96409-01-04-07	55587.503	pow×(bb+ga)	2.2(1)	-	-	0.2(1)	0.8(2)	0.0038(9)	0.60(2)	1640(422)	-	43	1.08	-8.34(3)	68(3)
D11	96409-01-04-08	55588.554	pow×(bb+ga)	2.3(2)	-	-	0.18(8)	0.8(1)	0.0031(6)	0.57(2)	2307(590)	-	43	1.35	-8.28(4)	75(4)
D11	96409-01-05-04	55590.441	pow×(bb+ga)	2.4(1)	-	-	0.3(1)	0.6(1)	0.0031(6)	0.58(3)	1787(610)	-	43	1.29	-8.38(4)	58(3)
D11	96409-01-05-05	55592.739	pow×(bb+ga)	2.1(1)	-	-	0.15(5)	0.94(9)	0.0046(6)	0.63(2)	1024(196)	-	43	1.93	-8.47(2)	68(3)
D11	96409-01-05-03	55594.902	pow×(bb+ga)	2.11(6)	-	-	0.20(3)	0.75(7)	0.0040(4)	0.66(2)	571(97)	-	43	1.86	-8.63(2)	53(2)
D11	96409-01-06-00	55597.264	pow×(bb+ga)	1.94(6)	-	-	0.17(3)	1.0(1)	0.0045(6)	0.76(3)	163(40)	-	43	1.40	-8.94(3)	35(2)
D11	96409-01-06-01	55598.677	pow×(bb+ga)	1.90(5)	-	-	0.14(2)	0.79(7)	0.0041(4)	0.74(2)	198(34)	-	43	1.24	-8.89(2)	41(2)
D11	96409-01-06-02	55601.891	pow×(bb+ga)	1.66(4)	-	-	0.09(1)	1.05(9)	0.0041(5)	0.83(3)	63(14)	-	43	0.72	-9.19(3)	25(2)
D11	96409-01-07-00	55603.992	pow×(bb+ga)	1.67(6)	-	-	0.10(2)	0.9(2)	0.0020(6)	0.8(1)	28(23)	-	43	0.88	-9.52(9)	13(3)
D11	96409-01-07-03	55604.912	pow×(bb+ga)	1.63(4)	-	-	0.088(9)	0.7(2)	0.0014(4)	0.76(7)	45(31)	-	43	0.93	-9.50(7)	14(2)

Trans. ID	Observation ID	MJD	Best−fit Model	Γ_1	$E_{\rm b}$ (keV)	Γ_2	$K_{\rm pow}$	σ (eV)	$K_{\rm line}$	$kT_{\rm in}$ (keV)	$K_{\rm disc}$	C	ν	χ^2_ν	$\log(F_{\rm disc})$ erg/s/cm^2	DF (%)

Table 2.3: Best-fit parameters and 1σ standard uncertainty in parentheses for all observations where a disc was deemed required. The spectral models employed for the disc and continuum were diskbb and powerlaw (or bknpower), respectively. The Fe Kα line at 6.4 keV is fit with the gauss model. The entire model is absorbed using phabs with $N_{\rm H} = 5.7 \times 10^{21}$ cm^{-2} (Miller et al. 2009b) and an energy-independent constant is applied to the HEXTE data to account for offset relative to the PCA. A 0.6% systematic error is added to all PCA energy channels. From *left* to *right*, the columns give the state transition ID, observation ID, MJD for the midpoint of the PCA observation, the best-fit XSPEC model, power-law index, break energy[a], high-energy power–law index[a], power-law normalisation, Gaussian line width, Gaussian line normalisation, disc colour temperature as returned by diskbb, disc normalisation, constant applied to the HEXTE data [b], number of degrees of freedom, reduced χ^2, disc flux over the 0.1-10 keV band, and disc fraction. Dashes indicate that a particular parameter was not applicable in the fit. [a]Applies for fits using the bknpower model; [b]Applies for fits using the HEXTE data. The full version of this table for all fits used in this work is available as an electronic supplement.

Chapter 3

A Physical Model for State Transitions in Black Hole X–ray Binaries

3.1   Preface

This paper was published in Monthly Notices of the Royal Astronomical Society, Volume 437, Issue 4, pp. 3994-3999 on February 01, 2014. The author list is: Nixon, C. & Salvesen, G., with both of us contributing equally. Specifically, I am responsible for most of the connections to black hole X-ray binary phenomenology, while Chris is responsible for the details of disc tearing. Here, we propose a toy model for black hole state transitions based on the phenomenon of accretion disc tearing.

Abstract

We present an accretion cycle which can explain state transitions and other observed phenomena in black hole X–ray binaries. This model is based on the process of disc tearing, where individual rings of gas break off the disc and precess effectively independently. This occurs when the Lense–Thirring effect is stronger than the local disc viscosity. We discuss implications of this model for quasi–periodic oscillations and the disc–jet–corona coupling. We also speculate on applying this model to active galactic nuclei and other accreting systems.

3.2   Introduction

Binary systems occur frequently in astrophysics, from supermassive black hole binaries in galaxy mergers to protostellar binaries in star forming regions. When one component of a stellar binary undergoes

a supernova explosion, the result may be an X–ray binary, where the companion star feeds the newly formed neutron star or black hole. These systems show evidence for accretion proceeding through a gas disc (e.g. Pringle & Rees, 1972; Pringle, 1981).

X–ray binaries display a wide variety of spectral and timing properties, with many observable features such as jets, disc winds, coronae, quasi–periodic oscillations and strong disc emission and reflection. Black hole state transitions exhibit all of these complex and interacting features, making a theoretical understanding challenging to construct. However, a powerful phenomenological description emerges from model–independent spectral and timing observations (for a recent review, see Belloni, 2010). Magnetohydrodynamical (MHD) effects are often supposed to be the underlying physics responsible for this behaviour. However, the aim of this paper is to propose a physically motivated and self–consistent mechanism, using mainly hydrodynamical effects, to explain black hole state transitions.

Accretion discs are often thought to be warped, with conclusive evidence from maser discs in active galactic nuclei (AGN; Greenhill et al., 2003) and suggestive observations in X–ray binaries (e.g. Katz, 1973; Wijers & Pringle, 1999; Ogilvie & Dubus, 2001; Miller et al., 2006c), protostellar discs (e.g. Hughes et al., 2009), and perhaps ultraluminous X–ray sources (e.g. Pasham & Strohmayer, 2013). In X–ray binaries the black hole spin can be strongly misaligned to the binary orbit by a supernova kick during formation (e.g. Jonker & Nelemans, 2004). This misalignment can persist for the entire lifetime of the system as the black hole angular momentum is much larger than the total angular momentum transferred through the disc (e.g. Maccarone, 2002; Nixon & King, 2013). For discs with angular momentum misaligned to the spin of the black hole, the differential precession induced by the Lense & Thirring (1918) effect is communicated through the disc by a viscosity (Bardeen & Petterson, 1975). This (effective) viscosity most likely arises from MHD turbulence induced by the magnetorotational instability (Balbus & Hawley, 1991). There is observational evidence for Lense–Thirring precession in X–ray binaries (e.g. Miller & Homan, 2005; Schnittman et al., 2006). Assuming the disc can efficiently communicate the precession, this results in an aligned inner disc joined to a misaligned outer disc by a smooth warp (see e.g. Pringle, 1992; Lodato & Pringle, 2006).

Most investigations into warped discs use simplistic forms of the disc viscosity (e.g. Pringle, 1992) as this allows for simulation of thin discs with $\alpha > H/R$ (Papaloizou & Pringle, 1983). Some simulations of

tilted discs explicitly include MHD effects to generate a turbulent viscosity, but these are currently restricted to thick discs (Fragile et al., 2007, 2009; McKinney et al., 2013; Sorathia et al., 2013a). To make progress on thin discs, Nixon & King (2012) simulated the disc evolution using the method of Pringle (1992) with the constrained isotropic viscosities derived from the fluid equations for a warped disc by Ogilvie (1999). Their simulations suggest that often the disc cannot communicate the precession as efficiently as required to maintain a smooth warp – instead the disc breaks. Follow–up 3D hydrodynamical simulations found that the disc is indeed unable to communicate the precession, and therefore breaks into distinct planes which precess effectively independently – this is disc tearing (Nixon et al., 2012a). These simulations also show significant dynamical evolution of the disc, predominantly infall of gas between interacting torn rings. In this paper, we explore an accretion picture for black hole state transitions which includes the disc tearing process.

3.3   Accretion picture

We describe an accretion cycle for black hole binary state transitions incorporating disc tearing (Nixon et al., 2012a). We begin with plausible, generic initial conditions summarised as follows.

1) *A black hole with non–negligible spin.* A modest value of the black hole spin, $a > 0.01$, is more than sufficient to drive disc tearing (eq. 8 of Nixon et al., 2012a). Current estimates of stellar mass black hole spins suggest moderate–to–high values with $0.1 \lesssim a \lesssim 1$ (e.g. Miller et al., 2009b; McClintock et al., 2014; Reynolds, 2014).

2) *A geometrically thin, optically thick disc of gas at some large radius from the black hole.* This is consistent with the accretion event being triggered by a disc instability, such as the thermal–viscous instability driven by hydrogen ionization (Meyer & Meyer-Hofmeister, 1982; Smak, 1982; Lasota, 2001).

3) *A misalignment between the angular momenta of the accretion disc and the black hole.* Again only a modest disc–spin misalignment angle, $\theta >$ a few degrees, is required (Nixon et al., 2012a). Large disc–spin misalignments may be common (e.g. Maccarone, 2002; Martin et al., 2010). There is currently little constraint on the disc–spin misalignment. Population synthesis studies (e.g. Fragos et al., 2010) can generate the likelihood of disc–spin misalignments, but much of the input physics of binary formation and black hole kicks is not understood. Therefore it is likely that the results of Fragos et al. (2010), that most binaries
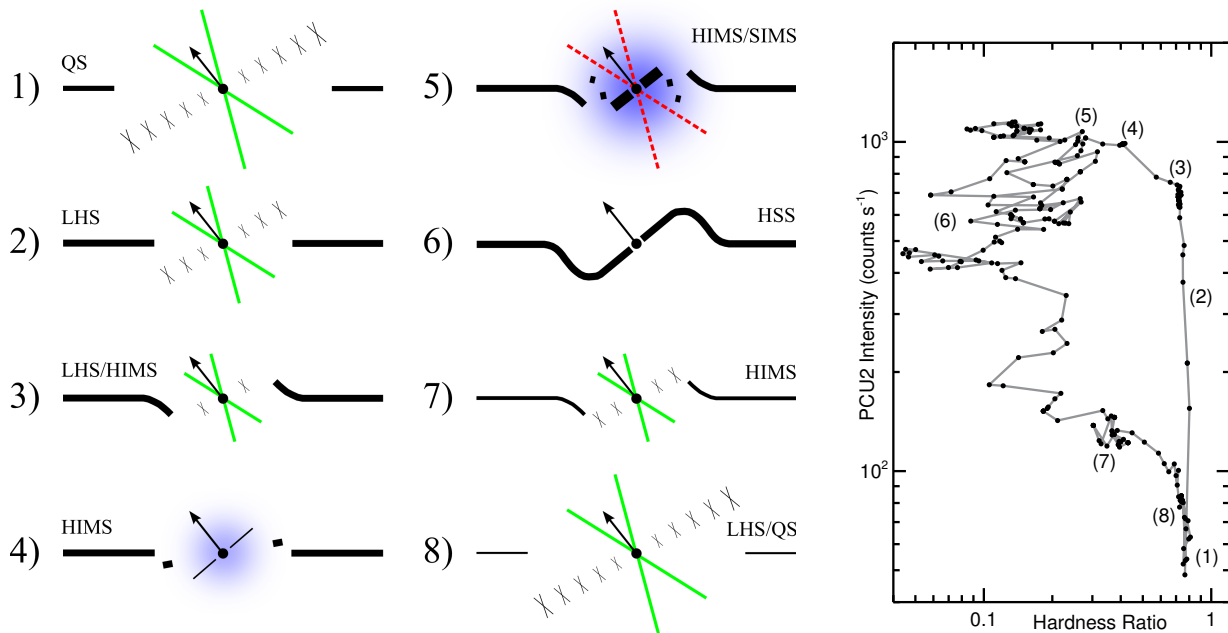
Figure 3.1: The *left panel* shows the different stages of the tearing accretion cycle. In each part the black circle represents the black hole, with the arrow showing the direction of its spin. Solid black lines show the (sometimes warped) Shakura–Sunyaev disc, which in (4) & (5) has torn, with the thickness approximately denoting its surface density. "X"s mark regions of hot, low–density gas. The quasi–spherical blue component is the corona. Possible jets are shown by lines leaving the central black hole, green solid lines suggest a steady jet and red dashed lines suggest a transient jet. The figure shows the progression of the system, with each black hole state labelled. The cycle starts with a disc approaching the black hole (1) → (2). The initial disc warps (3) and the first ring is torn off (4). The main tearing phase is (5): see Section 3.3.3. Once the inner disc aligns, the accretion is more stable (6). As the surface density drops, the hot inner disc is revived (7), and the system returns to its original quiescent state (8) & (1). We note that a precessing, warped disc is a 3D structure (see e.g. Fig. 3.2), so the 2D representation shown here is a simple conceptualisation. The *right panel* shows where these eight stages lie on a representative hardness–intensity diagram (data from the 2002/2003 GX 339–4 outburst, see e.g. Salvesen et al., 2013).

have $\theta \lesssim 10°$ but up to a third may have $\theta \gtrsim 10°$, represents a lower–bound on the possible disc–spin misalignments. Also, analysis of individual sources (e.g. Steiner & McClintock, 2012) can reveal some aspects of the disc–spin misalignment by comparing the binary inclination with the jet inclination. However, this only tests for misalignment along the line–of–sight, offering no constraint perpendicular to this plane. Therefore, one cannot constrain the true disc–spin misalignment, as noted by Steiner & McClintock (2012).

3.3.1 Disc evolution

Fig. 3.1 shows the disc evolution starting from the initial conditions described above. The eight stages in the accretion cycle are:

1) An outer Shakura–Sunyaev disc moves inwards towards the black hole, but is still at large radii. Interior to this disc, there is hot, low–density gas present from the last accretion event. This gas may provide the necessary conditions to produce the steady jet sometimes observed in the quiescent state.

2) The outer disc approaches the black hole, with increasing surface density, decreasing the size of the hot, low–density region.

3) The outer disc reaches a radius where the Lense–Thirring precession begins to affect the disc, driving a warp on the inner edge. This occurs at a radius where the inflow time (R^2/ν) becomes comparable to the Lense–Thirring precession time $(1/\Omega_{\rm p})$, which is at

$$R_{\rm tilt} \sim 2^{2/3} \left(\frac{a}{\alpha}\right)^{2/3} \left(\frac{R}{H}\right)^{4/3} R_{\rm g} \approx 1 \times 10^3 R_{\rm g} \tag{3.1}$$

where $R_{\rm g} = GM/c^2$ is the gravitational radius of a black hole of mass M and we have assumed a Shakura & Sunyaev (1973) viscosity $\nu = \alpha H^2 \Omega$ where α is the dimensionless viscosity parameter, H is the disc semi–thickness at a radius R and Ω is the disc angular velocity. We adopt typical parameters throughout: $a = 0.5$ (e.g. Miller et al., 2009b), $\alpha = 0.1$ (e.g. King et al., 2007) and $H/R = 0.02$ (e.g. Shakura & Sunyaev, 1973). Equation 1 is derived through analogous reasoning to Natarajan & Pringle (1998) who compared the precession time to the vertical viscous time to find the location of a warp in a steady state disc. Here we use the usual planar disc viscosity, appropriate for a disc approaching the black hole from large radius.

4) The first ring of gas is torn from the disc, precessing effectively independently. Any interaction of this

ring with the outer disc causes shocks which produce hot gas and dynamical infall after cooling. Any gas that cannot cool quickly enough fuels the corona. There may or may not be an inner disc during this phase. Tearing of disc rings occurs inside (Nixon et al., 2012a)

$$R_{\mathrm{break}} \sim \left(\frac{4}{3} |\sin\theta| \frac{a}{\alpha} \frac{R}{H} \right)^{2/3} R_{\mathrm{g}} \approx 50 \; R_{\mathrm{g}}. \tag{3.2}$$

This radius depends (weakly) on the disc–spin inclination angle. For angles $\lesssim$ a few $\times \, H/R$ the disc is unlikely to tear (see e.g. the discussion of Nixon et al., 2013). For a modest inclination angle of $30°$ the tearing radius is $R_{\mathrm{break}} \approx 30 R_{\mathrm{g}}$.

5) The disc reaches a quasi–steady tearing phase, where successive rings are torn off and interact (see Fig. 3.2). This produces both an aligned inner disc from gas that cools, and a strong corona from gas that remains hot (for more detail see Section 3.3.3). The main physics in this interaction is the shocks between adjacent rings. The inner disc, which extends down to the innermost stable circular orbit (ISCO), has a variable mass accretion rate and probably drives short–lived powerful jets while the accretion rate is high. The tearing phase continues as long as misaligned gas is supplied to the tearing region, which persists until the disc aligns from the inner regions outwards. Therefore, the tearing process proceeds for a time $\lesssim t_{\mathrm{align}}(R_{\mathrm{tilt}})$. The alignment timescale is given by King et al. (2013b), which (with $M = 10 \; M_{\odot}$) gives

$$t_{\mathrm{align}}(R_{\mathrm{tilt}}) \sim \frac{1}{4\alpha a^2} \left(\frac{H}{R} \right)^2 \left(\frac{R_{\mathrm{tilt}}}{R_{\mathrm{g}}} \right)^{9/2} \frac{GM}{c^3} \approx 35 \; \mathrm{days}. \tag{3.3}$$

We choose the radius for this timescale as R_{tilt}, rather than R_{break}, as the viscous communication of angular momentum causing alignment is significantly reduced in a strong warp (Ogilvie, 1999; Nixon & King, 2012; Lodato & Gerosa, 2013). To prevent tearing entirely the disc must be unable to feed the tearing region with misaligned angular momentum. This estimate is subject to some uncertainty, and requires further investigation (see e.g. the discussion by King et al., 2013b). As the disc is not in a steady state, it is plausible that alignment out to $\sim R_{\mathrm{tilt}}$ is required to halt tearing, but it is also possible that disc tearing can be halted sooner by alignment at a smaller radius, closer to R_{break}. However, the two main uncertainties in the alignment timescale are both likely to increase t_{align} by reducing the vertical viscosity responsible for transferring the misaligned angular momentum. First, this viscosity is expected to weaken as the warp amplitude increases (Lodato & Gerosa, 2013). Second, MHD effects are expected to weaken this viscosity

further (see e.g. Pringle, 1992; Nixon et al., 2012a; Sorathia et al., 2013b, and Section 3.4).

6) The inner disc is now closely aligned with the black hole spin beyond the break radius, which inhibits tearing. A strong Shakura–Sunyaev disc component extends down to the ISCO. The outer disc remains misaligned and joined to the inner disc by a warped region. The innermost disc is not subject to the strong depositions of gas present in (5). Therefore the jet probably switches off in this state (cf. King et al., 2004).

7) As the accretion event runs out of mass supplied from large radius, the disc surface density drops. Eventually, this allows inefficient cooling to revive the inner hot disc.

8) Finally, the accretion event is over and the system returns to the initial state.

3.3.2   State transitions

We now describe the behaviour of observed systems by stepping through the state transition phenomenology, while matching the observations (see e.g. Belloni, 2010, and references therein) to each of the eight stages of the disc tearing accretion picture in Fig. 3.1.

Quiescent state (QS): In quiescence there is no Shakura–Sunyaev disc inside $\sim 10^2 R_\mathrm{g}$, but a hot gas component may be present interior to this (e.g. Esin et al., 2001; Tomsick et al., 2009), possibly driving a steady low–luminosity jet. The accretion cycle starts (1) and ends (8) here.

Low/hard state (LHS): As the system comes out of quiescence, a Shakura–Sunyaev disc appears (e.g. Miller et al., 2006a; Reis et al., 2010). A persistent steady jet is seen (e.g. Fender, 2001), suggesting that some inner hot gas is still present (2) & (3). By the end of the LHS, type–C low–frequency quasi–periodic oscillations (LF QPOs), discussed below, emerge.

Hard–intermediate state (HIMS): This state is not marked by any sudden spectral or timing changes and is consistent with a continuation of the LHS. The steady jet turns off and the type–C LF QPOs evolve to higher frequencies in the LHS $\rightarrow$ HIMS transition. An inner disc extending to the ISCO is often observed contemporaneously with the LHS $\rightarrow$ HIMS transition and a corona emerges. In our accretion picture, this is when the first ring is torn from the disc (4). Shocks between this ring and the outer disc create the corona (see Section 3.3.3) and possibly a disc that spreads down to the ISCO. This gas sweeps away the hot flow still present in (3), turning off the steady jet.
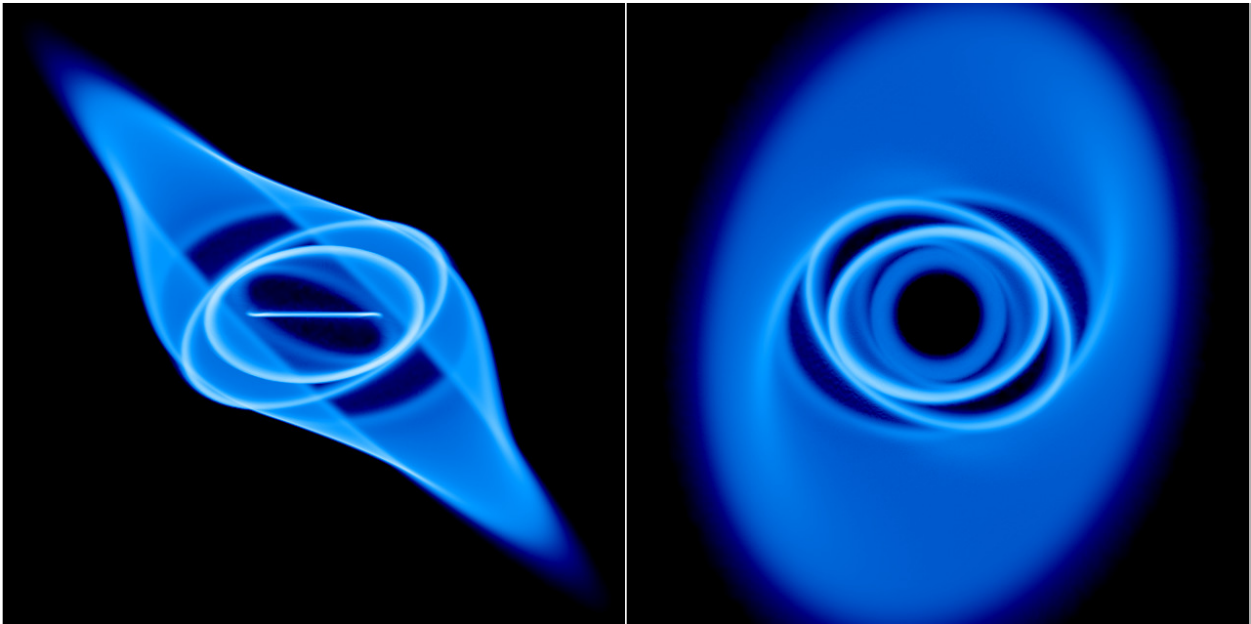
Figure 3.2: Column density projection showing the disc structure for a tearing disc simulation with a disc–spin misalignment of 45°. The two plots show the same disc from different angles. The *left panel* has the black hole spin pointing up the page, while the *right panel* has the spin pointing out of the page. The simulation, to be presented in a future paper, follows the method of Nixon et al. (2012a), but uses a smaller accretion radius allowing the innermost disc to be resolved. The innermost disc is closely aligned to the black hole spin because the tilted components of the angular momentum vectors cancel when the precessing rings interact, leading to dynamical infall (see eqns. 3 & 4 of Nixon et al., 2013).

Soft–intermediate state (SIMS): The transition from the HIMS to SIMS is marked by both the appearance of type–B LF QPOs, and relativistic transient (i.e. ballistic) jets. Much weaker type–A LF QPOs are sometimes seen, but type–C LF QPOs no longer persist. The compact corona becomes more prominent and a strong disc extends down to the ISCO, where it remains throughout HIMS $\leftrightarrow$ SIMS transitions (Reis et al., 2013). Section 3.3.3 elaborates on the details of this disc–jet–corona connection. This transition between the HIMS and SIMS is the main tearing phase (5), described in detail in Section 3.3.3. The tearing rings quasi–periodically fuel the corona and the inner disc. A powerful jet can be launched when the accretion rate through the inner disc is high.

High/soft state (HSS): This state is characterised by a spectrally dominant Shakura–Sunyaev disc component present down to the ISCO. This is well–matched by (6) where a stable, long–lived accretion disc extends down to the ISCO, aligned to the black hole spin. In this phase, the disc is thin, so jets are probably strongly suppressed (e.g. Tananbaum et al., 1972; Fender et al., 1999a). However, disc winds are common (e.g. Miller et al., 2008; King et al., 2013a). Tentative evidence for a warped disc in a microquasar was found by Miller et al. (2006c) who observed an obscured disc wind consistent with modulation by a disc warp. A standard thin disc closely following the $L_{\mathrm{disc}} - T_{\mathrm{eff}}^4$ relation is robustly detected across a broad range of mass accretion rates in the HSS, with departures from this relation arising in the intermediate states and LHS (e.g. Dunn et al., 2011). However, if a variable spectral hardening factor is permitted, this scaling relation may extend into the intermediate states and LHS (Salvesen et al., 2013; Reynolds & Miller, 2013).

Decay HSS $\rightarrow$ HIMS $\rightarrow$ LHS/QS: In the outburst decay, the system returns to the HIMS when the aligned inner disc is accreted and inefficient cooling allows the hot flow to again pervade the inner regions (7). The SIMS is not re-entered in outburst decay, which is consistent with our accretion picture of the inner disc aligning to the black hole spin (6), halting further disc tearing events that are responsible for the SIMS. The system finally evolves from the HIMS (7) to the LHS (8), accompanied by type-C LF QPOs of decreasing frequency, completing the state transition accretion cycle.

Quasi–periodic oscillations (QPOs): There are three main types of LF QPO observed (Casella et al., 2005). Type–C LF QPOs are predominantly observed in both the rise and decay of the system (e.g. Belloni et al., 2005), whereas types A & B are mostly observed in the SIMS and mark the transitions between the HIMS

and SIMS (Casella et al., 2004). In our accretion picture, the initial warping and precession of the inwardly propagating disc (3) may manifest itself as the evolving type-C LF QPO, which is consistent with previous suggestions (e.g. Ipser, 1996; Stella et al., 1999; Ingram et al., 2009). Type–C LF QPOs are also observed, decreasing in frequency, as the system decays back to the LHS (e.g. Kalemci et al., 2004).

Motta et al. (2011) suggest that type–C and type–A LF QPOs might be the result of the same underlying physics, at different evolutionary stages, with type–B being physically distinct. In the context of this disc tearing model, this result fits naturally with type–A being precessing torn rings or a precessing oblate corona. This also suggests a plausible reason why type–A are weak and sometimes not seen, as the flux from precessing rings is dominated by the stronger components in the system at that time (e.g. inner disc, corona and jet).

3.3.3   Disc–jet–corona coupling

In the transitions between the HIMS and SIMS, corresponding to (5) in Fig. 3.1 and the torn disc structure in Fig. 3.2, observations confirm the presence of an inner disc extending down to the ISCO (e.g. Dunn et al., 2011; Reis et al., 2013), powerful transient jets (e.g. Fender et al., 2004) and a strong dynamic corona (e.g. Reis et al., 2013). The production and interaction between the disc, jet and corona naturally arise from our tearing disc picture as follows. Multiple rings break from the disc in the quasi–steady disc tearing phase (see Fig. 3.2). As these rings precess they shock, cancelling some of their angular momentum but also heating strongly. The cancellation of angular momentum is dependent on the orientation of the rings, with larger disc–spin misalignment angles resulting in more efficient cancellation. Some of the gas cools efficiently to form an inner disc which accretes on to the black hole, while the rest of the gas cannot cool fast enough and so fuels the corona (see *right panel* of Fig. 3.3). While the accretion rate through the inner disc is high, and the disc therefore thick (cf. King et al., 2004), a powerful jet is launched. Recurring accretion events from interacting rings re–supply the inner disc, driving the observed transient jet. The observed decrease in hardness from the HIMS to the SIMS is therefore given by the cooling gas forming an inner disc, whose spectrum peaks in the soft X–ray band.

If *all* of the shocked gas from tearing rings is unable to cool, which seems unlikely but possible
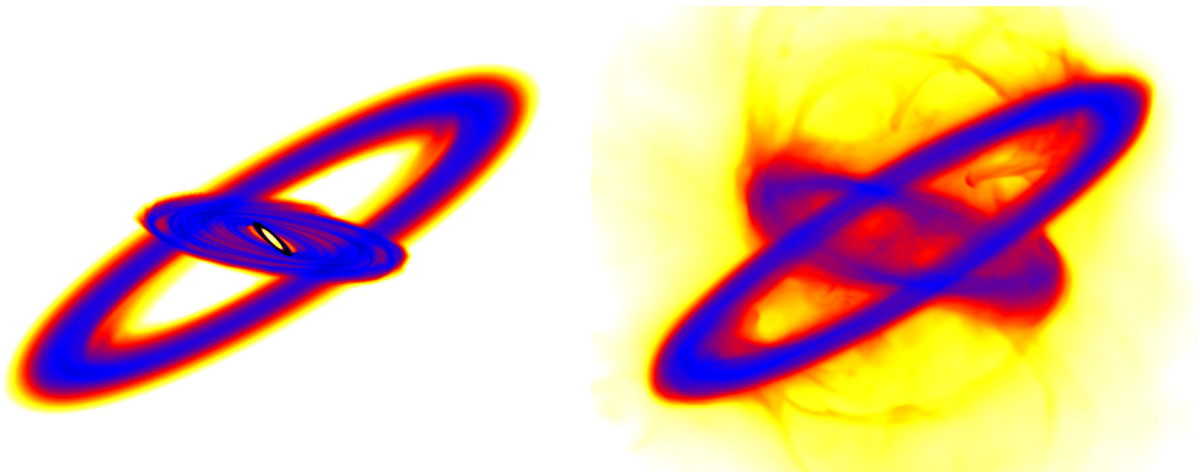
Figure 3.3: Column density projection showing the disc structure from a misaligned rings simulation in Nixon et al. (2012b). The *left panel* uses an isothermal equation of state where gas heating is assumed to be lost as radiation. In contrast, the *right panel* retains the shock heating in the gas, causing it to expand vigorously. In reality the equation of state lies somewhere between these two extremes. Most likely some gas is able to cool and subsequently fall to form an inner disc, while the gas that is unable to cool forms a low–density, quasi–spherical structure – the corona.

dependent on the local conditions (density, etc.), the resultant distribution of gas is quasi–spherical ($H/R \sim 1$) and robbed of a significant part of its angular momentum (implying an effective $\alpha \sim 1$). These are precisely the conditions required to generate radiatively inefficient accretion flows (Narayan & Yi, 1994; Esin et al., 1997; Blandford & Begelman, 1999) or magnetically arrested discs (Bisnovatyi-Kogan & Ruzmaikin, 1974; Narayan et al., 2003; Tchekhovskoy et al., 2011).

3.4   Discussion & conclusions

We have presented a new accretion picture for black hole X–ray binaries. The only assumptions needed in this accretion picture are the three generic initial conditions: (1) A black hole with non–negligible spin. (2) A geometrically thin, optically thick accretion disc far from the black hole. (3) A misalignment between the disc and black hole angular momenta. The new ingredient in the accretion cycle is the process of disc tearing (Nixon et al., 2012a, 2013), which is present in the hard–intermediate and soft–intermediate states. Tearing discs produce a variety of behaviour capable of explaining state transitions and many of the other observed black hole X–ray binary phenomena, including QPOs and the disc–jet–corona connection.

The phenomenological description of accretion in black hole X–ray binaries (e.g. Belloni, 2010) is powerful in explaining the general observed properties. However, these systems are complex and show different behaviour, not just from source to source, but from outburst to outburst in the same source. Our model may well prove robust in this regard as the equations for the various radii and timescales in Section 3.3 are not weakly (nor too strongly) dependent on the disc parameters. Therefore modest changes in the disc conditions can lead to a rich variety of behaviour. For example, the initial ring torn from the disc (4) may occur while the disc has a low surface–density, so cooling is probably inefficient. In this case, tearing may lead to heating of the disc, which temporarily stabilizes it against tearing while the surface density remains low. These details, and other important physical effects (e.g. radiation warping; Pringle, 1996), determine the exact evolution of any given system.

In addition to QPOs discussed in Section 3.3.2, black hole binaries show other timing properties. For example, a positive correlation is observed between rms variability and X–ray flux (Uttley & McHardy, 2001). The trend of increasing varibility with increasing flux is generally consistent with the accretion picture in

Fig 3.1, but requires further investigation. Strong X–ray flux above $2\,\mathrm{keV}$ is expected when a strong coronal component is present, which coincides with the most variable phases of accretion.

The viscous evolution of the disc is probably driven by turbulence induced by the magnetorotational instability (MRI; Balbus & Hawley, 1991). We do not anticipate that including MHD will restrict the tearing behaviour, but this is simply unknown. Progress is being made in this area: investigations using MHD grid codes are starting to look at disc warps (Fragile et al., 2007; Sorathia et al., 2013b), and smoothed particle hydrodynamics simulations are beginning to reliably include MHD (e.g. Price et al., 2012). Some investigations into the effective viscosities in a warped disc have already been performed. For example, Torkelsson et al. (2000) measured the coefficients of the viscosity tensor from MHD turbulence and concluded that they are consistent with an isotropic viscosity, as used in the disc tearing simulations by Nixon et al. (2012a) (cf. Ogilvie, 1999; Lodato & Price, 2010). Also, Ogilvie (2003) developed an analytical model for the dynamical evolution of magnetorotational turbulent stresses in good agreement with Torkelsson et al. (2000). These investigations, numerical *and* analytical, allow for the effective viscosity from MHD turbulence to be anisotropic, but conclude the result is (near) isotropic. Recently King et al. (2013b) placed observational constraints on this viscosity, finding that the precession in Her X-1 is consistent with an isotropic viscosity.

Sorathia et al. (2013a) have since claimed the opposite result, that the effective vertical viscosity is much stronger than predicted by an isotropic model. They simulate a misaligned disc subject to Lense–Thirring precession, including MHD to self-consistently generate a turbulent viscosity. However, due to their choice of parameters (thick, low–viscosity disc and a precession which is faster than dynamical at the inner edge of the grid) it is unclear how relevant this work is to the discs discussed here (cf. Papaloizou & Pringle, 1983). They report that the dominant mechanism transporting angular momentum is bending waves induced by radial pressure gradients, as shown for $\alpha < H/R$ by Papaloizou & Pringle (1983); Papaloizou & Lin (1995) and discussed by Lodato & Pringle (2007). Therefore it appears that this work is consistent with the literature. The main difference is the measurement of a significantly anisotropic effective viscosity, with the vertical viscosity much stronger than isotropy implies. This result appears at odds with previous work on MHD turbulence (Torkelsson et al., 2000; Ogilvie, 2003), but as remarked by Sorathia et al. (2013a), hydrodynamic effects dominate MHD effects and therefore this difference is probably not due to MHD.

Indeed for the parameters used in their simulation, the disc may be vulnerable to hydrodynamic instabilities (see e.g. the parametric instability; Gammie et al., 2000). Such extra dissipation can explain the discrepancy, but without further simulations we can only speculate. However, for typical black hole disc parameters such instabilities are not thought to be important, but certainly worthy of investigation (e.g. Ogilvie & Latter, 2013). For now it appears prudent to continue with the assumption of a (near) isotropic viscosity supported by numerical, analytical and observational results (Torkelsson et al., 2000; Ogilvie, 2003; King et al., 2013b).

The accretion picture proposed here is not particular to black hole X–ray binaries. We therefore briefly discuss some other systems in the context of this accretion picture:

Persistent sources: It is plausible that tearing is entirely suppressed for some system parameters. For example, the mass transfer rate in the X–ray binary SS433 is probably highly super–Eddington, so the disc remains thick all the way down to the ISCO (Begelman et al., 2006) and is therefore unable to experience tearing. Other sources which show persistent or "failed" state transition behaviour may have negligible black hole spin or disc–spin misalignment, thus inhibiting tearing.

Other stellar binaries: There appears no reason to assume that accretion far from the central object occurs differently for different central objects (e.g. Lasota, 2001). Therefore, any model should reduce to the standard accretion model (e.g. Frank et al., 2002) for white dwarf and magnetic neutron star accretion. For neutron stars with weak magnetic fields, a similar cycle as proposed above may arise, as the Lense–Thirring precession is also expected to act in these systems.

Ultraluminous X–ray sources (ULXs): These may be extreme stellar mass black hole binaries with the largest disc–spin misalignments, so the strong shocks induced by disc tearing produce both powerful X–ray emission and significantly enhance the accretion rate. If ULXs contain intermediate mass black holes they may correspond to (5) in Fig. 3.1, evolving on much longer timescales.

Active galactic nuclei: The timescales predicted for state changes in AGN are substantially longer than for X–ray binaries. Therefore, state transitions can only be understood by considering AGN populations. However, it is possible that the different stages of the proposed accretion cycle correspond to different types of AGN. For example, the type I *versus* type II AGN dichotomy may be states (5) & (6) in Fig. 3.1 viewed from the required angle to reveal or obscure the central accretion (cf. Nayakshin, 2005).

There are significant observational data with which we can test this model; high–quality spectral and timing information is available for numerous systems. Substantial progress can also be made on the theoretical side. For example, simulations of interacting rings of gas, with a realistic equation of state, are required to confirm our reasoning in Section 3.3.3. Also, the shocks between rings and the geometry of the disc may provide a physical motivation for disc reflection modelling. We are actively exploring both observational and theoretical considerations of the accretion picture presented in this paper to put this physically motivated black hole state transition model to the test.

Acknowledgments

Chapter 4

Black Hole Spin Measurements are Sensitive to Accretion Disc Spectral Hardening

4.1   Preface

This paper is submitted to Monthly Notices of the Royal Astronomical Society. The author is: Salvesen, G., & Begelman, M. C. The two well-established techniques used to measure black hole spin in X-ray binaries often yield conflicting results, which is troublesome if either method is to be deemed robust. Dissecting one of these methods, we show that incorporating uncertainties associated with the disc atmospheric structure dominates the error budget, particularly for low and moderate black hole spins.

abstract

Black hole spin has profound astrophysical importance, influencing the cosmological evolution of galaxies and offering an energy reservoir for powering relativistic jets. The two well-established techniques for measuring black hole spin often yield conflicting results, which must be resolved before either method may be deemed robust. In practice, the continuum fitting technique does not marginalize over the spectral hardening factor, $f_{\rm col}$, when measuring black hole spin. Considering representative model X-ray binaries, we demonstrate that realistic uncertainties in $f_{\rm col}$ dominate the error budget on the black hole spin. Moderate-to-low black hole spins cannot be reliably constrained when adopting erroneous $f_{\rm col}$ values and/or modest uncertainties on $f_{\rm col}$; however, high spins ($a \gtrsim 0.9$) are relatively insensitive to ignorance of $f_{\rm col}$. To demonstrate this, we incorporate $f_{\rm col}$ uncertainties into the original black hole spin probability distributions

for X-ray binaries with spin measurements vetted by the continuum fitting community. Finally, we suggest that by adopting black hole spin measurements from the iron line technique, absolute measurements of $f_{\rm col}$ can be made with the continuum fitting technique. This could potentially offer a novel way to observationally probe accretion disc atmospheric physics.

4.2   Introduction

The only intrinsic properties of an astrophysical black hole are its mass and angular momentum, or spin (e.g., Misner et al., 1973). While elegant, this "no-hair" theorem reveals a fundamental limitation to the available observational avenues with which to study black holes.

Black hole mass undoubtedly has important astrophysical implications across the mass spectrum, from understanding how supermassive black holes co-evolve with their host galaxies (Magorrian et al., 1998) to the details of the supernovae explosions that produce stellar mass black holes (Bailyn et al., 1998). Fortunately, black hole mass is observationally accessible with a variety of independent techniques. The masses of supermassive black holes can be measured with reverberation mapping (Blandford & McKee, 1982; Peterson et al., 2004), maser discs (e.g., Miyoshi et al., 1995), stellar dynamics (Kormendy & Richstone, 1995; Ghez et al., 2005), gas dynamics (e.g., Barth et al., 2001), and empirical methods such as the $M - \sigma$ relation (Gebhardt et al., 2000; Ferrarese & Merritt, 2000). The masses of stellar mass black holes can be obtained from optical light curve modeling of X-ray binaries (e.g., Orosz & Bailyn, 1997) and microlensing (Agol et al., 2002).

Black hole spin, while currently less-constrained than black hole mass, also has high astrophysical relevance. For instance, the cosmological evolution of the coupled growth between black holes and their host galaxies is imprinted on the spin distribution of supermassive black holes (Volonteri et al., 2013). Relativistic jets, which inject energy into their surroundings and are observed in many black hole systems, may be powered by tapping into the black hole spin energy reservoir (Penrose, 1969; Blandford & Znajek, 1977). Black holes in X-ray binaries cannot change the magnitude of their natal spin appreciably over the system lifetime (King & Kolb, 1999); therefore, these systems offer a laboratory for studying the core-collapse supernovae that produce stellar mass black holes. Accretion discs are also subject to interesting behaviour

in the presence of a spinning black hole. When the black hole spin vector is misaligned to the accretion disc rotational axis, the disc experiences a differential precession (Lense & Thirring, 1918). If strong enough, this precession can cause the disc to break into distinct interacting rings of gas (Nixon et al., 2012a), which may be the underlying mechanism responsible for black hole state transitions (Nixon & Salvesen, 2014). Robust measurements of black hole spin are necessary to realize these far-reaching astrophysical implications.

Observational X-ray astronomy recently commenced an era of measuring black hole spin, with two sophisticated techniques at the forefront of this effort. One method is based on modeling the fluorescent iron emission line profile (Fabian et al., 1989; Laor, 1991), which is a feature in the disc reflection spectrum (Lightman & White, 1988). The other method appeals to modeling the accretion disc continuum spectrum (Zhang et al., 1997). In practice, only the iron line technique can be applied to supermassive black holes. However, independent verification of the robustness of the iron line technique is required if the measured supermassive black hole spins are to be used to constrain cosmic evolution scenarios and other black hole spin-related phenomena. Both spin measurement methods are valid for stellar mass black holes in X-ray binaries; thus, providing two complementary and independent ways to measure black hole spin in these systems.

Miller et al. (2009b) were the first to employ both the iron line and continuum fitting techniques simultaneously to measure black hole spin for a sample of X-ray binaries by linking the spin parameter between the disc reflection and disc continuum spectral components. While broad agreement was found with previous spin measurements from the iron line technique alone, at least two systems (4U 1543–475 and GRO J1655–40) showed strong discrepancies with previous spin measurements from the continuum fitting technique. Steiner et al. (2011) measured the spin of the black hole X-ray binary XTE J1550–564 independently with the iron line and continuum fitting techniques, finding weak agreement between the two methods as a consequence of large uncertainties.

Currently, both black hole spin measurement methods are mature and well-established, each having been applied to a modest population of black hole X-ray binaries (Reynolds, 2014; McClintock et al., 2014). For the six black hole X-ray binaries with spins measured by both the iron line and continuum fitting techniques, there is either disagreement or broad consistency between the derived spins (see Figure 4.1 and

Table 4.1). Significant discrepancies in the black hole spin obtained with two different methods for the same source are troublesome. This warrants an investigation into the validity of the assumptions behind both of these spin measurement techniques, but in this paper we focus on the continuum fitting method.

The continuum fitting technique relies on reliably modeling the observed accretion disc spectrum. Standard models for the emitted disc spectrum neglect the effects of the vertical (i.e., perpendicular to the disc mid-plane) gas structure (e.g., Shakura & Sunyaev, 1973; Novikov & Thorne, 1973). However, as this "seed" disc spectrum propagates through the disc atmosphere, the emergent spectrum will be hardened due to the collective effects of electron scattering and absorptive/emissive opacities. The degree of disc spectral hardening is parametrized by the phenomenological spectral hardening factor (also called the colour correction factor), which is defined as the ratio of the colour-to-effective disc temperatures, $f_{\rm col} = T_{\rm col}/T_{\rm eff}$ (e.g., Shimura & Takahara, 1995). In practice (e.g., McClintock et al., 2006), the observed X-ray disc continuum is fit using a hybrid model consisting of a general relativistic multi-colour blackbody disc around a black hole (Li et al., 2005) and a tabulated grid of spectral energy distributions computed from disc atmospheric modeling, which determines $f_{\rm col}$ (Davis & Hubeny, 2006). In these disc atmospheric models, $f_{\rm col}$ is effectively confined to the narrow range $1.5 \lesssim f_{\rm col} \lesssim 1.7$ (Davis et al., 2005).

However, these determinations of $f_{\rm col}$ do not incorporate potentially important physics that may drastically alter the degree of spectral hardening. In particular, vertical magnetic pressure support in the disc is neglected, which alters the properties of the effective photosphere and hence the emergent disc spectrum. Blaes et al. (2006) showed that even relatively weak magnetic pressure support enhances $f_{\rm col}$ from 1.48 to 1.74, which if neglected would result in an erroneous spin measurement of $a \simeq 0.5$ for a non-spinning black hole (i.e., $a = 0$). Magnetic pressure-dominated discs would likely produce far more substantial disc spectral hardening (e.g., Begelman & Pringle, 2007). Indeed, the recent constraint on the strength of the magnetic field driving the accretion disc wind in the black hole X-ray binary GRS 1915+105 implies that the disc is strongly magnetized (Miller et al., 2016).

This paper is organized as follows. We outline the methodology for the basic continuum fitting technique, which implicitly assumes that the degree of accretion disc spectral hardening is modest and confined to a narrow range (§4.3). We then relax this assumption and show that the measured black hole
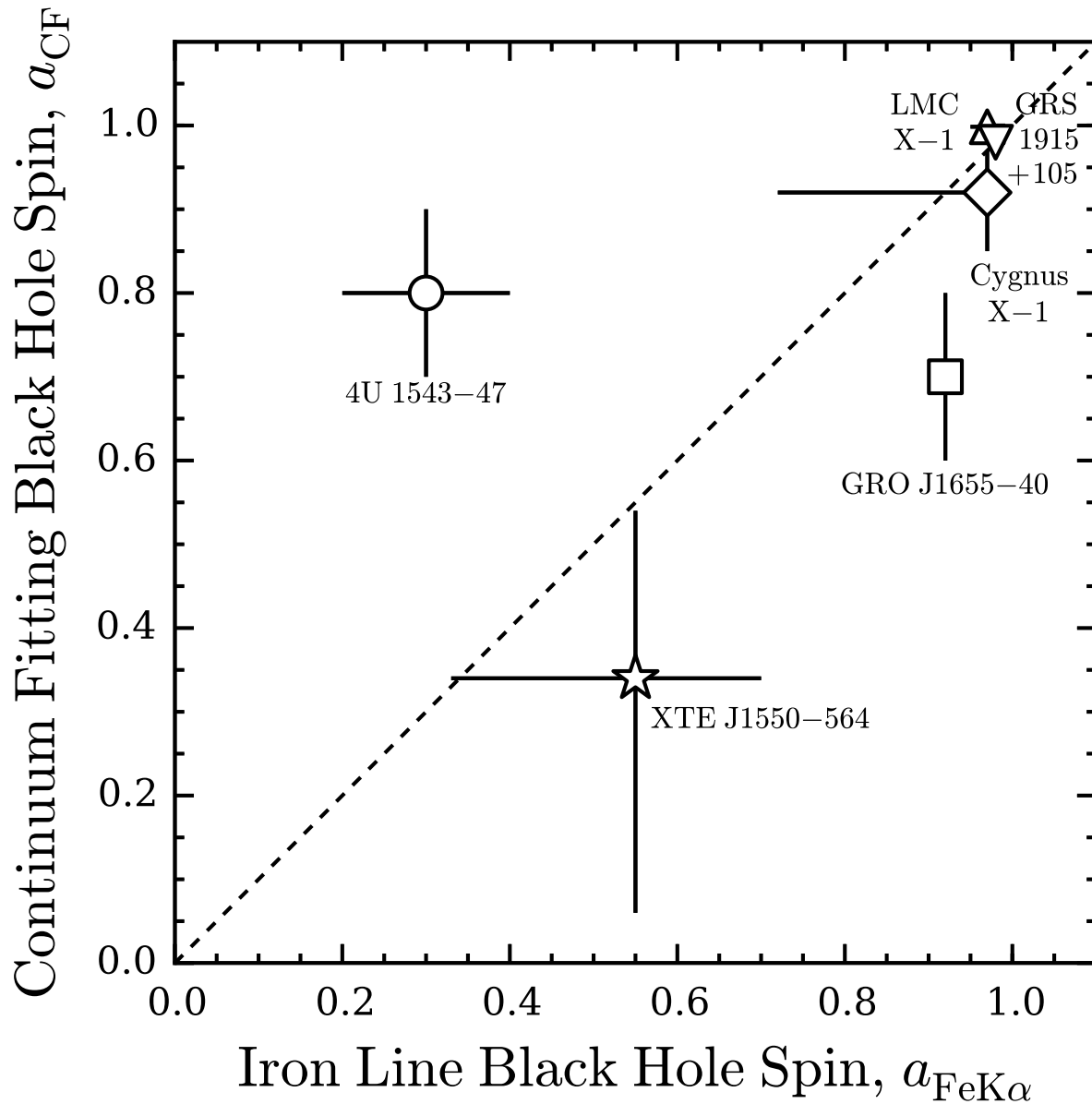
Figure 4.1: Black hole spin measurements from the iron line technique ($a_{\mathrm{FeK}\alpha}$) and the continuum fitting technique (a_{CF}) plotted against one another for the sources in Table 4.1. Spin measurements for 4U 1543–47, GRO J1655–40, and XTE J1550–564 are in disagreement at the 1σ level, as these points do not lie on the *dashed line* that indicates agreement between the two spin measurement techniques.

spin is sensitive to the adopted level of spectral hardening and its uncertainty (§4.4.2). We demonstrate that existing continuum fitting black hole spin measurements can become unconstrained when f_{col} uncertainty is included (§4.4.3). We discuss our results (§5.6), followed by a summary and conclusions (§5.7).

4.3   Disc Continuum Fitting Methodology

Here, we outline the greatly simplified version of the continuum fitting technique for measuring black hole spin that we adopt in our subsequent analysis. The spectrum of a geometrically thin, optically thick accretion disc (Shakura & Sunyaev, 1973) around a black hole is described by the two-parameter multi-colour disc blackbody model (e.g., Mitsuda et al., 1984; Makishima et al., 1986; Gierliński et al., 1999; Frank et al., 2002; Zimmerman et al., 2005). One parameter is the maximum colour temperature in the disc, $T_{\mathrm{col}}^{\max} = T_{\mathrm{col}}[(49/36)R_{\mathrm{in}}] = \left(6^6/7^7\right)^{1/4} T_*$, where,

$$T_{\mathrm{col}}(R) = T_* \left(\frac{R}{R_{\mathrm{in}}}\right)^{-3/4} \left[1 - \beta \left(\frac{R}{R_{\mathrm{in}}}\right)^{-1/2}\right]^{1/4}. \tag{4.1}$$

Here, R is the radial location in the disc and β describes the boundary condition on the inner disc edge, R_{in}, with $\beta = 1$ commonly adopted and corresponding to zero torque. The characteristic temperature crudely describing the inner disc colour temperature is,

$$T_* = f_{\mathrm{col}} \left(\frac{3GM\dot{M}}{8\pi\sigma_{\mathrm{SB}}R_{\mathrm{in}}^3}\right)^{1/4}, \tag{4.2}$$

where f_{col} is the spectral hardening factor (also called the colour correction factor), M is the black hole mass, $\dot{M}$ is the mass accretion rate, G is the gravitational constant, and σ_{SB} is the Stefan-Boltzmann constant. The colour temperature is related to the effective temperature of the disc by $T_{\mathrm{eff}} = T_{\mathrm{col}}/f_{\mathrm{col}}$. The second parameter of the multi-colour disc blackbody model is the flux normalization,

$$K_{\mathrm{flux}} = \frac{1}{f_{\mathrm{col}}^4} \left(\frac{R_{\mathrm{in}}}{D}\right)^2 \cos\left(\theta_{\mathrm{disc}}\right), \tag{4.3}$$

where D is the distance to the black hole and the inner disc inclination is $\theta_{\mathrm{disc}} = 0°$ and $90°$ for face-on and edge-on discs, respectively.

Once the disc spectrum is adequately fitted, independent knowledge of D, θ_{disc}, and f_{col} give R_{in} from Equation 4.3. Assuming that R_{in} coincides with the innermost stable circular orbit (ISCO), R_{ISCO},

a measurement of M then gives $r_{\mathrm{ISCO}} = R_{\mathrm{ISCO}}/R_{\mathrm{g}}$, where $R_{\mathrm{g}} = GM/c^2$ is the gravitational radius, with c being the speed of light. This dimensionless location of the ISCO, r_{ISCO}, can then be unambiguously interpreted as a measurement of the black hole spin parameter, $a = cJ/(GM^2)$, where J is the black hole angular momentum (Bardeen et al., 1972).

4.4   Analysis and Results

In §4.4.1, we show that modest uncertainty in f_{col} can easily dominate the uncertainty in the black hole spin parameter measured using the continuum fitting technique. Adopting a model black hole X-ray binary with known intrinsic parameters in §4.4.2, we show how uncertainties in f_{col} affect the black hole spin measured from continuum fitting. Finally, in §4.4.3 we fold uncertainties in f_{col} into vetted measurements of black hole spin from continuum fitting.

4.4.1   Continuum Fitting Technique: Individual Parameter Uncertainties

Measuring R_{in} from Equation 4.3 is the essence of the continuum fitting technique. Consequently, the main challenge in measuring black hole spin from disc continuum fitting is the need for tight constraints on K_{flux}, M, D, θ_{disc}, and f_{col}. Uncertainties associated with these parameters all contribute to the uncertainty in the measured black hole spin.

Here, we isolate the contribution to the measured black hole spin uncertainty due to each of these individual parameters with the following straightforward exercise. We construct a representative black hole X-ray binary with true parameter values: $a' = 0$, $M' = 7.5\ M_\odot$, $D' = 8.5$ kpc, $\theta'_{\mathrm{disc}} = 45°$, and $f'_{\mathrm{col}} = 1.6$. A prime on a parameter denotes a true value as opposed to an unprimed parameter, which is to be interpreted as a "measured" value with an associated uncertainty.

The simplified continuum fitting method will now be applied to make a mock measurement of the black hole spin probability density function (PDF), $f(a)$, for this model X-ray binary, where all but one parameter are taken to be measured perfectly (i.e., with zero uncertainty). For this single parameter of interest x — with K_{flux}, M, D, θ_{disc}, or f_{col} being acceptable choices — we suppose that x is measured with

PDF,

$$f\left(x\right) = N\left(x, \mu_x = x', \sigma_x = \xi x'\right).\tag{4.4}$$

Here, N is the normal distribution,

$$N\left(x, \mu_x, \sigma_x\right) = \frac{1}{\sigma_x\sqrt{2\pi}}\exp\left[\frac{-\left(x - \mu_x\right)^2}{2\sigma_x^2}\right],\tag{4.5}$$

where μ_x is the mean of the distribution and σ_x is the standard deviation. We choose to center our mock measurement of $f\left(x\right)$ on its true value (i.e., $\mu_x = x'$) with a 10% measurement uncertainty relative to the true value (i.e., $\sigma_x = \xi x'$ with $\xi = 0.1$). This level of measurement uncertainty for a given isolated parameter x is typical when applying the continuum fitting method to a black hole X-ray binary. All other parameters needed to measure the inner disc radius, r_{in}, are taken to be their true values. Therefore, when considering only the uncertainties on the parameter of interest, x, the PDF for the inner disc radius is obtained by change of variables from x to r_{in},

$$f_x\left(r_{\mathrm{in}}\right) = f\left(x\right)\left|J_x\right|,\tag{4.6}$$

where $J_x = \partial x / \partial r_{\mathrm{in}}$ is the Jacobian determinant for the change of variables and Equation A.1 relates x and r_{in}. We calculate $f_x\left(r_{\mathrm{in}}\right)$ for $x = (K_{\mathrm{flux}}, M, D, \theta_{\mathrm{disc}}, f_{\mathrm{col}})$, with each expression given in Appendix B. The black hole spin parameter PDF for the isolated parameter of interest, $f_x\left(a\right)$, then follows from assuming that $r_{\mathrm{ISCO}} = r_{\mathrm{in}}$ and performing the change of variables from r_{ISCO} to a (see §A.0.3).

Figure 4.2 shows the individual parameter contributions to the uncertainty in the black hole spin PDF as measured by the continuum fitting technique. For each parameter of interest with an adopted 10% relative uncertainty, the measured black hole spin, a_x, and its $\pm 1\sigma$ uncertainties are listed in the *upper left* corner of Figure 4.2. Uncertainty in f_{col} leads to the broadest black hole spin parameter PDF. Uncertainties in M and D contribute modestly to black hole spin measurement uncertainty, while uncertainties in K_{flux} and θ_{disc} also contribute to a lesser, but still significant, extent. Therefore, this demonstrated sensitivity of black hole spin measurement error to uncertainty in f_{col} justifies a targeted investigation into the assumptions regarding f_{col} made by the disc continuum fitting technique.
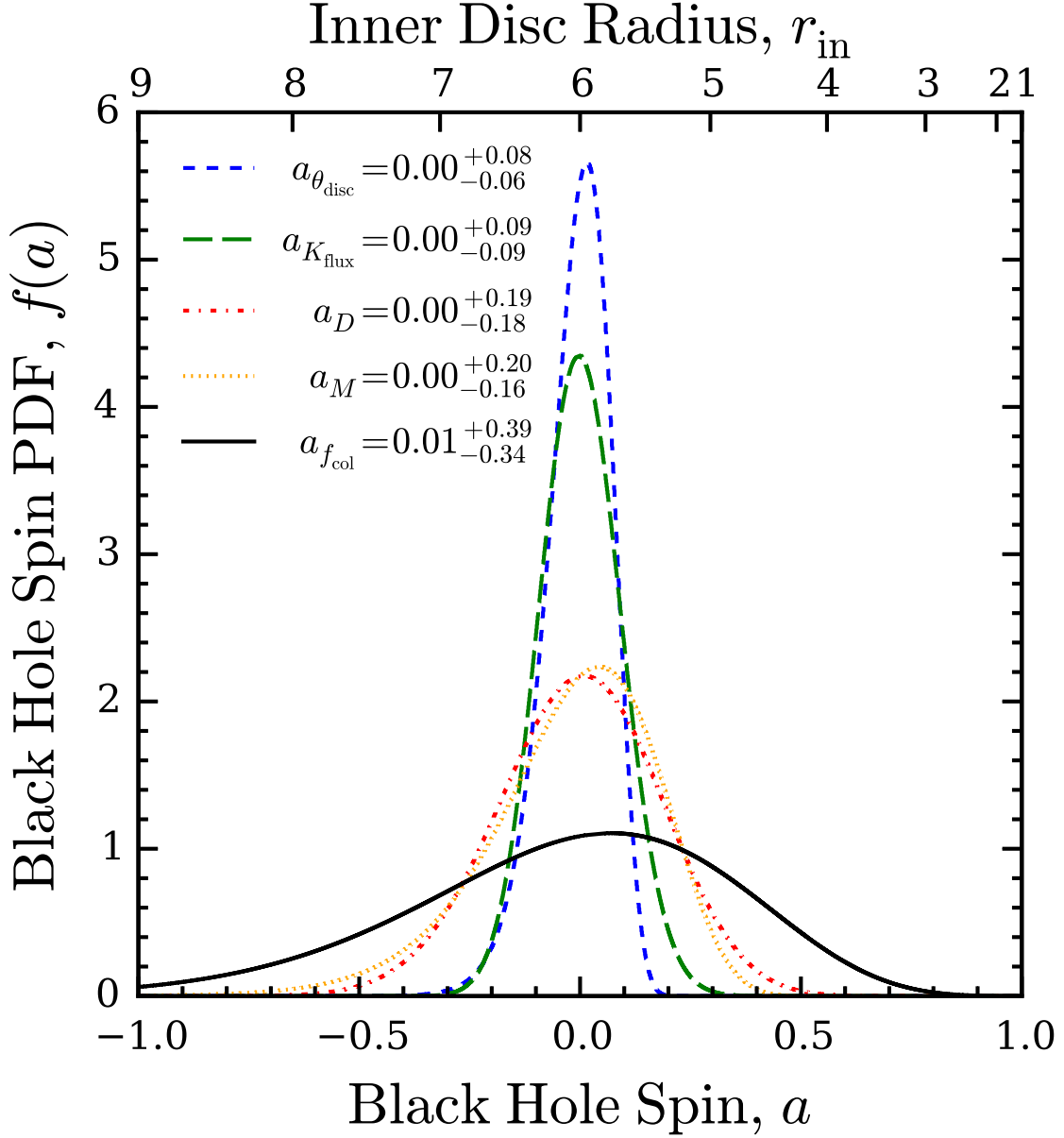
Figure 4.2: Black hole spin parameter PDFs, $f(a)$, resulting from isolating individual parameter uncertainties when measuring spin with the continuum fitting technique. The model black hole X-ray binary has true parameters $a' = 0$, $M' = 7.5\ M_\odot$, $D' = 8.5$ kpc, $\theta'_{\rm disc} = 45°$, and $f'_{\rm col} = 1.6$. When generating a given PDF, the 1σ uncertainty on the parameter of interest is taken to be 10% of its true value. The largest contribution to uncertainties in the measured black hole spin comes from uncertainties in $f_{\rm col}$.

4.4.2 Effects of Spectral Hardening on Black Hole Spin Measurements: Model X-ray Binaries

We now consider the full grid of true black hole spins, $-1 \leq a' \leq 1$, for our model black hole X-ray binary with true parameter values: $M' = 7.5 \, M_\odot$, $D' = 8.5$ kpc, $\theta'_{\mathrm{disc}} = 45°$, and $f'_{\mathrm{col}} = 1.6$.

4.4.2.1 Marginalizing Over f_{col} Uncertainties

Our objective here is to determine how uncertainties in f_{col} contribute to the error budget in the black hole spin as measured by the continuum fitting technique. Our approach is to obtain mock measurements of the black hole spin PDF, $f(a)$, given mock measurements of the PDFs $f(K_{\mathrm{flux}})$, $f(M)$, $f(D)$, $f(\theta_{\mathrm{disc}})$, and $f(f_{\mathrm{col}})$. The procedure for obtaining this mock spin measurement is as follows.

Starting with a known true spin parameter, a', we compute the true location of the ISCO, r'_{ISCO} (see Equation A.2). Given our model black hole X-ray binary with true intrinsic parameters M', D', θ'_{disc}, and f'_{col}, we obtain the true flux normalization, K'_{flux} (see Equation A.1). We are now in a position to construct the following mock observable PDFs required by the simplified continuum fitting technique outlined in §4.3 (see Equation 4.5),

$$f(K_{\mathrm{flux}}) = N\left(K_{\mathrm{flux}}, \mu_{K_{\mathrm{flux}}} = K'_{\mathrm{flux}}, \sigma_{K_{\mathrm{flux}}} = \xi K_{\mathrm{flux}'}\right) \tag{4.7}$$

$$f(M) = N\left(M, \mu_M = M', \sigma_M = \xi M'\right) \tag{4.8}$$

$$f(D) = N\left(D, \mu_D = D', \sigma_D = \xi D'\right) \tag{4.9}$$

$$f(\theta_{\mathrm{disc}}) = N\left(\theta_{\mathrm{disc}}, \mu_{\theta_{\mathrm{disc}}} = \theta'_{\mathrm{disc}}, \sigma_{\theta_{\mathrm{disc}}} = \xi \theta'_{\mathrm{disc}}\right) \tag{4.10}$$

$$f(f_{\mathrm{col}}) = N\left(f_{\mathrm{col}}, \mu_{f_{\mathrm{col}}} = f'_{\mathrm{col}}, \sigma_{f_{\mathrm{col}}} = \xi f'_{\mathrm{col}}\right), \tag{4.11}$$

where we choose $\xi = 0.1$ for all mock observables.

We transform $f(K_{\mathrm{flux}})$ to $f(r_{\mathrm{in}})$ using change of variables (see §A.0.2),

$$f(r_{\mathrm{in}}) = \int_{f_{\mathrm{col}}=1}^{\infty} \int_{\theta_{\mathrm{disc}}=0}^{\pi/2} \int_{D=0}^{\infty} \int_{M=0}^{\infty} dM \; dD \; d\theta_{\mathrm{disc}} \; df_{\mathrm{col}}$$
$$\times f(M) f(D) f(\theta_{\mathrm{disc}}) f(f_{\mathrm{col}}) f(K_{\mathrm{flux}}) \left|J_{K_{\mathrm{flux}} \to r_{\mathrm{in}}}\right|, \tag{4.12}$$
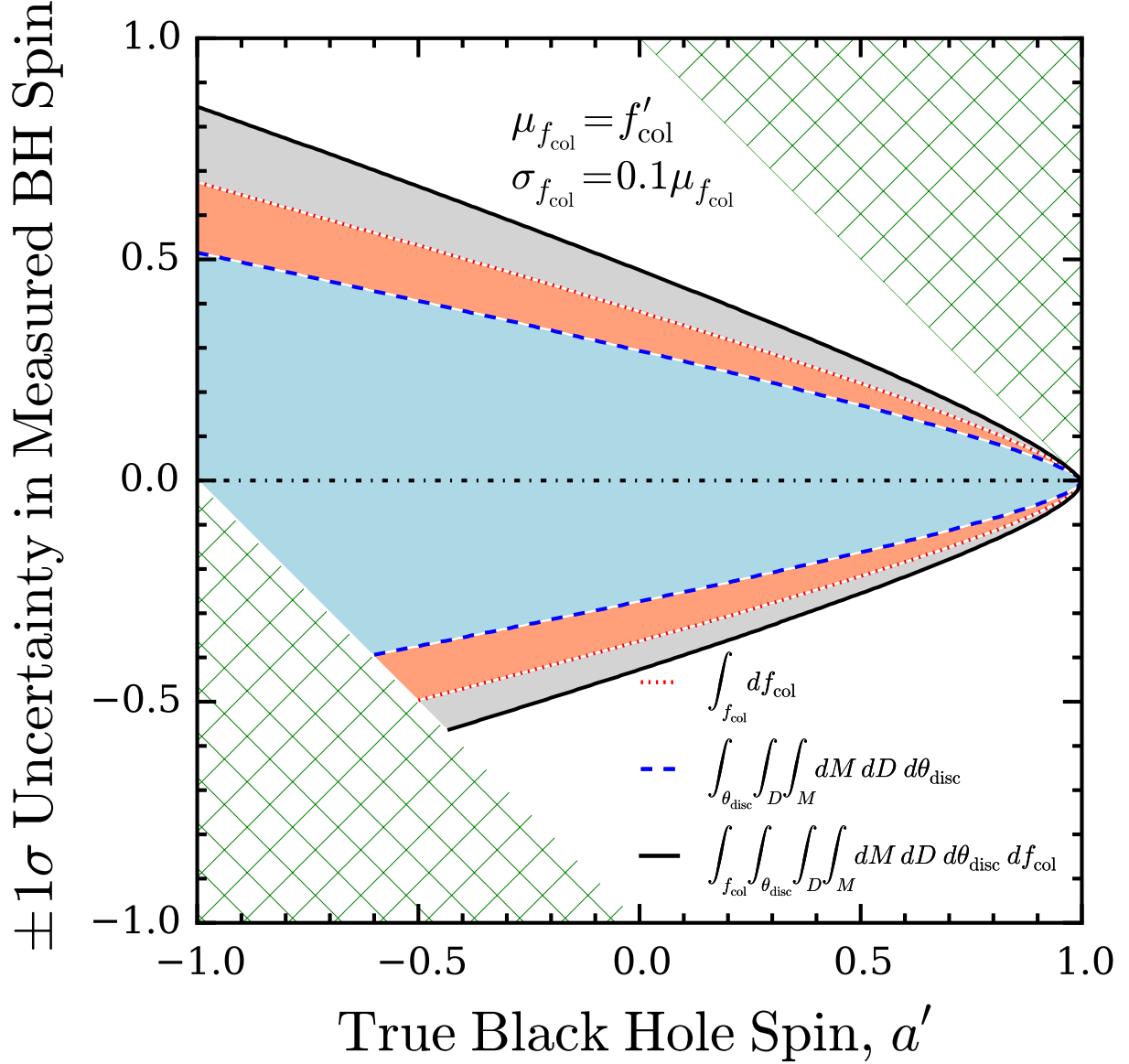
Figure 4.3: The $\pm 1\sigma$ uncertainties on the black hole spin measured from the continuum fitting method, plotted against the true black hole spin, a', for a representative model black hole X-ray binary. The adopted f_{col} PDF has mean $\mu_{f_{\mathrm{col}}} = f'_{\mathrm{col}}$ and standard deviation $\sigma_{f_{\mathrm{col}}} = 0.1\mu_{f_{\mathrm{col}}}$. *Solid black lines* and error bands show the $\pm 1\sigma$ uncertainties on a from marginalizing over all parameters M, D, θ_{disc}, and f_{col}. *Dashed blue lines* result from marginalizing over only M, D, θ_{disc}. *Dotted red lines* result from marginalizing over only f_{col}. Folding f_{col} uncertainties into the black hole spin error budget leads to significantly larger spin measurement uncertainties, especially for low-to-moderate a' values. *Green hatched regions* show the uncertainty levels at which a black hole spin measurement becomes a lower or upper limit.

where $J_{K_{\mathrm{flux}} \to r_{\mathrm{in}}}$ is the Jacobian determinant for the change of variables from K_{flux} to r_{in} (see Equation A.14). The integration of Equation 4.12 is done numerically and verified with Monte Carlo techniques.

Assuming that $f(r_{\mathrm{in}}) = f(r_{\mathrm{ISCO}})$, the output black hole spin as measured by the continuum fitting technique is then obtained by transforming $f(r_{\mathrm{ISCO}})$ to $f(a)$ using change of variables (see §A.0.3). This procedure is repeated across the full range of true black hole spins, $-1 \leq a' \leq 1$.

Figure 4.3 plots the $\pm 1\sigma$ uncertainties on the black hole spin that are measured from the above procedure against the true spin value. In this case, the measurement technique recovers the true black hole spin by design because the PDFs for M, D, θ_{disc}, and f_{col} are all centered on their true values. The $\pm 1\sigma$ error band enclosed by the *solid black lines* comes from marginalizing over M, D, θ_{disc}, and f_{col}, as done in Equation 4.12. In practice, the continuum fitting technique does not marginalize over f_{col},

$$
\begin{aligned}
f(r_{\mathrm{in}}) = &\int_{f'_{\mathrm{col}}-\epsilon}^{f'_{\mathrm{col}}+\epsilon} \int_{\theta_{\mathrm{disc}}=0}^{\pi/2} \int_{D=0}^{\infty} \int_{M=0}^{\infty} df_{\mathrm{col}} \ dM \ dD \ d\theta_{\mathrm{disc}} \\
&\times \delta(f_{\mathrm{col}} - f'_{\mathrm{col}}) f(M) f(D) f(\theta_{\mathrm{disc}}) \\
&\times f(K_{\mathrm{flux}}) |J_{K_{\mathrm{flux}} \to r_{\mathrm{in}}}|,
\end{aligned}
\tag{4.13}
$$

which is shown by *dashed blue lines*. For the sake of comparison, *dotted red lines* show the results from marginalizing over only f_{col},

$$
\begin{aligned}
f(r_{\mathrm{in}}) = &\int_{f_{\mathrm{col}}=1}^{\infty} \int_{M'-\epsilon}^{M'+\epsilon} \int_{D'-\epsilon}^{D'+\epsilon} \int_{\theta'_{\mathrm{disc}}-\epsilon}^{\theta'_{\mathrm{disc}}+\epsilon} df_{\mathrm{col}} \ dM \ dD \ d\theta_{\mathrm{disc}} \\
&\times f(f_{\mathrm{col}}) \delta(M - M') \delta(D - D') \delta(\theta_{\mathrm{disc}} - \theta'_{\mathrm{disc}}) \\
&\times f(K_{\mathrm{flux}}) |J_{K_{\mathrm{flux}} \to r_{\mathrm{in}}}|.
\end{aligned}
\tag{4.14}
$$

In Equations 4.13 and 4.14, $\epsilon > 0$ such that the Dirac delta function, $\delta(x)$, is integrated over its peak.

Figure 4.3 shows that if f_{col} is known accurately and precisely, then the continuum fitting technique used in practice can provide fairly tight constraints on the black hole spin (*dashed blue lines*). However, the uncertainties on the measured black hole spin increase dramatically when f_{col} uncertainties are also marginalized over (*solid black lines*). Indeed, marginalizing over only f_{col} (*dotted red lines*) leads to greater uncertainty in the measured black hole spin than from marginalizing over M, D, and θ_{disc} (*dashed blue lines*), supposing that all of these parameters have a 10% relative uncertainty. If we instead adopt a 7% relative
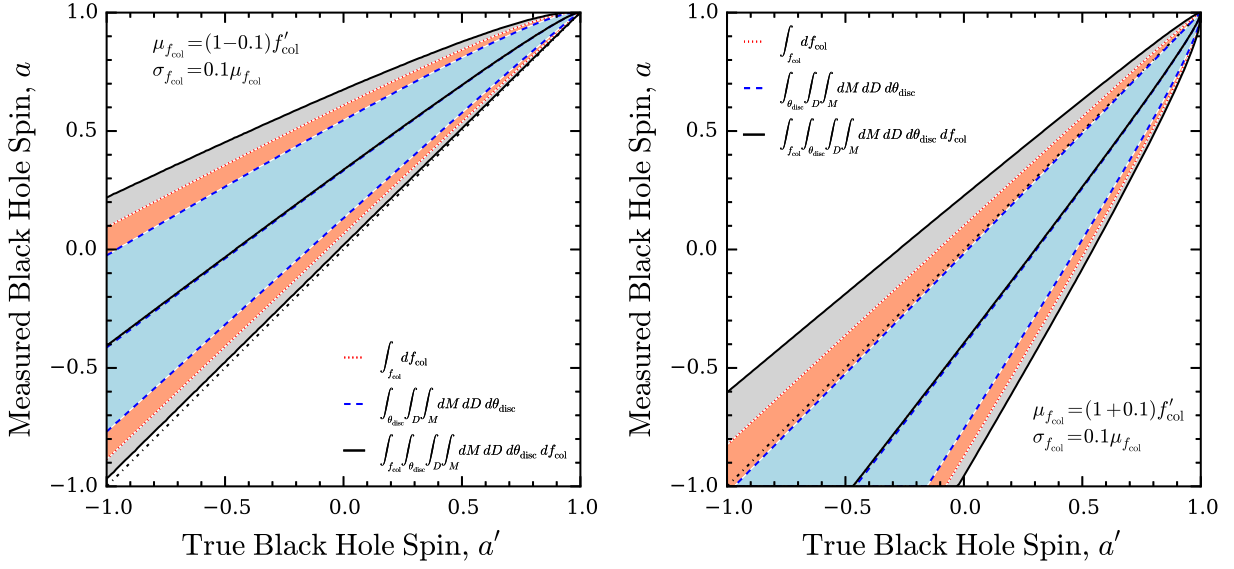
Figure 4.4: Continuum fitting measured black hole spin, a, plotted against the true black hole spin for a representative model black hole X-ray binary, a'. *Left*: The adopted $f_{\rm col}$ PDF has mean $\mu_{f_{\rm col}} = 1.44$ and standard deviation $\sigma_{f_{\rm col}} = 0.1\mu_{f_{\rm col}}$. *Right*: The adopted $f_{\rm col}$ PDF has mean $\mu_{f_{\rm col}} = 1.76$ and standard deviation $\sigma_{f_{\rm col}} = 0.1\mu_{f_{\rm col}}$. The line styles and error bands have the same interpretation as in Figure 4.3. The *dash-dotted black line* marks agreement between the true and measured black hole spins. These figures show that adopting even a mildly erroneous $f_{\rm col}$ leads to black hole spin measurements that are inconsistent with the true values.

uncertainty for f_{col}, the error contribution from f_{col} alone (*dotted red lines*) can be made to match that from M, D, and θ_{disc} (*dashed blue lines*). Therefore, we suggest as a general guideline that if f_{col} is known to within $\sim 5\%$, then f_{col} will probably not dominate the error budget on the measured black hole spin.

Figure 4.3 also shows that high prograde black hole spins are relatively insensitive to uncertainties in f_{col}. For $a' = 0.9$, the standard continuum fitting practice finds $a = 0.90^{+0.05}_{-0.05}$ while also marginalizing over f_{col} yields the similar constraint $a = 0.90^{+0.09}_{-0.08}$. However, low-to-moderate prograde spins cannot be tightly constrained given modest uncertainties in f_{col}. Taking $a' = 0.5$ ($a' = 0$) as examples, neglecting f_{col} uncertainties results in $a = 0.50^{+0.17}_{-0.16}$ ($a = 0.00^{+0.30}_{-0.27}$), while incorporating all parameter uncertainties gives $a = 0.50^{+0.27}_{-0.26}$ ($a = 0.00^{+0.47}_{-0.43}$). Most affected by uncertainties in f_{col} are retrograde spinning black holes, as all but the most extreme retrograde spins could be distinguished from a prograde spin at the 1σ confidence level (i.e., $\sigma_a^+ \gtrsim a$).

4.4.2.2   Adopting Erroneous f_{col} Values

We now aim to determine how adopting an erroneous f_{col} value (i.e., $\mu_{f_{\text{col}}} \neq f'_{\text{col}}$ in Equation 4.11) affects the black hole spin parameter, a, as measured by the continuum fitting method.

To quantify the impact of choosing an erroneous f_{col} value on black hole spin measurements, we consider two different spectral hardening factor PDFs: one slightly underestimating and one slightly overestimating the true spectral hardening factor $f'_{\text{col}} = 1.6$, respectively,

$$f^- (f_{\text{col}}) = N \left(f_{\text{col}}, \mu_{f_{\text{col}}} = f^-_{\text{col}}, \sigma_{f_{\text{col}}} = \xi f^-_{\text{col}} \right) \tag{4.15}$$

$$f^+ (f_{\text{col}}) = N \left(f_{\text{col}}, \mu_{f_{\text{col}}} = f^+_{\text{col}}, \sigma_{f_{\text{col}}} = \xi f^+_{\text{col}} \right). \tag{4.16}$$

Here, $f^-_{\text{col}} = (1 - 0.1) f'_{\text{col}} = 1.44$, $f^+_{\text{col}} = (1 + 0.1) f'_{\text{col}} = 1.76$, and $\xi = 0.1$ to represent a 1σ measurement uncertainty at the 10% level. We then repeat the procedure of §4.4.2.1, but replace $f (f_{\text{col}})$ in Equations 4.12 and 4.14 with either $f^- (f_{\text{col}})$ or $f^+ (f_{\text{col}})$. In Equation 4.13 we replace $\delta (f_{\text{col}} - f'_{\text{col}})$ with either $\delta (f_{\text{col}} - f^-_{\text{col}})$ or $\delta (f_{\text{col}} - f^+_{\text{col}})$ and adjust the f_{col} integration limits accordingly. The Jacobians in these equations also replace f_{col} with the appropriate f^-_{col} or f^+_{col}.

Figure 4.4 shows the black hole spin that is measured (compared to its true value) when the adopted

mean of the $f_{\rm col}$ PDF undershoots ($\mu_{f_{\rm col}} = 1.44$; *left panel*) or overshoots ($\mu_{f_{\rm col}} = 1.76$; *right panel*) the true value $f'_{\rm col} = 1.6$ by modest amounts. Figure 4.4 demonstrates that adopting even these mildly incorrect values for $f_{\rm col}$ leads to black hole spin measurements that are generally inconsistent with the true spin values at the 1σ level.

We now consider how adopting the correct M, D, and $\theta_{\rm disc}$, but an erroneous value of the spectral hardening factor over the range $1.0 \leq f_{\rm col} \leq 3.0$, affects the measured black hole spin value. Using Equation 4.14, we obtain a mock measurement of the black hole spin parameter, a, for each assumed $f_{\rm col}$. Figure 4.5 shows the grid of assumed spectral hardening factors, $f_{\rm col}$, and true black hole spins, a', where the contour lines show the measured black hole spin parameter, a, and the colours show the difference between the true and measured black hole spins, $\Delta a = a' - a$. *Blue* (*red*) regions are where the black hole spin is measured to be less (greater) than the true value; therefore, selecting a value for $f_{\rm col}$ that is greater (less) than the true value causes the measured black hole spin to be too small (large). Erroneous black hole spin measurements due to choosing an incorrect $f_{\rm col}$ are most severe in the *darker regions*.

The inset of Figure 4.5 shows that choosing $f_{\rm col}$ values that deviate from $f'_{\rm col}$ at the 10% level (i.e., $f_{\rm col} = 1.76$ or $f_{\rm col} = 1.44$, when $f'_{\rm col} = 1.6$), can lead to substantially incorrect spin measurements (e.g., $|\Delta a| \simeq 0.4$ for $a' = 0$). The lines plotted in the inset merely show the measured black hole spins from Figure 4.4 subtracted from the true spins. With decreasing true black hole spin and for a given erroneous $f_{\rm col}$ "measurement," the measured spin deviates further from its true value. This means that low-to-moderate black hole spin measurements (e.g., $a < 0.9$) from continuum fitting suffer greatly (i.e., $|\Delta a > 0.1|$) from adopting $f_{\rm col}$ values that are incorrect by an amount $\gtrsim 10\%$ of the true value. High spin measurements (e.g., $a > 0.9$) are less affected from adopting mildly erroneous $f_{\rm col}$ values.

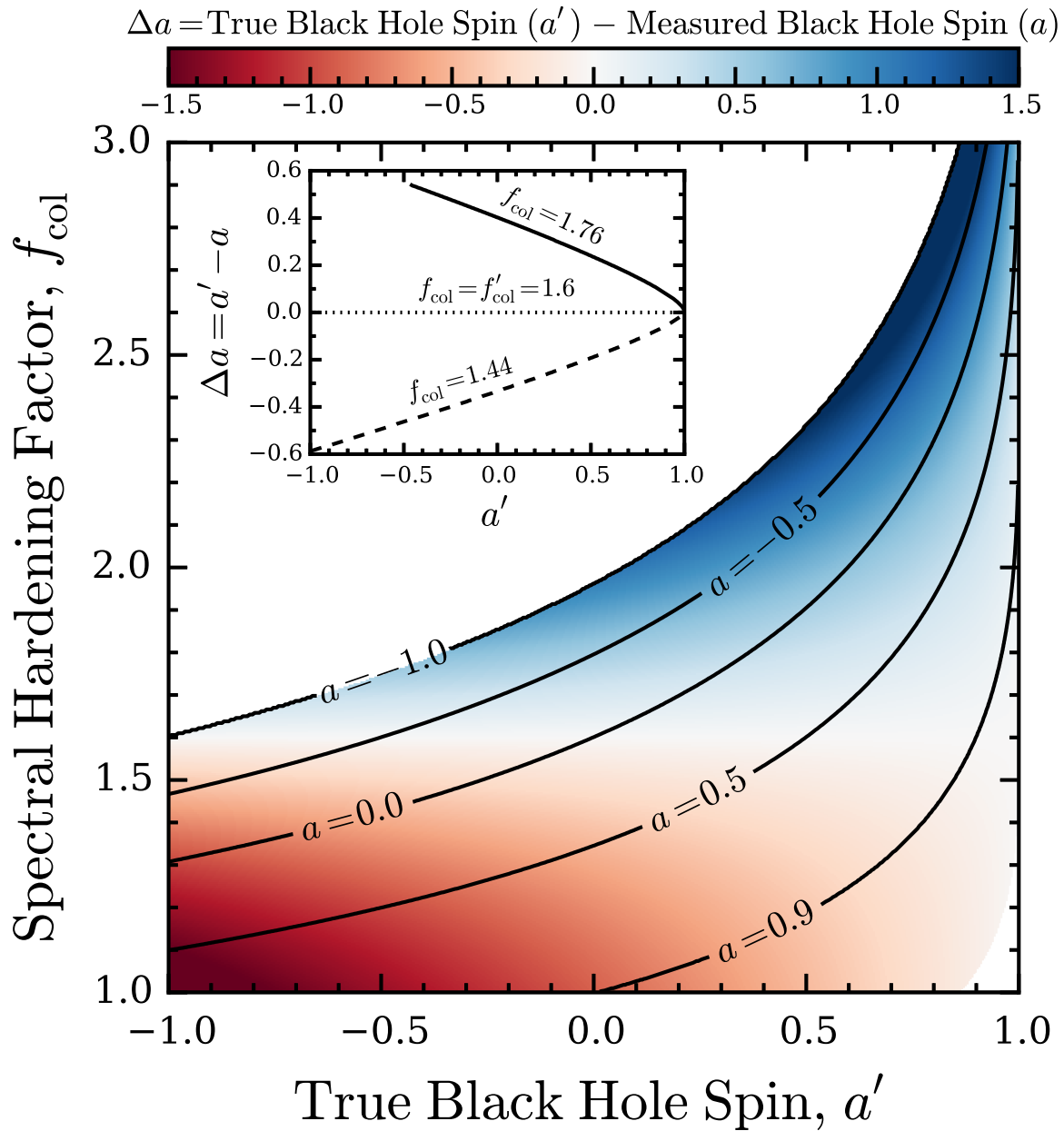### 4.4.3 Effects of Spectral Hardening on Black Hole Spin Measurements: Observed X-ray Binaries

Figure 4.5: Consider a representative black hole X-ray binary with true black hole spin, a', (x-axis) and true spectral hardening factor, $f'_{col} = 1.6$. Adopting some measured f_{col} value (y-axis) to be used by the continuum fitting technique, *black contour lines* show the resulting measured black hole spin, a, and the *coloured contours* show $\Delta a = a' - a$. *White regions* are where no solution for a exists under the $r_{in} = r_{ISCO}$ assumption (i.e., $r_{in} < 1$ or $r_{in} > 9$). The discrepancy between a and a' worsens (*dark regions*) with either decreasing a' or increasing $|f'_{col} - f_{col}|$. The inset shows Δa plotted against a' for $f_{col} = 1.76$ (*solid line*) and $f_{col} = 1.44$ (*dashed line*), emphasizing that even mildly incorrect values of f_{col} cause non-negligible discrepancies between a and a', particularly for low-to-moderate a' values.

Source	$a_{\mathrm{FeK\alpha}}$	a_{CF}	f_{col}	M [$M_\odot$]	θ_{binary} [°]	D [kpc]
GRS 1915+105	0.98 ± 0.01 (1)	$> 0.95^{\mathrm{a}}$ (12)	1.6^{b} (—)	14.0 ± 4.4 (9)	$66 \pm 2^{\mathrm{c}}$ (4)	11.2 ± 0.8 (4)
Cygnus X-1	$0.97^{+0.014\mathrm{d}}_{-0.02}$ (3)	$0.9985^{+0.0005}_{-0.0148}$ (7)	1.610 (7)	14.8 ± 1.0 (18)	27.1 ± 0.8 (18)	$1.86^{+0.12}_{-0.11}$ (22)
LMC X-1	$0.97^{+0.02}_{-0.25}$ (27)	$0.92^{+0.05}_{-0.07}$ (5)	1.562 ± 0.008 (5)	10.91 ± 1.41 (17)	36.38 ± 1.92 (17)	48.10 ± 2.22 (17)
4U 1543-47	0.3 ± 0.1 (13)	$0.80 \pm 0.10^{\mathrm{a}}$ (24)	1.5^{e} (24)	9.4 ± 1.0 (14, 15)	20.7 ± 1.5 (14, 15)	$7.5 \pm 1.0^{\mathrm{f}}$ (24)
GRO J1655-40	$0.92 \pm 0.02^{\mathrm{d}}$ (23)	$0.70 \pm 0.10^{\mathrm{a}}$ (24)	1.65^{e} (24)	6.30 ± 0.27 (8)	70.2 ± 1.2 (8)	3.2 ± 0.2 (10)
XTE J1550-564	$0.55^{+0.15\mathrm{g}}_{-0.22}$ (25)	$0.34^{+0.20}_{-0.28}$ (25)	1.6^{b} (—)	9.10 ± 0.61 (19)	74.7 ± 3.8 (19)	$4.38^{+0.58}_{-0.41}$ (19)
M33 X-7	–	0.84 ± 0.05 (11)	1.765 ± 0.015 (11)	15.65 ± 1.45 (16)	74.6 ± 1.0 (16)	840 ± 20 (16)
LMC X-3	–	$0.25^{+0.13}_{-0.16}$ (28)	1.6^{b} (—)	7.0 ± 0.6 (20)	69.2 ± 0.7 (20)	48.10 ± 2.22 (17)
H1743-322	–	$0.20^{+0.34}_{-0.33}$ (26)	1.6^{b} (—)	$-^{\mathrm{h}}$ (21)	75 ± 3 (26)	8.5 ± 0.8 (26)
A0620-00	–	0.12 ± 0.19 (6)	1.6^{b} (—)	6.61 ± 0.25 (2)	51.0 ± 0.9 (2)	1.06 ± 0.12 (2)

Table 4.1: Black hole X-ray binaries with spin measurements vetted by the continuum fitting community (McClintock et al., 2014). Six of these sources also have black hole spins vetted by the iron line community (Reynolds, 2014). From *left* to *right* the columns are the source name, iron line spin, continuum fitting spin, spectral hardening factor, black hole mass, binary orbital inclination, and distance to the source. Errors are at the 1σ confidence level unless indicated otherwise. Instances where the confidence interval was unclear are assumed to be 1σ. The values listed for f_{col}, M, θ_{binary}, and D are those from the original cited works used in determining a_{CF}. Each measurement has its reference number in parentheses according to the following list: (1) Blum et al. (2009); (2) Cantrell et al. (2010); (3) Fabian et al. (2012); (4) Fender et al. (1999b); (5) Gou et al. (2010); (6) Gou et al. (2009); (7) Gou et al. (2011); (8) Greene et al. (2001); (9) Harlaftis & Greiner (2004); (10) Hjellming & Rupen (1995); (11) Liu et al. (2008); (12) McClintock et al. (2006); (13) Miller et al. (2009b); (14) Orosz et al. (1998); (15) Orosz (2003); (16) Orosz et al. (2007); (17) Orosz et al. (2009); (18) Orosz et al. (2011a); (19) Orosz et al. (2011b); (20) Orosz et al. (2014); (21) Özel et al. (2010); (22) Reid et al. (2011); (23) Reis et al. (2009); (24) Shafee et al. (2006); (25) Steiner et al. (2011); (26) Steiner et al. (2012a); (27) Steiner et al. (2012b); (28) Steiner et al. (2014). $^{\mathrm{a}}$The wider error range suggested in Table 1 of McClintock et al. (2014) is adopted. $^{\mathrm{b}}$The fiducial $f_{\mathrm{CF}} = 1.6$ is adopted because a value is not given explicitly in the cited paper. $^{\mathrm{c}}$The binary orbital plane is not measured directly, but instead assumed to be perpendicular to the measured inclination of the jet axis. $^{\mathrm{d}}$Errors are at the 90% confidence level. $^{\mathrm{e}}f_{\mathrm{col}}$ is estimated from the figures in the cited paper. $^{\mathrm{f}}$This distance appears to be unpublished, with Orosz et al. (1998) quoting $D = 9.1 \pm 1.1$ kpc. $^{\mathrm{g}}$See also Miller et al. (2009b), who find $a = 0.76 \pm 0.01$. $^{\mathrm{h}}$In the absence of a dynamical mass measurement, the mass distribution of Özel et al. (2010) was assumed.

At the time of writing, spin measurements that pass stringent quality criteria using the iron line technique exist for at least 20 supermassive black holes in active galactic nuclei and 14 stellar mass black holes in X-ray binaries (Reynolds, 2014). Similarly, the continuum fitting technique has yielded at least 10 stellar mass black hole spins that also underwent a rigorous vetting process (McClintock et al., 2014). Of the stellar mass black hole spins measured independently by both the iron line and continuum fitting communities, there are six overlapping X-ray binary sources. These are listed in Table 4.1.

Figure 4.1 plots the continuum fitting spin, a_{CF}, against the iron line spin, $a_{\mathrm{FeK}\alpha}$, for these six sources. Three sources are in agreement with near-maximal spin (Cygnus X–1, GRS 1915+105, and LMC X–1), one source is in very weak agreement due to large uncertainties (XTE J1550–564), and two sources are in disagreement at the 1σ level (4U 1543–47 and GRO J1655–40). By adopting the slightly different values $f_{\mathrm{col}} = 1.96$, 1.46, and 1.32 than those listed in Table 4.1 for 4U 1543–47, XTE J1550–564, and GRO J1655–40, respectively, the continuum fitting black hole spins can be made to match those from the iron line method. This illustrates that physically plausible deviations from the f_{col} values selected by the continuum fitting methodology can completely account for discrepancies between the two leading black hole spin measurement techniques.

Figures 4.6 and 4.7 show the normalized black hole spin PDFs measured by the continuum fitting technique, $f(a_{\mathrm{CF}})$. We extracted published black hole spin PDFs with the `DataThief` program (B. Tummers 2006; http://datathief.org/) for the X-ray binaries: LMC X–1 (Gou et al., 2009), XTE J1550–564 (Steiner et al., 2011), M33 X–7 (Liu et al., 2008), LMC X–3 (Steiner et al., 2014), H1743–322, (Steiner et al., 2012a), and A0620–00 (Gou et al., 2010). We assumed normal distributions for 4U 1543–47 and GRO J1655–40 based on the a_{CF} values and uncertainties listed in Table 4.1, as the actual PDFs were not published.

As show in §4.4.2.2, adopting even a slightly incorrect f_{col} can cause the continuum fitting technique to fail. Alleviating this problem would require either direct f_{col} measurements or a firmer understanding of the dominant physical processes in accretion disc atmospheres (see §4.5.2). Therefore, we cannot easily explore how an erroneous f_{col} choice alters the measured black hole spin PDFs for real X-ray binaries. Instead, we suppose that the f_{col} values for each source listed in Table 4.1 are correct — we stress that this may not be true — in order to investigate how including uncertainties in f_{col} modifies the measured black hole spin
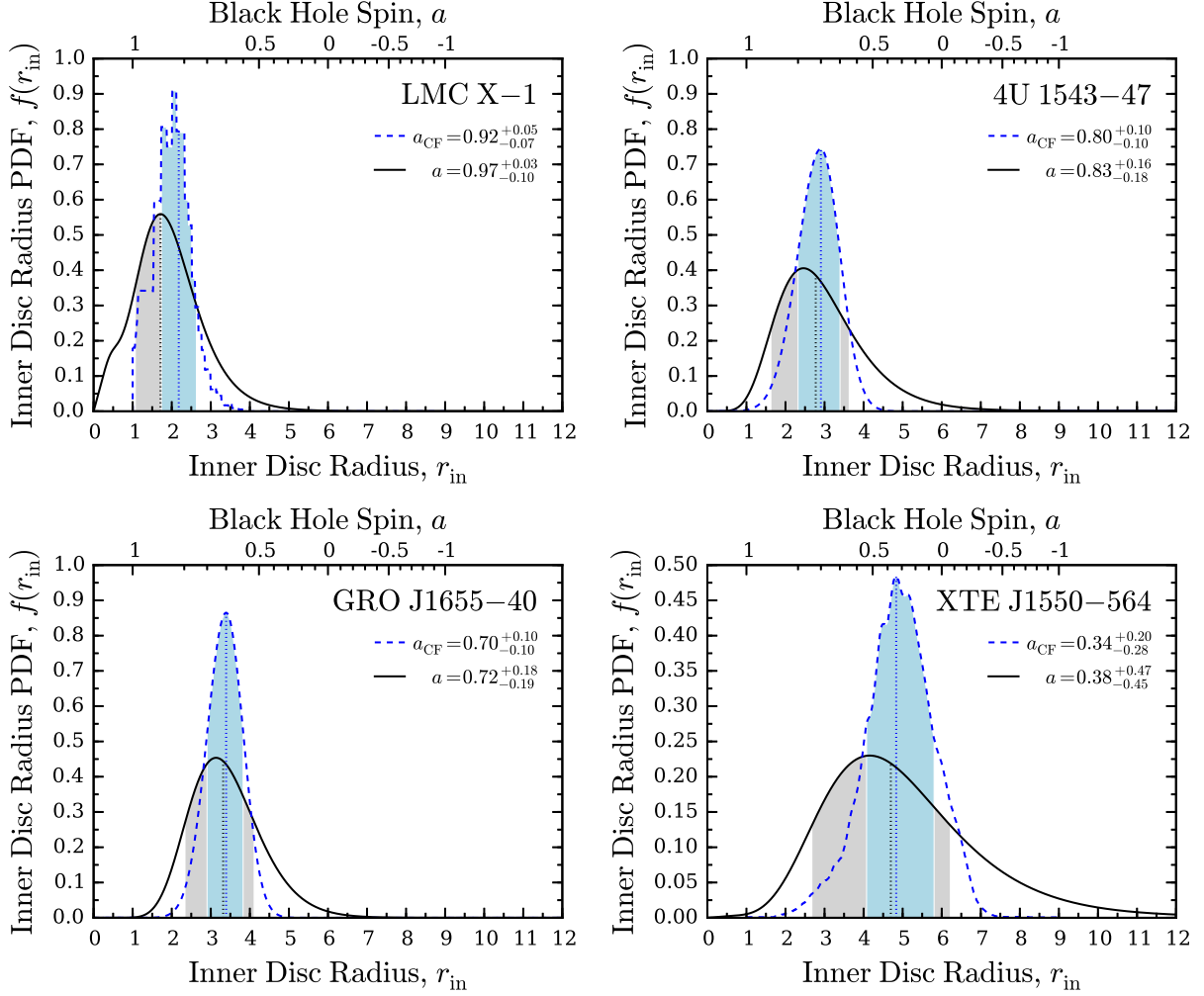
Figure 4.6: Inner disc radius PDFs measured with the continuum fitting technique (*solid lines*) for X-ray binaries LMC X–1 (*top left*; $\mu_{f_{col}} = 1.562$), 4U 1543–47 (*top right*; $\mu_{f_{col}} = 1.5$), GRO J1655–40 (*bottom left*; $\mu_{f_{col}} = 1.65$), and XTE J1550–564 (*bottom right*; $\mu_{f_{col}} = 1.6$). *Dashed blue lines* show the original black hole spin PDFs obtained from the continuum fitting technique. *Solid black lines* show the black hole spin PDFs when f_{col} is also marginalized over assuming a representative dispersion of $\sigma_{f_{col}} = 0.1\mu_{f_{col}}$. Shaded areas enclose the $\pm 1\sigma$ confidence regions.
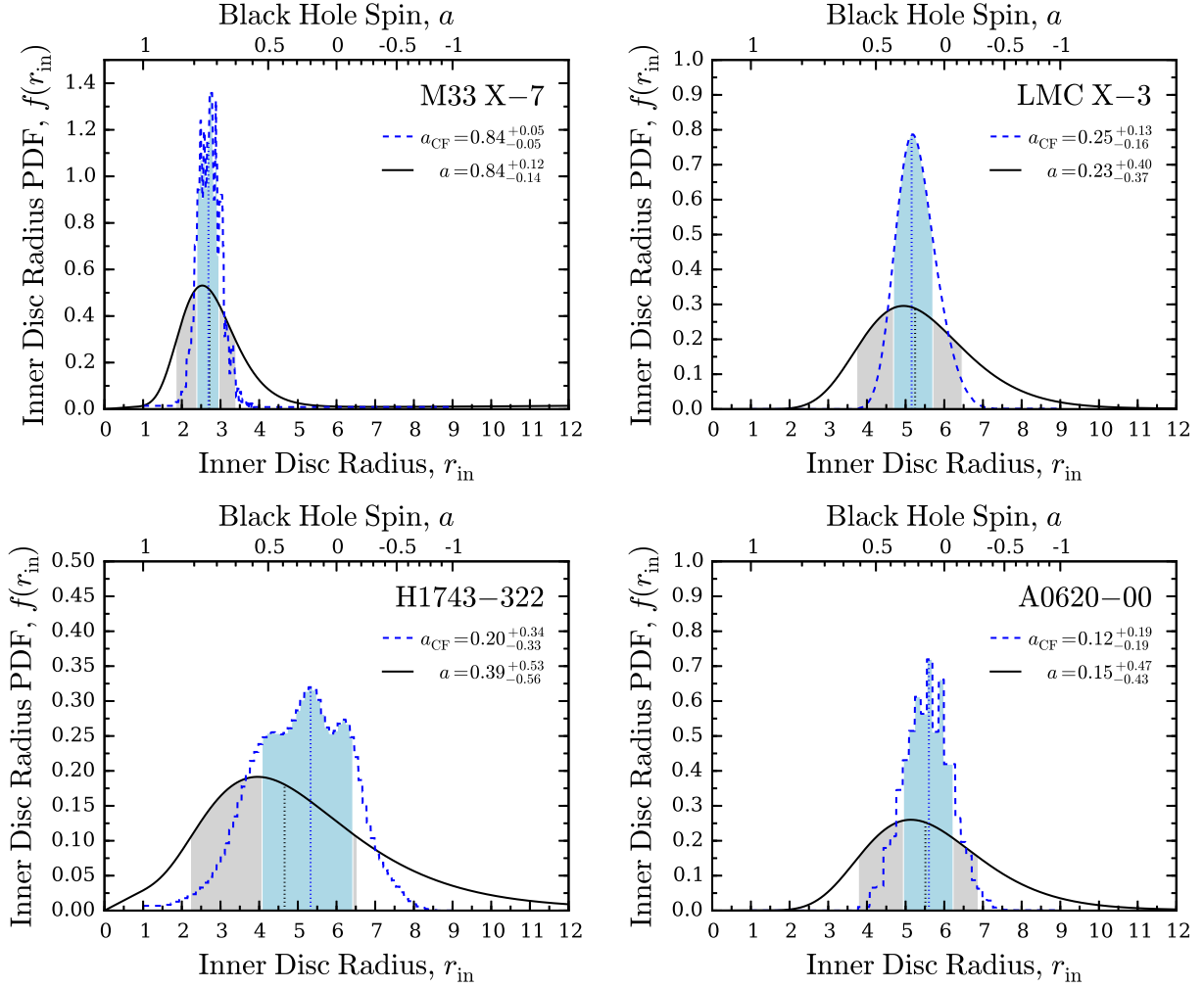
Figure 4.7: Inner disc radius PDFs measured with the continuum fitting technique (*solid lines*) for X-ray binaries M33 X–7 (*top left*; $\mu_{f_{col}} = 1.765$), LMC X–3 (*top right*; $\mu_{f_{col}} = 1.6$), H1743–322 (*bottom left*; $\mu_{f_{col}} = 1.6$), and A0620–00 (*bottom right*; $\mu_{f_{col}} = 1.6$). *Dashed blue lines* show the original black hole spin PDFs obtained from the continuum fitting technique. *Solid black lines* show the black hole spin PDFs when f_{col} is also marginalized over assuming a representative dispersion of $\sigma_{f_{col}} = 0.1\mu_{f_{col}}$. Shaded areas enclose the $\pm 1\sigma$ confidence regions.

PDF. In practice, when measuring the black hole spin PDF, the continuum fitting technique either does not marginalize over the spectral hardening factor or its uncertainty is taken to be incredibly small (i.e., $\sigma_{f_{\mathrm{col}}} \lesssim 0.01$). Our aim here is to incorporate reasonable uncertainties on f_{col} (e.g., at the 10% level) into the actual measured black hole spin PDFs with the following procedure.

Given a measured black hole spin PDF, $f\left(a_{\mathrm{CF}}\right)$, we convert this to a PDF for the ISCO, $f\left(r_{\mathrm{ISCO,CF}}\right)$, by change of variables from a_{CF} to $r_{\mathrm{ISCO,CF}}$ (see §A.0.4). Adopting the assumption that the ISCO coincides with the location of the inner disc edge, we obtain the measured PDF for the inner disc radius, $f\left(r_{\mathrm{in,CF}}\right) = f\left(r_{\mathrm{ISCO,CF}}\right)$. Next, we obtain $f\left(K_{\mathrm{flux}}\right)$ by change of variables from $r_{\mathrm{in,CF}}$ to K_{flux} and marginalizing over M, D, and θ_{disc} (see §A.0.1),

$$
\begin{aligned}
f\left(K_{\mathrm{flux}}\right) = \int_{f_{\mathrm{col,CF}}-\Delta}^{f_{\mathrm{col,CF}}+\Delta} \int_{\theta_{\mathrm{disc}}=0}^{\pi/2} \int_{D=0}^{\infty} \int_{M=0}^{\infty} & df_{\mathrm{col}} \; dM \; dD \; d\theta_{\mathrm{disc}} \\
& \times \delta\left(f_{\mathrm{col}} - f_{\mathrm{col,CF}}\right) f\left(M\right) f\left(D\right) f\left(\theta_{\mathrm{disc}}\right) \\
& \times f\left(r_{\mathrm{in,CF}}\right) \left|J_{r_{\mathrm{in}} \to K_{\mathrm{flux}}}\right|,
\end{aligned}
\tag{4.17}
$$

where we adopt normal distributions for M, D, and θ_{disc}, and a Dirac delta function for f_{col} based on the values and uncertainties used by the continuum fitting technique in Table 4.1 (denoted by subscript "CF"),

$$
f\left(M\right) = N\left(M, \mu_M = M_{\mathrm{CF}}, \sigma_M = \sigma_{M_{\mathrm{CF}}}\right)
\tag{4.18}
$$

$$
f\left(D\right) = N\left(D, \mu_D = D_{\mathrm{CF}}, \sigma_D = \sigma_{D_{\mathrm{CF}}}\right)
\tag{4.19}
$$

$$
f\left(\theta_{\mathrm{disc}}\right) = N\left(\theta_{\mathrm{disc}}, \mu_{\theta_{\mathrm{disc}}} = \theta_{\mathrm{disc,CF}}, \sigma_{\theta_{\mathrm{disc}}} = \sigma_{\theta_{\mathrm{disc,CF}}}\right).
\tag{4.20}
$$

We integrate Equation 4.17 numerically and confirm the result with Monte Carlo integration. Importantly, in obtaining $f\left(K_{\mathrm{flux}}\right)$ we do not marginalize over f_{col} because the original $f\left(a_{\mathrm{CF}}\right)$ for a given source did not marginalize over f_{col}.

With the "observed" flux normalization PDF in hand from Equation 4.17, we can now perform a change of variables from K_{flux} to r_{in} (see §A.0.2), marginalizing over all continuum fitting parameters — M, D, θ_{disc}, and f_{col} (see Equation 4.12) — to arrive at $f\left(r_{\mathrm{in}}\right)$. In doing so, we choose a normal distribution for f_{col} centered on the continuum fitting value listed in Table 4.1,

$$
f\left(f_{\mathrm{col}}\right) = N\left(f_{\mathrm{col}}, \mu_{f_{\mathrm{col}}} = f_{\mathrm{col,CF}}, \sigma_{f_{\mathrm{col}}} = \xi f_{\mathrm{col,CF}}\right),
\tag{4.21}
$$

with $\xi = 0.1$ to assume a 10% relative uncertainty on $f_{\rm col,CF}$. Under the usual assumption that $r_{\rm ISCO} = r_{\rm in}$, we have $f(r_{\rm ISCO}) = f(r_{\rm in})$. Finally, we arrive at the desired PDF for the black hole spin parameter, $f(a)$, by change of variables from $r_{\rm ISCO}$ to a (see §A.0.3).

For black hole X-ray binaries with $a_{\rm CF} < 0.95$ in Table 4.1, Figures 4.6 and 4.7 show how incorporating uncertainties in $f_{\rm col}$ at the 10% level modify the black hole spin PDFs. We found that our methodology has difficulty with particularly steep PDFs associated with high-spin measurements, such as Cygnus X–1 (Gou et al., 2011) and GRS 1915+105. However, we saw in §4.4.2.1 that spins measured to be near-maximal will not be strongly affected by including $f_{\rm col}$ uncertainties. Figures 4.6 and 4.7 show that black hole spin becomes poorly constrained for X-ray binaries with $a \lesssim 0.5$ measured from continuum fitting when a 10% relative uncertainty in $f_{\rm col}$ is included in the error budget.

4.5   Discussion

4.5.1   Continuum Fitting Technique in Practice

The description of the continuum fitting procedure for measuring black hole spin outlined in §4.3 is a simplified version of the more sophisticated modern technique used in practice.

Great care is taken to select observations where the black hole X-ray binary of interest is in the high/soft state where the disc is the dominant spectral component (e.g., McClintock et al., 2006); thus, minimizing the number of model components and free parameters required to fit the spectrum. Observations of black hole X-ray binaries in this disc-dominated state support the $L_{\rm disc} - T_{\rm eff}^4$ scaling relation expected for a multi-colour disc blackbody model for disc luminosities $0.01 \lesssim L_{\rm disc}/L_{\rm Edd} \lesssim 0.5$ (Gierliński & Done, 2004); thus, justifying the basic continuum fitting methodology. Furthermore, only the observations corresponding to luminosity states $L_{\rm disc}/L_{\rm Edd} \lesssim 0.3$ are used because the assumption of a geometrically thin disc breaks down for disc luminosities in excess of this limit (e.g., Shafee et al., 2006; McClintock et al., 2006).

A fully relativistic version of the multi-colour disc blackbody model is adopted in practice (e.g., Novikov & Thorne, 1973; Gierliński et al., 2001), which can also handle effects such as limb-darkening, self-irradiation, and a non-zero inner disc torque (Li et al., 2005). This disc continuum model chooses mass

accretion rate, $\dot{M}$, and black hole spin, a, as free parameters, rather than $T_{\text{col}}^{\text{max}}$ and K_{flux} as presented in §4.3. Given independent measurements of M, D, and θ_{disc}, the final parameter that must be constrained is f_{col}, which is determined from disc atmospheric modeling as follows.

The seed disc spectrum is altered by various physical processes that conspire to produce a hardened emergent spectrum, which is parametrized by f_{col} (e.g., Shimura & Takahara, 1995). Davis et al. (2005) calculated non-local thermodynamic equilibrium relativistic accretion disc models that self-consistently treat the radiative transfer and vertical disc temperature + ionization structure, accounting for Comptonization and free-free/bound-free opacities. For restricted values of the disc luminosity and effective α-viscosity parameter, Davis & Hubeny (2006) ran a suite of the Davis et al. (2005) models over a grid of relevant parameter space. Each realization produced an emergent disc spectrum with an associated f_{col} value. These "look-up tables" were implemented into XSPEC (Arnaud, 1996) and coupled to a relativistic multi-colour disc blackbody model (McClintock et al., 2006). Therefore, when using the current disc continuum fitting approach to constrain black hole spin, the chosen value for f_{col} is based on the detailed disc atmospheric modeling of Davis et al. (2005). However, the uncertainty range in f_{col} is inherently restricted by the physics included in this disc atmospheric model. As a result, uncertainties in f_{col} are either ignored or so small that f_{col} is effectively not marginalized over in the error analysis. We suggest in §4.5.2 that additional physics could significantly expand the allowable range of f_{col} values.

Another assumption of the continuum fitting technique that deserves mentioning here is that the inclination of the inner disc regions, θ_{disc}, is not measured directly. Rather, θ_{disc} is regularly assumed to be aligned with the binary orbital inclination, θ_{binary}, which is measured from the periodic eclipsing by the accretion disc of the companion star's optical light curve (e.g., Orosz & Bailyn, 1997). However, θ_{disc} and θ_{binary} are not necessarily aligned (e.g., Maccarone, 2002; Martin et al., 2010).

4.5.2   Measuring f_{col} with the Continuum Fitting Technique

Estimating f_{col} from a physically motivated model when characterizing the disc continuum is commendable and is what the continuum fitting technique now does in practice. However, the physics considered in the disc atmospheric modeling effectively confines f_{col} to the range $1.5 \lesssim f_{\text{col}} \lesssim 1.7$ (see Table 4.1; Davis

& Hubeny, 2006). Recent observational investigations suggest that the spectral hardening factor can exceed $f_{\rm col} \simeq 2$ (e.g., Salvesen et al., 2013; Reynolds & Miller, 2013), even in the disc-dominated high/soft state applicable to the continuum fitting technique (Maitra et al., 2014). Given the scaling $r_{\rm in} \propto f_{\rm col}^2$ (see Equation A.1), realistic $f_{\rm col}$ values and uncertainties should be fully considered when measuring black hole spin.

There may be additional physics not included in the disc atmospheric modeling adopted by the continuum fitting technique that could have a strong influence on the degree of spectral hardening. A diminishment to $f_{\rm col} \simeq 1$ can arise from disc inhomogeneities, which allow the preferential escape of radiation through low-density channels. Strong disc inhomogeneity can arise in radiation pressure-dominated discs susceptible to photon bubble instability (Begelman, 2002, 2006) and/or magnetic pressure-dominated discs (e.g., Salvesen et al., 2016b,a). An enhancement to $f_{\rm col} \simeq 2$ can arise from considering dissipation of accretion power in the corona (Merloni et al., 2000) and/or significant vertical magnetic pressure support (e.g., Blaes et al., 2006). Indeed, strongly magnetized accretion discs may achieve $f_{\rm col} \sim 5$ (Begelman & Pringle, 2007) and we are currently working to determine how the emergent disc spectrum is altered due to substantial vertical magnetic pressure support (Salvesen et al., in preparation).

Current X-ray data are sufficient to constrain the two free parameters in the multi-colour disc black-body model (i.e., $\dot{M}$ and a); however, the data cannot also constrain $f_{\rm col}$ as a third free parameter. Placing firm observational constraints on $f_{\rm col}$ is challenging, with previous relative (e.g., Salvesen et al., 2013) and absolute (Maitra et al., 2014) measurements of $f_{\rm col}$ suggesting that the fiducial $1.5 \lesssim f_{\rm col} \lesssim 1.7$ range may be too restrictive.

We point out that the continuum fitting technique is capable of making absolute measurements of $f_{\rm col}$. The key to making these $f_{\rm col}$ measurements is to adopt the black hole spin as a known intrinsic (i.e., unchanging) system parameter, as is done for M, D, and $\theta_{\rm disc}$. With this approach, $f_{\rm col}$ becomes a free parameter in the X-ray spectral fitting, rather than being inferred from the model-dependent approach used in practice. The advantage to this modified version of continuum fitting is its ability to simultaneously constrain two *extrinsic* parameters; namely, $\dot{M}$ and $f_{\rm col}$ (instead of a). Figure 4.1 shows there are at least six viable sources for which the iron line black hole spin could be adopted and the continuum fitting technique used to measure $f_{\rm col}$. Directly measuring $f_{\rm col}$ has the exciting potential to probe disc atmospheric physics

and variability in an unprecedented way.

To determine the continuum fitting technique's potential to constrain f_{col}, we performed the following exercise. For a model black hole X-ray binary with true parameters $M' = 7.5\ M_\odot$, $D' = 8.5$ kpc, $\theta'_{disc} = 45°$, $f'_{col} = 1.6$, and inner disc radius r'_{in} coinciding with the ISCO, we suppose that each of these parameters is measured accurately with a 10% relative uncertainty. Using the methodology of §4.4.2, but now with f_{col} as the parameter of interest rather than r_{in}, we find that the simplified continuum fitting technique yields $f_{col} = 1.60 \pm 0.09$ from marginalizing over only r_{in} and $f_{col} = 1.60 \pm 0.15$ from marginalizing over M, D, θ_{disc}, and r_{in}. Whether continuum fitting could achieve these encouraging f_{col} constraints remains to be seen. In practice, modeling black hole X-ray binary spectra will always require a hard X-ray component. The difficultly in measuring where this hard spectral component turns over leads to significant uncertainty in the flux, which is likely to be a major limitation to using continuum fitting to make absolute measurements of f_{col}.

4.6   Summary and Conclusions

We quantified the consequences of neglecting uncertainties in the spectral hardening factor, f_{col}, on black hole spin measurements obtained with the continuum fitting technique. Our main conclusions are the following:

- When all parameters required by the continuum fitting method adopt the same relative uncertainty, f_{col} dominates the error budget on the measured black hole spin (see Figure 4.2).

- Allowing for modest uncertainty in f_{col} (e.g., at the 10% level) leads to significantly larger black hole spin measurement uncertainty (see Figure 4.3).

- For black holes with low-to-moderate intrinsic spin (i.e., $a < 0.9$), adopting a slightly incorrect f_{col} value (e.g., 10% off from the true value) results in a spin measurement that is inconsistent with the true spin (see Figures 4.4 and 4.5). Therefore, non-maximal black hole spins derived from the continuum fitting technique are only robust if f_{col} is known with high accuracy.

- In some cases (e.g., XTE J1550–564, LMC X–3, H1743–322, A0620–00), considering a fiducial 10%

uncertainty in $f_{\rm col}$ leads to substantial broadening of the black hole spin PDFs obtained with the continuum fitting technique (see Figures 4.6 and 4.7).

- Of the six black hole X-ray binaries with vetted spin measurements from two independent techniques, the three non-extreme (i.e., $a < 0.9$) cases are in disagreement at the 1σ level (see Figure 4.1). These sources could be brought into agreement with $f_{\rm col}$ values in the range $1.3 \leq f_{\rm col} \leq 2.0$.

- The physically plausible range for $f_{\rm col}$ may be wider than is typically considered by the continuum fitting community. We are currently working to determine just how large $f_{\rm col}$ can become as a result of strong vertical magnetic pressure support in the accretion disc atmosphere (Salvesen et al., in preparation).

- Observational studies of disc atmospheric physics could be conducted by making absolute measurements of $f_{\rm col}$ with the continuum fitting technique. This would require adopting independent measurements of black hole spin, as is already done for the other intrinsic system parameters; namely, black hole mass, source distance, and inner disc inclination.

Acknowledgements

Chapter 5

Accretion Disc Dynamo Activity in Local Simulations Spanning Weak-to-Strong Net Vertical Magnetic Flux Regimes

5.1   Preface

This paper was published in Monthly Notices of the Royal Astronomical Society, Volume 457, Issue 1, pp. 857-874 on March 21, 2016. The author list is: Salvesen, G., Simon, J. B., Armitage, P. J., & Begelman, M. C. We performed local simulations of accretion discs spanning magnetic pressure-dominated to gas pressure-dominated regimes. We characterized the relationship between the disc magnetization level and dynamo activity, showing that the numerical results are well-described by a relatively simple analytic model.

Abstract

Strongly magnetized accretion discs around black holes have attractive features that may explain enigmatic aspects of X-ray binary behaviour. The structure and evolution of these discs are governed by a dynamo-like mechanism, which channels part of the accretion power liberated by the magnetorotational instability (MRI) into an ordered toroidal magnetic field. To study dynamo activity, we performed three-dimensional, stratified, isothermal, ideal magnetohydrodynamic shearing box simulations. The strength of the self-sustained toroidal magnetic field depends on the net vertical magnetic flux, which we vary across almost the entire range over which the MRI is linearly unstable. We quantify disc structure and dynamo properties as a function of the initial ratio of mid-plane gas pressure to vertical magnetic field pressure,

$\beta_0^{\mathrm{mid}} = p_{\mathrm{gas}}/p_B$. For $10^5 \geq \beta_0^{\mathrm{mid}} \geq 10$ the effective α-viscosity parameter scales as a power-law. Dynamo activity persists up to and including $\beta_0^{\mathrm{mid}} = 10^2$, at which point the entire vertical column of the disc is magnetic pressure-dominated. Still stronger fields result in a highly inhomogeneous disc structure, with large density fluctuations. We show that the turbulent steady state β^{mid} in our simulations is well-matched by the analytic model of Begelman et al. (2015) describing the creation and buoyant escape of toroidal field, while the vertical structure of the disc can be broadly reproduced using this model. Finally, we discuss the implications of our results for observed properties of X-ray binaries.

5.2   Introduction

The magnetorotational instability (MRI; Balbus & Hawley, 1991) is a well-understood mechanism for generating turbulence and angular momentum transport in accretion discs. In the limit where the disc has no net magnetic field, the MRI acts as a true dynamo in which the majority of the magnetic energy resides in large-scale toroidal magnetic fields. Local magnetohydrodynamic (MHD) simulations with zero net vertical flux show that the rate of angular momentum transport, parametrized by the effective α-viscosity (Shakura & Sunyaev, 1973), is then of the order of $\alpha \sim 0.01$ (Davis et al., 2010).

The zero net field limit of the MRI provides an answer to the fundamental question of why discs accrete, but it may not be the relevant regime for most astrophysical systems. The rate of angular momentum transport increases with net magnetic flux (Hawley et al., 1995) above a threshold — an initial mid-plane ratio of gas to vertical magnetic field pressure $\beta_0^{\mathrm{mid}} \sim 10^5$ — that is quite low. At much stronger field strength, $\beta_0^{\mathrm{mid}} \sim 10^2$, this turbulent transport can be substantial with $\alpha \sim 1$ (Bai & Stone, 2013). The importance of magnetic pressure also increases with net flux. In simulations with weak net flux, magnetic pressure dominates only in a coronal region (Miller & Stone, 2000), whereas fields stronger than $\beta_0^{\mathrm{mid}} \sim 10^3$ lead to suprathermal toroidal fields in the disc mid-plane (Bai & Stone, 2013) and qualitative changes to the disc structure. Finally, disc winds appear to accompany the MRI whenever a dynamically significant net field is present (Suzuki & Inutsuka, 2009; Fromang et al., 2013; Bai & Stone, 2013).

Except in special circumstances (such as near magnetospheres, or when discs in binaries are threaded by a secondary star's magnetic field; Meyer-Hofmeister et al., 1996), determining the net field from first

principles is a hard problem. Depending on circumstances, a local net field may be the remnant of that present when the disc formed (Sikora & Begelman, 2013), the product of dynamo action from zero net field conditions (Beckwith et al., 2011), or the result of a competition between advection and diffusion processes (Lubow et al., 1994). None of these processes is fully understood, but it is plausible that they could typically lead to net fields stronger than the very low threshold for changes to α. At a more phenomenological level, disc models that invoke strong fields show promise for modeling observed disc properties that are otherwise inexplicable. The structure of magnetically dominated discs is stable against thermal/viscous instability (Begelman & Pringle, 2007), and less susceptible to gravitational fragmentation (Pariev et al., 2003; Begelman & Pringle, 2007; Gaburov et al., 2012). Moreover, since the *evolution* of the net field occurs on a time scale that is intermediate between the dynamical and viscous time scales, it has the potential to act as a slowly varying control parameter in models of X-ray binary state transitions (Begelman & Armitage, 2014).

Our goal in this study is to quantify the properties of MRI disc turbulence across almost the entire range of net fluxes that admit linearly unstable MRI modes. Following a long line of prior work, we adopt a local approximation and consider vertically stratified isothermal discs for which the net flux is a conserved quantity. We adopt the basic computational approach of Bai & Stone (2013), who performed shearing box simulations with a net vertical magnetic flux that had a ratio of gas to magnetic pressure, $\beta \equiv p_{\mathrm{gas}}/p_B$, whose initial value at the disc mid-plane ranged from $\beta_0^{\mathrm{mid}} = 10^2 - 10^4$. We extend their work to stronger fields ($\beta_0^{\mathrm{mid}} = 10$, previously considered by Lesur et al., 2013), and test the sensitivity of the results to the size of the simulation domain, which affects the variability properties of the zero net flux MRI (Simon et al., 2012). More important than these technical differences, we focus our analysis on the properties of the "MRI-dynamo" — the periodic reversals of the large-scale toroidal magnetic field that are characteristic of the weak-field MRI in both the local (Brandenburg et al., 1995; Shi et al., 2010; Davis et al., 2010; Simon et al., 2011, 2012) and global limits (O'Neill et al., 2011; Beckwith et al., 2011). If the MRI-dynamo persists at high magnetizations, the Poynting flux associated with the periodic expulsion of magnetic field from the disc could play a dominant role in the energetics of the disc atmosphere (Begelman et al., 2015). Whether this occurs is unclear. Johansen & Levin (2008), using short duration simulations, found apparently stable

highly magnetized disc structures, while Bai & Stone (2013) found that the MRI-dynamo petered out once the net field reached $\beta_0^{\mathrm{mid}} = 10^2$. Perhaps as a consequence of our larger domain size, we find instead that MRI-dynamo activity can be present even when the toroidal magnetic field is suprathermal throughout the disc. We also find that the strongest net fields result in the formation of a highly inhomogeneous disc, and we show that the structure of the simulated discs is well approximated by a simple analytic model of buoyant toroidal field escape.

The outline of the paper is as follows. After describing our simulations (§6.3), we characterize the properties of MRI turbulence (§5.4) and the MRI-dynamo (§5.5) as a function of net vertical magnetic flux. We discuss our results in the context of X-ray binary phenomenology and strongly magnetized accretion discs (§5.6), followed by a summary and conclusions (§5.7).

5.3   Numerical Simulations

We use the `Athena` code to solve the equations of ideal MHD in the shearing box approximation. We refer the reader to Gardiner & Stone (2005, 2008) for descriptions of the `Athena` algorithms and to Stone et al. (2008) for descriptions of their implementation.

5.3.1   Shearing Box Simulations

The shearing box (Goldreich & Lynden-Bell, 1965) models a relatively small patch of a differentially rotating fluid by expanding the equations of motion in a locally co-rotating frame. To apply the shearing box geometry to an accretion disc (Hawley et al., 1995; Brandenburg et al., 1995), we go from a cylindrical frame (R, ϕ, z) into a local Cartesian frame (x, y, z) using the coordinate transformations: $x = R - R_0$, $y = R_0\phi$, $z = z$, where R_0 is the reference radius corresponding to the center of the shearing box and co-rotating with the disc at angular frequency $\mathbf{\Omega} = \Omega\hat{\mathbf{k}}$. For a shearing box with vertical density stratification, the equations of compressible, isothermal, ideal MHD in conservative form with unit vectors $\hat{\mathbf{i}}, \hat{\mathbf{j}}, \hat{\mathbf{k}}$ are (Hawley et al., 1995;

Stone et al., 1996),

$$\frac{\partial \rho}{\partial t} = - \nabla \cdot (\rho \mathbf{v}) \tag{5.1}$$

$$\frac{\partial (\rho \mathbf{v})}{\partial t} = - \nabla \cdot \left[\rho \mathbf{v}\mathbf{v} - \mathbf{B}\mathbf{B} + \left(p_{\text{gas}} + \frac{B^2}{2} \right) \mathbf{I} \right]$$

$$+ 2q\rho\Omega^2 x\hat{\mathbf{i}} - \rho\Omega^2 z\hat{\mathbf{k}} - 2\mathbf{\Omega} \times (\rho \mathbf{v}) \tag{5.2}$$

$$\frac{\partial \mathbf{B}}{\partial t} = - \nabla \cdot (\mathbf{v}\mathbf{B} - \mathbf{B}\mathbf{v}) . \tag{5.3}$$

Here ρ is the gas density, p_{gas} is the gas pressure, $\mathbf{v}$ is the velocity, $\rho\mathbf{v}$ is the momentum density, and $\mathbf{B}$ is the magnetic field, which in our convention absorbs a factor of $\mu/\left(\sqrt{4\pi}\right)$, where $\mu = 1$ is the adopted magnetic permeability. $\mathbf{I}$ is the identity matrix that acts on the total pressure $p_{\text{gas}} + B^2/2$. We adopt an isothermal equation of state, $p_{\text{gas}} = \rho c_{\text{s}}^2$, where c_{s} is the sound speed. The shear parameter is defined as, $q = -d\ln\left(\Omega\right)/d\ln\left(R\right)$, and we choose the value $q = 3/2$ corresponding to a Keplerian accretion disc.

There are various options for numerically integrating Equations 6.1-6.3 within `Athena`. We use the shearing box implementation of Stone & Gardiner (2010), with an orbital advection scheme to separately evolve the background shear flow, $\mathbf{v}_{\text{sh}} = -q\Omega x\hat{\mathbf{j}}$, and the velocity fluctuations, $\mathbf{v}' = \mathbf{v} - \mathbf{v}_{\text{sh}}$. Using orbital advection gives a substantial improvement in computational performance and solution accuracy. We use the Harten-Lax-van Leer discontinuities (HLLD) Riemann solver (Miyoshi & Kusano, 2005; Mignone, 2007) (see, e.g., Salvesen et al. (2014) for a comparison of solvers in `Athena`). Radial (x), toroidal (y), and vertical (z) boundary conditions are shearing periodic, strictly periodic, and outflowing, respectively (Hawley et al., 1995; Simon et al., 2011).

The shearing box has well-known limitations, including the neglect of curvature terms and radial gradients, and symmetry between positive and negative x that leaves the location of the central object undefined. Two limitations are of particular concern for our application. First, the shearing box is not an ideal setup for representing disc winds, which are present in all net flux MRI simulations. Although the shearing box effective potential is locally the same as for a global (Blandford & Payne, 1982) wind, the derived solutions can have an unphysical geometry and additionally depend in detail on the vertical boundary conditions (Bai & Stone, 2013; Fromang et al., 2013). Winds are not the focus of this paper, but they are present and we cannot readily quantify the extent to which uncertainties in the strength of disc

winds propagate to other aspects of the solution. Second is the issue of domain size. The effective turbulent α measured in local MRI simulations converges at modest domain size, but other properties of interest (such as the level of variability) continue to vary even in spatially extended shearing boxes (Simon et al., 2012). There is no way to internally assess whether an unconverged solution in a small box is better or worse than a converged solution in a box so large that neglect of curvature terms (for some assumed disc thickness) is formally unjustified. Ultimately, global simulations are needed to avoid these limitations that are inherent to the shearing box.

5.3.2   Initial Setup and Parameters

ID	(N_x, N_y, N_z) $[N_{\rm zones}]$	Grid Res. $[N_{\rm zones}/H]$	MRI Res. $[\lambda_{\rm fg}/\Delta x_i]$	$\beta_0^{\rm mid}$	B_z	$\langle Q_x^{\rm mid}\rangle_t$	$\langle Q_y^{\rm mid}\rangle_t$	$\langle Q_z^{\rm mid}\rangle_t$	Initial Field Configuration
ZNVF	(480, 960, 480)	48	15	413	0	18.1(8)	47(2)	11.2(5)	Flux Tube
NVF-$\beta5$	(360, 720, 360)	36	1.0	10^5	4.47e-3	17.3(6)	46(2)	10.9(3)	B_z+Sinusoid
NVF-$\beta4$	(360, 720, 360)	36	3.3	10^4	1.41e-2	29(1)	70(3)	19.7(8)	B_z+Sinusoid
NVF-$\beta3$	(240, 480, 240)	24	7.0	10^3	4.47e-2	6(2)e1	1.4(3)e2	4(1)e1	B_z+Sinusoid
NVF-$\beta2$	(240, 480, 240)	24	22	10^2	1.41e-1	1.2(2)e2	3.3(7)e2	9(1)e1	B_z+Sinusoid
NVF-$\beta1$	(180, 360, 180)	18	52	10^1	4.47e-1	1.1(1)e2	2.4(4)e2	1.2(1)e2	B_z+Sinusoid

Table 5.1: Basic information for the suite of shearing box simulations. From *left* to *right* the columns are: simulation identification label, total number of grid zones in each dimension, grid resolution (applies to all dimensions), number of grid zones spanning the fastest growing MRI wavelength (applies to all dimensions), initial ratio of gas pressure-to-magnetic pressure at the disc mid-plane, net vertical magnetic flux density (code units), saturated state time-averaged Q_x, Q_y, Q_z (see Equation 5.9) at the disc mid-plane, and the initial magnetic field configuration. Parentheses indicate the $\pm 1\sigma$ range on the last digit. The domain size for all simulations is $(L_x, L_y, L_z) = (10H_0, 20H_0, 10H_0)$ and all simulations begin at time $t = 0$ and terminate at time $t_{\rm f} = 225$ orbits, while the time-averaging is done over the domain $[t_i, t_{\rm f}] = [25, 225]$ orbits.

Our initial setup is based on Stone et al. (1996) and closely follows that of Simon et al. (2012). We initialize all simulations with a vertically stratified density profile according to isothermal hydrostatic equilibrium,

$$\rho_0\left(x,y,z\right) = \rho_0^{\mathrm{mid}}\exp\left(\frac{-z^2}{2H_0^2}\right),\tag{5.4}$$

where ρ_0^{mid} is the initial (i.e., $t = 0$) gas density at the disc mid-plane (i.e., $z = 0$) and H_0 is the initial gas density scale height of the disc[1] ,

$$H_0 = \frac{c_{\mathrm{s}}}{\Omega}.\tag{5.5}$$

In code units the initial parameter choices are $\Omega = 1$, $\rho_0^{\mathrm{mid}} = 1$, and $c_{\mathrm{s}} = 1$, which correspond to $H_0 = 1$ and initial disc mid-plane gas pressure $p_{\mathrm{gas},0}^{\mathrm{mid}} = 1$.

We run shearing box simulations with and without an imposed net vertical magnetic flux. The magnetization of the gas is parametrized by the ratio of gas pressure-to-magnetic pressure, defined as,

$$\beta = \frac{p_{\mathrm{gas}}}{p_{\mathrm{B}}} = \frac{\rho c_{\mathrm{s}}^2}{B^2/2},\tag{5.6}$$

with β_0 being the initial plasma-β parameter and β_0^{mid} being its value at the disc mid-plane. Our net vertical magnetic flux simulations adopt an initial magnetic field configuration, $\mathbf{B}_0$, consisting of a uniform vertical field with an additional sinusoidal component (added to improve numerical stability during the initial transient growth of the MRI),

$$B_{x,0}\left(x,y,z\right) = 0$$

$$B_{y,0}\left(x,y,z\right) = 0$$

$$B_{z,0}\left(x,y,z\right) = B_0\left[1 + \frac{1}{2}\sin\left(\frac{2\pi x}{L_x}\right)\right].\tag{5.7}$$

Because of the spatial variation of $B_{z,0}$ in the initial conditions, slightly different definitions of the relation between B_0 and β_0^{mid} are possible. We adopt $B_0 = \sqrt{2p_{\mathrm{gas},0}/\beta_0^{\mathrm{mid}}}$. For these simulations initialized with a net vertical magnetic flux, β_0 refers only to the vertical component.

The only physical parameter we vary in our suite of net vertical magnetic flux simulations is β_0^{mid} (see Table 5.1). We choose initial net vertical magnetic flux — NVF prefix in the simulation naming convention —

---

[1] We note that Simon et al. (2012) define $H_0 = \sqrt{2}c_{\mathrm{s}}/\Omega$; therefore, one must keep this in mind if comparing our results to theirs.

values corresponding to very weak (NVF-$\beta5$; $\beta_0^{\mathrm{mid}} = 10^5$), weak (NVF-$\beta4$; $\beta_0^{\mathrm{mid}} = 10^4$), moderate (NVF-$\beta3$; $\beta_0^{\mathrm{mid}} = 10^3$), strong (NVF-$\beta2$; $\beta_0^{\mathrm{mid}} = 10^2$), and very strong (NVF-$\beta1$; $\beta_0^{\mathrm{mid}} = 10^1$) magnetization levels.

For comparison we also run a zero net vertical magnetic flux simulation (ZNVF; see Table 5.1), which adopts an identical initial magnetic field configuration to that of Simon et al. (2012), based on the twisted toroidal flux tube setup of Hirose et al. (2006). As was done in Simon et al. (2012), the initial toroidal and poloidal plasma-β parameters for this simulation are $\beta_{y,0} = 100$ and $\beta_{p,0} = 1600$, respectively, corresponding to $\beta_0^{\mathrm{mid}} = 413$.

In order to seed the MRI, we populate the grid at time $t = 0$ with perturbations — drawn randomly from a uniform distribution with zero mean value — to the gas density and each velocity component. The maximum density and velocity perturbation amplitudes are $|\delta\rho|/\rho = 0.01$ and $|\delta v_i| = (0.01/5)\,c_s$, respectively (e.g., Hawley et al., 1995), where $i = (x, y, z)$ denotes the spatial dimension.

To prevent time-steps from becoming too small as a result of large Alfvén speeds in regions of very low gas density, we enforce a gas density floor of $\rho_{\mathrm{floor}} = 10^{-4}\rho_0^{\mathrm{mid}}$. For all simulations, the vertical profiles of horizontally-averaged gas density remain well above this lower limit for all heights above/below the disc mid-plane.

For all simulations, we choose a domain size of $(L_x, L_y, L_z) = (10H_0, 20H_0, 10H_0)$. This choice is motivated by the vertically stratified shearing box simulations of Simon et al. (2012), which provide compelling evidence for non-local, "mesoscale" structures (i.e., on scales $\gg H$) contributing to angular momentum transport as the domain size increases (see also Guan & Gammie, 2011). It also allows us to explore the sensitivity of the results to changes in domain size by comparison (where our parameters overlap) with the results of Bai & Stone (2013), who used very similar computational methods. As we have already remarked, the neglect of curvature terms in large local domains, such as ours, is only formally justified when modeling very thin discs (with $H/R \sim 0.01$). Explicit comparisons of dynamo behavior in mesoscale and global simulations (Beckwith et al., 2011), however, show that this aspect of the dynamics remains well-modeled locally even when the formal criterion for validity is only marginally satisfied. Simulations NVF-$\beta5$ and NVF-$\beta4$ have a spatial resolution of 36 grid zones/H_0 in each dimension, or $(N_x, N_y, N_z) = (360, 720, 360)$. Simulations NVF-$\beta3$ and NVF-$\beta2$ have a spatial resolution of 24 grid zones/H_0 in each

dimension, or $(N_x, N_y, N_z) = (240, 480, 240)$. Simulation NVF-$\beta$1 has a spatial resolution of 18 grid zones/H_0 in each dimension, or $(N_x, N_y, N_z) = (180, 360, 180)$. The zero net magnetic flux simulation ZNVF has a spatial resolution of 48 grid zones/H_0 in each dimension, or $(N_x, N_y, N_z) = (480, 960, 480)$. Table 5.1 summarizes the suite of shearing box simulations considered in this work.

Ideally, we would like to resolve both the most unstable linear MRI modes in the initial conditions (which can be assessed analytically), and the non-linear properties of turbulence in the saturated state (which can only be assessed empirically). This aspiration is very hard to achieve across the range of net fluxes we consider, because the most unstable linear modes are of much smaller scale in the weak field simulations[2]. Considering first the linear criterion, the fastest growing wavelength for the MRI for an *unstratified* isothermal Keplerian accretion disc is (Hawley et al., 1995),

$$\lambda_{\text{fg}} = \frac{8\pi}{\sqrt{15}} \frac{v_{\text{A},0}}{\Omega}, \tag{5.8}$$

where $v_{\text{A},0} = B_0/\sqrt{\rho_0}$ is the initial Alfvén speed. Table 5.1 lists the number of grid zones resolving λ_{fg} at the disc mid-plane for each of our simulations. Clearly our two weakest net field runs (NVF-β5 and NVF-β4) fail to properly resolve this mode (the run with *zero* net vertical flux is initialized with a moderately strong toroidal field, whose instability is easier to resolve). We can also consider the resolution needed to reproduce the fastest growing modes in *stratified* discs. Latter et al. (2010) performed one-dimensional numerical simulations to compute MRI growth rates in this case and suggest that at least $25, 50, 200$ grid zones/H are needed for simulations with $\beta_0^{\text{mid}} = 10^2, 10^3, 10^4$, respectively, in order to resolve the fastest growing linear MRI modes that develop into channel flows. We meet this requirement for NVF-β2, but not for the weaker net field cases.

The above discussion indicates that the linear growth of the MRI in the two weakest net field runs cannot be reliably captured by our simulations. Our analyses exclude this phase. All of the runs, however, are unstable and develop into a turbulent saturated state in which the magnetic field is substantially stronger (and hence easier to resolve). Empirically, the resolution of the turbulent steady state can be parametrized

---

[2] In principle, the weak field simulations could be run in smaller boxes, with higher spatial resolution, but this would introduce different but equally problematic issues of convergence with domain size.

by the quality factor (Sano et al., 2004),

$$Q_i = \frac{\lambda_{\mathrm{MRI},i}}{\Delta x_i}, \tag{5.9}$$

where $\lambda_{\mathrm{MRI},i} = 2\pi v_{\mathrm{A},i}/\Omega$ is the characteristic MRI wavelength along spatial dimension i, $v_{\mathrm{A},i} = \sqrt{B_i^2/\rho}$ is the Alfvén speed in direction i, and Δx_i is the size of a grid zone in direction i. Sano et al. (2004) suggest a turbulent steady state time-averaged quality factor $\langle Q_i \rangle_t \gtrsim 6$, while Hawley et al. (2011) recommend a more stringent $\langle Q_y \rangle_t \gtrsim 20$ and $\langle Q_z \rangle_t \gtrsim 10$. These criteria are good rules of thumb, though clearly the specific $\langle Q_i \rangle_t$ values needed to properly resolve turbulence are code dependent. Table 5.1 lists the horizontally- and time-averaged quality factors evaluated at the disc mid-plane (i.e., where Q_i is minimized). For all of our simulations, the turbulent steady state is well-resolved by the standards just outlined.

Due to the net vertical magnetic flux we impose, significant mass outflows develop that would deplete the entire disc on timescales shorter than the 200 orbits that we study in the turbulent steady state. Therefore, after every time step, we maintain a constant mass in the domain by multiplying the gas density in every grid zone by an appropriate common factor (Bai & Stone, 2013).

5.3.3 Notation Convention

In the analyses described in subsequent sections, angled brackets surrounding a quantity denote an average. The subscript on the brackets indicates the dimension being averaged over, where $\langle G \rangle_t$, $\langle G \rangle_{xy}$, and $\langle G \rangle_V$ indicate a time average, horizontal (i.e., disc-plane) average, and volume average of the quantity $G(x, y, z, t)$, respectively, given by,

$$\langle G \rangle_t = \frac{1}{t_{\mathrm{f}} - t_{\mathrm{i}}} \int_{t_{\mathrm{i}}}^{t_{\mathrm{f}}} G \, dt \tag{5.10}$$

$$\langle G \rangle_{xy} = \frac{1}{L_x L_y} \int_{-\frac{1}{2}L_y}^{+\frac{1}{2}L_y} \int_{-\frac{1}{2}L_x}^{+\frac{1}{2}L_x} G \, dx \, dy \tag{5.11}$$

$$\langle G \rangle_V = \frac{1}{L_z} \int_{-\frac{1}{2}L_z}^{+\frac{1}{2}L_z} \langle G \rangle_{xy} \, dz. \tag{5.12}$$

Time averages span 200 orbits over the range $[t_{\mathrm{i}}, t_{\mathrm{f}}] = [25, 225]$, where we measure time units in orbits at the center of the shearing box. Horizontal averages encompass the domain $(L_x, L_y) = (10H_0, 20H_0)$. Volume averages encompass the domain $(L_x, L_y, L_z) = (10H_0, 20H_0, 10H_0)$.

Nested angled brackets denote averages over multiple dimensions, where $\langle\langle G\rangle_V\rangle_t$ means that the quantity G was volume-averaged and then time-averaged. A quantity with the superscript G^{mid} means that G was evaluated at the disc mid-plane. A quantity with the subscript G_0 means that G was evaluated at $t = 0$. Quoted uncertainty ranges or error bands shown in figures denote the $\pm 1\sigma$ range corresponding only to the dimension indicated by the subscript on the outermost angled brackets.

Finally, we introduce the notations of a bar ($-$) and a hat ($\wedge$) over a parameter that is defined as the ratio of two quantities, such as $\beta \equiv p_{\mathrm{gas}}/p_B$ (Equation 6.6) and $\alpha \equiv T_{xy}/p_{\mathrm{gas}}$ (Equation 5.20). Using β as an example, the bar and hat have the following meanings,

$$\overline{\beta} \equiv \frac{\langle p_{\mathrm{gas}}\rangle_V}{\langle p_B\rangle_V} \tag{5.13}$$

$$\widehat{\beta} \equiv \frac{\langle p_{\mathrm{gas}}\rangle_{xy}}{\langle p_B\rangle_{xy}}. \tag{5.14}$$

5.4 Basic Properties of MRI Turbulence

A standard diagnostic of MRI turbulence is the rate of angular momentum transport. For a Keplerian accretion disc, this is parametrized by the non-dimensional effective α-viscosity parameter (Shakura & Sunyaev, 1973),

$$\alpha = \frac{T_{xy}}{p_{\mathrm{gas}}} \tag{5.15}$$

$$\alpha_{\mathrm{Rey}} = \frac{T_{xy,\mathrm{Rey}}}{p_{\mathrm{gas}}} \tag{5.16}$$

$$\alpha_{\mathrm{Max}} = \frac{T_{xy,\mathrm{Max}}}{p_{\mathrm{gas}}}, \tag{5.17}$$

where $T_{xy} = T_{xy,\mathrm{Rey}} + T_{xy,\mathrm{Max}}$ is the xy (i.e., $r\phi$) component of the total stress tensor, with Reynolds stress and Maxwell stress components,

$$T_{xy,\mathrm{Rey}} = \rho v_x v_y' \tag{5.18}$$

$$T_{xy,\mathrm{Max}} = -B_x B_y. \tag{5.19}$$

For each simulation, Table 5.2 provides values for $\widehat{\beta}$ and $\widehat{\alpha}$, along with their individual components, all evaluated at the disc mid-plane and time-averaged.
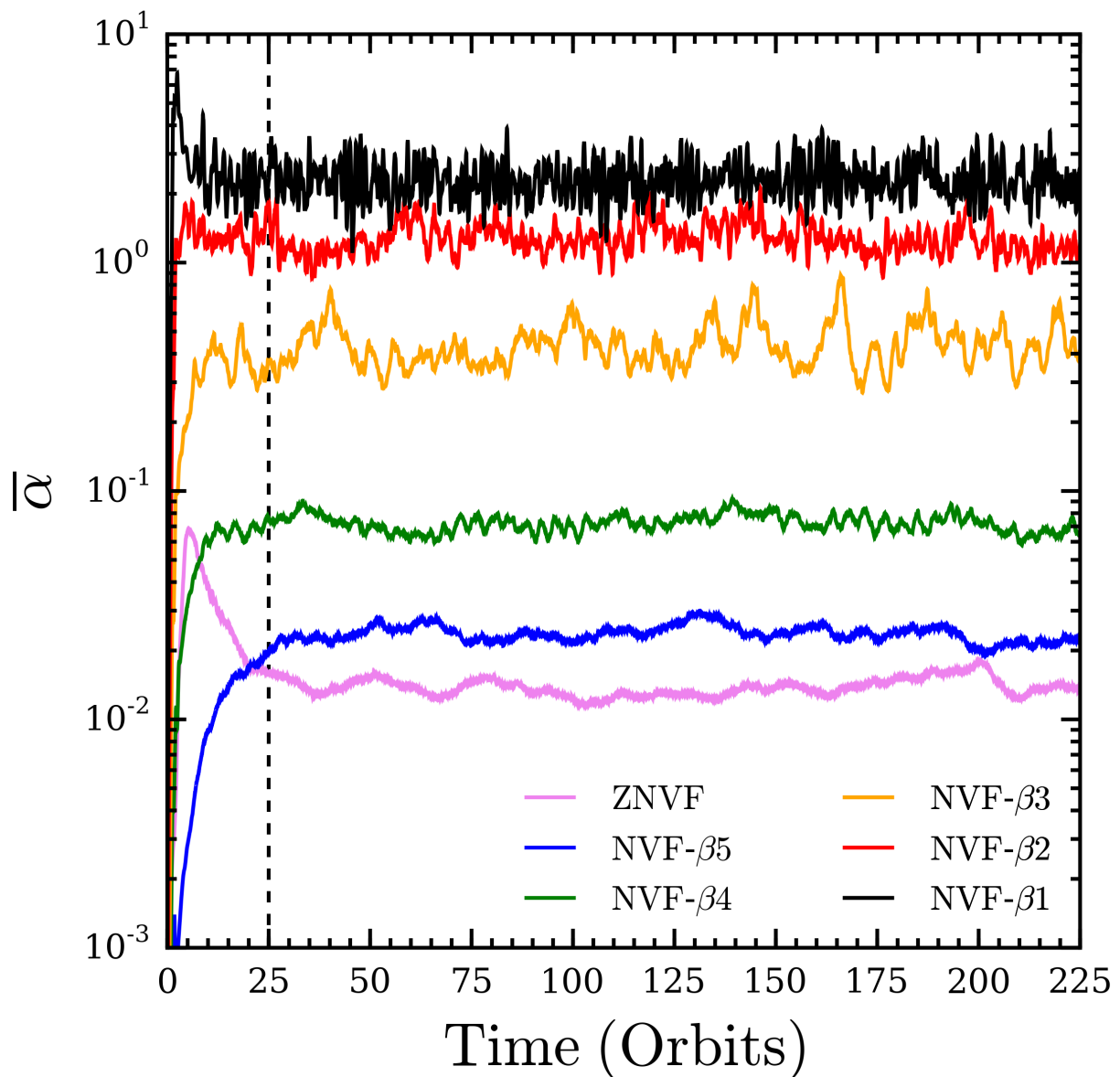
Figure 5.1: Time evolution of the effective viscosity parameter $\overline{\alpha} = \langle T_{xy} \rangle_V / \langle p_{\text{gas}} \rangle_V$ for each simulation: ZNVF (*purple lines*), NVF-$\beta 5$ (*blue lines*), NVF-$\beta 4$ (*green lines*), NVF-$\beta 3$ (*orange lines*), NVF-$\beta 2$ (*red lines*), and NVF-$\beta 1$ (*black lines*). The *vertical dashed line* at time $t = 25$ orbits marks the start of all time averaging in this work. The effective viscosity parameter is relatively small for the zero net vertical magnetic flux simulation ZNVF, but increases dramatically with increasing net vertical magnetic flux, even exceeding unity for simulations NVF-$\beta 2$ and NVF-$\beta 1$.
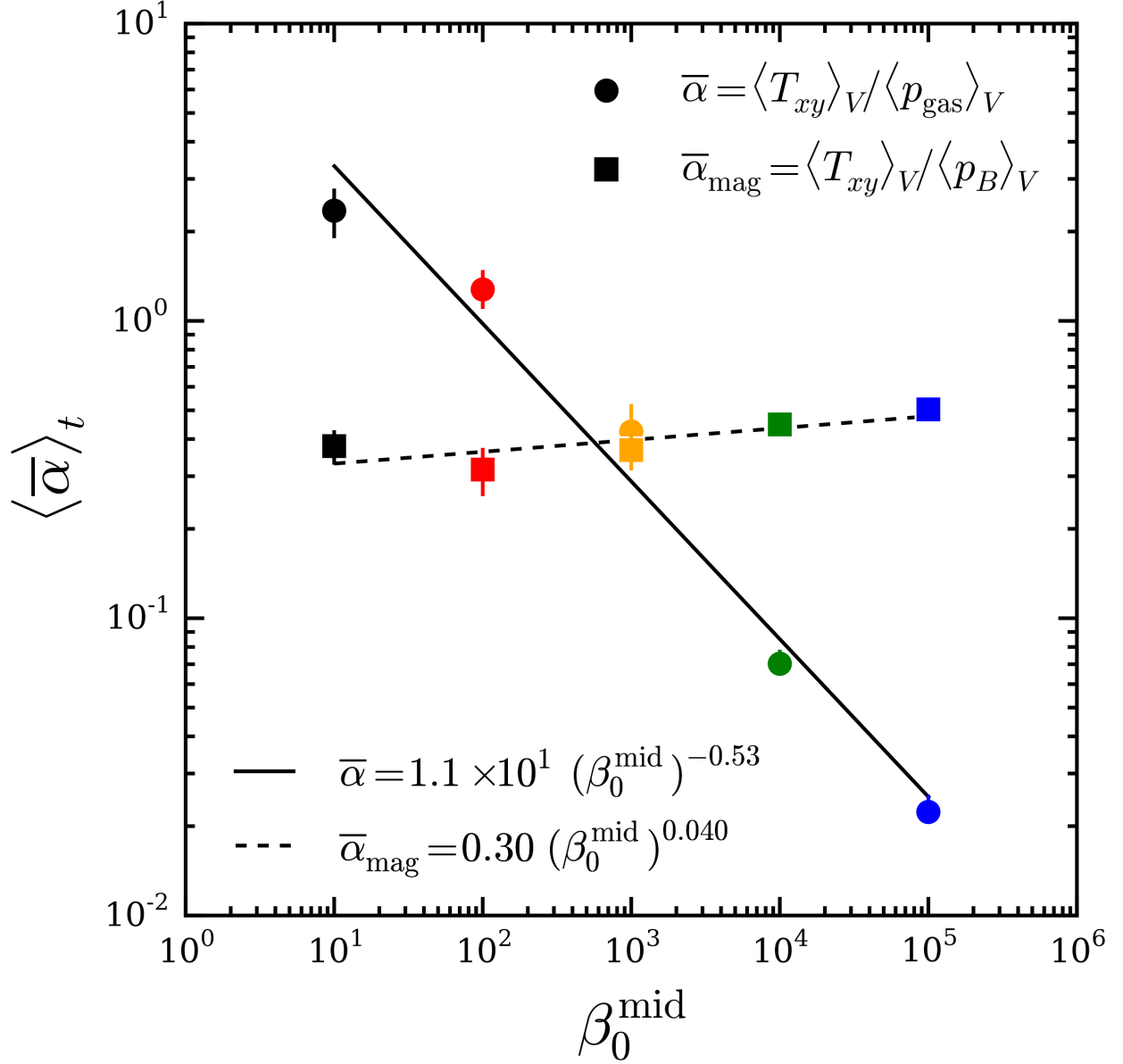
Figure 5.2: Time-averaged effective $\overline{\alpha}$-viscosity parameter as a function of the initial disc mid-plane ratio of gas pressure-to-magnetic pressure for simulations with a net vertical magnetic flux. The angular momentum transport rate $\langle\overline{\alpha}\rangle_t$ is set by β_0^{mid}, following a power-law relation with the net vertical magnetic flux. Rather than normalizing the total stress by the gas pressure, $\overline{\alpha} = \langle T_{xy}\rangle_V / \langle p_{\mathrm{gas}}\rangle_V$ (*circles*), if we instead normalize by the magnetic pressure, $\overline{\alpha}_{\mathrm{mag}} = \langle T_{xy}\rangle_V / \langle p_B\rangle_V$ (*squares*), then $\overline{\alpha}_{\mathrm{mag}}$ becomes essentially independent of β_0^{mid}.
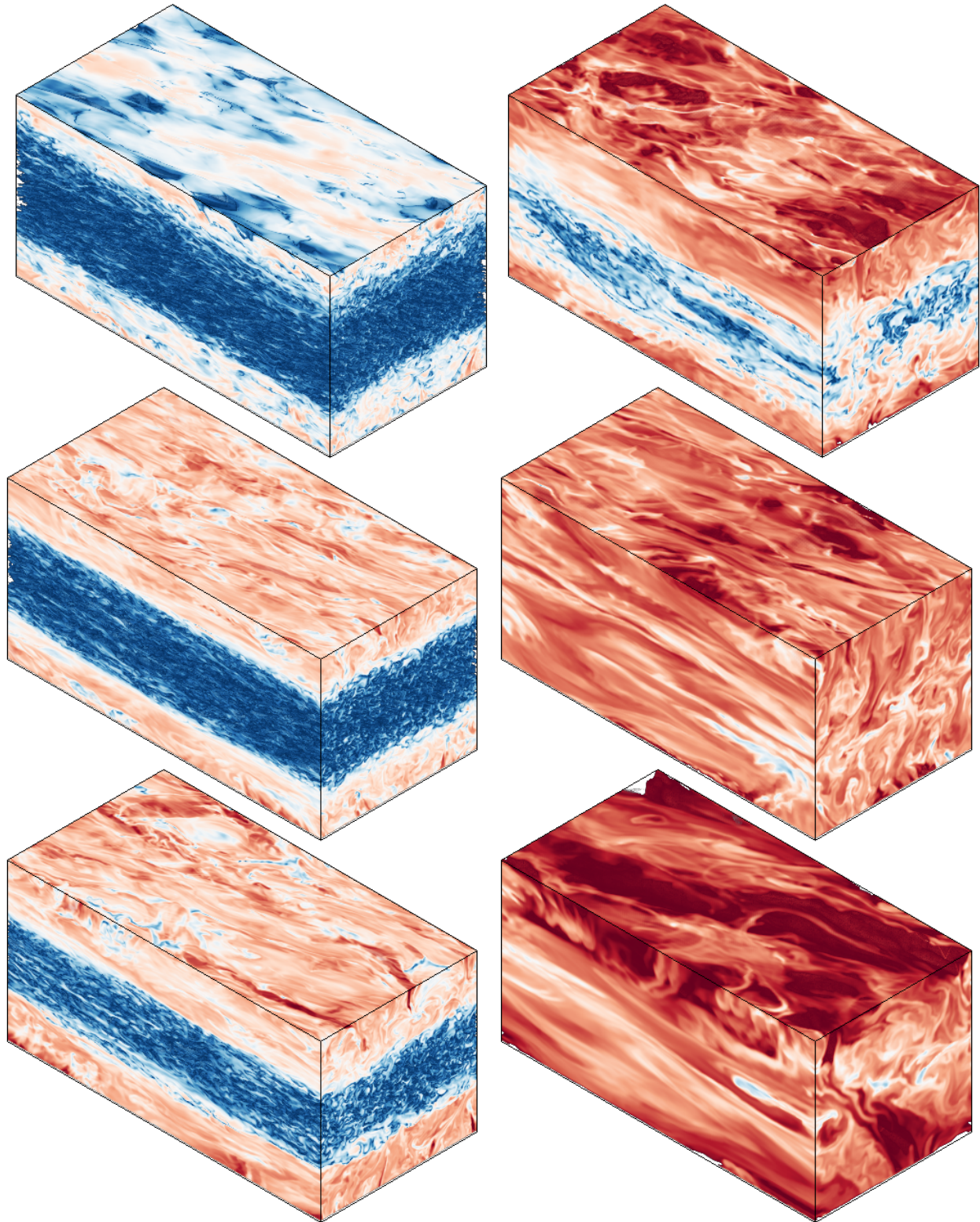
Figure 5.3: Volume renderings of the ratio of gas pressure-to-magnetic pressure, $\beta \equiv p_{\mathrm{gas}}/p_{\mathrm{B}}$, at time $t = 125$ orbits. From *top* to *bottom*, the *left column* shows simulations ZNVF, NVF-β5, NVF-β4 and the *right column* shows simulations NVF-β3, NVF-β2, NVF-β1. *Red*, *white*, and *blue* colours denote regions with $\beta < 1$, $\beta \simeq 1$, and $\beta > 1$, respectively, with the colours being logarithmically rendered over the range $\log_{10}(\beta) = [-2, 2]$. Larger scale turbulent structures develop with decreasing β_0^{mid}. The full simulation domain is magnetic pressure-dominated for NVF-β2 and NVF-β1.
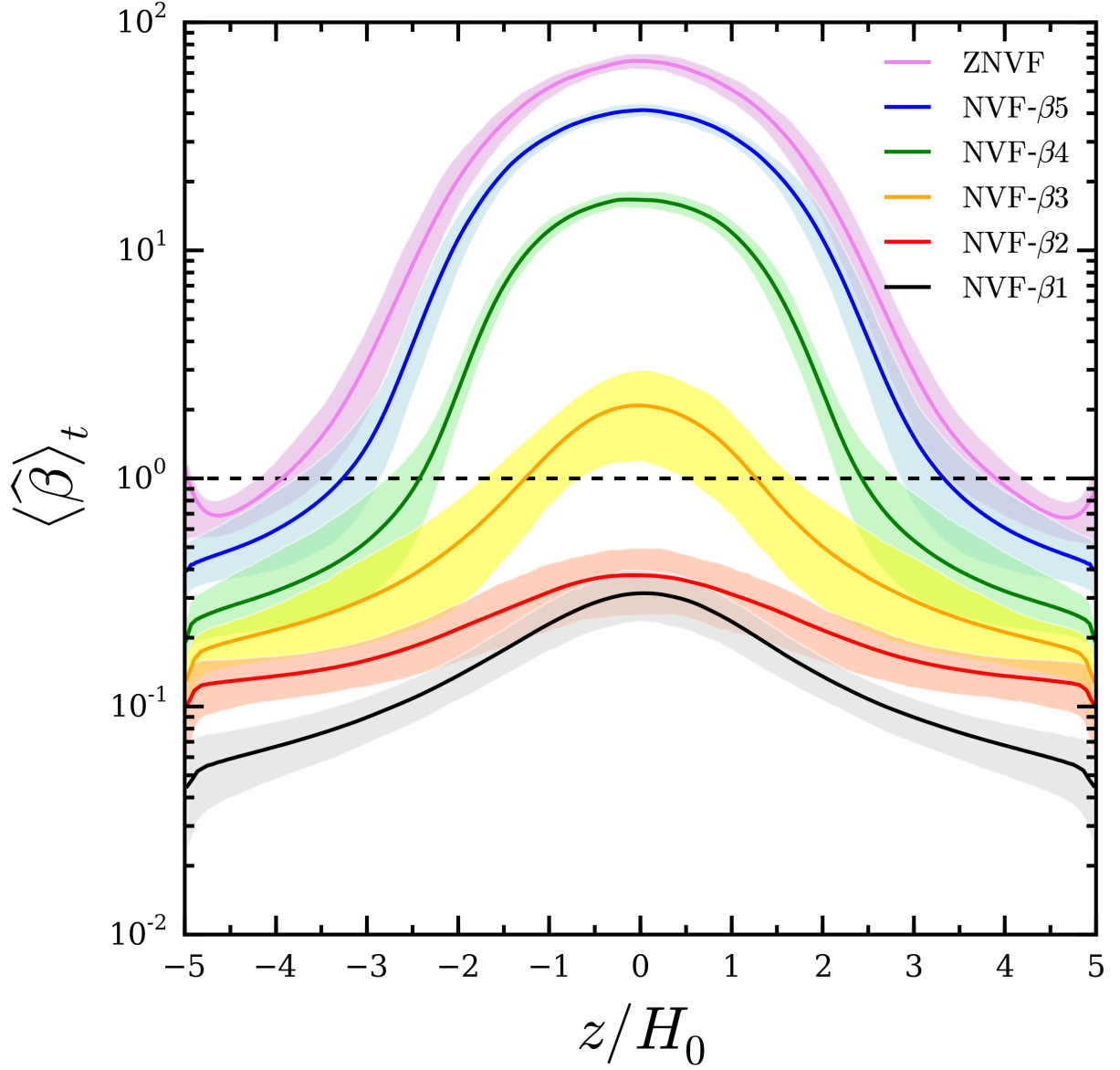
Figure 5.4: Vertical profiles of the time-averaged $\widehat{\beta}$ (Equation 5.14) for each simulation (see Figure 5.1 for line colour conventions). Coloured bands show the $\pm 1\sigma$ range about the average for the dimension indicated by the outermost angled bracket (time in this case). The *horizontal dashed line* marks equipartition between gas pressure and magnetic pressure. A magnetic pressure-dominated corona forms for all simulations. The location of the transition from gas to magnetic pressure-domination (i.e., $\beta = 1$) moves toward the disc mid-plane with increasing net vertical magnetic flux, with the entire domain becoming magnetic pressure-dominated (i.e., $\beta < 1$) for simulations NVF-$\beta 2$ and NVF-$\beta 1$.
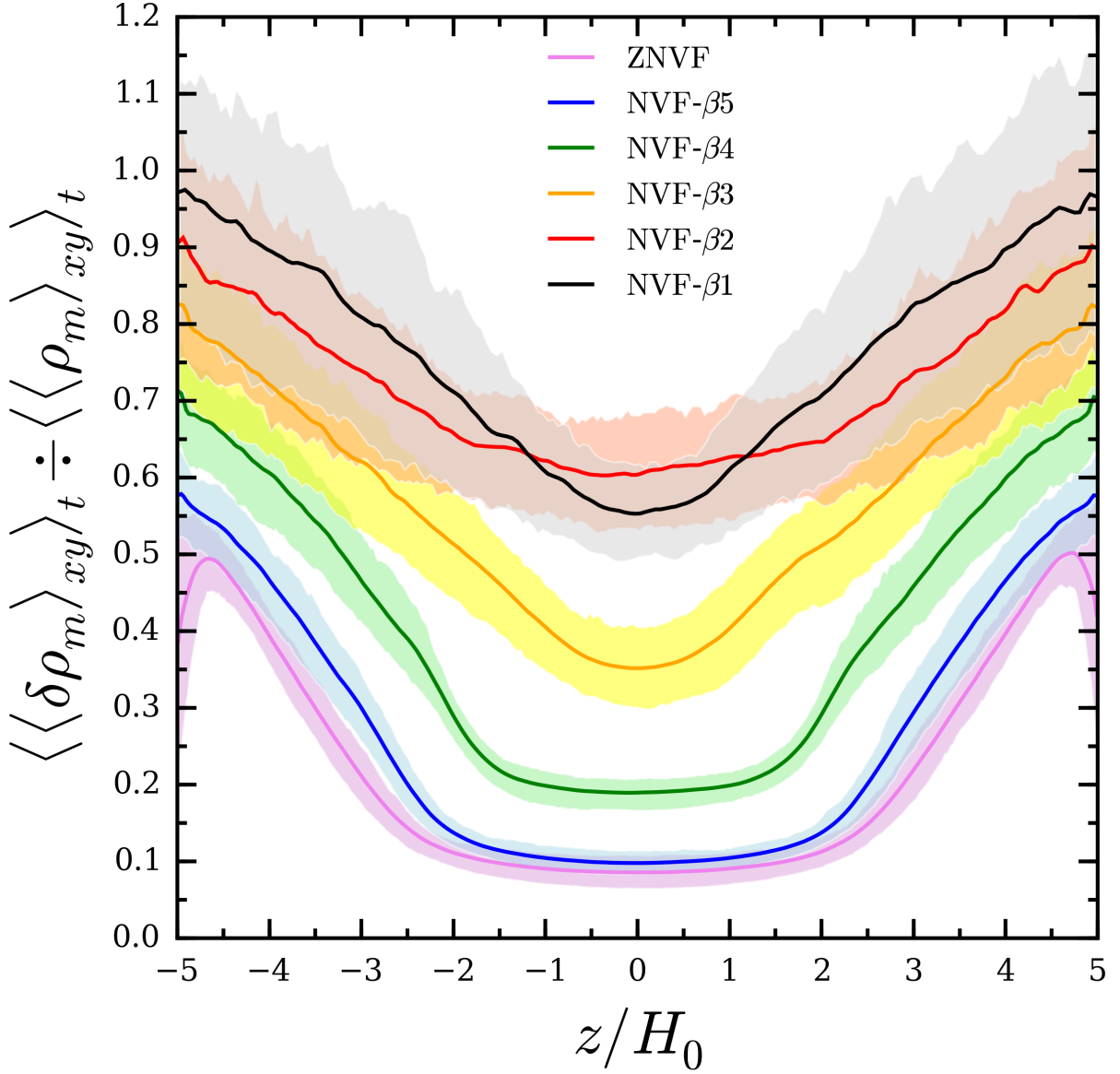
Figure 5.5: Vertical profiles of the horizontally- and time-averaged gas density fluctuations relative to the horizontally- and time-averaged gas density weighted by mass (see Figure 5.1 for line colour conventions). For the zero net vertical magnetic flux simulation ZNVF, the normalized gas density r.m.s. fluctuations are at the $\simeq 10\%$ ($\sim 20 - 50\%$) level in the disc (corona) regions. These gas density fluctuations increase with the amount of net vertical magnetic flux, with large variations about the $\simeq 65\%$ ($\sim 75 - 100\%$) level in the disc (corona) regions for the most strongly magnetized simulations NVF-$\beta 2$ and NVF-$\beta 1$.

Figure 5.1 shows the time evolution of $\overline{\alpha}$ for each simulation. The zero net vertical magnetic flux simulation ZNVF shows a relatively small $\langle\overline{\alpha}\rangle_t = 0.015 \pm 0.003$ with little temporal variability, consistent with the results from Davis et al. (2010) and Simon et al. (2012). When a net vertical magnetic flux is introduced, the rate of angular momentum transport becomes both enhanced and more variable, achieving $\langle\overline{\alpha}\rangle_t = 2.3 \pm 0.5$ for the simulation with the strongest net vertical magnetic flux NVF-β1.

Treating the initial value of β at the disc mid-plane as a control parameter, Figure 5.2 shows how $\overline{\alpha}$ scales with β_0^{mid}. We find that the scaling is well-fit by a single power-law, which closely matches the expected slope of $-1/2$. Our best fit has the form,

$$\langle\overline{\alpha}\rangle_t = 1.1 \times 10^1 \left(\beta_0^{\mathrm{mid}}\right)^{-0.53}. \tag{5.20}$$

This relation holds over four orders of magnitude in β_0^{mid} (two orders of magnitude in B_z), and covers almost the entire range of net fluxes for which the flux (a) boosts the efficiency of transport as compared to zero-net field simulations and (b) allows linearly unstable MRI modes. Alternatively, we can choose to normalize the stress by the magnetic pressure, $\overline{\alpha}_{\mathrm{mag}} = \langle T_{xy}\rangle_V/\langle p_B\rangle_V$. With this definition, the effective viscosity becomes essentially independent of β_0^{mid},

$$\langle\overline{\alpha}_{\mathrm{mag}}\rangle_t = 0.30 \left(\beta_0^{\mathrm{mid}}\right)^{-0.040}. \tag{5.21}$$

These results are consistent with previous works that find power-law and nearly constant scalings with β for $\overline{\alpha}$ and $\overline{\alpha}_{\mathrm{mag}}$ (Hawley et al., 1995; Blackman et al., 2008). Finally, we can combine Equations 5.20 and 5.21 to assess how the disc magnetization (which in the saturated state is dominated by the toroidal component) scales with the imposed net flux. We find,

$$\langle\overline{\beta}\rangle_t \sim 0.03 \left(\beta_0^{\mathrm{mid}}\right)^{1/2}, \tag{5.22}$$

which implies that the net flux threshold for the disc to become magnetically dominated (in a volume-averaged sense) is at approximately $\beta_0^{\mathrm{mid}} \sim 10^3$. As a caveat, we mention that results derived from volume averages of α and β will be somewhat dependent on the vertical domain size. For instance, results would be weighted more to the corona for a more vertically extended box.

Figure 5.3 shows volume renderings of β at $t = 125$ orbits for each simulation. The gas is turbulent, with *blue* and *red* indicating gas pressure-dominated ($\beta > 1$) and magnetic pressure-dominated ($\beta < 1$)
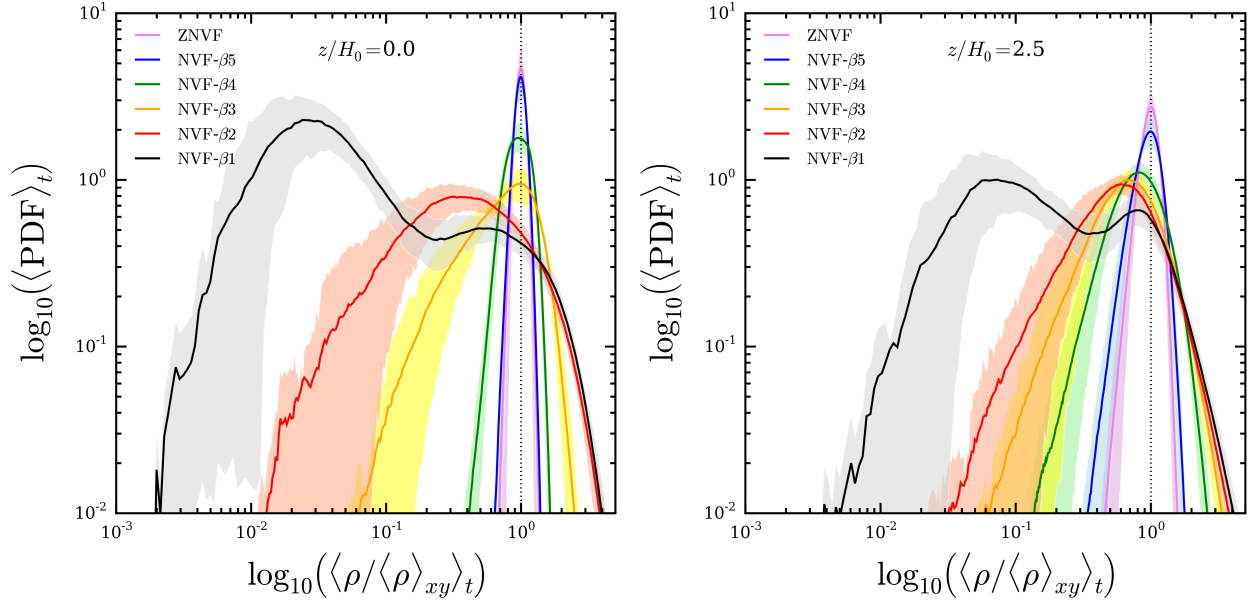
Figure 5.6: Normalized probability density function of gas density relative to its mean value, evaluated at $z/H_0 = 0$ (*left*) and $z/H_0 = 2.5$ (*right*) for each simulation (see Figure 5.1 for line colour conventions). Simulations ZNVF, NVF-$\beta 5$, and NVF-$\beta 4$ have highly homogeneous density structures at the disc mid-plane region, with modest inhomogeneity developing in the coronal regions. The strongly magnetized simulations NVF-$\beta 3$ and NVF-$\beta 2$ are inhomogeneous throughout the domain, while the very strongly magnetized simulation NVF-$\beta 1$ is highly inhomogeneous.

regions, respectively, while *white* shows regions near equipartition ($\beta \simeq 1$). As the amount of net vertical magnetic flux increases, the simulation domain becomes more magnetic pressure-dominated and the turbulence develops larger-scale structure. Figure 6.1 shows the corresponding vertical profile of the horizontally- and time-averaged plasma-β. All of the simulations show the formation of a low-density magnetic pressure-dominated corona (Miller & Stone, 2000). The vertical location where the $\langle\widehat{\beta}\rangle_t = 1$ transition occurs moves closer to the disc mid-plane with increasing net vertical magnetic flux. The entire domain, including the mid-plane, becomes magnetic pressure-dominated for simulations NVF-$\beta 2$ and NVF-$\beta 1$.

Our two strongest net field runs become fully magnetically dominated, reducing the mid-plane density and pressure in the saturated state as compared to the initial conditions. As a result, while the average vertical magnetic flux is a conserved quantity, the mid-plane value of β associated with the vertical field is not. The reduction in β_0^{mid} due to the onset of magnetic pressure support means that it is conceivable that an initially unstable disc, with a vertical flux close to the linear stability threshold, could evolve into a magnetically dominated state where the vertical field was no longer unstable. We see no evidence for such an effect, though a simple estimate suggests that our strongest net field simulation does access a regime where the tension of the vertical field is dynamically highly important on all scales. Nominally, magnetic tension from a strong vertical magnetic field will suppress MRI when $v_{\mathrm{A},z}^2 \gtrsim 6c_{\mathrm{s}}^2/\pi^2$ (Balbus & Hawley, 1998), where $v_{\mathrm{A},z}$ is the vertical component of the Alfvén speed, $v_{\mathrm{A}} = B/\sqrt{\rho}$. In the context of our simulations this stability criterion can be written as $\beta_z \lesssim 3.3$. Simulation NVF-$\beta 1$, with $\langle\beta_z^{\mathrm{mid}}\rangle_t = 1.8 \pm 0.3$, is sufficiently magnetized as to approach this limit, but only in the saturated state whose structure is dramatically different from the equilibrium used to compute the linear stability threshold. To quantify this, we measure the variance of the horizontally-averaged gas density at every snapshot in time for each simulation, weighted by mass in order to account for how mass is distributed across regions of a given density,

$$\langle\sigma_m^2\rangle_{xy} = \left\langle \frac{\rho^3}{\langle\rho\rangle_{xy}} \right\rangle_{xy} - \left\langle \frac{\rho^2}{\langle\rho\rangle_{xy}} \right\rangle_{xy}^2. \tag{5.23}$$

Figure 5.5 shows the vertical profile of the horizontally- and time-averaged mass-weighted gas density fluctuations, $\delta\rho_m = \sqrt{\sigma_m^2}$, normalized to the horizontally- and time-averaged mass-weighted gas density vertical profile. For the zero-net field[3] and weak field runs, the r.m.s. density fluctuations near the mid-plane are

---

[3] The boundary features seen in Figures 6.1 and 5.5 for simulation ZNVF are a consequence of a non-negligible fraction of

ID	$\langle\widehat{\beta}^{\mathrm{mid}}\rangle_t$	$\langle\widehat{\beta}_y^{\mathrm{mid}}\rangle_t$	$\langle\widehat{\beta}_p^{\mathrm{mid}}\rangle_t$	$\langle\widehat{\alpha}^{\mathrm{mid}}\rangle_t$	$\langle\widehat{\alpha}_{\mathrm{Rey}}^{\mathrm{mid}}\rangle_t$	$\langle\widehat{\alpha}_{\mathrm{Max}}^{\mathrm{mid}}\rangle_t$
ZNVF	68(6)	81(7)	1.6(1)e3	0.0088(7)	0.0020(2)	0.0067(5)
NVF-β5	41(3)	49(3)	9.3(6)e2	0.014(1)	0.0034(3)	0.0111(8)
NVF-β4	17(1)	21(2)	2.9(4)e2	0.035(3)	0.008(1)	0.027(2)
NVF-β3	2.1(9)	3(1)	3(1)e1	0.3(1)	0.06(2)	0.22(9)
NVF-β2	0.4(1)	0.5(2)	7(2)	1.0(4)	0.16(8)	0.9(3)
NVF-β1	0.31(8)	0.5(1)	2.8(5)	1.1(3)	0.12(5)	1.0(3)

Table 5.2: Fundamental properties of the MRI turbulence, all evaluated at the disc mid-plane and time-averaged. From *left* to *right* the columns are: simulation identification label, plasma-$\widehat{\beta}$ parameter, toroidal component of $\widehat{\beta}$, poloidal component of $\widehat{\beta}$, effective $\widehat{\alpha}$-viscosity parameter, Reynolds component of $\widehat{\alpha}$, and Maxwell component of $\widehat{\alpha}$. Parentheses indicate the $\pm 1\sigma$ range on the last digit.

at the 10% level, consistent with the usual expectation that compressibility is ignorable for mid-plane MRI dynamics. (Note that even in these simulations, substantially stronger density fluctuations occur in the corona.) For NVF-β2 and NVF-β1, conversely, the density fluctuation amplitude is extremely strong, with $\delta\rho/\rho \approx 0.6 - 1$.

To further investigate the inhomogeneous nature of strongly magnetized discs, we compute the normalized probability density function (PDF) of the gas density relative to its mean value at a given height in the disc. Figure 5.6 shows these PDFs at the disc mid-plane ($z/H_0 = 0$; *left panel*) and in the corona ($z/H_0 = 2.5$; *right panel*). In other words, Figure 5.6 shows what fraction of volume at a given height is occupied by gas with density $\rho/\langle\rho\rangle_{xy}$. For the zero-net field and weak field runs, the gas density PDFs are narrowly concentrated about the mean value, which indicates a relatively homogeneous density structure. However, the moderate and strong field runs have an inhomogeneous density structure, as evidenced by the peak in the gas density PDF shifting to lower $\rho/\langle\rho\rangle_{xy}$ values and the distribution broadening. Interestingly, a two-component structure develops for the strongest net field simulation NVF-β1. As expected for a disc with $\alpha \sim 1$, NVF-β1 has become highly inhomogeneous, such that the relevance of the linear stability analysis for the vertical field is limited. Indeed, we cannot exclude the possibility that clumpy MRI-unstable discs with even stronger net fields might be possible, at least in situations where the net field evolves slowly toward higher values.

---

grid zones reaching the imposed gas density floor.

ID	P_{dyn} [orbits]	ξ	$\langle\langle\eta\rangle_V\rangle_t$	$\langle\alpha_B^{\mathrm{mid}}\rangle_t$	$\langle\beta_{\mathrm{B15}}^{\mathrm{mid}}\rangle_t$
ZNVF	12(3)	0.5(1)	0.029(4)	0.016(2)	7(2)e1
NVF-β5	10(2)	0.6(1)	0.043(3)	0.029(3)	4(1)e1
NVF-β4	8(2)	0.7(2)	0.068(6)	0.09(1)	1.7(4)e1
NVF-β3	15(4)	0.4(1)	0.12(2)	0.3(1)	2(1)
NVF-β2	8(5)e1	0.08(5)	0.21(3)	0.3(2)	$0.7^{+1}_{-0.7}$
NVF-β1	–	–	0.30(5)	$0.4^{+0.2}_{-0.4}$	$0.6^{+1}_{-0.6}$

Table 5.3: Fundamental properties of the MRI-dynamo. From *left* to *right* the columns are: simulation identification label, period of MRI-dynamo cycles (P_{dyn}), ξ parameter (see Equation 5.24), volume- and time-averaged efficiency parameter for the rise of toroidal magnetic flux (η), disc mid-plane evaluated and time-averaged parameter for the toroidal magnetic flux production (α_B), and disc mid-plane evaluated and time-averaged plasma-β predicted from Equation 5.31 ($\beta_{\mathrm{B15}}^{\mathrm{mid}}$). All of these parameters are defined in the text. Parentheses indicate the $\pm 1\sigma$ range on the last digit.

5.5   Properties of the MRI-Dynamo

Having established the basic properties of MRI turbulence in our simulations, this section quantifies the properties of the MRI-dynamo.

5.5.1   Toroidal Magnetic Field Reversals

For each simulation, Figure 5.7 shows the space-time diagram of the horizontally-averaged toroidal magnetic field, $\langle B_y\rangle_{xy}$. These so-called "butterfly diagrams" exhibit quasi-periodic reversals of $\langle B_y\rangle_{xy}$, which is a hallmark of accretion disc MRI-dynamo activity (e.g., Brandenburg et al., 1995). The amount of net vertical magnetic flux increases from *top* to *bottom* in Figure 5.7 and *black contours* show the transitional vertical location where $\widehat{\beta} = 1$. Reversals in the large-scale toroidal magnetic field showcase regular periodicity for the zero net vertical magnetic flux simulation and simulations with $\beta_0^{\mathrm{mid}} \gtrsim 10^4$. This is a well-known result for stratified shearing boxes (e.g., Simon et al., 2012) and global disc simulations (e.g., O'Neill et al., 2011) with zero net vertical magnetic flux. However, previous shearing box simulations with a net vertical magnetic flux and $\beta_0^{\mathrm{mid}} \gtrsim 10^4$ (Fromang et al., 2013; Bai & Stone, 2013) show highly irregular dynamo patterns.

In the moderately magnetized regime with $\beta_0^{\mathrm{mid}} = 10^3$, Figure 5.7 shows that the toroidal magnetic field reversals become less frequent and more sporadic, with temporary episodes where the entire disc domain becomes magnetic pressure-dominated. This behaviour was also observed in the $\beta_0^{\mathrm{mid}} = 10^3$ shearing box
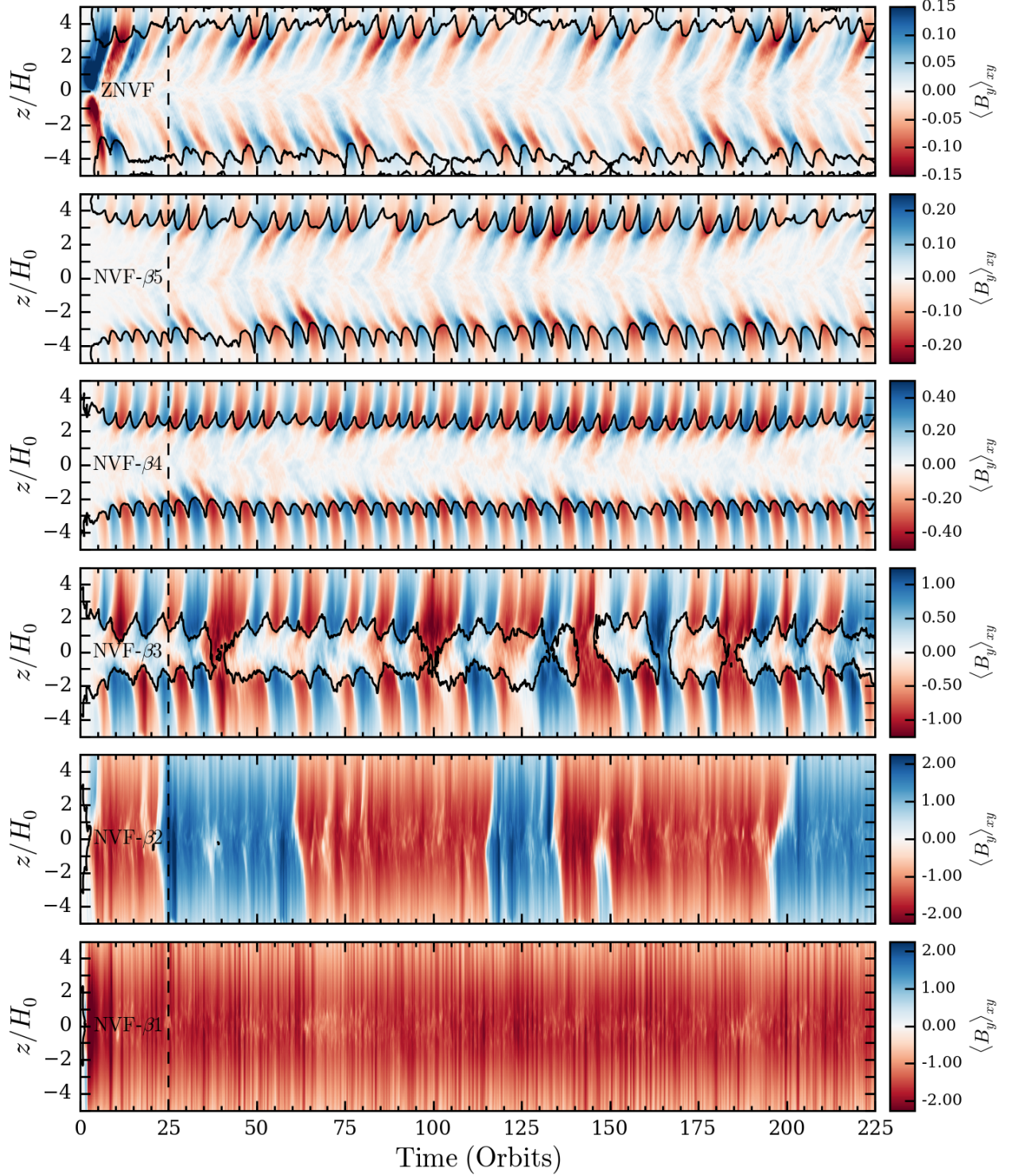
Figure 5.7: Time evolution of the horizontally-averaged toroidal magnetic field, $\langle B_y \rangle_{xy}$, with height from the disc mid-plane, z/H_0. From *top* to *bottom* are space-time diagrams for simulations ZNVF, NVF-β5, NVF-β4, NVF-β3, NVF-β2, NVF-β1. MRI-dynamo behaviour occurs in all but the most strongly magnetized simulation NVF-β1. The period of the MRI-dynamo cycle generally becomes longer and reversals become more sporadic with increasing net vertical magnetic flux. *Black lines* show the $\widehat{\beta} = 1$ contour. The entire disc becomes magnetic pressure-dominated for brief episodes in simulation NVF-β3 and for all times in simulations NVF-β2 and NVF-β1.
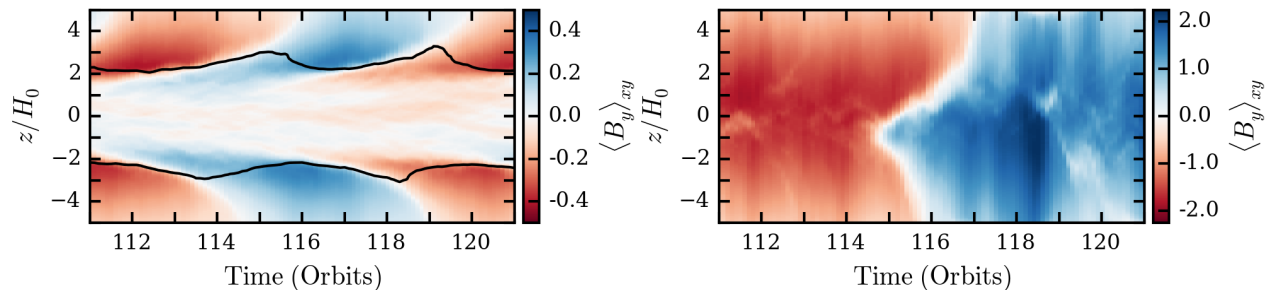
Figure 5.8: Butterfly diagrams for simulations NVF-$\beta4$ (*left*) and NVF-$\beta2$ (*right*), zoomed in over 10 orbits to highlight the $\langle B_y \rangle_{xy}$ structure during a reversal. *Black lines* show the $\widehat{\beta} = 1$ contour. The current sheet sweeping through the vertical domain during a reversal in $\langle B_y \rangle_{xy}$ propagates faster in strongly magnetized discs (*right*) than in weakly magnetized discs (*left*).
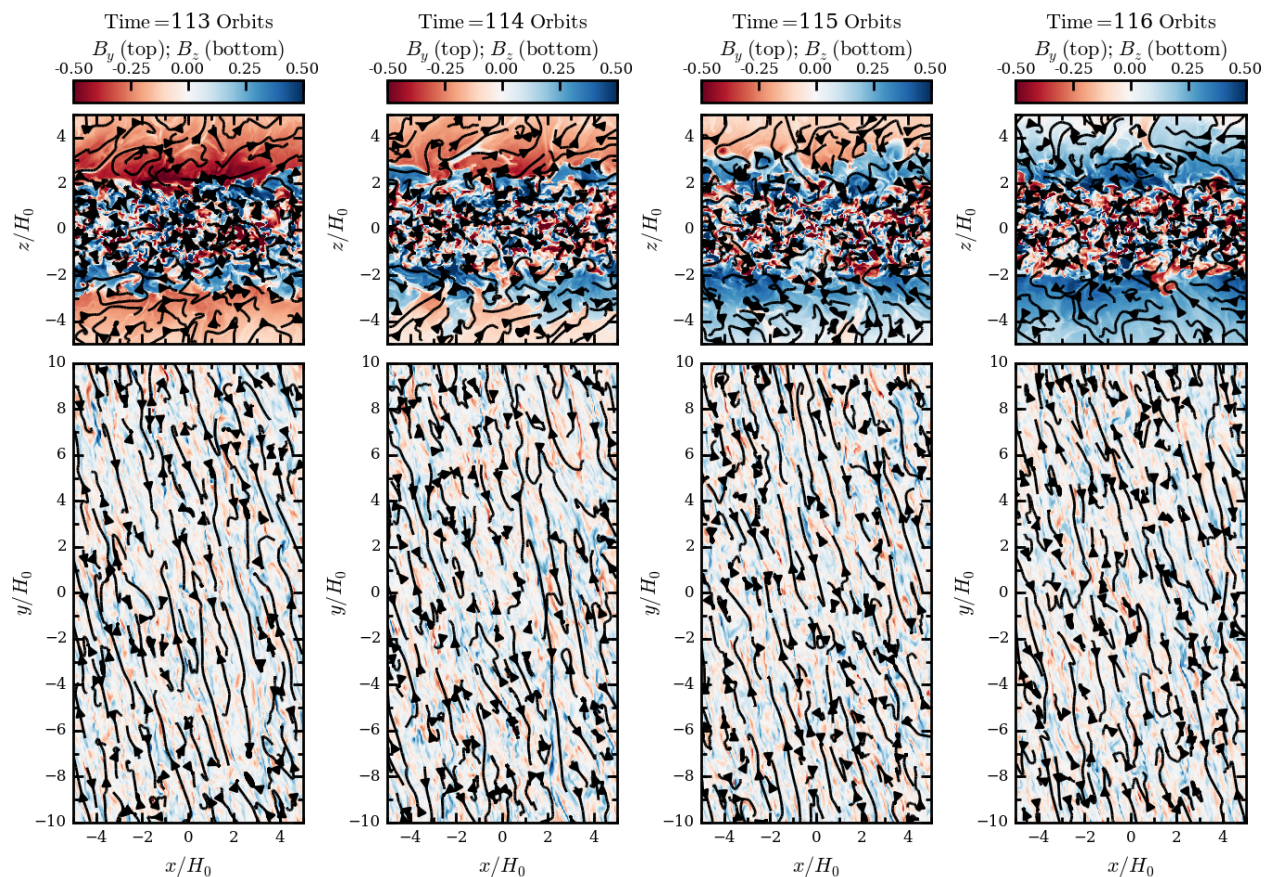

Figure 5.9: Magnetic field structure during an MRI-dynamo reversal in the large-scale toroidal magnetic field (see *left panel* of Figure 5.8) for the weak net vertical magnetic flux simulation NVF-$\beta4$. The *top panels* show colour renderings of the toroidal magnetic field and poloidal magnetic field components for a slice through the xz-plane at $y = 0$. The *bottom panels* show colour renderings of the vertical magnetic field and horizontal magnetic field components for a slice through the xy-plane at $z = 0$. Panels from *left* to *right* show times $t = 113, 114, 115, 116$ orbits. B_y is fairly turbulent, but relatively well-organized, near the equator and is more organized above/below the disc mid-plane.
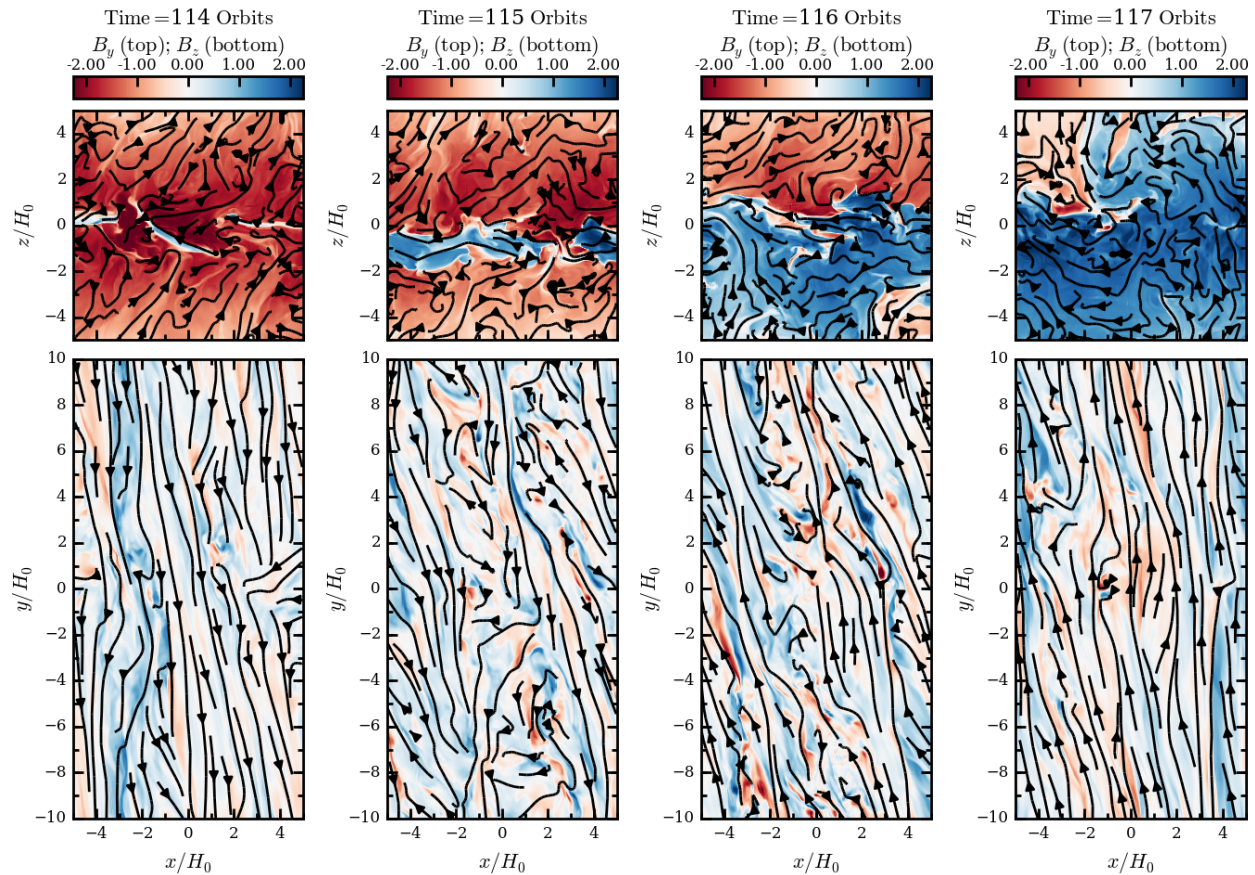
Figure 5.10: Magnetic field structure during an MRI-dynamo reversal in the large-scale toroidal magnetic field (see *right panel* of Figure 5.8) for the strong net vertical magnetic flux simulation NVF-β2. The *top panels* show colour renderings of the toroidal magnetic field and poloidal magnetic field components for a slice through the xz-plane at $y = 0$. The *bottom panels* show colour renderings of the vertical magnetic field and horizontal magnetic field components for a slice through the xy-plane at $z = 0$. Panels from *left* to *right* show times $t = 114, 115, 116, 117$ orbits. Organized B_y structures dominate throughout the domain and are highly organized on the equator.
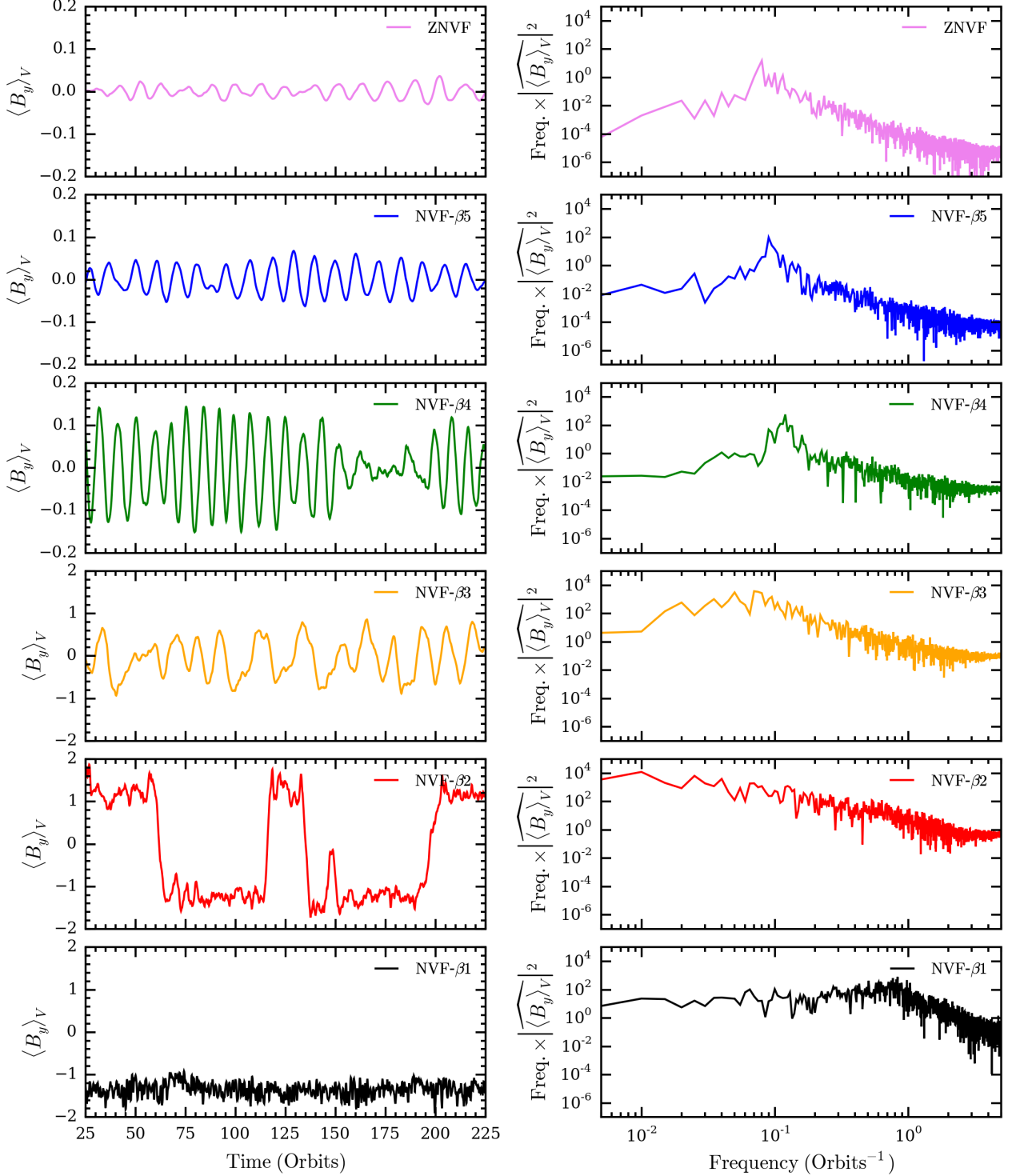
Figure 5.11: Time evolution of the volume-averaged toroidal magnetic field (*left panels*) and its power spectrum (*right panels*). From *top* to *bottom* are simulations ZNVF, NVF-β5, NVF-β4, NVF-β3, NVF-β2, NVF-β1. For simulations with a zero or weak ($\beta_0^{\mathrm{mid}} \lesssim 10^4$) net vertical magnetic flux, a coherent peak appears in the power spectrum resulting from a regular MRI-dynamo period of $P_{\mathrm{dyn}} \simeq 10$ orbits. This feature is substantially broadened for the moderately magnetized simulation NVF-β3 due to the MRI-dynamo flips becoming more sporadic and having a longer period. The strongly magnetized simulation NVF-β2 shows no discernible power spectral peak. The very strongly magnetized simulation NVF-β1 does not exhibit MRI-dynamo cycles and has a flat power spectrum with a high-frequency cutoff at $\simeq 1$ orbit^{-1}.

simulations of Bai & Stone (2013). In the $\beta_0^{\mathrm{mid}} = 10^2$ strong net vertical magnetic flux simulation, the entire disc domain achieves $\widehat{\beta} < 1$ for all times and the toroidal field reversals become still less frequent and more sporadic. However, they still occur. To our knowledge this is the first time that the MRI-dynamo butterfly pattern has been observed to persist in a magnetic pressure-dominated disc. The toroidal magnetic field flip-flops disappear for the very strongly magnetized $\beta_0^{\mathrm{mid}} = 10^1$ simulation, though it is possible that the simulation was not evolved to an adequately long time and/or a larger domain size is necessary to observe this behaviour.

Figure 5.7 also shows that the MRI-dynamo generates an ordered toroidal magnetic field near the disc mid-plane, which buoyantly rises and reaches a maximal amplification near the height where $\widehat{\beta} \simeq 1$. The colour bars in Figure 5.7 show that the peak strength that the toroidal magnetic field reaches is similar for the zero net vertical magnetic flux simulation ZNVF and the very weak net vertical magnetic flux simulation NVF-$\beta5$. This peak toroidal field strength roughly doubles with each order of magnitude decrease in β_0^{mid} until the $\beta_0^{\mathrm{mid}} = 10^1$ simulation, where the toroidal field strength appears to saturate to the same level as in the $\beta_0^{\mathrm{mid}} = 10^2$ simulation. This is suggestive of a threshold value to the toroidal magnetic field that the MRI-dynamo can produce from an imposed net vertical magnetic flux.

The period of MRI-dynamo cycles can be measured as $P_{\mathrm{dyn}} = \Delta t / N_{\mathrm{cycles}}$. Over the time interval $\Delta t = t_{\mathrm{f}} - t_{\mathrm{i}} = 200$ orbits, we measure the number of MRI-dynamo cycles, $N_{\mathrm{cycles}} = N_{\mathrm{flips}}/2$, by counting the number of $\langle B_y \rangle_V$ reversals separately in the top ($z > 0$) and bottom ($z < 0$) simulation domains and averaging them together to get $N_{\mathrm{flips}} = \left(N_{\mathrm{flips}}^{\mathrm{top}} + N_{\mathrm{flips}}^{\mathrm{bot}} \right)/2$. We measure P_{dyn} and estimate its uncertainty as $P_{\mathrm{dyn}}/\sqrt{N_{\mathrm{cycles}}}$. The MRI-dynamo period (in units of orbits) can also be parametrized as,

$$P_{\mathrm{dyn}} = \frac{2\pi}{\xi\Omega} \ [\mathrm{orbits}], \tag{5.24}$$

and we list the results for P_{dyn} and ξ in Table 5.3. The ξ parameter will be important in §5.5.2 and §5.5.3.

Figure 5.8 shows zoomed-in subsets of Figure 5.7 for simulations NVF-$\beta4$ (*left*) and NVF-$\beta2$ (*right*) to highlight the space-time structure of toroidal magnetic field reversals for weak and strong net vertical magnetic flux cases, respectively. Notably, the rise speed of the current sheets launched during each reversal of the toroidal magnetic field increases with net vertical magnetic flux.

Figures 5.9 and 5.10 show the detailed magnetic field structure for simulations NVF-$\beta4$ and NVF-$\beta2$, respectively, over the course of the $\langle B_y \rangle_{xy}$ reversals highlighted in Figure 5.8. Comparing Figures 5.9 and 5.10 demonstrates that the MRI-dynamo behaves differently in the weak and strong net vertical flux cases.

For the weakly magnetized NVF-$\beta4$, the azimuthal slice (xz-plane) of Figure 5.9 shows small-scale, turbulent magnetic field structure concentrated to the disc mid-plane regions, with B_y becoming more organized at heights where $\beta \lesssim 1$. While there is a mildly dominant B_y polarity in the mid-plane regions at any given time, a blend of both positive and negative B_y structures is always present. The equatorial slice (xy-plane) shows that even at the equator, B_y is relatively well-organized.

For the strongly magnetized NVF-$\beta2$, Figure 5.10 shows that B_y dominates at all heights and is highly organized at the disc mid-plane. In the *leftmost panel*, a precursor of the MRI-dynamo flip is present in the form of a few ribbon-like positive (*blue*) B_y structures. While the entire domain is dominated by either positive or negative B_y at a given time preceding or following an MRI-dynamo reversal, wispy B_y structures of the non-dominant polarity always persist in the vicinity of the disc mid-plane. Indeed, the *rightmost panel* shows that a negative (*red*) B_y ribbon-like precursor is now present near the mid-plane following an MRI-dynamo flip. For both NVF-$\beta4$ and NVF-$\beta2$, the MRI-dynamo launches current sheets into the corona — although they do not propagate perfectly synchronously above/below the disc mid-plane — and the large-scale toroidal magnetic field in the coronal region reverses sign.

Several authors have attempted to understand the origin of the MRI-dynamo field reversals, and quantitative properties such as the period, using $\alpha\Omega$ dynamo theory (see e.g. Gressel & Pessah, 2015, and references therein). In a different approach, Herault et al. (2011) computed exactly time-periodic dynamo solutions to an incompressible model at modest Reynolds and magnetic Reynolds numbers. They argued that the MRI-dynamo results from interactions between the dominant toroidal field and non-axisymmetric perturbations. The relevance of these simplified models to our simulations — which as we have noted are highly compressible when the net flux is strong — is unclear, but it is possible that sufficient small-scale turbulence is a prerequisite for MRI-dynamo reversals. We observe a clear decrease in small-scale turbulence as the net field increases (see Figures 5.9 and 5.10).

The *left panel* of Figure 5.11 shows the time-evolution of the volume-averaged toroidal magnetic field,

$\langle B_y \rangle_V$, for each simulation. The MRI-dynamo cycles are apparent from the sinusoidal behaviour of $\langle B_y \rangle_V$. A dynamo flip in one disc hemisphere is nearly always mirrored by a similar response in the other disc hemisphere; however, this response is not necessarily instantaneous. For instance, consider the time range $t \simeq 150 - 200$ in simulation NVF-$\beta 4$. Figure 5.7 shows a well-defined butterfly pattern for $\langle B_y \rangle_{xy}$, but Figure 5.11 shows that the top ($z > 0$) and bottom ($z < 0$) domains are anti-synchronized, as evidenced by $\langle B_y \rangle_V \simeq 0$ in this time range.

The *right panel* of Figure 5.11 shows the temporal power spectrum generated from $\langle B_y \rangle_V$ for each simulation. These are not significantly altered by the occasional offset nature of $\langle B_y \rangle_V$ in the top and bottom disc hemispheres just described. The weakly magnetized simulations with a well-defined MRI-dynamo pattern (ZNVF, NVF-$\beta 5$, NVF-$\beta 4$) display a coherent peak in the power spectrum, while this feature broadens/disappears for the strongly magnetized simulations because the MRI-dynamo cycles are either sporadic (NVF-$\beta 3$, NVF-$\beta 2$) or non-existent (NVF-$\beta 1$).

5.5.2 Production and Escape of Toroidal Magnetic Field

The MRI-dynamo channels accretion power into ordered toroidal magnetic fields near the disc mid-plane, which buoyantly rise through the disc atmosphere and escape. In the model for the MRI-dynamo proposed by Begelman et al. (2015), accretion energy is being liberated locally by the MRI and some fraction of this is channeled into the toroidal magnetic field. This toroidal field rises due to the Parker instability and carries a vertical flux of magnetic energy (i.e., Poynting flux). However, this buoyant rise of toroidal field is hampered by field buckling and reconnection, causing energy to be lost to the gas by the magnetic field as it rises. The details of this complicated energy exchange process are simplified by assuming that all of the energy lost by the toroidal magnetic field as it rises goes into locally heating the gas. In this model for toroidal magnetic flux production and escape, the governing energy balance equation is,

$$\frac{d}{dz}\left(p_B v_B^2\right) = \Omega v_B \left[\alpha_B \left(p_{\text{gas}} + p_B\right) - 2\xi p_B\right], \tag{5.25}$$

where α_B measures the portion of accretion energy liberated locally by the MRI that goes into the toroidal magnetic field and we recall the MRI-dynamo period parameter ξ from Equation 5.24. The vertical profile
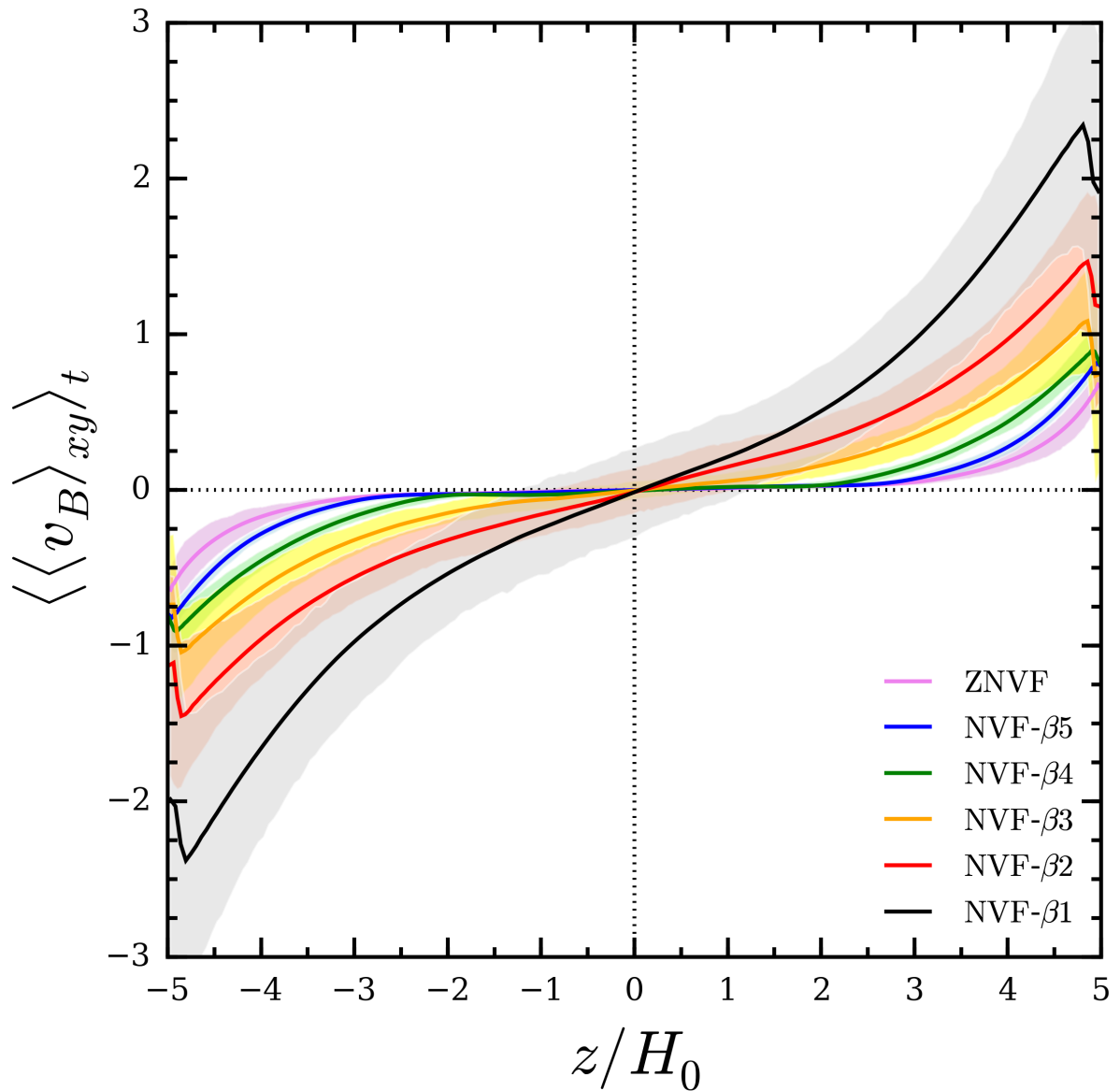
Figure 5.12: Vertical profiles of the horizontally- and time-averaged rise speed (in code units) of the toroidal magnetic flux (see Figure 5.1 for line colour conventions). For all simulations, $v_B \simeq 0$ within the gas-pressure dominated regions (i.e., interior to the z-locations where $\langle \widehat{\beta} \rangle_t \simeq 1$). Outside of this vertical location, $v_B > 0$ and increases with disc altitude. As the net vertical magnetic flux increases, v_B increases and even reaches supersonic speeds (i.e., $v_B > c_s = 1$) for simulations NVF-$\beta 2$ and NVF-$\beta 1$.

for the rise speed of the toroidal magnetic flux can be expressed as,

$$v_B(z) = \eta \Omega z, \tag{5.26}$$

where $\eta = 1$ would correspond to the field rising at the free-fall speed. Values of $\eta \leq 1$ phenomenologically account for effects that slow down the rise speed of the toroidal magnetic field, such as tangling of magnetic field lines and magnetic reconnection.

Here, we use our simulations to measure quantities that characterize toroidal magnetic flux production (α_B) and escape (v_B, η) within the context of this model. We measure the horizontally-averaged rise speed of the toroidal magnetic field, $\langle v_B \rangle_{xy}$, as follows. The flux of magnetic energy — or Poynting flux, $\mathbf{F}_B = \mathbf{B} \times (\mathbf{v} \times \mathbf{B})$ — has vertical component,

$$F_{B,z} = B_x (v_z B_x - v_x B_z) - B_y (v_y B_z - v_z B_y). \tag{5.27}$$

If we assume that the magnetic field is purely toroidal, $B \simeq B_y$, which is justified by our simulations, then the z-component of the Poynting flux becomes,

$$F_{B,z} = v_B B_y^2, \tag{5.28}$$

where $v_B = v_z$ is a measure of the rise speed of the toroidal magnetic field defined by Equation 5.26. To measure v_B from our simulations, we equate Equations 5.27 and 5.28, solve for v_B, and horizontally-average the result to obtain,

$$\langle v_B \rangle_{xy} = \frac{\langle B_x (v_z B_x - v_x B_z) - B_y (v_y B_z - v_z B_y) \rangle_{xy}}{\langle B_y^2 \rangle_{xy}}. \tag{5.29}$$

Figure 5.12 shows the horizontally- and time-averaged v_B for each simulation. The toroidal magnetic field rise speed is essentially zero in the gas pressure-dominated regions where the disc exhibits small-scale turbulence and the large-scale toroidal magnetic field is not strongly ordered. For vertical locations exterior to the $\langle \widehat{\beta} \rangle_t \simeq 1$ transition (see Figure 6.1), where the toroidal magnetic field dominates the vertical pressure support in the disc, v_B is increasing with disc altitude. As the amount of net vertical magnetic flux increases, v_B at any given height above/below the disc mid-plane also increases, even becoming supersonic for simulations NVF-$\beta 2$ and NVF-$\beta 1$. Recall that $c_s = 1$ throughout the domain for our isothermal simulations.

We measure the vertical profile of the toroidal magnetic flux escape speed parameter $\eta(z)$ by inserting $\langle v_B \rangle_{xy}$ from Equation 5.29 into Equation 5.26. We average over z to obtain $\langle \eta \rangle_V$, ignoring numerical artifacts concentrated only very close to the disc mid-plane and the vertical boundaries. Table 5.3 lists $\langle \langle \eta \rangle_V \rangle_t$ for each simulation. As the amount of net vertical magnetic flux increases, the toroidal magnetic field is able to rise more efficiently (i.e., η increases), with the speed reaching 20-30% of the free-fall speed for the two magnetically dominated runs. Presumably, this is a consequence of the toroidal magnetic field becoming more ordered with increasing net vertical magnetic flux (see Figures 5.9 and 5.10), i.e., there is less tangling and reconnection of magnetic field lines.

We measure the vertical profile of the toroidal magnetic flux production parameter α_B by rearranging Equation 5.25 to obtain,

$$\alpha_B(z) = \frac{1}{\langle p_{\text{gas}} \rangle_{xy} + \langle p_B \rangle_{xy}} \left[\frac{1}{\Omega} \left(\langle v_B \rangle_{xy} \frac{d\langle p_B \rangle_{xy}}{dz} + 2\langle p_B \rangle_{xy} \frac{d\langle v_B \rangle_{xy}}{dz} \right) + 2\xi \langle p_B \rangle_{xy} \right]. \tag{5.30}$$

In the vertical locations near the disc mid-plane α_B has an essentially flat profile, which is not shown here for the sake of brevity. We adopted a constant value for ξ; therefore our measured values for α_B account for energy dissipation during MRI-dynamo flips in a volume-averaged sense and not as a function of disc altitude. Given that α_B parametrizes the amount of accretion power liberated by the MRI that goes into the toroidal magnetic field and that we measure α_B to have a flat vertical profile in the MRI-active disc mid-plane regions (i.e., $|z/H_0| < 1$), we choose to evaluate α_B at the disc mid-plane. Table 5.3 lists $\langle \alpha_B^{\text{mid}} \rangle_t$ for each simulation. As the amount of the net vertical magnetic flux increases, the MRI channels a fractionally larger amount of the liberated accretion energy into toroidal magnetic fields.

Notably, as shown by inspecting Equation 5.30, the values reported for α_B are heavily influenced by the frequency of MRI-dynamo cycles, as parametrized by ξ. A current sheet sweeps vertically through the domain with each MRI-dynamo reversal in the large-scale toroidal magnetic field. These strong current sheets are likely sites of magnetic reconnection and could potentially deposit substantial amounts of accretion power in the coronal regions, presumably through heating by magnetic reconnection. For the zero and weak/moderate ($\beta_0^{\text{mid}} \gtrsim 10^3$) net vertical magnetic flux simulations, this heating caused by MRI-dynamo cycles dominates the α_B values we measure. For the NVF-$\beta 2$ simulation, MRI-dynamo cycles are infrequent and contribute

in an ancillary way to α_B.

By considering the interplay of toroidal magnetic flux production and its buoyant escape, along with the effects of heating by current sheets launched during each MRI-dynamo cycle, Begelman et al. (2015) show that the plasma-β at the disc mid-plane can be determined via a regularity condition,

$$\beta_{\mathrm{B15}}^{\mathrm{mid}} = \frac{2\eta}{\alpha_B} + \nu - 1, \tag{5.31}$$

where $\nu \equiv 2\xi/\alpha_B$ is the reconnection efficiency parameter. For each simulation, Table 5.3 gives the values of $\langle \beta_{\mathrm{B15}}^{\mathrm{mid}} \rangle_t$ calculated from the values of ξ, η, and α_B also listed in Table 5.3. Comparing these model-dependent values for the mid-plane plasma-β to those that we measure *directly* in our simulations (see $\langle \widehat{\beta}^{\mathrm{mid}} \rangle_t$ in Table 5.2), we find extremely good agreement. The mid-plane magnetization can thus be understood in terms of a very simple model that balances toroidal field production against vertical escape at a rate tied to the free-fall speed, though simulations are needed (especially for weak net fields) to measure the efficiency of these processes as a function of the net field strength.

5.5.3 Vertical Disc Structure

We can also compare our simulation results to the analytic predictions for the vertical disc structure in the context of the MRI-dynamo model discussed in §5.5.2. Figure 5.13 shows the vertical profiles of the horizontally- and time-averaged gas pressure (*left panels*) and magnetic pressure (*right panels*), where disc altitude is in units of the gas density scale height H that develops in the turbulent steady state of each simulation and not its initial value H_0. Given the isothermal equation of state that we adopt, the gas pressure profiles are equivalent to the gas density profiles.

Using Equation 5.31 and combining equations for hydrostatic equilibrium and the Poynting flux, Begelman et al. (2015) derive coupled ordinary differential equations that govern the vertical structure,

$$\frac{d}{dy} \left(\tilde{p}_{\mathrm{B}} + \beta^{\mathrm{mid}} \tilde{p}_{\mathrm{gas}} \right) = -\beta^{\mathrm{mid}} \tilde{\rho} \tag{5.32}$$

$$y \frac{d\tilde{p}_{\mathrm{B}}}{dy} = \frac{\beta^{\mathrm{mid}}}{1 + \beta^{\mathrm{mid}} - \nu} \left(\tilde{p}_{\mathrm{gas}} - \tilde{p}_{\mathrm{B}} \right), \tag{5.33}$$

where $\tilde{\rho} = \rho/\rho^{\mathrm{mid}}$, $\tilde{p}_{\mathrm{gas}} = p_{\mathrm{gas}}/p_{\mathrm{gas}}^{\mathrm{mid}}$, $\tilde{p}_B = p_B/p_B^{\mathrm{mid}}$, and $y = z^2/(2H^2)$.
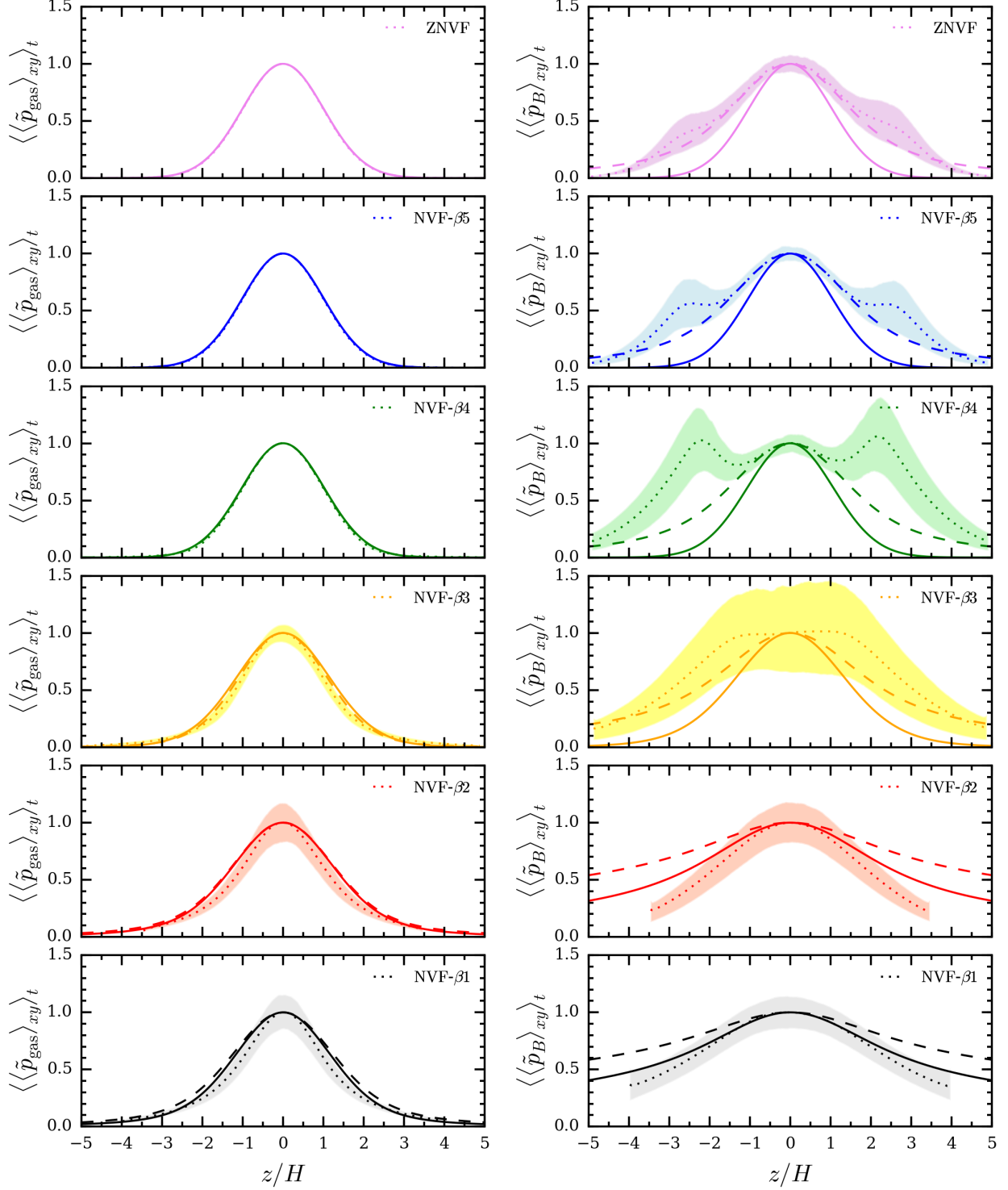
Figure 5.13: *Dotted lines* show the vertical profiles of the horizontally- and time-averaged gas pressure (*left panel*) and magnetic pressure (*right panel*), each normalized to their value at the disc mid-plane (see Figure 5.1 for line colour conventions). Also plotted are the analytic model predictions (Equations 5.32 and 5.33; Begelman et al., 2015): *solid lines* adopt $\beta^{\mathrm{mid}} = \langle \beta_{\mathrm{B15}}^{\mathrm{mid}} \rangle_t$ and $\nu = 2\xi/\langle \alpha_B^{\mathrm{mid}} \rangle_t$ from Table 5.3; *dashed lines* adopt $\beta^{\mathrm{mid}} = \langle \widehat{\beta}^{\mathrm{mid}} \rangle_t$ from Table 5.2 and $\nu = 0$. From *top* to *bottom* are simulations ZNVF, NVF-$\beta5$, NVF-$\beta4$, NVF-$\beta3$, NVF-$\beta2$, NVF-$\beta1$. We note that z is plotted in units of the gas density scale height, H, that develops for each individual simulation and not its initial value, H_0.

Combining Equations 5.32 and 5.33 with an isothermal equation of state, Figure 5.13 shows the vertical profiles of gas pressure (*left panels*) and magnetic pressure (*right panels*) predicted by the Begelman et al. (2015) model and compared to the simulation results. The *solid lines* show the results from choosing $\beta^{\mathrm{mid}} = \langle \beta^{\mathrm{mid}}_{\mathrm{B15}} \rangle_t$ and $\nu = 2\xi/\langle \alpha^{\mathrm{mid}}_B \rangle_t$ (see Table 5.3). The *dashed lines* show the results from choosing $\beta^{\mathrm{mid}} = \langle \widehat{\beta}^{\mathrm{mid}} \rangle_t$ (see Table 5.2) and $\nu = 0$. The main effect of including the magnetic reconnection efficiency parameter ν is to steepen the magnetic pressure profile. The model that does not include ν (*dashed lines*) roughly matches the magnetic pressure profiles for the zero and weak/moderate ($\beta^{\mathrm{mid}}_0 \gtrsim 10^3$) net vertical magnetic flux simulations. The model that does include ν (*solid lines*) does a better job of capturing the steepening of the magnetic pressure profiles observed in the magnetic pressure-dominated simulations ($\beta^{\mathrm{mid}}_0 \lesssim 10^2$).

5.6 Discussion

5.6.1 MRI-Dynamo Cycles

We find that the cyclic MRI-dynamo reversals in the large-scale toroidal magnetic field have a regular $\simeq 10$ orbit periodicity for simulations with zero and weak ($\beta^{\mathrm{mid}}_0 \gtrsim 10^3$) net vertical magnetic flux. For $\beta^{\mathrm{mid}}_0 \lesssim 10^3$, these reversals become more scattered and increase in period with increasing net vertical magnetic flux, until they are no longer observed for the most strongly magnetized simulation with $\beta^{\mathrm{mid}}_0 = 10^1$.

Previous shearing box simulations with a zero net vertical magnetic flux show the same MRI-dynamo cycle regularity and periodicity that we observe, provided that the domain size is sufficiently large (e.g., Simon et al., 2012). The strong ($\beta^{\mathrm{mid}}_0 \lesssim 10^3$) net vertical magnetic flux simulations of Bai & Stone (2013) also display MRI-dynamo cycle characteristics that are consistent with our simulations. However, some differences from our results arise for weaker net fluxes, with previous works finding the butterfly pattern to be highly irregular for $\beta^{\mathrm{mid}}_0 \gtrsim 10^4$ (e.g., Fromang et al., 2013; Bai & Stone, 2013). Given that Bai & Stone (2013) used very similar methods to ours, the most likely origin for the differences we observe is differences in the domain size. The shearing box simulations of Bai & Stone (2013) used a substantially smaller horizontal domain $(L_x, L_y) = (4H_0, 8H_0)$, which has been shown in zero net vertical magnetic flux simulations to affect

the dynamo properties (Simon et al., 2012).

The smooth transition that we observe in the cyclic MRI-dynamo behaviour across the zero-to-weak net vertical magnetic flux regimes suggests that we have obtained numerically converged solutions, that are physically reasonable in the local limit. However, the requirement for such large horizontal domains means that we are pushing the limits of the shearing box's validity by neglecting curvature terms. We cannot rule out the possibility that the MRI-dynamo is intrinsically periodic in a shearing box and even the strong field models may become periodic for larger domain sizes. Similarly, the absence of MRI-dynamo cycles we observe for $\beta_0^{\mathrm{mid}} = 10^1$ may be a consequence of an insufficiently small domain size and/or short integration time. Ultimately, global disc simulations are needed to determine if the sporadic nature of MRI-dynamo cycles that we see in the strong ($\beta_0^{\mathrm{mid}} \lesssim 10^3$) net vertical magnetic flux regime is an intrinsic property of MRI-dynamo behaviour.

5.6.2   Quasi-Periodic Oscillations

Black hole X-ray binaries showcase complicated evolutionary cycles, called state transitions (e.g., Remillard & McClintock, 2006; Belloni, 2010), where the source transitions between "low/hard" and "high/soft" states. The low/hard state is characterized by a low luminosity ($\lesssim 10^{-3} L_{\mathrm{Edd}}$) and a non-thermal hard X-ray spectrum, while the high/soft state is characterized by a high luminosity ($\gtrsim 0.1 L_{\mathrm{Edd}}$) and a quasi-thermal soft X-ray spectrum. The soft quasi-thermal X-rays are attributed to a geometrically thin, optically thick accretion disc (Shakura & Sunyaev, 1973), while the non-thermal hard X-rays are thought to arise from energetic electrons in a surrounding "corona" that inverse Compton scatter the seed disc photons (Haardt & Maraschi, 1991). In a complete state transition hysteresis cycle (~ 100 days), the source rises out of the low/hard state along a high-luminosity track into the high/soft state, but then decays on a different low-luminosity track back to the low/hard state, passing through hybrid "intermediate" states along the way. The outburst decay track is typically $\sim 10 - 100$ times fainter than the outburst rise track.

During a low/hard $\leftrightarrow$ high/soft state transition, low-frequency quasi-periodic oscillations (QPOs) are observed (van der Klis, 1989; Casella et al., 2005), which are coherent features in the temporal power spectrum of the X-ray light curve. The QPO centroid frequency evolves from $\nu_{\mathrm{Q},0} \simeq 0.01 \rightarrow 10$ Hz during

a low/hard $\rightarrow$ high/soft state transition (e.g., Belloni et al., 2005; Belloni, 2010). These QPOs ultimately disappear in the high/soft state. The origin of QPOs is still unknown, but if understood, QPOs would be a powerful diagnostic for measuring disc evolution (e.g., Miller & Miller, 2015).

The MRI-dynamo cycles of flip-flopping toroidal magnetic field shown in Figure 5.7 are promising candidates for QPOs (e.g., O'Neill et al., 2011; Begelman et al., 2015). Figure 5.11 shows that a coherent QPO-like feature appears for the weakly magnetized discs ($\beta_0^{\mathrm{mid}} \gtrsim 10^4$) with peak frequency $\nu_{\mathrm{peak}} \sim 0.1$ orbits^{-1}. A strong peak is not seen for the strongly magnetized discs ($\beta_0^{\mathrm{mid}} \lesssim 10^3$) due to the irregularity of the MRI-dynamo cycles, but this result may be a consequence of domain size restrictions as previously mentioned. We consider the increase in MRI-dynamo period with net flux to be a robust result; therefore, the frequency of a resulting power spectral peak would increase with decreasing magnetization. However, we emphasize that Figure 5.11 cannot be directly compared to an observed power spectrum because the toroidal magnetic field was not mapped to an emission mechanism. If, as suggested by Begelman & Armitage (2014), the disc becomes decreasingly magnetized during the low/hard $\rightarrow$ high/soft state transition, MRI-dynamo cycles could potentially produce a QPO-like feature that fits the observed evolutionary behaviour of ν_{Q}. Global simulations are needed to address these speculations (e.g., O'Neill et al., 2011) because QPO frequency and strength would likely be set far from the black hole, and the modulations would have to take into account radial propagation of the MRI-dynamo cycles.

5.6.3   Spectral Hardening

Understanding the consequences of vertical magnetic pressure support for the observed accretion disc spectrum is necessary for assessing the robustness of any observational results based on disc continuum modeling. A disc with magnetic pressure support has a lower gas density at the effective photosphere, which enhances electron scattering and leads to a harder spectrum compared to a disc without magnetic pressure support (Davis et al., 2005; Blaes et al., 2006).

The degree of spectral hardening is parametrized by the colour correction factor f_{col} (Shimura & Takahara, 1995). Discs without a vertical magnetic pressure contribution tend to have f_{col} values confined to the narrow range $f_{\mathrm{col}} \simeq 1.5 - 1.7$ (e.g., Davis et al., 2005). However, observations of disc evolution

in X-ray binary state transitions (Salvesen et al., 2013; Reynolds & Miller, 2013) and sophisticated joint-spectral fitting of the disc in a steady high/soft state (Maitra et al., 2014) demonstrate that the data permit $f_{\rm col} \gtrsim 2$. Post-processing of a weakly magnetized shearing box simulation with zero net vertical magnetic flux showed that magnetic pressure support in the disc surface layers leads to enhanced spectral hardening, with $f_{\rm col} = 1.74$ (1.48) when magnetic pressure support was included (neglected) in the vertical hydrostatic balance (Blaes et al., 2006). Analytic models of very strongly magnetized discs predict substantial spectral hardening of $f_{\rm col} \sim 5$ (Begelman & Pringle, 2007). The two main contributing effects to spectral hardening are the ratio of electron scattering to absorption being higher at the disc photosphere and the profile of MRI dissipation being concentrated higher in the disc (i.e., there is a lot of dissipation just below the photosphere). However, the quantitative details of how significant magnetic pressure support influences the observed disc spectrum are not yet understood.

Measurements of black hole spin with the disc continuum fitting technique (Zhang et al., 1997; Mc-Clintock et al., 2006) ignore vertical magnetic pressure support in the disc when modeling the disc spectrum. This may lead to erroneously overestimated spins and explain the inconsistencies between the two leading black hole spin measurement techniques. Given a non-spinning black hole ($a = 0$) with typical X-ray binary system parameters, one would obtain the incorrect spin parameter $a \simeq 0.5$ by ignoring fairly weak vertical magnetic pressure support (Blaes et al., 2006). We are currently quantifying the impact of spectral hardening on black hole spin measurements (Salvesen et al., in preparation).

5.7   Summary and Conclusions

We have studied the structure and dynamo-related variability of accretion discs, using isothermal local simulations that include vertical stratification. The simulations span almost the full range of net vertical fluxes that lead to MRI-unstable initial conditions ($\beta_0^{\rm mid} = 10^1 - 10^5$), and were run in large domains that capture mesoscale structures that are important for disc variability. Our two strongest net field runs, with $\beta_0^{\rm mid} = 10$ and 100, result in the formation of magnetically dominated discs whose structure differs qualitatively from that of gas pressure-dominated solutions. Our main conclusions are:

- The α-viscosity parameter, $\overline{\alpha} = \langle T_{xy} \rangle_V / \langle p_{\mathrm{gas}} \rangle_V$, follows a power-law spanning two orders of magnitude in net vertical magnetic flux (four orders of magnitude in β_0^{mid}). Alternatively, normalizing the stress to the magnetic pressure yields a constant viscosity parameter $\overline{\alpha}_{\mathrm{mag}} = \langle T_{xy} \rangle_V / \langle p_B \rangle_V$ that is independent of the initial mid-plane β (Hawley et al., 1995; Blackman et al., 2008).

- Gas density fluctuations (relative to the time-averaged gas density vertical profile) increase with net vertical magnetic flux, reaching the $\sim 60 - 100\%$ level for our magnetic-pressure dominated disc simulations NVF-$\beta2$ and NVF-$\beta1$. These highly magnetized but still MRI-unstable discs are highly inhomogeneous, clumpy structures.

- MRI-dynamo cycles are highly regular for simulations with either zero net vertical magnetic flux or weak ($\beta_0^{\mathrm{mid}} \gtrsim 10^4$) net vertical magnetic flux. The MRI-dynamo period increases and becomes more sporadic for moderate-to-strong ($\beta_0^{\mathrm{mid}} \lesssim 10^3$) net vertical magnetic flux simulations. A large horizontal domain appears to be necessary to capture this behaviour, in net field as well as zero net field simulations (Simon et al., 2012).

- Entry into the fully magnetic pressure-dominated regime is not a sufficient condition for the complete suppression of cyclic MRI-dynamo reversals. We observe multiple reversals in the magnetic pressure-dominated NVF-$\beta2$ simulation, and cannot exclude the possibility that very long time scale reversals occur for even more strongly magnetized discs. With increasing magnetization, even longer integration times and/or larger domain sizes than we considered may be necessary to properly study these MRI-dynamo cycles.

- The magnetization at the disc mid-plane is very well-described by the regularity condition (see Equation 5.31) given by Begelman et al. (2015), which is derived from a model based on the balance between the MRI-dynamo production of toroidal field and its buoyant escape.

- The Begelman et al. (2015) model provides a reasonable first-order description of the vertical disc structure seen in the simulation results. Incorporating a magnetic reconnection efficiency parameter ν into the model helps to match the steep magnetic pressure profiles from the magnetic pressure-

dominated disc simulations ($\beta_0^{\mathrm{mid}} \lesssim 10^2$).

Our results support aspects of a currently speculative scenario in which the net poloidal flux is the key parameter controlling the structure and evolution of accretion discs in black hole X-ray binaries. Net fluxes that remain in the MRI-unstable regime can still be strong enough to stimulate qualitative changes to the disc structure, and lead to the formation of magnetically supported and highly inhomogeneous discs. Analytic models of such discs suggest that many of the observationally interesting consequences occur as a consequence of the work done by the toroidal field as it escapes, and future simulations will need to relax the isothermal assumption adopted here to study such effects.

Acknowledgments

Chapter 6

Strongly Magnetized Accretion Discs Require Poloidal Flux

6.1   Preface

This paper was published in Monthly Notices of the Royal Astronomical Society, Volume 460, Issue 4, pp. 3488-3493 on August 21, 2016. The author list is: Salvesen, G., Armitage, P. J., Simon, J. B., & Begelman, M. C. We find that local simulations of accretion discs with realistic vertical boundary conditions can only develop into a magnetic pressure-dominated state if a sufficiently strong background poloidal net flux is present.

Abstract

Motivated by indirect observational evidence for strongly magnetized accretion discs around black holes, and the novel theoretical properties of such solutions, we investigate how a strong magnetization state can develop and persist. To this end, we perform local simulations of accretion discs with an initially purely toroidal magnetic field of equipartition strength. We demonstrate that discs with zero net vertical magnetic flux and realistic boundary conditions cannot sustain a strong toroidal field. However, a magnetic pressure-dominated disc can form from an initial configuration with a sufficient amount of net vertical flux and realistic boundary conditions. Our results suggest that poloidal flux is a necessary prerequisite for the sustainability of strongly magnetized accretion discs.

6.2   Introduction

Magnetic fields are fundamental to the physics of accretion discs. The magnetorotational instability (MRI) causes an accretion disc to enter a self-sustaining turbulent steady state, wherein an effective viscosity is generated that drives accretion (Balbus & Hawley, 1991, 1998). The disc magnetization is parametrized by the ratio of gas-to-magnetic pressure, $\beta \equiv p_{\mathrm{gas}}/p_B$. While some numerical simulations examine MRI turbulence in strongly magnetized discs ($\beta \lesssim 1$; e.g., Johansen & Levin, 2008; Bai & Stone, 2013; Salvesen et al., 2016b), the majority focus on the weakly magnetized regime.

Several lines of evidence suggest that real accretion discs around black holes in X-ray binaries and galactic nuclei may be strongly magnetized. Observations of powerful disc winds (e.g., Miller et al., 2006b) and relativistic jets (e.g., Fender et al., 2004) in black hole X-ray binary systems suggest the presence of a significant poloidal flux, which catalyzes a much stronger toroidal field in MRI-active discs. On larger scales, the gas supplied to the disc by the donor star is expected to be strongly magnetized ($\beta \lesssim 1$; Johansen & Levin, 2008). In the Galactic Center, dust polarization measurements in the inner $\sim 10^2$ pc reveal both a toroidal magnetic field near the Galactic plane, and a large-scale poloidal field at higher Galactic latitudes (Nishiyama et al., 2010).

At a more circumstantial level, strongly magnetized discs provide a promising theoretical framework for addressing longstanding problems that plague their weakly magnetized counterparts. In particular, magnetically dominated discs are not prone to thermal instability in radiation pressure dominated regions (Begelman & Pringle, 2007), a result which appears consistent with the low levels of variability seen in luminous X-ray binary states. They are also less susceptible to gravitational fragmentation that would inhibit continued accretion onto the black hole in active galactic nuclei (Pariev et al., 2003; Begelman & Pringle, 2007; Gaburov et al., 2012). Furthermore, the effective α-viscosity (Shakura & Sunyaev, 1973), which parametrizes the rate of angular momentum transport, is observationally constrained to be $\alpha \sim 0.1 - 0.4$ in dwarf novae systems (King et al., 2007). Local disc simulations with weak magnetic pressure support and zero net vertical flux find $\alpha \sim 0.01$ (Stone et al., 1996; Davis et al., 2010; Simon et al., 2011) . However, local disc simulations with net vertical flux allow the disc to develop significant magnetic pressure support

and boost α to values $\sim 0.1 - 1$ (e.g., Hawley et al., 1995; Salvesen et al., 2016b). Finally, recent theoretical models for X-ray binary state transitions appeal to strongly magnetized accretion discs (Begelman et al., 2015) and the evolution of a net poloidal flux (Begelman & Armitage, 2014).

In this paper, we address the question of whether there are multiple routes by which an accretion disc can sustain a strongly magnetized state. One well-studied route requires a net poloidal flux (typically in the window $10^3 > \beta_p > 10$) that is strong enough to affect the MRI dynamics but weak enough to admit MRI-driven turbulence. Simulations show that this leads to a supra-thermal mid-plane field that is replenished by dynamo action as it buoyantly escapes (Bai & Stone, 2013; Salvesen et al., 2016b). An alternate route could involve processes other than the MRI. In particular, Johansen & Levin (2008) argued that a dynamo mediated by the Parker instability could maintain a strongly magnetized state from an initial configuration of a purely toroidal field in equipartition with the gas. This suggestion is particularly interesting as — if correct — it would imply that discs with zero net poloidal flux could exist in two distinct states depending upon the history of the system.

Here we consider local disc simulations that have zero net vertical magnetic flux and are initialized with an equipartition toroidal field. We adopt two sets of vertical boundary conditions, one which traps toroidal magnetic flux and one which allows it to escape freely. We show that the disc cannot maintain its strongly magnetized initial state for the more physically realistic outflow boundary conditions, and hence conclude that strongly magnetized astrophysical accretion discs require a background poloidal magnetic flux.

6.3   Numerical Simulations

Following Salvesen et al. (2016b), we use the `Athena` code (Gardiner & Stone, 2005, 2008; Stone et al., 2008) to solve the equations of compressible, isothermal, ideal magnetohydrodynamics in the "shearing box"

approximation (Hawley et al., 1995; Stone & Gardiner, 2010) including vertical density stratification,

$$\frac{\partial \rho}{\partial t} = - \nabla \cdot (\rho \mathbf{v}) \tag{6.1}$$

$$\frac{\partial (\rho \mathbf{v})}{\partial t} = - \nabla \cdot \left[\rho \mathbf{v} \mathbf{v} - \mathbf{B} \mathbf{B} + \left(p_{\mathrm{gas}} + \frac{B^2}{2} \right) \mathbf{I} \right]$$

$$+ 2 q \rho \Omega^2 x \hat{\mathbf{i}} - \rho \Omega^2 z \hat{\mathbf{k}} - 2 \boldsymbol{\Omega} \times (\rho \mathbf{v}) \tag{6.2}$$

$$\frac{\partial \mathbf{B}}{\partial t} = - \nabla \cdot (\mathbf{v} \mathbf{B} - \mathbf{B} \mathbf{v}) \,. \tag{6.3}$$

In order, Equations 6.1 - 6.3 describe the conservation of mass, the conservation of momentum, and magnetic induction, with the various parameters having their usual meanings: ρ is the gas density, p_{gas} is the gas pressure, $\mathbf{v}$ is the gas velocity, and $\mathbf{B}$ is the magnetic field. Our magnetic field definition subsumes a factor of $\mu/\sqrt{4\pi}$, with $\mu = 1$ being the magnetic permeability. We choose an equation of state, $p_{\mathrm{gas}} = \rho c_{\mathrm{s}}^2$, corresponding to an isothermal gas with sound speed c_{s}. $\mathbf{I}$ is the identity matrix and $(\hat{\mathbf{i}}, \hat{\mathbf{j}}, \hat{\mathbf{k}})$ are the Cartesian (x, y, z) unit vectors. Specific to the shearing box geometry, $\boldsymbol{\Omega} = \Omega \hat{\mathbf{k}}$ is the angular frequency corresponding to co-rotation with the disc. The simulation domain is centered on the arbitrary reference radial location $R = R_0$ and $q = -\mathrm{dln}\,(\Omega)\,/\mathrm{dln}\,(R) = 3/2$ is the shear parameter corresponding to Keplerian rotation.

The question we are interested in answering is whether a background poloidal magnetic flux is necessary to sustain a strongly magnetized accretion disc. The net vertical magnetic flux simulations of Salvesen et al. (2016b) with $\beta_0^{\mathrm{mid}} \lesssim 10^3$ and outflow boundary conditions developed into a magnetic pressure-dominated state. The zero net vertical flux simulations of Johansen & Levin (2008) were initialized with an equipartition toroidal field and remained strongly magnetized, but adopted boundary conditions that confined the magnetic flux within the domain. The simulations presented in this Letter (see Table 6.1) are very similar to those of Salvesen et al. (2016b), but have the following two differences: (1) initial conditions with a purely toroidal magnetic field configuration (§6.3.1) and (2) boundary conditions that either do or do not permit magnetic flux to escape (§6.3.2).

6.3.1   Initial Conditions

As did Johansen & Levin (2008), we initialize zero net vertical magnetic flux simulations with a

vertical gas density profile in hydrostatic equilibrium and a purely toroidal magnetic field configuration,

$$\rho\left(x, y, z\right) = \rho_0^{\text{mid}} \exp\left(\frac{-z^2}{2H_\beta^2}\right) \tag{6.4}$$

$$B_{y,0}\left(x, y, z\right) = \left[2\beta_0^{-1} c_{\text{s}}^2 \rho_0^{\text{mid}} \exp\left(\frac{-z^2}{2H_\beta^2}\right)\right]^{1/2}, \tag{6.5}$$

with $\rho_0^{\text{mid}} = 1$. The gas scale height is $H_\beta = \sqrt{1 + \beta_0^{-1}} c_{\text{s}}/\Omega$. Because we choose $c_{\text{s}} = 1$ and $\Omega = 1$, the scale

height resulting from thermal pressure support alone opposing vertical gravity is $H_0 = c_{\text{s}}/\Omega = 1$, which we

adopt as our unit of length. The domain size for all simulations is $(L_x, L_y, L_z) = (10H_0, 20H_0, 10H_0)$. Disc

magnetization is parametrized by the ratio of gas-to-magnetic pressure,

$$\beta \equiv \frac{p_{\text{gas}}}{p_B} = \frac{\rho c_{\text{s}}^2}{B^2/2}. \tag{6.6}$$

We choose an equipartition initial magnetic field $\beta_0 = 1$, which makes the vertical domain size $7.1H_\beta$ when

the magnetic field contribution to hydrostatic equilibrium is included. Random perturbations to the gas

density and velocity are introduced at $t = 0$ in order to initiate the MRI (Hawley et al., 1995). We impose

a density floor $\rho_{\text{floor}} = 10^{-4} \rho_0^{\text{mid}}$.

ID	Grid Res. $[N_\mathrm{zones}/H_0]$	β_0^mid	B_z	Vertical BCs	t_f [orbits]	$\langle Q_y^\mathrm{mid}\rangle_t$	$\langle Q_z^\mathrm{mid}\rangle_t$	$\langle T_{xy,\mathrm{Rey}}^\mathrm{mid}\rangle_t$	$\langle T_{xy,\mathrm{Max}}^\mathrm{mid}\rangle_t$	$\langle \widehat{\alpha}^\mathrm{mid}\rangle_t$	$\langle \widehat{\beta}^\mathrm{mid}\rangle_t$
ZNVF-O	36	1	0	Outflowing	125	44(2)	10.3(5)	0.0038(5)	0.013(1)	0.013(1)	45(4)
ZNVF-P	24	1	0	Periodic	125	35(2)	8.4(4)	0.008(1)	0.022(2)	0.019(2)	32(3)
NVF-$\beta2$*	24	10^2	0.141	Outflowing	225	3.3(7)e2	9(1)e1	0.10(6)	0.5(1)	1.0(4)	0.4(1)

Table 6.1: Summary of simulations. From *left* to *right* the columns are: simulation identification label, grid resolution (applies to all dimensions), initial plasma-β at the disc mid-plane, net vertical magnetic flux density (code units), vertical boundary conditions, and simulation termination time. All subsequent quantities, which are defined in the text, are evaluated at the disc mid-plane and time-averaged from $t_\mathrm{i} = 25$ to t_f. Parentheses indicate the $\pm 1\sigma$ range on the last digit from the time averaging. *Reference net vertical magnetic flux simulation from Salvesen et al. (2016b).

6.3.2   Boundary Conditions

We adopt the usual shearing box boundary conditions of shearing periodic in x (radial) and strictly periodic in y (toroidal) (Hawley et al., 1995; Simon et al., 2011). Table 6.1 summarizes our simulations, which fundamentally differ only in their choice of z (vertical) boundary conditions:

- ZNVF-O adopts the modified outflowing vertical boundary conditions of Simon et al. (2011) and Simon et al. (2013), in which the gas density, pressure, and in-plane components of the magnetic field are exponentially extrapolated from the physical domain into the ghost zones. This method prevents the unphysical accumulation of magnetic flux at the vertical boundaries, thus allowing magnetic flux to escape the simulation domain.

- ZNVF-P adopts periodic vertical boundary conditions, which do *not* allow magnetic flux to escape the simulation domain.

Neither condition is fully realistic, but outflowing boundary conditions are closer to the physical situation. Any significant differences between the zero net vertical flux simulations ZNVF-O and ZNVF-P can be ascribed to their differences in vertical boundary conditions. We performed resolution and vertical domain size convergence studies that corroborated the results from simulation ZNVF-P. We contrast these runs to NVF-$\beta 2$ from Salvesen et al. (2016b), which combines outflow boundary conditions with a net poloidal field $\beta_0^{\mathrm{mid}} = 10^2$.

6.4   Analysis and Results

We are interested in the turbulent steady states arising from zero net vertical flux shearing box simulations that differ in their choice of vertical boundary conditions. Empirically, the saturated state is considered well-resolved for quality factors $Q_i \gtrsim 6$ (Sano et al., 2004), given by[1] ,

$$Q_i = \frac{\lambda_{\mathrm{MRI}}}{\Delta x_i}, \tag{6.7}$$

where, for spatial dimension i, the characteristic MRI wavelength is $\lambda_{\mathrm{MRI},i} = 2\pi v_{\mathrm{A},i}/\Omega$ and the Alfvén speed is $v_{\mathrm{A},i} = \sqrt{B_i^2/\rho}$. Table 6.1 shows that all of our simulations are well-resolved according to the Q_y and Q_z

---

[1] Hawley et al. (2011) suggest $Q_y \gtrsim 20$ and $Q_z \gtrsim 10$.

benchmarks.

Table 6.1 also lists diagnostics of MRI turbulence, each evaluated at the disc mid-plane and time-averaged over the saturated state (i.e., $t \geq 25$ orbits). The rate of angular momentum transport is parametrized by the effective α-viscosity (Shakura & Sunyaev, 1973),

$$\widehat{\alpha} = \frac{\langle T_{xy,\mathrm{Rey}} \rangle_{xy} + \langle T_{xy,\mathrm{Max}} \rangle_{xy}}{\langle p_{\mathrm{gas}} \rangle_{xy}}, \tag{6.8}$$

where the notation $\langle \cdot \rangle_{xy}$ indicates that the quantity is horizontally-averaged. The Reynolds and Maxwell contributions to the xy component of the total stress tensor are $T_{xy,\mathrm{Rey}} = \rho v_x v_y'$ and $T_{xy,\mathrm{Max}} = -B_x B_y$, where v_y' are the remaining fluctuations when the background shear is subtracted from v_y. The plasma-β parameter in Table 6.1 is defined as,

$$\widehat{\beta} = \frac{\langle p_{\mathrm{gas}} \rangle_{xy}}{\langle p_B \rangle_{xy}}. \tag{6.9}$$

Figure 6.1 shows the vertical profiles of $\widehat{\beta}$ for each simulation.

To our surprise, the *mid-plane* diagnostics of MRI turbulence are only weakly dependent on the vertical boundary conditions for the zero net flux simulations. In the saturated turbulent steady state of runs ZNVF-O and ZNVF-P, we find $T_{xy,\mathrm{Max}}^{\mathrm{mid}} \simeq 4 T_{xy,\mathrm{Rey}}^{\mathrm{mid}}$, $\widehat{\alpha}^{\mathrm{mid}} \sim 0.01$, and $\widehat{\beta}^{\mathrm{mid}} \gg 1$, consistent with previous shearing box simulations with zero net vertical magnetic flux (e.g., Stone et al., 1996; Davis et al., 2010; Simon et al., 2011). Conversely, the strong net vertical magnetic flux simulation NVF-β2 shows an enhanced $\widehat{\alpha}^{\mathrm{mid}} \simeq 1.0$ and a magnetic pressure-dominated disc with $\widehat{\beta}^{\mathrm{mid}} \simeq 0.4$ (Salvesen et al., 2016b).

Larger differences between the zero net flux simulations are apparent from the vertical profiles of magnetization shown in Figure 6.1. With outflowing boundary conditions, we find that the initially strong (equipartition level) toroidal field buoyantly escapes in the transient stage. The disc evolves into a generally weakly magnetized state, with $\widehat{\beta} \sim 1$ being reached only in a coronal region at $|z| > 3.5 H_0$. With periodic boundary conditions, on the other hand, the final magnetized state is determined by the redistribution of the initial equipartition toroidal field. After a sufficiently long interval, this leads to a weakly magnetized disc core within about one scale height of the disc mid-plane, with extremely strong magnetization at higher altitudes. We are only able to sustain a strongly magnetized disc mid-plane with the aid of poloidal field. Simulation NVF-β2, which also adopts outflowing boundary conditions, evolves from a net vertical flux
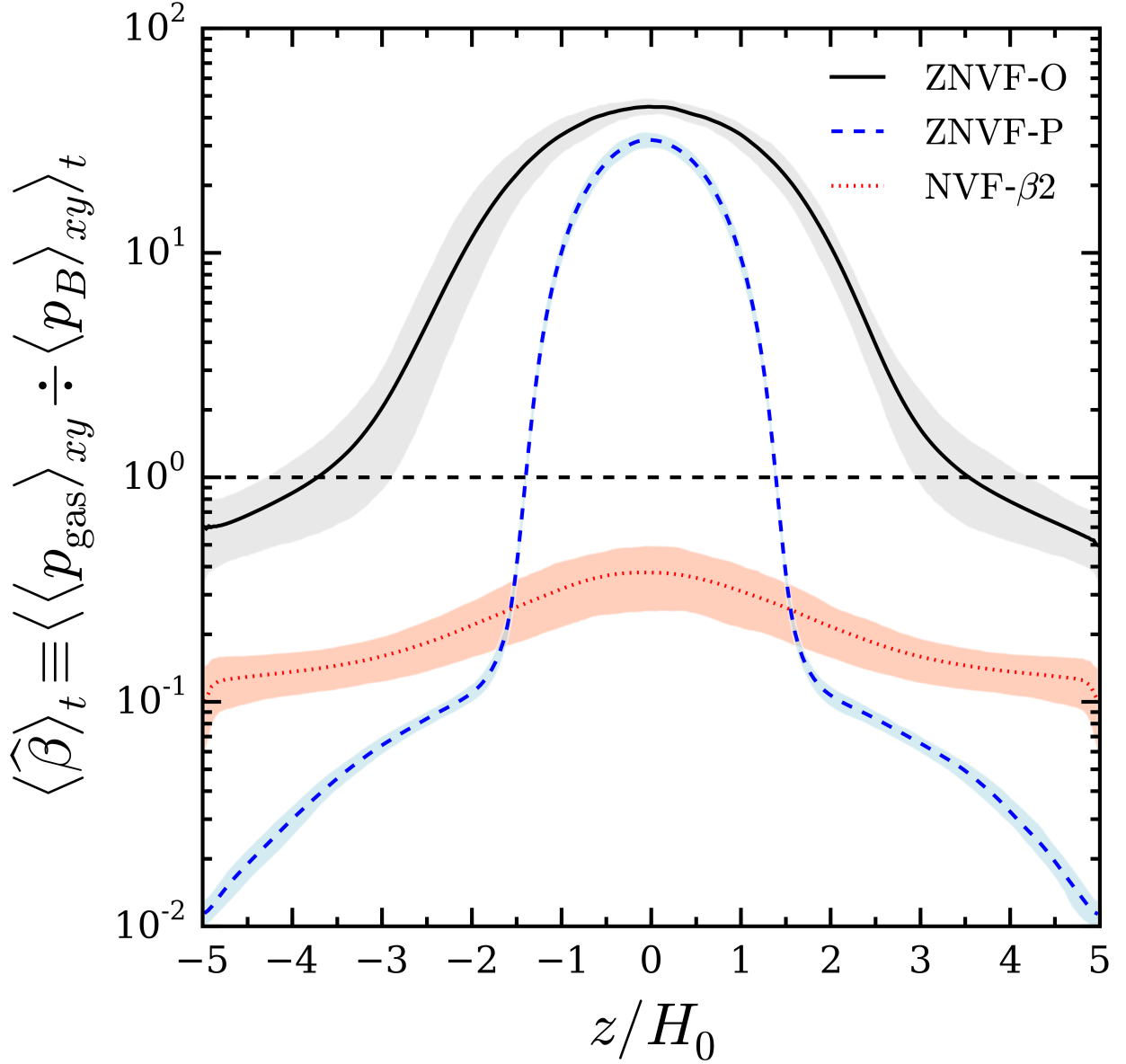
Figure 6.1: Vertical profiles of the time-averaged plasma-β for zero net vertical flux simulations with outflowing (*solid black line*) and periodic (*dashed blue line*) vertical boundary conditions. The strongly magnetized net vertical flux simulation with outflowing boundary conditions (*dotted red line*) from Salvesen et al. (2016b) is shown for reference. Coloured bands show the respective $\pm 1\sigma$ range in $\widehat{\beta}$ from the time averaging. The *horizontal dashed line* marks equipartition $\widehat{\beta} = 1$.
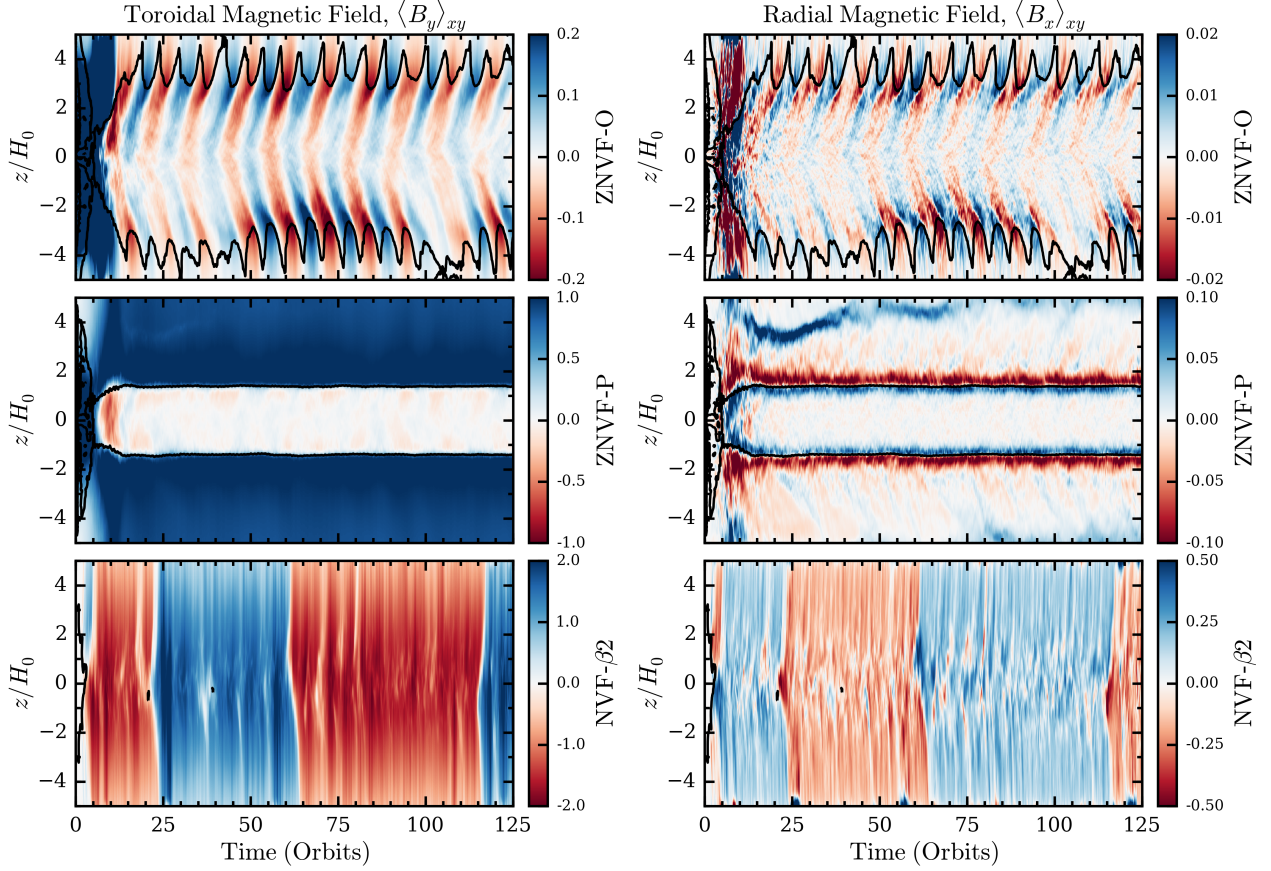
Figure 6.2: *Left panels:* Space-time diagrams of the horizontally-averaged toroidal magnetic field, $\langle B_y \rangle_{xy}$. *Right panels:* Space-time diagrams of the horizontally-averaged radial magnetic field, $\langle B_x \rangle_{xy}$. Shown are simulations ZNVF-O (*top panels*), ZNVF-P (*middle panels*), and NVF-β2 (*botom panels*). *Black lines* mark the $\beta = 1$ contour, exterior (interior) to which $\beta < 1$ ($\beta > 1$). The magnetic field reversals characteristic of the MRI-dynamo are only observed in the simulations with outflowing boundary conditions (i.e., ZNVF-O and NVF-β2). This suggests that simulations with vertical boundary conditions that confine magnetic flux within the domain cannot capture important accretion disc physics.

configuration with $\beta_0^{\mathrm{mid}} = 10^2$ into a strongly magnetized state with $\widehat{\beta} \lesssim 1$. In this run the MRI-dynamo constantly replenishes the escaping toroidal field from the imposed vertical field.

Figure 6.2 (*left panels*) shows the space-time diagrams of the toroidal magnetic field for each simulation. The simulations with outflowing vertical boundary conditions (ZNVF-O and NVF-β2) exhibit the toroidal field reversals characteristic of MRI-dynamo activity, albeit with differing periods. Simulation ZNVF-P, which confines magnetic flux within the domain, does not show this behaviour of periodically launching current sheets across the full vertical domain. This illustrates that other important aspects of MRI-dynamo activity in accretion discs, beyond the vertical profile of magnetization, are sensitive to the vertical boundary conditions and cannot be captured by simulations that do not permit magnetic flux to buoyantly escape the domain.

Figure 6.2 (*right panels*) also shows space-time diagrams for the radial component of the magnetic field. Similarly to the toroidal field, the radial field experiences dynamo cycles of escape and replenishment for simulations ZNVF-O and NVF-β2. In simulation ZNVF-P, the radial field develops long-lived banded structures at the $\beta \simeq 1$ interfaces ($|z/H_0| \simeq 1.5$). The simulations of Johansen & Levin (2008) developed similar peaks in the radial field, but at larger scale heights and also at the disc mid-plane, which we do not observe in simulation ZNVF-P.

Figure 6.3 shows the magnetic field structure at the snapshot in time $t = 100$ orbits. In all cases, the toroidal magnetic field is the dominant component. Small-scale turbulent magnetic structures exist in the vicinity of the disc mid-plane for the weakly magnetized simulations (ZNVF-O and ZNVF-P). Compared to ZNVF-O, simulation ZNVF-P shows an abrupt transition from the highly-turbulent disc core regions into the magnetically dominated disc atmosphere. The ordered toroidal magnetic field structure in the disc mid-plane is similar for both ZNVF-O and ZNVF-P. As discussed in Salvesen et al. (2016b), the strongly magnetized disc simulation NVF-β2 develops ribbon-like field structures near the disc mid-plane and the field is remarkably well-ordered at the mid-plane.

Our results do not support suggestions that there are non-MRI dynamo routes to sustaining strong magnetization in the absence of poloidal field. For zero net vertical flux simulations with vertical boundary conditions that enforce the confinement of toroidal magnetic flux, we do find a very strongly magnetized
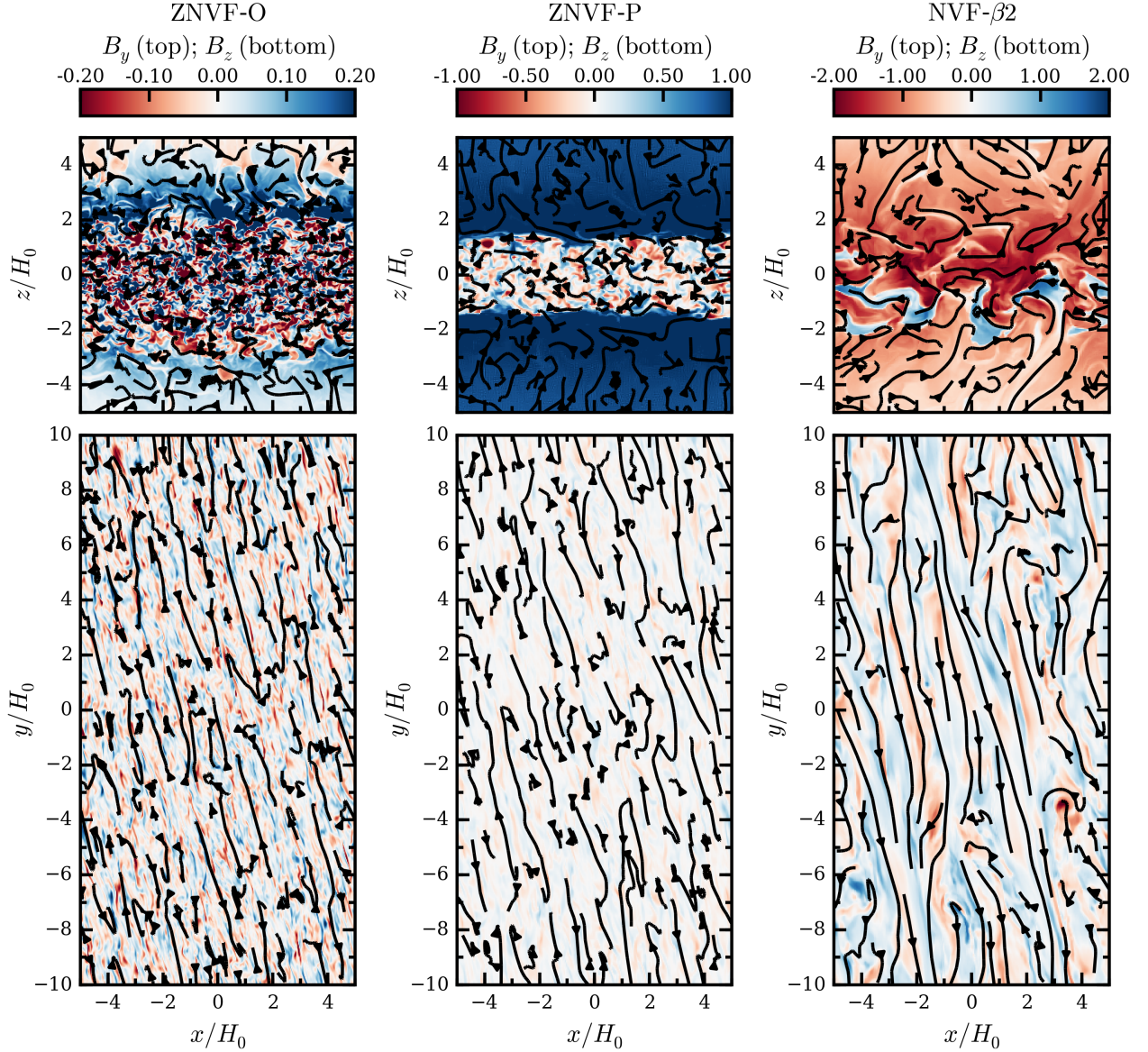
Figure 6.3: Magnetic field structure for simulations ZNVF-O (*left panels*), ZNVF-P (*center panels*), and NVF-$\beta2$ (*right panels*) at the snapshot in time $t = 100$ orbits. The *top panels* show streamlines for the poloidal magnetic field components and colours show the toroidal magnetic field strength for a slice through the xz-plane at $y = 0$. The *bottom panels* show streamlines for the horizontal magnetic field components and colours show the vertical magnetic field strength for a slice through the xy-plane at $z = 0$. In all cases, the toroidal magnetic field dominates and is well-organized at the disc mid-plane. Notably, the toroidal magnetic field has large-scale coherence and is most highly organized for the strongly magnetized disc simulation NVF-$\beta2$.

corona ($\widehat{\beta} < 0.1$ for $|z| > 2H_0$). However, even in this case the disc evolves toward a weakly magnetized core ($\widehat{\beta}^{\mathrm{mid}} \simeq 32$). For more physically meaningful boundary conditions that allow mass and magnetic flux to buoyantly escape, the initially strong toroidal flux is quickly expelled and the disc settles into a weakly magnetized state ($\widehat{\beta}^{\mathrm{mid}} \simeq 45$) that appears identical to similar simulations initialized with much weaker toroidal fields. We find no local limit in which a strongly magnetized disc (i.e., $\widehat{\beta}^{\mathrm{mid}} \lesssim 1$) can be sustained given an initial configuration with zero net vertical flux and outflow boundary conditions.

6.5   Discussion and Conclusions

In this paper we have argued that a strong poloidal magnetic flux threading the accretion disc is necessary in order to generate and sustain a magnetically dominated state. This conclusion differs from that of Johansen & Levin (2008), who observed a strong magnetization ($\beta^{\mathrm{mid}} \simeq 2$) in zero net vertical flux simulations that was sustained for at least a moderate duration (20-30 orbits). It appears likely that the difference between our results is a consequence of the different vertical boundary conditions. Although we never find a strongly magnetized disc mid-plane, we do find strong magnetization at quite small heights above the mid-plane if we adopt periodic boundary conditions that — like those used by Johansen & Levin (2008) — confine the toroidal flux within the simulation domain[2] . In the more physically-motivated situation where magnetic flux can escape, the initially strong flux is buoyantly expelled and the disc settles into a weakly magnetized state characteristic of local disc simulations with zero/weak net vertical flux. As we have noted previously (Salvesen et al., 2016b), the properties of the MRI dynamo do vary when the disc becomes strongly magnetized, with the characteristic reversals of toroidal field becoming increasingly infrequent and possibly entirely absent. Given this, it is possible that the Parker instability (Parker, 1966; Shu, 1974) plays a role in the dynamo process in highly magnetized discs, as envisaged by Tout & Pringle (1992) and Johansen & Levin (2008). We suggest, however, that a net poloidal flux is a pre-requisite for any dynamo that leads to strongly magnetized accretion discs.

Even without a zero net vertical flux route to strong magnetization, there are plausible pathways to forming strongly magnetized discs via poloidal fields. The requisite field threading the disc may be generated

---

[2] For technical reasons, we have not been able to run a case with *identical* boundary conditions to those used by Johansen & Levin (2008), and hence some differences are expected between our run ZNVF-P and theirs.

in situ and/or externally. In the *in situ* scenario, random small-scale field generated by dynamo activity within local patches of the disc could combine coherently to form a large-scale poloidal magnetic field (Tout & Pringle, 1996; King et al., 2004). It is known that this process generates poloidal fields of sufficient strength to locally modify the MRI (Sorathia et al., 2010; Beckwith et al., 2011), but whether the ultimate outcome of such an inverse cascade is sufficient to form a strongly magnetized disc is unclear. In the external field scenario, a pervading background magnetic field could provide the poloidal flux. This "fossil field" could be an interstellar magnetic field or a galactic field in the context of accretion discs in X-ray binaries and around supermassive black holes, respectively. Regardless of the origin of the net poloidal flux, the efficiency of radial transport of flux through the accretion disc depends upon the effective magnetic diffusivity and the geometric thickness of the disc (Lubow et al., 1994; Guilet & Ogilvie, 2012). Given favorable conditions for accumulation of poloidal magnetic flux, a strongly magnetized disc would necessarily follow. In X-ray binaries, where there is strong evidence that the disc alternates between geometrically thick and thin configurations near the black hole, changes in the transport efficiency could lead to cyclic accumulation and loss of flux (Begelman & Armitage, 2014).

Direct measurement of disc magnetic fields remains difficult. Numerous accretion disc phenomena, however, appear to be sensitive to the degree of magnetization, and further study of these may allow for useful constraints. Examples include the variability properties of radiation pressure dominated discs, which are predicted to be viscously/thermally stable when magnetic pressure-dominated (Begelman & Pringle, 2007), unlike standard disc models without magnetic pressure support (Lightman & Eardley, 1974; Shakura & Sunyaev, 1976), and the size of discs in active galactic nuclei, which are predicted to be more stable against fragmentation into stars when strongly magnetized (Pariev et al., 2003; Begelman & Pringle, 2007; Gaburov et al., 2012) than otherwise (Shlosman & Begelman, 1987). From a more directly observational perspective, vertical magnetic pressure support acts to harden the emergent accretion disc spectrum (e.g., Blaes et al., 2006). For extremely magnetized discs, Begelman & Pringle (2007) predict dramatic spectral hardening with a colour correction factor of $f_{\rm col} \sim 5$. We have previously argued that the evolution of the disc spectral component during black hole X-ray binary state transitions can be explained by a variable $f_{\rm col}$, arising from changes in the disc vertical structure (Salvesen et al., 2013), and we are currently working to

quantify the degeneracies between $f_{\rm col}$ and black hole spin determined via the continuum fitting technique (Salvesen et al., in preparation).

For a geometrically thin disc supporting an MRI-dynamo, buoyant fields escape vertically on a time scale (comparable to the free-fall time scale; Begelman et al., 2015; Salvesen et al., 2016b) that is short compared to the time scale for viscous radial advection of B_ϕ. The local approximation, used by both Johansen & Levin (2008) and ourselves, should then be appropriate. For somewhat thicker discs, long-duration global accretion disc simulations with varying levels of background poloidal magnetic flux are needed. Promising initial studies of strongly magnetized discs in the global limit have already been completed (Machida et al., 2000; Gaburov et al., 2012; Sądowski, 2016). Currently, however, the presence of a net poloidal magnetic flux is the only demonstrated way to generate and maintain an accretion disc with a dynamically important magnetic field (i.e., $\beta^{\rm mid} \sim 1$). Future work on disc accretion physics in this strongly magnetized regime may help decipher the enigmatic phenomena associated with accretion discs in X-ray binaries and galactic nuclei.

Acknowledgments

Chapter 7

Conclusions

Over 40 years ago, Shakura & Sunyaev (1973) revolutionized our understanding of astrophysical accretion discs around compact objects. The X-ray spectrum emitted by an accretion disc in a black hole X-ray binary system was subsequently definitively observed (Mitsuda et al., 1984; Makishima et al., 1986); thus, validating the basic multi-colour disc blackbody model. Some time later, Balbus & Hawley (1991) identified the magnetorotational instability (MRI) as the physical mechanism that allows accretion to proceed, which solidified magnetic fields as playing a fundamental role in disc accretion.

With the launch of X-ray observatories with unprecedented timing (e.g., *RXTE*) and spectral (e.g., *XMM-Newton*, *Chandra*) capabilities, a rich phenomenology of black hole X-ray binaries emerged (Remillard & McClintock, 2006). Any explanations for the enigmatic behavior of black hole X-ray binaries (e.g., spectral state transitions) would have to consider the time-dependent interplay between the accretion disc, wind, corona, and jet. Empirically, this behavior could be explained by a truncated disc model (e.g., Esin et al., 1997). However, this picture has not yet been unambiguously confirmed observationally nor has a physical mechanism been identified for a migrating inner disc edge. Chapter 2 was inspired by the largely unconstrained geometry of the inner disc regions. Fitting X-ray data of the transient black hole X-ray binary GX 339–4, we showed that a radially fixed (i.e., non-truncated) disc with a variable vertical structure — perhaps due to an evolving magnetic state of the disc — is a viable explanation for the observed disc spectral evolution. In Chapter 3, we introduced a toy model that appeals to disc tearing — a process that awaits observational (in)validation — as a potential mechanism for black hole state transitions. While this model is in its infancy, it is one of few attempts to understand the complete black hole state transition accretion

cycle.

Computational advances and the application of the "shearing box" approximation ushered in a new era for accretion disc physics (Hawley et al., 1995). Numerical simulations of accretion discs in this local limit opened the door to studying the MRI and its non-linear evolution into turbulence. A major finding from these simulations is that the MRI turbulent stresses — arising from correlated radial and azimuthal fluctuations in the magnetic field and fluid velocity — responsible for transporting angular momentum and driving accretion appear to be inherently local (but see Simon et al., 2012). This is precisely the basis for the α prescription of Shakura & Sunyaev (1973), which therefore might be an adequate description of MRI turbulence. Shearing box simulations with vertical density stratification and zero net vertical magnetic flux show that α converges to ~ 0.01 (Davis et al., 2010), while a net vertical magnetic flux couples the field to the fluid and enhances turbulent transport of angular momentum (Hawley et al., 1995). In Chapter 5, we performed shearing box simulations that included a background net vertical magnetic flux of varying strength that spanned nearly the full range over which the MRI is linearly unstable. We found that the MRI-driven turbulent stress parametrized by α is tightly correlated with the net vertical flux, achieving $\alpha \sim 0.01 - 1$. Accretion discs in dwarf novae (a subclass of cataclysmic variables) have $\alpha \sim 0.1 - 0.4$ (King et al., 2004), while α has yet to be measured in a black hole accretion disc.

Dynamo activity materializes in simulations that incorporate stratification of the disc atmosphere due to the vertical gravity of the black hole (Brandenburg et al., 1995). The linearly unstable vertical field generates radial field, which is stretched into a dominant azimuthal field by the differential rotation. This growing azimuthal field buoyantly rises, producing vertical field and completing the cycle. What's more, the MRI-dynamo continually produces quasi-periodic alternating signs of azimuthal magnetic field that buoyantly escapes. In the presence of a net vertical magnetic flux, the dynamo can constantly feed off of this background field to generate an even stronger azimuthal field. In Chapter 5, we characterized the properties of the MRI-dynamo for a very wide range in net vertical magnetic flux and found that the quasi-periodic flip-flops in the azimuthal field can persist even when the disc mid-plane is magnetic pressure-dominated. We also found that these simulations support the simple model for dynamo activity given by Begelman et al. (2015).

Inspired by observations of accretion disc winds in black hole X-ray binaries that imply strong magnetic fields (e.g., Miller et al., 2006b, 2016), we investigated how such a strongly magnetized accretion disc might form. In Chapter 5, we showed that given a sufficiently strong background poloidal flux, a strong azimuthal field will develop in the disc mid-plane regions and be sustained by dynamo activity. In Chapter 6, we considered the alternative initial condition of a zero net vertical magnetic flux and an initial azimuthal magnetic field in equipartition with the gas pressure. This initially strong azimuthal field could not be sustained by dynamo activity; therefore, we conclude that strongly magnetized discs require poloidal flux.

While understanding the phenomena and physics of black hole accretion discs is interesting in its own right, these machines can also be used as tools for measuring black hole spin as follows. The location of the innermost stable circular orbit (ISCO) is uniquely set by the black hole spin. Because regions interior to the ISCO are thought to be devoid of emitting gas, a measurement of the ISCO interpreted as the inner edge of the accretion disc acts as a measurement of the black hole spin. In Chapter 4 we showed that the black hole spin measured by two well-established techniques are often at odds with each other for the same X-ray binary. Dissecting the continuum fitting method for measuring black hole spin, we demonstrated that uncertainties related to the vertical structure of the disc dominate the error budget, yet these are not properly taken into consideration. We emphasize that the observed accretion disc spectrum is sensitive to the contribution from magnetic pressure support to the vertical hydrostatic equilibrium (Blaes et al., 2006), particularly if the disc is strongly magnetized (Begelman & Pringle, 2007). Therefore, the magnetic state of the disc should be considered before these spin measurements may be deemed robust.

The compelling evidence for and important implications of strongly magnetized accretion discs justifies their further study, which is what I plan to do in the near future. However, whether or not black hole accretion discs turn out to be strongly magnetized remains to be seen.

Bibliography

Abramowicz M. A., Kato S., 1989, ApJ, 336, 304

Afshordi N., Paczyński B., 2003, ApJ, 592, 354

Agol E., Kamionkowski M., Koopmans L. V. E., Blandford R. D., 2002, ApJ, 576, L131

Agol E., Krolik J. H., 2000, ApJ, 528, 161

Armitage P. J., Reynolds C. S., Chiang J., 2001, ApJ, 548, 868

Arnaud K. A., 1996, in Astronomical Society of the Pacific Conference Series, Vol. 101, Astronomical Data Analysis Software and Systems V, G. H. Jacoby & J. Barnes, ed., p. 17

Arons J., 1992, ApJ, 388, 561

Bai X.-N., Stone J. M., 2013, ApJ, 767, 30

Bailyn C. D., Jain R. K., Coppi P., Orosz J. A., 1998, ApJ, 499, 367

Balbus S. A., Hawley J. F., 1991, ApJ, 376, 214

Balbus S. A., Hawley J. F., 1998, Reviews of Modern Physics, 70, 1

Bardeen J. M., Petterson J. A., 1975, ApJ, 195, L65

Bardeen J. M., Press W. H., Teukolsky S. A., 1972, ApJ, 178, 347

Barth A. J., Sarzi M., Rix H.-W., Ho L. C., Filippenko A. V., Sargent W. L. W., 2001, ApJ, 555, 685

Beckwith K., Armitage P. J., Simon J. B., 2011, MNRAS, 416, 361

Beckwith K., Hawley J. F., Krolik J. H., 2009, ApJ, 707, 428

Begelman M. C., 2001, ApJ, 551, 897

Begelman M. C., 2002, ApJ, 568, L97

Begelman M. C., 2006, ApJ, 643, 1065

Begelman M. C., Armitage P. J., 2014, ApJ, 782, L18

Begelman M. C., Armitage P. J., Reynolds C. S., 2015, ApJ, 809, 118

Begelman M. C., King A. R., Pringle J. E., 2006, MNRAS, 370, 399

Begelman M. C., Pringle J. E., 2007, MNRAS, 375, 1070

Belloni T., Homan J., Casella P., van der Klis M., Nespoli E., Lewin W. H. G., Miller J. M., Méndez M., 2005, A&A, 440, 207

Belloni T. M., 2010, in Lecture Notes in Physics, Berlin Springer Verlag, Vol. 794, Lecture Notes in Physics, Berlin Springer Verlag, Belloni T., ed., p. 53

Beloborodov A. M., 1999, ApJ, 510, L123

Bisnovatyi-Kogan G. S., Ruzmaikin A. A., 1974, Ap&SS, 28, 45

Blackman E. G., Penna R. F., Varnière P., 2008, New A, 13, 244

Blaes O., 2014, Space Sci. Rev., 183, 21

Blaes O. M., Davis S. W., Hirose S., Krolik J. H., Stone J. M., 2006, ApJ, 645, 1402

Blandford R. D., Begelman M. C., 1999, MNRAS, 303, L1

Blandford R. D., McKee C. F., 1982, ApJ, 255, 419

Blandford R. D., Payne D. G., 1982, MNRAS, 199, 883

Blandford R. D., Znajek R. L., 1977, MNRAS, 179, 433

Blum J. L., Miller J. M., Fabian A. C., Miller M. C., Homan J., van der Klis M., Cackett E. M., Reis R. C., 2009, ApJ, 706, 60

Bondi H., 1952, MNRAS, 112, 195

Bradt H. V., Rothschild R. E., Swank J. H., 1993, A&AS, 97, 355

Brandenburg A., Nordlund A., Stein R. F., Torkelsson U., 1995, ApJ, 446, 741

Cabanac C., Fender R. P., Dunn R. J. H., Körding E. G., 2009, MNRAS, 396, 1415

Cantrell A. G. et al., 2010, ApJ, 710, 1127

Casella P., Belloni T., Homan J., Stella L., 2004, A&A, 426, 587

Casella P., Belloni T., Stella L., 2005, ApJ, 629, 403

Chandrasekhar S., 1961, Hydrodynamic and hydromagnetic stability

Cowley A. P., Schmidtke P. C., Hutchings J. B., Crampton D., 2002, AJ, 123, 1741

Cui W., 2004, ApJ, 605, 662

Cunningham C. T., 1975, ApJ, 202, 788

Davis S. W., Blaes O. M., Hubeny I., Turner N. J., 2005, ApJ, 621, 372

Davis S. W., Hubeny I., 2006, ApJS, 164, 530

Davis S. W., Stone J. M., Pessah M. E., 2010, ApJ, 713, 52

Dexter J., Agol E., 2011, ApJ, 727, L24

Dexter J., Quataert E., 2012, MNRAS, 426, L71

Dunn R. J. H., Fender R. P., Körding E. G., Belloni T., Cabanac C., 2010, MNRAS, 403, 61

Dunn R. J. H., Fender R. P., Körding E. G., Belloni T., Merloni A., 2011, MNRAS, 411, 337

Dunn R. J. H., Fender R. P., Körding E. G., Cabanac C., Belloni T., 2008, MNRAS, 387, 545

Ebisawa K., Mitsuda K., Hanawa T., 1991, ApJ, 367, 213

Ebisuzaki T., Sugimoto D., Hanawa T., 1984, PASJ, 36, 551

Esin A. A., McClintock J. E., Drake J. J., Garcia M. R., Haswell C. A., Hynes R. I., Muno M. P., 2001, ApJ, 555, 483

Esin A. A., McClintock J. E., Narayan R., 1997, ApJ, 489, 865

Fabian A. C., Rees M. J., Stella L., White N. E., 1989, MNRAS, 238, 729

Fabian A. C. et al., 2012, MNRAS, 424, 217

Felten J. E., Rees M. J., 1972, A&A, 17, 226

Fender R., Belloni T., 2004, ARA&A, 42, 317

Fender R. et al., 1999a, ApJ, 519, L165

Fender R. P., 2001, MNRAS, 322, 31

Fender R. P., Belloni T. M., Gallo E., 2004, MNRAS, 355, 1105

Fender R. P., Garrington S. T., McKay D. J., Muxlow T. W. B., Pooley G. G., Spencer R. E., Stirling A. M., Waltman E. B., 1999b, MNRAS, 304, 865

Feng H., Kaaret P., 2006, ApJ, 650, L75

Ferrarese L., Merritt D., 2000, ApJ, 539, L9

Fragile P. C., 2014, Space Sci. Rev., 183, 87

Fragile P. C., Blaes O. M., Anninos P., Salmonson J. D., 2007, ApJ, 668, 417

Fragile P. C., Lindner C. C., Anninos P., Salmonson J. D., 2009, ApJ, 691, 482

Fragos T., Tremmel M., Rantsiou E., Belczynski K., 2010, ApJ, 719, L79

Frank J., King A., Raine D., 1992, Accretion power in astrophysics., Frank, J., King, A., & Raine, D., ed.

Frank J., King A., Raine D. J., 2002, Accretion Power in Astrophysics: Third Edition

Fromang S., Latter H., Lesur G., Ogilvie G. I., 2013, A&A, 552, A71

Gaburov E., Johansen A., Levin Y., 2012, ApJ, 758, 103

Gallo E., Corbel S., Fender R. P., Maccarone T. J., Tzioumis A. K., 2004, MNRAS, 347, L52

Gammie C. F., 1998, MNRAS, 297, 929

Gammie C. F., 1999, ApJ, 522, L57

Gammie C. F., Goodman J., Ogilvie G. I., 2000, MNRAS, 318, 1005

Gardiner T. A., Stone J. M., 2005, Journal of Computational Physics, 205, 509

Gardiner T. A., Stone J. M., 2008, Journal of Computational Physics, 227, 4123

Gebhardt K. et al., 2000, ApJ, 539, L13

Ghez A. M., Salim S., Hornstein S. D., Tanner A., Lu J. R., Morris M., Becklin E. E., Duchêne G., 2005, ApJ, 620, 744

Giannios D., Spruit H. C., 2004, A&A, 427, 251

Gierliński M., Done C., 2004, MNRAS, 347, 885

Gierliński M., Done C., Page K., 2008, MNRAS, 388, 753

Gierliński M., Maciołek-Niedźwiecki A., Ebisawa K., 2001, MNRAS, 325, 1253

Gierliński M., Zdziarski A. A., Poutanen J., Coppi P. S., Ebisawa K., Johnson W. N., 1999, MNRAS, 309, 496

Gladstone J. C., Roberts T. P., Done C., 2009, MNRAS, 397, 1836

Goldreich P., Lynden-Bell D., 1965, MNRAS, 130, 125

Gou L. et al., 2009, ApJ, 701, 1076

Gou L. et al., 2011, ApJ, 742, 85

Gou L., McClintock J. E., Steiner J. F., Narayan R., Cantrell A. G., Bailyn C. D., Orosz J. A., 2010, ApJ, 718, L122

Greene J., Bailyn C. D., Orosz J. A., 2001, ApJ, 554, 1290

Greenhill L. J. et al., 2003, ApJ, 590, 162

Gressel O., Pessah M. E., 2015, ApJ, 810, 59

Guan X., Gammie C. F., 2011, ApJ, 728, 130

Guilet J., Ogilvie G. I., 2012, MNRAS, 424, 2097

Haardt F., Maraschi L., 1991, ApJ, 380, L51

Harlaftis E. T., Greiner J., 2004, A&A, 414, L13

Hawley J. F., Gammie C. F., Balbus S. A., 1995, ApJ, 440, 742

Hawley J. F., Guan X., Krolik J. H., 2011, ApJ, 738, 84

Hawley J. F., Krolik J. H., 2001, ApJ, 548, 348

Hawley J. F., Krolik J. H., 2002, ApJ, 566, 164

Herault J., Rincon F., Cossu C., Lesur G., Ogilvie G. I., Longaretti P.-Y., 2011, Phys. Rev. E, 84, 036321

Hirose S., Krolik J. H., Blaes O., 2009, ApJ, 691, 16

Hirose S., Krolik J. H., Stone J. M., 2006, ApJ, 640, 901

Hjellming R. M., Rupen M. P., 1995, Nature, 375, 464

Homan J., Wijnands R., van der Klis M., Belloni T., van Paradijs J., Klein-Wolt M., Fender R., Méndez M., 2001, ApJS, 132, 377

Hua X.-M., Titarchuk L., 1995, ApJ, 449, 188

Hughes A. M. et al., 2009, ApJ, 698, 131

Hynes R. I., Steeghs D., Casares J., Charles P. A., O'Brien K., 2003, ApJ, 583, L95

Hynes R. I., Steeghs D., Casares J., Charles P. A., O'Brien K., 2004, ApJ, 609, 317

Ibragimov A., Poutanen J., Gilfanov M., Zdziarski A. A., Shrader C. R., 2005, MNRAS, 362, 1435

Ingram A., Done C., Fragile P. C., 2009, MNRAS, 397, L101

Ipser J. R., 1996, ApJ, 458, 508

Jahoda K., Markwardt C. B., Radeva Y., Rots A. H., Stark M. J., Swank J. H., Strohmayer T. E., Zhang W., 2006, ApJS, 163, 401

Jahoda K., Swank J. H., Giles A. B., Stark M. J., Strohmayer T., Zhang W., Morgan E. H., 1996, in Society of Photo-Optical Instrumentation Engineers (SPIE) Conference Series, Vol. 2808, Society of Photo-Optical Instrumentation Engineers (SPIE) Conference Series, O. H. Siegmund & M. A. Gummin, ed., pp. 59–70

Johansen A., Levin Y., 2008, A&A, 490, 501

Jonker P. G., Nelemans G., 2004, MNRAS, 354, 355

Kaaret P., Corbel S., Prestwich A. H., Zezas A., 2003, Science, 299, 365

Kalemci E., Tomsick J. A., Rothschild R. E., Pottschmidt K., Kaaret P., 2004, ApJ, 603, 231

Kato S., 1990, PASJ, 42, 99

Katz J. I., 1973, Nature Physical Science, 246, 87

King A. L. et al., 2013a, ApJ, 762, 103

King A. R., Davies M. B., Ward M. J., Fabbiano G., Elvis M., 2001, ApJ, 552, L109

King A. R., Kolb U., 1999, MNRAS, 305, 654

King A. R., Livio M., Lubow S. H., Pringle J. E., 2013b, MNRAS, 431, 2655

King A. R., Pringle J. E., Livio M., 2007, MNRAS, 376, 1740

King A. R., Pringle J. E., West R. G., Livio M., 2004, MNRAS, 348, 111

Kolehmainen M., Done C., 2010, MNRAS, 406, 2206

Kolehmainen M., Done C., Díaz Trigo M., 2011, MNRAS, 416, 311

Kormendy J., Richstone D., 1995, ARA&A, 33, 581

Krolik J. H., 1999, ApJ, 515, L73

Laor A., 1991, ApJ, 376, 90

Lasota J.-P., 2001, New A Rev., 45, 449

Latter H. N., Fromang S., Gressel O., 2010, MNRAS, 406, 848

Lense J., Thirring H., 1918, Physikalische Zeitschrift, 19, 156

Lesur G., Ferreira J., Ogilvie G. I., 2013, A&A, 550, A61

Li L.-X., Zimmerman E. R., Narayan R., McClintock J. E., 2005, ApJS, 157, 335

Lightman A. P., Eardley D. M., 1974, ApJ, 187, L1

Lightman A. P., White T. R., 1988, ApJ, 335, 57

Liu J., McClintock J. E., Narayan R., Davis S. W., Orosz J. A., 2008, ApJ, 679, L37

Lodato G., Gerosa D., 2013, MNRAS, 429, L30

Lodato G., Price D. J., 2010, MNRAS, 405, 1212

Lodato G., Pringle J. E., 2006, MNRAS, 368, 1196

Lodato G., Pringle J. E., 2007, MNRAS, 381, 1287

Lubow S. H., Papaloizou J. C. B., Pringle J. E., 1994, MNRAS, 268, 1010

Maccarone T. J., 2002, MNRAS, 336, 1371

Machida M., Hayashi M. R., Matsumoto R., 2000, ApJ, 532, L67

Madhusudhan N., Justham S., Nelson L., Paxton B., Pfahl E., Podsiadlowski P., Rappaport S., 2006, ApJ, 640, 918

Magorrian J. et al., 1998, AJ, 115, 2285

Maitra D., Miller J. M., Reynolds M. T., Reis R., Nowak M., 2014, ApJ, 794, 85

Makishima K., Maejima Y., Mitsuda K., Bradt H. V., Remillard R. A., Tuohy I. R., Hoshi R., Nakagawa M., 1986, ApJ, 308, 635

Markert T. H., Canizares C. R., Clark G. W., Lewin W. H. G., Schnopper H. W., Sprott G. F., 1973, ApJ, 184, L67

Martin R. G., Tout C. A., Pringle J. E., 2010, MNRAS, 401, 1514

McClintock J. E., Narayan R., Rybicki G. B., 2004, ApJ, 615, 402

McClintock J. E., Narayan R., Steiner J. F., 2014, Space Sci. Rev., 183, 295

McClintock J. E., Shafee R., Narayan R., Remillard R. A., Davis S. W., Li L.-X., 2006, ApJ, 652, 518

McKinney J. C., Tchekhovskoy A., Blandford R. D., 2013, Science, 339, 49

Merloni A., Fabian A. C., 2002, MNRAS, 332, 165

Merloni A., Fabian A. C., Ross R. R., 2000, MNRAS, 313, 193

Meyer F., Meyer-Hofmeister E., 1982, A&A, 106, 34

Meyer-Hofmeister E., Vogt N., Meyer F., 1996, A&A, 310, 519

Mignone A., 2007, Journal of Computational Physics, 225, 1427

Miller J. M., Cackett E. M., Reis R. C., 2009a, ApJ, 707, L77

Miller J. M. et al., 2004, ApJ, 606, L131

Miller J. M., Homan J., 2005, ApJ, 618, L107

Miller J. M., Homan J., Steeghs D., Rupen M., Hunstead R. W., Wijnands R., Charles P. A., Fabian A. C., 2006a, ApJ, 653, 525

Miller J. M., Pooley G. G., Fabian A. C., Nowak M. A., Reis R. C., Cackett E. M., Pottschmidt K., Wilms J., 2012, ApJ, 757, 11

Miller J. M., Raymond J., Fabian A., Steeghs D., Homan J., Reynolds C., van der Klis M., Wijnands R., 2006b, Nature, 441, 953

Miller J. M. et al., 2016, ApJ, 821, L9

Miller J. M. et al., 2006c, ApJ, 646, 394

Miller J. M., Raymond J., Reynolds C. S., Fabian A. C., Kallman T. R., Homan J., 2008, ApJ, 680, 1359

Miller J. M., Reynolds C. S., Fabian A. C., Miniutti G., Gallo L. C., 2009b, ApJ, 697, 900

Miller K. A., Stone J. M., 2000, ApJ, 534, 398

Miller M. C., Miller J. M., 2015, Phys. Rep., 548, 1

Miniutti G., Fabian A. C., 2004, MNRAS, 349, 1435

Misner C. W., Thorne K. S., Wheeler J. A., 1973, Gravitation

Mitsuda K. et al., 1984, PASJ, 36, 741

Miyoshi M., Moran J., Herrnstein J., Greenhill L., Nakai N., Diamond P., Inoue M., 1995, Nature, 373, 127

Miyoshi T., Kusano K., 2005, Journal of Computational Physics, 208, 315

Motta S., Muñoz-Darias T., Casella P., Belloni T., Homan J., 2011, MNRAS, 418, 2292

Muñoz-Darias T., Casares J., Martínez-Pais I. G., 2008, MNRAS, 385, 2205

Muñoz-Darias T., Fender R. P., Motta S. E., Belloni T. M., 2014, MNRAS, 443, 3270

Nandi A., Debnath D., Mandal S., Chakrabarti S. K., 2012, A&A, 542, A56

Narayan R., Igumenshchev I. V., Abramowicz M. A., 2003, PASJ, 55, L69

Narayan R., Yi I., 1994, ApJ, 428, L13

Natarajan P., Pringle J. E., 1998, ApJ, 506, L97

Nayakshin S., 2005, MNRAS, 359, 545

Nishiyama S. et al., 2010, ApJ, 722, L23

Nixon C., King A., 2013, ApJ, 765, L7

Nixon C., King A., Price D., 2013, MNRAS, 434, 1946

Nixon C., King A., Price D., Frank J., 2012a, ApJ, 757, L24

Nixon C., Salvesen G., 2014, MNRAS, 437, 3994

Nixon C. J., King A. R., 2012, MNRAS, 421, 1201

Nixon C. J., King A. R., Price D. J., 2012b, MNRAS, 422, 2547

Noble S. C., Krolik J. H., Hawley J. F., 2010, ApJ, 711, 959

Novikov I. D., Thorne K. S., 1973, in Black Holes (Les Astres Occlus), C. Dewitt & B. S. Dewitt, ed., pp. 343–450

Nowak M. A., Wagoner R. V., 1991, ApJ, 378, 656

Nowak M. A., Wagoner R. V., 1992, ApJ, 393, 697

Nowak M. A., Wagoner R. V., 1993, ApJ, 418, 187

Nowak M. A., Wilms J., Dove J. B., 2002, MNRAS, 332, 856

Ogilvie G. I., 1999, MNRAS, 304, 557

Ogilvie G. I., 2003, MNRAS, 340, 969

Ogilvie G. I., Dubus G., 2001, MNRAS, 320, 485

Ogilvie G. I., Latter H. N., 2013, MNRAS, 433, 2420

O'Neill S. M., Reynolds C. S., Miller M. C., Sorathia K. A., 2011, ApJ, 736, 107

Orosz J. A., 2003, in IAU Symposium, Vol. 212, A Massive Star Odyssey: From Main Sequence to Supernova, van der Hucht K., Herrero A., Esteban C., eds., p. 365

Orosz J. A., Bailyn C. D., 1997, ApJ, 477, 876

Orosz J. A., Jain R. K., Bailyn C. D., McClintock J. E., Remillard R. A., 1998, ApJ, 499, 375

Orosz J. A., McClintock J. E., Aufdenberg J. P., Remillard R. A., Reid M. J., Narayan R., Gou L., 2011a, ApJ, 742, 84

Orosz J. A. et al., 2007, Nature, 449, 872

Orosz J. A. et al., 2009, ApJ, 697, 573

Orosz J. A., Steiner J. F., McClintock J. E., Buxton M. M., Bailyn C. D., Steeghs D., Guberman A., Torres M. A. P., 2014, ApJ, 794, 154

Orosz J. A., Steiner J. F., McClintock J. E., Torres M. A. P., Remillard R. A., Bailyn C. D., Miller J. M., 2011b, ApJ, 730, 75

Özel F., Psaltis D., Narayan R., McClintock J. E., 2010, ApJ, 725, 1918

Paczyńsky B., Wiita P. J., 1980, A&A, 88, 23

Page D. N., Thorne K. S., 1974, ApJ, 191, 499

Papaloizou J. C. B., Lin D. N. C., 1995, ApJ, 438, 841

Papaloizou J. C. B., Pringle J. E., 1983, MNRAS, 202, 1181

Pariev V. I., Blackman E. G., Boldyrev S. A., 2003, A&A, 407, 403

Parker E. N., 1966, ApJ, 145, 811

Pasham D. R., Strohmayer T. E., 2013, ApJ, 764, 93

Penrose R., 1969, Nuovo Cimento Rivista Serie, 1, 252

Pessah M. E., Chan C.-k., Psaltis D., 2007, ApJ, 668, L51

Pessah M. E., Psaltis D., 2005, ApJ, 628, 879

Peterson B. M. et al., 2004, ApJ, 613, 682

Price D. J., 2007, PASA, 24, 159

Price D. J., Tricco T. S., Bate M. R., 2012, MNRAS, 423, L45

Pringle J. E., 1981, ARA&A, 19, 137

Pringle J. E., 1992, MNRAS, 258, 811

Pringle J. E., 1996, MNRAS, 281, 357

Pringle J. E., Rees M. J., 1972, A&A, 21, 1

Protassov R., van Dyk D. A., Connors A., Kashyap V. L., Siemiginowska A., 2002, ApJ, 571, 545

Reid M. J., McClintock J. E., Narayan R., Gou L., Remillard R. A., Orosz J. A., 2011, ApJ, 742, 83

Reis R. C., Fabian A. C., Miller J. M., 2010, MNRAS, 402, 836

Reis R. C., Fabian A. C., Ross R. R., Miller J. M., 2009, MNRAS, 395, 1257

Reis R. C., Fabian A. C., Ross R. R., Miniutti G., Miller J. M., Reynolds C., 2008, MNRAS, 387, 1489

Reis R. C., Miller J. M., Reynolds M. T., Fabian A. C., Walton D. J., Cackett E., Steiner J. F., 2013, ApJ, 763, 48

Remillard R. A., McClintock J. E., 2006, ARA&A, 44, 49

Reynolds C. S., 2014, Space Sci. Rev., 183, 277

Reynolds C. S., Armitage P. J., 2001, ApJ, 561, L81

Reynolds C. S., Miller M. C., 2009, ApJ, 692, 869

Reynolds M. T., Miller J. M., 2013, ApJ, 769, 16

Ross R. R., Fabian A. C., Mineshige S., 1992, MNRAS, 258, 189

Ross R. R., Weaver R., McCray R., 1978, ApJ, 219, 292

Rothschild R. E. et al., 1998, ApJ, 496, 538

Rutledge R. E., Bildsten L., Brown E. F., Pavlov G. G., Zavlin V. E., 1999a, ApJ, 514, 945

Rutledge R. E. et al., 1999b, ApJS, 124, 265

Rybicki G. B., Lightman A. P., 1979, Radiative processes in astrophysics, Rybicki, G. B. & Lightman, A. P., ed.

Salvesen G., Armitage P. J., Simon J. B., Begelman M. C., 2016a, ArXiv e-prints

Salvesen G., Beckwith K., Simon J. B., O'Neill S. M., Begelman M. C., 2014, MNRAS, 438, 1355

Salvesen G., Miller J. M., Reis R. C., Begelman M. C., 2013, MNRAS, 431, 3510

Salvesen G., Simon J. B., Armitage P. J., Begelman M. C., 2016b, MNRAS, 457, 857

Sano T., Inutsuka S.-i., Turner N. J., Stone J. M., 2004, ApJ, 605, 321

Sądowski A., 2016, MNRAS, 459, 4397

Schnittman J. D., Homan J., Miller J. M., 2006, ApJ, 642, 420

Schnittman J. D., Krolik J. H., Noble S. C., 2013, ApJ, 769, 156

Shafee R., McClintock J. E., Narayan R., Davis S. W., Li L.-X., Remillard R. A., 2006, ApJ, 636, L113

Shakura N. I., Sunyaev R. A., 1973, A&A, 24, 337

Shakura N. I., Sunyaev R. A., 1976, MNRAS, 175, 613

Shapiro S. L., Lightman A. P., Eardley D. M., 1976, ApJ, 204, 187

Shaposhnikov N., Titarchuk L., 2009, ApJ, 699, 453

Shi J., Krolik J. H., Hirose S., 2010, ApJ, 708, 1716

Shimura T., Takahara F., 1995, ApJ, 445, 780

Shlosman I., Begelman M. C., 1987, Nature, 329, 810

Shu F. H., 1974, A&A, 33, 55

Sikora M., Begelman M. C., 2013, ApJ, 764, L24

Simon J. B., Bai X.-N., Armitage P. J., Stone J. M., Beckwith K., 2013, ApJ, 775, 73

Simon J. B., Beckwith K., Armitage P. J., 2012, MNRAS, 422, 2685

Simon J. B., Hawley J. F., Beckwith K., 2011, ApJ, 730, 94

Smak J., 1982, Acta Astron., 32, 199

Sorathia K. A., Krolik J. H., Hawley J. F., 2013a, ApJ, 777, 21

Sorathia K. A., Krolik J. H., Hawley J. F., 2013b, ApJ, 768, 133

Sorathia K. A., Reynolds C. S., Armitage P. J., 2010, ApJ, 712, 1241

Steiner J. F., McClintock J. E., 2012, ApJ, 745, 136

Steiner J. F., McClintock J. E., Orosz J. A., Remillard R. A., Bailyn C. D., Kolehmainen M., Straub O., 2014, ApJ, 793, L29

Steiner J. F., McClintock J. E., Reid M. J., 2012a, ApJ, 745, L7

Steiner J. F., Narayan R., McClintock J. E., Ebisawa K., 2009, PASP, 121, 1279

Steiner J. F. et al., 2012b, MNRAS, 427, 2552

Steiner J. F. et al., 2011, MNRAS, 416, 941

Stella L., Vietri M., Morsink S. M., 1999, ApJ, 524, L63

Stiele H., Motta S., Muñoz-Darias T., Belloni T. M., 2011, MNRAS, 418, 1746

Stone J. M., Gardiner T. A., 2010, ApJS, 189, 142

Stone J. M., Gardiner T. A., Teuben P., Hawley J. F., Simon J. B., 2008, ApJS, 178, 137

Stone J. M., Hawley J. F., Gammie C. F., Balbus S. A., 1996, ApJ, 463, 656

Suzuki T. K., Inutsuka S.-i., 2009, ApJ, 691, L49

Svensson R., Zdziarski A. A., 1994, ApJ, 436, 599

Swank J. H., 1999, Nuclear Physics B Proceedings Supplements, 69, 12

Tagger M., Pellat R., 1999, A&A, 349, 1003

Tananbaum H., Gursky H., Kellogg E. M., Levinson R., Schreier E., Giacconi R., 1972, ApJ, 174, L143

Tchekhovskoy A., Narayan R., McKinney J. C., 2011, MNRAS, 418, L79

Thorne K. S., 1974, ApJ, 191, 507

Titarchuk L., 1994, ApJ, 434, 570

Tomsick J. A. et al., 2008, ApJ, 680, 593

Tomsick J. A., Yamaoka K., Corbel S., Kaaret P., Kalemci E., Migliari S., 2009, ApJ, 707, L87

Torkelsson U., Ogilvie G. I., Brandenburg A., Pringle J. E., Nordlund Å., Stein R. F., 2000, MNRAS, 318, 47

Tout C. A., Pringle J. E., 1992, MNRAS, 259, 604

Tout C. A., Pringle J. E., 1996, MNRAS, 281, 219

Turk M. J., Smith B. D., Oishi J. S., Skory S., Skillman S. W., Abel T., Norman M. L., 2011, ApJS, 192, 9

Uttley P., McHardy I. M., 2001, MNRAS, 323, L26

Uzdensky D. A., 2013, ApJ, 775, 103

van der Klis M., 1989, ARA&A, 27, 517

Varnière P., Rodriguez J., Tagger M., 2002, A&A, 387, 497

Varnière P., Tagger M., 2002, A&A, 394, 329

Velikhov E., 1959, Zhur. Eksptl'. i Teoret. Fiz., 36

Volonteri M., Sikora M., Lasota J.-P., Merloni A., 2013, ApJ, 775, 94

Wijers R. A. M. J., Pringle J. E., 1999, MNRAS, 308, 207

Wilkinson T., Uttley P., 2009, MNRAS, 397, 666

Wilms J., Nowak M. A., Pottschmidt K., Pooley G. G., Fritz S., 2006, A&A, 447, 245

Yamada S. et al., 2009, ApJ, 707, L109

Zavlin V. E., Pavlov G. G., Shibanov Y. A., 1996, A&A, 315, 141

Zdziarski A. A., Gierliński M., Mikołajewska J., Wardziński G., Smith D. M., Harmon B. A., Kitamoto S., 2004, MNRAS, 351, 791

Zhang S. N., Cui W., Chen W., 1997, ApJ, 482, L155

Zimmerman E. R., Narayan R., McClintock J. E., Miller J. M., 2005, ApJ, 618, 832

Appendix A

Probability Density Functions and Change of Variables

We wish to obtain the probability density function (PDF) for the black hole spin parameter from the simplified version of the continuum fitting technique described in §4.3. This requires developing the necessary mathematics for transforming between various PDFs by change of variables as follows.

Using change of variables, we develop the equations to transform between the flux normalization PDF, $f(K_{\text{flux}})$, and the inner disc radius PDF, $f(r_{\text{in}})$, in §A.0.1 and §A.0.2. We can relate the flux normalization, K_{flux}, to the non-dimensional inner disc radius, $r_{\text{in}} = R_{\text{in}}/R_{\text{g}}$, by rewriting Equation 4.3 as,

$$K_{\text{flux}} = \frac{1}{f_{\text{col}}^4} \left(\frac{GM/c^2}{D} \right)^2 \cos\left(\theta_{\text{disc}} \right) r_{\text{in}}^2. \tag{A.1}$$

Similarly, we will also derive the transformation between the innermost stable circular orbit PDF, $f(r_{\text{ISCO}})$, and the black hole spin parameter PDF, $f(a)$, in §A.0.3 and §A.0.4. The equation relating the innermost stable circular orbit, r_{ISCO}, to the black hole spin parameter, a, is (Bardeen et al., 1972),

$$r_{\text{ISCO}} = \begin{cases} 3 + Z_2 - \sqrt{(3 - Z_1)(3 + Z_1 + 2Z_2)} : 0 \leq a \leq +1 \\ \\ 3 + Z_2 + \sqrt{(3 - Z_1)(3 + Z_1 + 2Z_2)} : -1 \leq a < 0, \end{cases} \tag{A.2}$$

where,

$$Z_1 \equiv 1 + \left(1 - a^2\right)^{1/3} \left[(1 + a)^{1/3} + (1 - a)^{1/3} \right] \tag{A.3}$$

$$Z_2 \equiv \sqrt{3a^2 + Z_1^2}. \tag{A.4}$$

A.0.1 Flux Normalization PDF, $f\left(K_{\text{flux}}\right)$

Given the set of independent[1] random variables M, D, θ_{disc}, f_{col}, and r_{in} with corresponding PDFs $f\left(M\right)$, $f\left(D\right)$, $f\left(\theta_{\text{disc}}\right)$, $f\left(f_{\text{col}}\right)$, and $f\left(r_{\text{in}}\right)$, we wish to find the PDF $f\left(K_{\text{flux}}\right)$ for random variable K_{flux}, where $K_{\text{flux}} = K_{\text{flux}}\left(M, D, \theta_{\text{disc}}, f_{\text{col}}, r_{\text{in}}\right)$ according to Equation A.1. The multivariate PDF $f\left(M, D, \theta_{\text{disc}}, f_{\text{col}}, r_{\text{in}}\right)$ transforms to $f\left(M, D, \theta_{\text{disc}}, f_{\text{col}}, K_{\text{flux}}\right)$ by change of variables,

$$f\left(M, D, \theta_{\text{disc}}, f_{\text{col}}, K_{\text{flux}}\right) = f\left(M, D, \theta_{\text{disc}}, f_{\text{col}}, r_{\text{in}}\right)\left|J_{r_{\text{in}} \rightarrow K_{\text{flux}}}\right|, \tag{A.5}$$

where, since the random variables are independent,

$$f\left(M, D, \theta_{\text{disc}}, f_{\text{col}}, r_{\text{in}}\right) = f\left(M\right) f\left(D\right) f\left(\theta_{\text{disc}}\right) f\left(f_{\text{col}}\right) f\left(r_{\text{in}}\right), \tag{A.6}$$

and $J_{r_{\text{in}} \rightarrow K_{\text{flux}}}$ is the Jacobian determinant for the change of variables given by,

$$
\begin{aligned}
J_{r_{\text{in}} \rightarrow K_{\text{flux}}} &= \det\left(\frac{\partial\left(M, D, \theta_{\text{disc}}, f_{\text{col}}, r_{\text{in}}\right)}{\partial\left(M, D, \theta_{\text{disc}}, f_{\text{col}}, K_{\text{flux}}\right)}\right) \\
&= \frac{\partial r_{\text{in}}}{\partial K_{\text{flux}}} \\
&= \frac{1}{2} f_{\text{col}}^2 \left(\frac{D}{GM/c^2}\right) \frac{1}{\sqrt{\cos\left(\theta_{\text{disc}}\right)}} K_{\text{flux}}^{-1/2}.
\end{aligned}
\tag{A.7}
$$

To find the flux normalization PDF, $f\left(K_{\text{flux}}\right)$, we marginalize $f\left(M, D, \theta_{\text{disc}}, f_{\text{col}}, K_{\text{flux}}\right)$ over M, D, θ_{disc}, and f_{col} to get,

$$f\left(K_{\text{flux}}\right) = \iiiint_{R_{\mathbf{x}}} f\left(\mathbf{x}\right) f\left(r_{\text{in}}\right) \left|J_{r_{\text{in}} \rightarrow K_{\text{flux}}}\right| d\mathbf{x}, \tag{A.8}$$

where,

$$\iiiint_{R_{\mathbf{x}}} \equiv \int_{f_{\text{col}}=1}^{\infty} \int_{\theta_{\text{disc}}=0}^{\pi/2} \int_{D=0}^{\infty} \int_{M=0}^{\infty} \tag{A.9}$$

$$f\left(\mathbf{x}\right) \equiv f\left(M\right) f\left(D\right) f\left(\theta_{\text{disc}}\right) f\left(f_{\text{col}}\right) \tag{A.10}$$

$$d\mathbf{x} \equiv dM\ dD\ d\theta_{\text{disc}}\ df_{\text{col}}. \tag{A.11}$$

Equation A.8 allows us to transform from $f\left(r_{\text{in}}\right)$ to $f\left(K_{\text{flux}}\right)$.

---

[1] Here and throughout, we assume that the random variables undergoing a transformation by change of variables are independent.

A.0.2   Inner Disc Radius PDF, $f(r_{\mathrm{in}})$

We will also have cause to run the PDF transformation described in §A.0.1 in reverse, as follows. Given the set of independent random variables M, D, θ_{disc}, f_{col}, and K_{flux} with corresponding PDFs $f(M)$, $f(D)$, $f(\theta_{\mathrm{disc}})$, $f(f_{\mathrm{col}})$, and $f(K_{\mathrm{flux}})$, we wish to find the PDF $f(r_{\mathrm{in}})$ for random variable r_{in}, where $r_{\mathrm{in}} = r_{\mathrm{in}}(M, D, \theta_{\mathrm{disc}}, f_{\mathrm{col}}, K_{\mathrm{flux}})$ according to Equation A.1. The multivariate PDF $f(M, D, \theta_{\mathrm{disc}}, f_{\mathrm{col}}, K_{\mathrm{flux}})$ transforms to $f(M, D, \theta_{\mathrm{disc}}, f_{\mathrm{col}}, r_{\mathrm{in}})$ by change of variables,

$$f(M, D, \theta_{\mathrm{disc}}, f_{\mathrm{col}}, r_{\mathrm{in}}) = f(M, D, \theta_{\mathrm{disc}}, f_{\mathrm{col}}, K_{\mathrm{flux}}) \left| J_{K_{\mathrm{flux}} \to r_{\mathrm{in}}} \right|, \tag{A.12}$$

where, since the random variables are independent,

$$f(M, D, \theta_{\mathrm{disc}}, f_{\mathrm{col}}, K_{\mathrm{flux}}) = f(M) f(D) f(\theta_{\mathrm{disc}}) f(f_{\mathrm{col}}) f(K_{\mathrm{flux}}) \tag{A.13}$$

and $J_{K_{\mathrm{flux}} \to r_{\mathrm{in}}}$ is the Jacobian determinant for the change of variables given by,

$$\begin{aligned} J_{K_{\mathrm{flux}} \to r_{\mathrm{in}}} &= \det \left(\frac{\partial(M, D, \theta_{\mathrm{disc}}, f_{\mathrm{col}}, K_{\mathrm{flux}})}{\partial(M, D, \theta_{\mathrm{disc}}, f_{\mathrm{col}}, r_{\mathrm{in}})} \right) \\ &= \frac{\partial K_{\mathrm{flux}}}{\partial r_{\mathrm{in}}} \\ &= \frac{2}{f_{\mathrm{col}}^4} \left(\frac{GM/c^2}{D} \right)^2 \cos(\theta_{\mathrm{disc}})\, r_{\mathrm{in}}. \end{aligned} \tag{A.14}$$

To find the inner disc radius PDF, $f(r_{\mathrm{in}})$, we marginalize $f(M, D, \theta_{\mathrm{disc}}, f_{\mathrm{col}}, r_{\mathrm{in}})$ over M, D, θ_{disc}, and f_{col} to get,

$$f(r_{\mathrm{in}}) = \iiiint_{R_{\mathbf{x}}} f(\mathbf{x}) f(K_{\mathrm{flux}}) \left| J_{K_{\mathrm{flux}} \to r_{\mathrm{in}}} \right| d\mathbf{x}. \tag{A.15}$$

Equation A.15 allows us to transform from $f(K_{\mathrm{flux}})$ to $f(r_{\mathrm{in}})$.

A.0.3   Black Hole Spin Parameter PDF, $f(a)$

While the measurable quantity is the inner disc radius PDF, we are interested in converting this to a black hole spin parameter PDF under the assumption that $r_{\mathrm{in}} = r_{\mathrm{ISCO}}$. Given the PDF $f(r_{\mathrm{ISCO}})$ for random variable r_{ISCO}, we can transform this to the PDF $f(a)$ for random variable a according to Equation A.2 by change of variables,

$$f(a) = f(r_{\mathrm{ISCO}}) \left| J_{r_{\mathrm{ISCO}} \to a} \right|, \tag{A.16}$$

where $J_{r_{\mathrm{ISCO}} \to a}$ is the Jacobian determinant for the change of variables given by,

$$
\begin{aligned}
J_{r_{\mathrm{ISCO}} \to a} &= \frac{dr_{\mathrm{ISCO}}}{da} \\
&= \begin{cases}
\dfrac{dZ_2}{da} - \dfrac{(3 - Z_1) \frac{dZ_2}{da} - (Z_1 + Z_2) \frac{dZ_1}{da}}{\sqrt{(3 - Z_1)(3 + Z_1 + 2Z_2)}} & : 0 \leq a \leq +1 \\[4ex]
\dfrac{dZ_2}{da} + \dfrac{(3 - Z_1) \frac{dZ_2}{da} - (Z_1 + Z_2) \frac{dZ_1}{da}}{\sqrt{(3 - Z_1)(3 + Z_1 + 2Z_2)}} & : -1 \leq a < 0,
\end{cases}
\end{aligned}
\tag{A.17}
$$

where,

$$
\begin{aligned}
\frac{dZ_1}{da} &= \frac{1}{3}\left[(1 + a)^{-2/3} - (1 - a)^{-2/3}\right](1 - a^2)^{1/3} \\
&\quad - \frac{2}{3}a\left[(1 + a)^{1/3} + (1 - a)^{1/3}\right](1 - a^2)^{-2/3}
\end{aligned}
\tag{A.18}
$$

$$
\frac{dZ_2}{da} = \frac{3a + Z_1 \frac{dZ_1}{da}}{\sqrt{3a^2 + Z_1^2}}.
\tag{A.19}
$$

Equation A.16 allows us to transform from $f(r_{\mathrm{ISCO}})$ to $f(a)$.

A.0.4   Innermost Stable Circular Orbit PDF, $f(r_{\mathrm{ISCO}})$

The reverse of the PDF transformation process in §A.0.3 is to compute the PDF $f(r_{\mathrm{ISCO}})$ for random variable r_{ISCO} given the PDF $f(a)$ for random variable a. However, solving Equation A.2 for a is analytically intractable, which prohibits computing the Jacobian determinant for the change of variables, $J_{a \to r_{\mathrm{ISCO}}} = da/dr_{\mathrm{ISCO}}$. Instead, we compute the unnormalized innermost stable circular orbit PDF, $f^*(r_{\mathrm{ISCO}})$, by iteratively solving Equation A.2 for the black hole spin parameter, a, across all values of r_{ISCO}. We then renormalize $f^*(r_{\mathrm{ISCO}})$ to obtain the desired innermost stable circular orbit PDF, $f(r_{\mathrm{ISCO}})$. This process allows us to transform from $f(a)$ to $f(r_{\mathrm{ISCO}})$.

Appendix B

Effects of Individual Parameter Uncertainties on Black Hole Spin Measurements

For the basic continuum fitting technique of §4.3, Equation A.1 relates the "ancillary observables," K_{flux}, M, D, θ_{disc}, and f_{col} to the "primary observable," r_{in}, which is needed to obtain a black hole spin measurement. Consider a black hole X-ray binary for which all but one ancillary observable are measured exactly. This one ancillary observable of interest, x, is measured with probability density function (PDF),

$$f(x) = N\left(x, \mu_x = x', \sigma_x = 0.1x'\right),$$ (B.1)

where $N(x, \mu_x, \sigma_x)$ is the normal distribution (Equation 4.5) and a prime represents the true parameter value. The PDFs for all other ancillary observables, $\mathbf{y}$, are Dirac delta functions centered on the true parameter values,

$$f(\mathbf{y}) = \delta\left(\mathbf{y} - \mathbf{y}'\right).$$ (B.2)

We now seek to determine the contribution to the uncertainty in the primary observable r_{in} (and ultimately the black hole spin parameter a) by each individual ancillary observable. The PDF for the ancillary observable of interest, $f(x)$, is related to the PDF for the inner disc radius $f_x(r_{\text{in}})$ by change of variables from x to r_{in},

$$f_x(r_{\text{in}}) = f(x)\,|J_x|,$$ (B.3)

where the Jacobian determinant for the change of variables is $J_x = \partial x / \partial r_{\text{in}}$ and Equation A.1 relates x to

r_{in}. The Jacobian determinants for each individual ancillary parameter of interest are,

$$J_{K_{\mathrm{flux}}} = \frac{\partial K_{\mathrm{flux}}}{\partial r_{\mathrm{in}}} = \frac{2K'_{\mathrm{flux}}}{r'^2_{\mathrm{in}}}r_{\mathrm{in}} \tag{B.4}$$

$$J_M = \frac{\partial M}{\partial r_{\mathrm{in}}} = -M'r'_{\mathrm{in}}r_{\mathrm{in}}^{-2} \tag{B.5}$$

$$J_D = \frac{\partial D}{\partial r_{\mathrm{in}}} = \frac{D'}{r'_{\mathrm{in}}} \tag{B.6}$$

$$J_{\theta_{\mathrm{disc}}} = \frac{\partial \theta_{\mathrm{disc}}}{\partial r_{\mathrm{in}}}$$
$$= 2\cos\left(\theta'_{\mathrm{disc}}\right) r'^2_{\mathrm{in}} \left[1 - \cos^2\left(\theta'_{\mathrm{disc}}\right)\left(\frac{r'_{\mathrm{in}}}{r_{\mathrm{in}}}\right)^4\right]^{-1/2} r_{\mathrm{in}}^{-3} \tag{B.7}$$

$$J_{f_{\mathrm{col}}} = \frac{\partial f_{\mathrm{col}}}{\partial r_{\mathrm{in}}} = \frac{f'_{\mathrm{col}}}{2\sqrt{r'_{\mathrm{in}}}}r_{\mathrm{in}}^{-1/2}. \tag{B.8}$$

Pairing each $f(x)$ (Equation B.1) with the corresponding J_x, Equation B.3 gives,

$$f_{K_{\mathrm{flux}}}\left(r_{\mathrm{in}}\right) = \frac{2K'_{\mathrm{flux}}}{r'^2_{\mathrm{in}}\sigma_{K_{\mathrm{flux}}}\sqrt{2\pi}}r_{\mathrm{in}}$$
$$\times \exp\left[\frac{-\left(K'_{\mathrm{flux}}\left(\frac{r_{\mathrm{in}}}{r'_{\mathrm{in}}}\right)^2 - \mu_{K_{\mathrm{flux}}}\right)^2}{2\sigma^2_{K_{\mathrm{flux}}}}\right] \tag{B.9}$$

$$f_M\left(r_{\mathrm{in}}\right) = \frac{M'r'_{\mathrm{in}}}{\sigma_M\sqrt{2\pi}}r_{\mathrm{in}}^{-2}\exp\left[\frac{-\left(M'\frac{r'_{\mathrm{in}}}{r_{\mathrm{in}}} - \mu_M\right)^2}{2\sigma^2_M}\right] \tag{B.10}$$

$$f_D\left(r_{\mathrm{in}}\right) = \frac{D'}{r'_{\mathrm{in}}\sigma_D\sqrt{2\pi}}\exp\left[\frac{-\left(D'\frac{r_{\mathrm{in}}}{r'_{\mathrm{in}}} - \mu_D\right)^2}{2\sigma^2_D}\right] \tag{B.11}$$

$$f_{\theta_{\mathrm{disc}}}\left(r_{\mathrm{in}}\right) = \frac{2\cos\left(\theta'_{\mathrm{disc}}\right)r'^2_{\mathrm{in}}}{\sigma_{\theta_{\mathrm{disc}}}\sqrt{2\pi}}\left[1 - \cos^2\left(\theta'_{\mathrm{disc}}\right)\left(\frac{r'_{\mathrm{in}}}{r_{\mathrm{in}}}\right)^4\right]^{-1/2}r_{\mathrm{in}}^{-3}$$
$$\times \exp\left[\frac{-\left(\cos^{-1}\left[\cos\left(\theta'_{\mathrm{disc}}\right)\left(\frac{r'_{\mathrm{in}}}{r_{\mathrm{in}}}\right)^2\right] - \mu_{\theta_{\mathrm{disc}}}\right)^2}{2\sigma^2_{\theta_{\mathrm{disc}}}}\right] \tag{B.12}$$

$$f_{f_{\mathrm{col}}}\left(r_{\mathrm{in}}\right) = \frac{f'_{\mathrm{col}}}{2\sqrt{r'_{\mathrm{in}}}\sigma_{f_{\mathrm{col}}}\sqrt{2\pi}}r_{\mathrm{in}}^{-1/2}$$
$$\times \exp\left[\frac{-\left(f'_{\mathrm{col}}\sqrt{\frac{r_{\mathrm{in}}}{r'_{\mathrm{in}}}} - \mu_{f_{\mathrm{col}}}\right)^2}{2\sigma^2_{f_{\mathrm{col}}}}\right]. \tag{B.13}$$

Finally, we obtain $f_x(a)$ from $f_x(r_{\mathrm{in}})$ from the methodology of §A.0.3 and plot the results in Figure

4.2.